Characterisation Studies of Proton Beamlines for Medical Applications and Beam Diagnostics Integration

Thesis submitted in accordance with the requirements of
the University of Liverpool for the degree of Doctor in Philosophy by

Jacinta Yap

October, 2020

Abstract

Recent advancements in accelerator technology and increasing experience with utilising charged particle beams for medical applications have supported the growing presence of ion beam therapy worldwide. The advantageous dosimetric properties enable high amounts of radiation to be precisely shaped and delivered to target sites while sparing surrounding healthy tissue. Accelerators, beam transport and delivery systems are designed to optimally and safely deliver the beam according to the prescribed treatment. This is maintained by beam instrumentation devices however limitations are seen with conventional tools. Therefore advanced diagnostics are needed to fully exploit fundamental benefits, for enhanced functionality and to accommodate new developments in particle therapy. A novel online beam monitor based on LHCb VELO detector technology is being developed, capable of providing non-interceptive, active measurements of the beam halo and was optimised for the 60 MeV ocular proton beamline at the Clatterbridge Cancer Centre, UK.

The facility offers a unique environment to assess the viability of the detectors however in order to integrate the system, the propagation and behaviour of the beam must be well understood. Several computational tools were developed to precisely model and completely characterise the facility. Simulation studies were performed using a GEANT4 model of the treatment line to generate transverse beam distributions which showed minimal impact of the sensors on the beam whilst revealing a dependency on the input beam parameters. Experimental measurements were performed using EBT3 film and benchmarked with a Medipix3 detector to verify the model and also to test for the first time, its performance and applicability in a clinical proton environment.

An alternative approach was necessary to resolve beam information upstream and an extensive review was required to overcome facility related limitations to determine fundamental beamline parameters. An optical lattice was defined in MAD-X and BDSIM, enabling the possibility of end-to-end modelling and yielding parameters ($\sigma_{x,y}$ = 6.89, 2.14 mm, $\beta_{x,y}$ = 9.52, 4.59 m and $D_{x,y}$ = 0.01, 0.00 m) which were used to define

the treatment beam. This was utilised in a redeveloped TOPAS model of the CCC delivery system which also incorporated the progress made with multiple codes, providing a single platform for future use. Simulations of the dose deposition, transverse beam profiles and linear energy transfer were achieved. Measurements were also performed with a MiniPIX-Timepix detector to experimentally verify the model for correlation with radiobiological applications.

These methods provide a basis to reproduce the physical properties of the beam given the present state of the Clatterbridge facility. This approach was also applied for proof of concept measurements performed at the University of Birmingham. Several uncertainties and improvements are discussed however the achieved results demonstrate the possibilities of the adapted VELO sensors as a beam monitoring system. This thesis combines computational modelling, experimental studies and accelerator concepts to establish a framework to characterise, optimise and realistically simulate medical proton beamlines. The application of this work supports the development and integration of novel diagnostics as explored at existing facilities, for improvements in the delivery and outcomes of proton therapy.

Acknowledgements

It has been a truly momentous adventure filled with countless lasting memories, challenges and milestones. There are many people I would like to give my warmest thanks to: each of you have shaped this journey, taught me lifelong lessons and made this time enjoyable. This work would not have been achievable without you.

Firstly, a big thank you to my supervisors. Carsten Welsch for the vision and effort to provide the opportunities which made all of this possible. I've learnt so much and this experience has enabled me to develop into a capable researcher. Javier Resta-López for always having time for me, your ongoing support and kind feedback. Jason Parsons for your guidance and readiness to help, especially with CCC beamtime and work.

Thank you to everyone who also contributed their experience and technical support to progress this work. Simon Jolly for the help, advice, chats and for being a friendly face at so many events. I'm grateful for the resources you provided and for involving me with your group. Andrzej Kacperek for your time, contributions, suggestions and assistance with everything clinic related. Stewart Boogert for your valuable input and BDSIM help. Tony Price for your feedback and facilitating our beamtime at Birmingham. Hywel Owen for your insight and supervision by proximity − prime office allocation. Thank you Matthieu Hentz and Volodymyr for your help with troubleshooting code and at many times, persistent simulation related issues.

It's been a privilege to be an OMA fellow and I appreciate the experiences, connections and opportunities I had to grow my research whilst travelling the world. I'll always remember the good times and our events (plus the shenanigans afterwards!). Thank you to Sam, for your proofreading and continual support; my friends in the UK, Australia or someplace else around the world. I've been fortunate to meet and get to know many along the way - QUASARs and other colleagues at CI and DL. The many conversations,

discussions, coffees and laughs helped me to navigate this European PhD endeavour and it was made especially better by you all: Ewa, Lina, Magda, Mark, Navrit and Ruta.

The majority of time I was actually on campus was most likely spent in the sports centre and I often looked forward to this after a day at the lab. Special thanks to all the basketball girls and coach Ruth for the fun times and letting me truly enjoy and develop this first and other, most certain passion of mine. The benefits of all those hours of sessions, games and socials go beyond just keeping me balanced. I will always cherish my memories of the seasons we played and what we were able to achieve together.

Finally, my dearest thanks to my family. To my Mum and Dad, for always supporting me to independently explore my passions and the world, even if it meant letting me fly the nest early to move to far away places − who knew all that precocious wanting to learn and read was preparation for this? To my sister Jasmine, my closest ally and my brother Leslie, always an avid listener and supporter. To Julie, for your efficient proofing and being another member of the exclusive club of readers of this thesis. To Darren and Elijah. Thank you all for always believing in me and encouraging me to pursue my aspirations.

Contents

Chapter 1

Introduction

1.1 Overview

The pursuit of a cure for cancer has long challenged the medical and scientific community. Cancer is a universal burden and is a leading cause of death worldwide. It imposes a costly and significant impact on communities yet rates of incidence are continuing to rise. In recent years it was estimated that there were more than 18 million diagnosed cases and over 9.5 million related deaths annually, contributing to 1 in 6 deaths globally [1, 2]. In developed nations these rates are slightly higher and in the United Kingdom, this equates to an estimate of 1 in 2 people who will be diagnosed with cancer in their lifetime. Despite these alarming statistics, the presence of cancer does not always result in loss of life; cancer survival rates are at approximately 50% and steadily increasing [3]. Today, several methods are employed on their own or as a multi-modal approach to treat cancer: surgery, chemotherapy, immunotherapy, hormonal therapy and radiation therapy. Advancements in modern technologies and improvements in these methods have enabled progressive steps toward this common goal of combatting cancer.

One such development is the administering of ionising radiation to cancerous sites: radiotherapy or radiation therapy (RT). RT is one of the more economical methods of treatment however its availability, accessibility and usage varies significantly. This is associated with aspects of demographics, cost and income levels which are significant factors limiting the effective nature of RT for curative and palliative applications [4]. In the UK around 40% of all cancer patients were treated with radiotherapy yet it is

predicted that more than half of all cases could benefit from RT [3, 5]. The efficacy of RT is well established however there is still an ongoing demand for accessible, affordable and effective cancer care [6]. These global goals have driven further work and innovation in the understanding and delivery of radiation for cancer care; these motivations also provide the context of which this thesis aims to ultimately contribute toward.

1.2 Medical Applications of Radiation

Following their discovery by Röntgen in 1895 [7], X-rays were recognised foremost for their useful application in medicine, as a diagnostic tool and then as a means of treatment. The biological effects and knowledge surrounding this new method were explored, initiating the start of radiation therapy; a field which set out to utilise these newfound ionising capabilities to irradiate malignant tissue sites.

1.2.1 Conventional Radiotherapy

Today, the application of X-rays still form the basis of conventional external beam radiation therapy (EBRT). Countless developments in technology have since transformed rudimentary methods of X-ray production by emitting tubes to modern accelerators and delivery systems which are found in clinics today. Primarily, this was made possible due to improvements in the ways beams were generated and transported, as well as innovations in the computational proficiencies of systems which image, shape and calculate the resulting dose. For the former, this includes the introduction of shielding, multi-leaf collimators and electron linear accelerators (linac). The latter describes computed tomography (CT), positron emission tomography (PET), magnetic resonance (MR) and dose calculation algorithms. This led to the creation of treatment planning and the development of conformal treatment modalities such as intensity-modulated radiotherapy (IMRT), volumetric-modulated arc therapy, image guided radiotherapy and stereotactic radiotherapy [8]. More novel delivery methods also include spatially fractionated schemes (i.e. GRID/LATTICE) and microbeam radiation therapy [9–11].

These techniques allow the beam to be manipulated and delivered in such a way as to reduce the amount of radiation deposited in surrounding normal tissue; the dose is distributed and directed precisely to the tumour volume. Radiotherapy is often performed in conjunction with surgery or chemotherapy and depending on tumour localisation or metastasis, also presents as an effective alternative for palliative care. Given the needs of the patient, the premise of radiotherapy is the non-invasive delivery of radiation to a target, such that tumour cells are sufficiently irradiated whilst sparing surrounding healthy tissue.

In order to provide the most optimal and effective treatments, significant progress in the field of high energy physics (HEP) led to the development of advanced concepts. New horizons were made possible by new accelerating machines (cyclotrons, synchrocyclotrons, synchrotrons), facilitating the application of different particle types for treatment. Further improvements in the technological and radiobiological aspects alongside growing experience have supported the emergence of the next generation of radiation treatment: charged particle therapy (CPT).

1.2.2 Charged Particle Therapy

The rationale to use charged particles for radiotherapy was first conceived in the 1940's by Robert Wilson [12], based on the phenomenon of the '*Bragg Peak*': the increased ionisation seen at the very end of an energy dependent range, originally observed in alpha particles by William Bragg in 1904 [13]. The idea to use protons was explored firstly with preclinical work at the Lawrence Berkeley National Laboratory (LBNL), California, followed by the Gustav Werner Institute, Uppsala and the Harvard University Cyclotron Laboratory (HCL), Massachusetts. In 1954, the first patients were treated at the LBNL and shortly after, a clinical program was run at the HCL in collaboration with the Massachusetts General Hospital (MGH) at the end of the 1950's. Over the next years with growing research interests and funding, MGH realised the potential of proton therapy for ocular, skull-based and head-and-neck region cancers and continued to treat thousands of patients at the HCL until its closure in 2002.

In Europe and beyond, several programs had commenced in mostly research institutes in the early 1990's; Paul Scherrer Institute (PSI) was the first in Switzerland, along with centres in Nice and Orsay, France as well as Chiba, Japan [14]. Most notably, in the United Kingdom, the Douglas cyclotron was built in Bebington, Merseyside and commissioned in 1984 at the Clatterbridge Cancer Centre (CCC). Although initially purposed for neutron therapy trials, it became a proton therapy service and treated the first set of ocular patients in 1989 [15]. This marked the establishment of the world's first hospital based proton beam therapy facility and in the next year was joined by the Loma Linda University Medical Center in California, United States and soon after, more centres across America and Europe.

1.2.3 Current Status

Since these beginnings, over 190,000 patients have been treated with protons [16]. At present there are more than 100 operating CPT facilities worldwide, almost 40 under construction and a further 30 planned. New participation in regions without CPT mean multiple continents will see their first centres in locations such as India, Egypt, Norway, UAE, Singapore and Australia. In the UK, there has been a recent rapid growth in the market for proton therapy, 4 clinics have been built and started treatments in the past 2 years and at least 3 more centres are anticipated [17].

The physical characteristics, observed biological effects and patient outcomes have affirmed proton use as a viable option for therapy. This success suggested the possibility of using alternative particle types in clinical beams to deliver a more precise beam with greater radiobiological impact. As seen in Fig. 1.1, other heavier charged particles also exhibit similar dose deposition behaviour. Thus neutrons, pions, helium, neon and carbon ions for particle therapy were studied and further work led to another modality of CPT: carbon-ion therapy. This was pioneered in 1994 at the National Institute of Radiological Sciences in Chiba, Japan and was followed by centres in Germany, Austria, Italy and China [8].

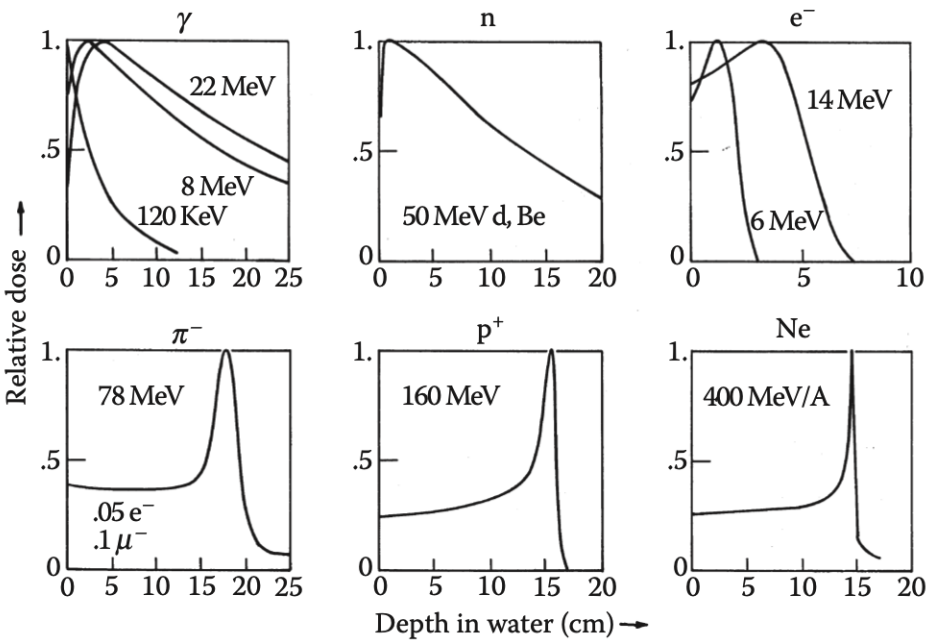

Figure 1.1: Dose profiles in water for various particle types. Peaks of high dose followed by a significant drop off are demonstrated for heavier particles (bottom row) [18].

These dosimetric characteristics of heavy charged particles were recognised to offer advantages over conventional photon radiotherapy. Protons are the lightest in this category and easiest to use, hence are the most commonly used particle type for CPT and have treated the highest number of patients. As the purview of work carried out in this project relates specifically to protons for CPT, proton beam therapy (PBT) will be the focus throughout this thesis.

1.3 Proton Beam Therapy

1.3.1 Rationale

The primary benefit of using protons over conventional X-ray radiation therapy relates to the advantage of delivering a beam with a finite range. In essence, due to their mass and charge, protons will continually undergo interactions and transfer energy along their path. Consequently they slow down and before coming to a complete stop, there is a culmination of dose where the majority of their remaining energy is deposited. This is known as the aforementioned Bragg Peak (BP). Following this, there is a steep fall-off with negligible transfer of energy and this enables the beam to be manipulated and delivered to targeted sites for the purposes of treatment. The specifics of these

interactions which occur between protons and matter are discussed in greater detail later in Section 2.1.1.

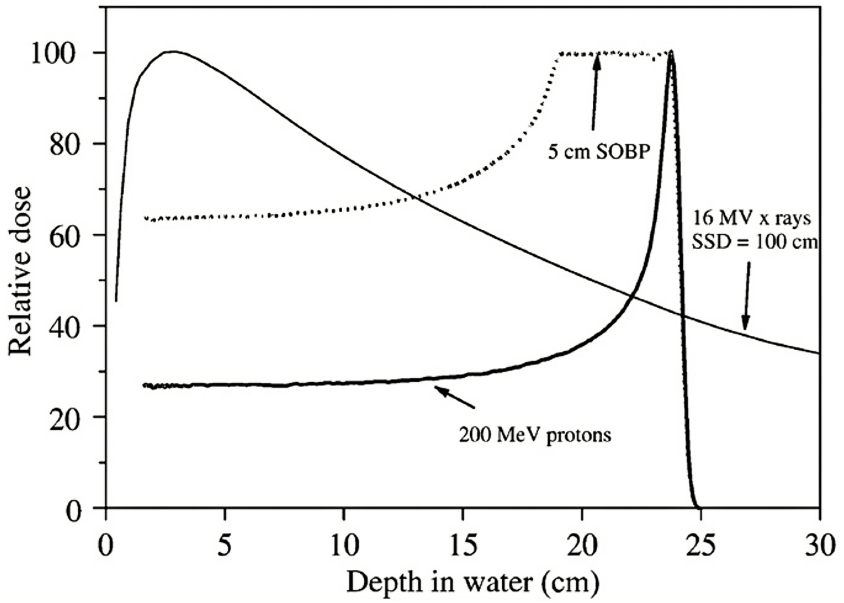

Figure 1.2: Direct comparison between the depth dose distributions of a conventional 16 MV photon beam and 200 MeV proton beam [19].

In X-ray EBRT, healthy tissues are often exposed to higher amounts of radiation as photons have a larger surface and exit dose; this can have significant and adverse effects (Fig. 1.2). Although in PBT several proton beams are superimposed to form a '*spread out Bragg peak*' (SOBP) to cover the whole tumour volume, the localised energy transfer can offer an increased cell kill efficiency and higher biological damage. As a conservative estimate, it is generalised that protons inflict damage by a factor of 1.1 times more than photons. This is given the term '*Relative Biological Effect*' (RBE) which is a quantitative representation of radiation quality and is used to measure the potential biological impact of two different modalities. In practice, this translates to the application of this generic factor to the physical doses calculated for photon plans for an equivalent proton plan [20]. There is ongoing debate over the discrepancy of RBE as a single value despite its dependence on numerous parameters [21] which are not discussed in this thesis. An exception to this is the linear energy transfer (LET) which correlates to cellular damage as a result of energy losses; this value changes across the total path length, according to the particle type. Protons and heavier charged particles have much higher LET values than photons, this is discussed further in Section 5.4.

Moreover, there can be remarkable differences when comparing the dose distributions and treatment plans between the two modalities, particularly for specific cases (Figs. 1.3 and 1.4). This is especially a concern when the tumour is in close proximity to critical organs or deep within the body and normal tissue may be exposed to excess amounts of radiation.

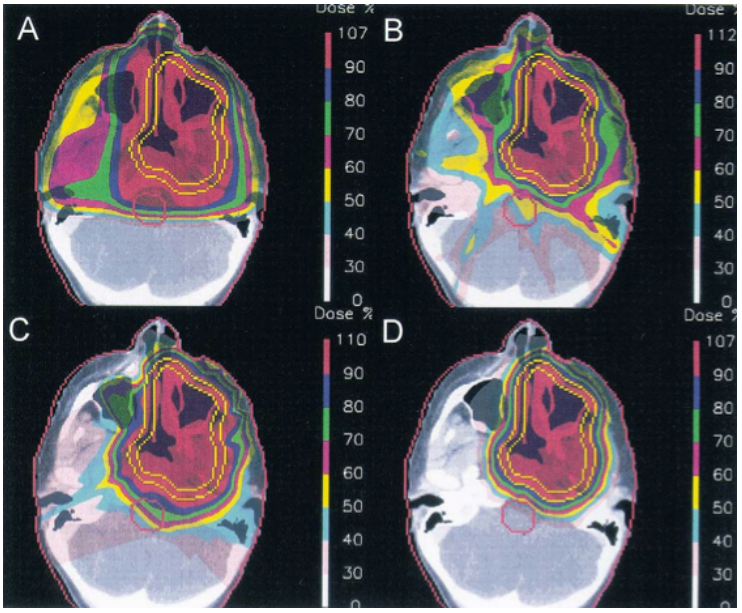

Figure 1.3: Example of treatment plans for: A) Conventional photons. B) Intensity modulated photons. C) Spot-scanned protons and D) Intensity modulated protons. This is a head and neck case for a paediatric patient, lower integral doses outside the target volume can be seen for protons [22].

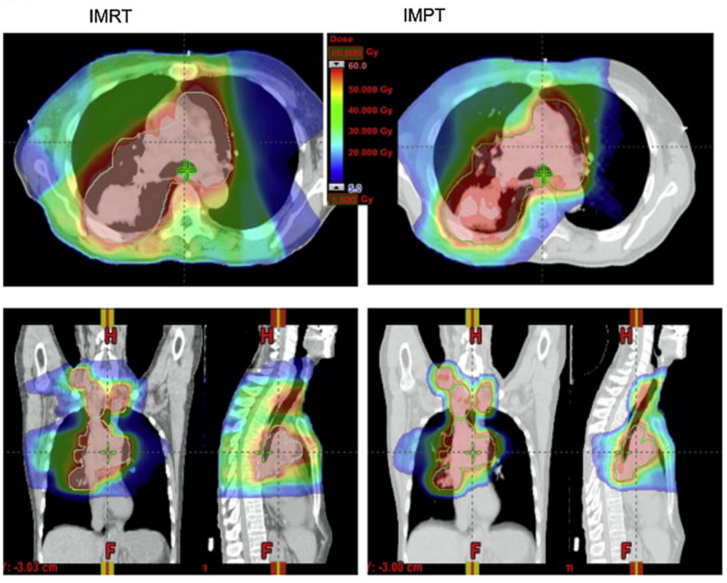

Figure 1.4: Comparison between treatment plans for a spine case with intensity modulated photons (left) and protons (right) [19].

PBT is often more commonly accepted for paediatric cases to lower the risk of secondary or future malignancies. Protons have been proven to be especially effective for paediatric patients and against certain carcinomas. Improved clinical outcomes have also been realised for skull based, head and neck, brain carcinomas and radiation resistant or other challenging cases [19].

All these characteristics suggest the great potentials and opportunities for a significant reduction in adverse effects, toxicity, recurrence rates and better local control. Even though there are clear physical advantages offered by the Bragg peak, the option of PBT against other treatment modalities is still uncommon: there are several considerations and uncertainties which limit the complete clinical exploitation of protons.

1.3.2 Challenges and Motivations

Clinical studies have provided mixed evidence regarding PBT as an effective treatment modality. In adherence to policies for medical care, several countries have national guidelines defining specific candidates and cases where PBT is recommended only if there are clear advantages [19]. This holds true for ocular melanoma, which is well suited for and has seen consistently high success rates since the inception of PBT [23]. These sites are almost always treated with passively scattered beams where the dose is mechanically shaped laterally and longitudinally to the tumour. In contrast, modern facilities mostly use an active approach of pencil beam scanning (PBS), where multiple small '*beamlets*' are magnetically directed to cover the extent of the target and shifted longitudinally by varying the beam energy (described in Section 2.2.4). Many features of PBT have also emulated conventional techniques, such as dosimetry, protocols, intensity modulated (IMPT) schemes and treatment planning. Although proficiencies have been established, PBT still suffers from complexities associated with biological and physical uncertainties, robustness of plans, positioning and beam delivery [19]. Conversely, significant developments have improved the effectiveness of photon EBRT and maintained its prominence as common practice. Much recent research and development have been done in the field to keep PBT competitive however there are several areas needing improvement and are well identified in research [24–26].

These challenges can be related to three main themes: biology, physics and technology. The following points are briefly explained for context:

- **Biology**: There are deficiencies in precisely quantifying radiobiological effects and cellular responses which may account for sub-optimal treatment planning and clinical outcomes. The generic RBE value doesn't account for variations in LET and the unknowns of mechanisms at the molecular to macroscopic scale [27–29].

- **Physics**: Uncertainties with heterogeneities in the beam path as well as changes to tumour size and position, result in discrepancies identifying the depth of the Bragg peak. Enhanced imaging is needed for in-vivo range verification, adaptive treatment planning, delivery with moving targets, online and in-room capabilities. The application of these with superior dose calculation methods (Monte Carlo, algorithms, robust optimisation, biological implementations etc.) for utilisation with treatment planning systems (TPS) [30, 31].

- **Technology**: There are high capital costs of building a PBT facility, accommodating for the large footprint required for the accelerator system, beamlines and shielding. Further considerations are associated with the intended throughput, delivery methods, gantry system, maximum energy and other specific beam requirements. Reductions and better conformity of resulting dose distributions (decreasing the beam penumbra with contouring and collimation, spot weighting etc.), better beam control and delivery (higher uptime and shorter times required when changing beam parameters, more efficient PBS approaches etc.) [31, 32].

The issue of cost is becoming less significant as the availability of smaller and cheaper systems for clinical PBT is increasing. Several vendors offer complete single or multiple room gantry systems and facilities have become well equipped to treat large numbers of patients. Treatment costs can also be suggested as more economical due to the potential of better quality of life with more effective therapy and therefore will have lesser long term complications [33].

New novel accelerators and methods of beam generation (dielectric wall, laser driven plasma [34], high-gradient linacs [35] and fixed-field alternating gradient [36]) along with

the implementation of rapid cycling and superconducting technology may also lower costs [37, 38]. Work in these areas provide the possibility to achieve superior delivery and more effective treatments in the future. Nevertheless, current improvements to PBT can be met by advancements to existing technologies and those which address the previously listed themes [32]. As PBT evolves on a whole (also for different or mixed particle species and better beam quality), the increased complexity of beam transport and accuracy of treatment verification necessitate advanced beam instrumentation and dosimetry systems.

Therefore, this thesis delves into aspects related to all three themes with a practical focus on tools to improve beam delivery related to the accelerator and beam transport system, as well as the capacity to accurately model and examine this computationally. Beam diagnostics are fundamental for monitoring and ensuring effective delivery of the beam for treatment. There are several promising developments in particle beam detector technologies and this work centres around solid state silicon devices: specifically their application in medical proton facilities.

A major part of this project involved the study and characterisation of these facilities, in order to understand the behaviour of the generated beam and model this precisely in several simulation codes. This also enabled studies into the integration of various silicon detectors, their feasibility, performance, impact on the beam and to support experimental measurements performed at two different proton beamlines.

Significant original contributions in this scope relate to: development of a novel online beam (halo) monitor, first tests with instrumentation in clinical environments, developed tools to analyse and obtain beam profiles, comprehensive studies and characterisation of the Clatterbridge facility, development of extensive beam transport (optical lattice) and tracking simulation models (treatment delivery system) and their use for radiobiological applications.

1.4 Project Objectives and Overview

The main goals of this project were to study the behaviour and propagation of the CCC clinical proton beam, in order to contribute to the development of the LHCb **VE**rtex **LO**cator (VELO) detector as a clinical proton beam monitor [39]. The detector operates a novel concept of measurement, by only detecting the halo of the beam distribution. As a result, the extensive characterisation of relevant medical proton facilities were necessary to investigate the feasibility of the detector. The physics surrounding PBT, definitions, quantities, accelerators, beam transport and delivery, instrumentation technology and an overview of relevant clinical practices are described in Chapter 2.

Simulation studies of the CCC beamline were done with GEANT4 [40] to investigate the integration and impact of the VELO detector which is discussed in Chapter 3. These studies revealed that minute differences with the input parameters affect the beam distribution, necessitating other approaches to overcome these. Measurements were performed with EBT3 film [41] and compared with beam profiles achieved using a Medipix3 detector [42] to validate and improve the simulation model. Alternatively, as detailed in Chapter 4, an extensive beam dynamics study of the CCC beamline was carried out in order to model the beam optics. An optimised optical lattice representing present day conditions was developed using the accelerator codes MAD-X [43] and BDSIM [44] and combined with the treatment line geometry to generate an end-to-end model (exit of cyclotron to treatment nozzle). These were used to determine the input beam distribution and the RMS sigma sizes for integration of additional diagnostics systems to measure beam properties along the transport line.

The verified geometry of treatment line components were combined with the optics calculated input beam and implemented in TOPAS, another Monte Carlo simulation code specifically for proton therapy. The code, finalised model and simulated results are presented in Chapter 5 alongside experimental measurements using a MiniPIX-Timepix detector [45] to verify the LET. Lastly, a measurement campaign with VELO at the medical research beamline at the University of Birmingham is described in Chapter 6. First test results with the upgraded detector, simulation and film results are shown and

further prospects of clinical impact are discussed. A summary and outlook is presented in Chapter 7.

This thesis endeavours to provide a better understanding of the beam produced, transported and delivered at these facilities; to explore the capabilities and support the development of several beam instrumentation systems. Comprehensive studies were performed to characterise the beamlines for detector integration and to develop computational tools to accurately model these facilities. These simulation models also aim to facilitate further study into the current understanding of radiobiological effects from protons. Each of these aspects contribute to the framework established in this work, outlining a method to simulate, optimise and characterise medical proton beamlines. This thesis combines beam optics, beam diagnostics, simulation modelling and particle accelerator concepts in the context of radiotherapy for improvements in the delivery, efficacy and outcomes of proton beam therapy.

Chapter 2

Clinical Proton Beams

The goal of radiotherapy is to deliver a sufficient amount of radiation to the target tumour volume whilst sparing healthy tissue. Unwanted exposure to radiation can increase the risk of second malignancies or other treatment induced, adverse late effects and these outcomes limit the therapeutic effectiveness of EBRT. However, the treatment efficacy can be enhanced by delivering the dose such that it is more conformal to the tumour site or also, by increasing the concentration of dose delivered to the target site.

Although the advanced methods of conventional RT delivery allow comparable dose distributions to PBT, this modality is limited by the nature of photon beams. Photons readily transfer their energy through interactions which mobilise atomic electrons such as Compton scattering, the photoelectric effect or pair production: these are stochastic, statistical processes which occur over a continuous length [46]. Even though the distribution can be rearranged geometrically, normal tissue will always be included in the total energy deposition [47]. In contrast, the physical advantages of protons enable the beam and dose deposition to be shaped better than with conventional photon beams. Advanced PBT delivery methods can deliver a highly conformal dose distribution with a lesser number of beams and particularly for complex cases, can result in a decreased amount of radiation to critical structures. The finite interaction range results in a reduction in energy transfer following the BP, also enabling a higher ratio of dose delivered within the target [48].

2.1 The Physics of Proton Beam Therapy

Protons lose energy with depth as a result of multiple types of interactions along their path. These can be classified broadly as either atomic or nuclear, where primary protons are slowed predominantly due to coulombic interactions with atomic electrons or nuclei. The rate of energy loss ($\frac{\text{MeV}}{\text{cm}}$) for a beam of particles can be described by the stopping power S:

$$S = -\frac{\mathrm{d}E}{\mathrm{d}x}, \tag{2.1}$$

where E is the mean energy loss and x is the distance. As this represents the energy lost by the particle along its length of travel due to opposing forces, it is a function of the kinetic energy of the incident particle and the absorbing medium. It is often more useful to express the mass stopping power ($\frac{\text{MeV}}{\text{g cm}^2}$), correcting for the density ρ of the stopping material [49]:

$$\frac{S}{\rho} = -\frac{\mathrm{d}E}{\rho\,\mathrm{d}x}. \tag{2.2}$$

The amount of energy lost is the sum of contributions from electronic, radiative and nuclear processes. These must be considered across the range of particle energies for CPT and also account for relativistic effects. Therefore, the total mean energy loss for a charged particle can be more completely expressed by the equation derived by Bethe and Bloch [50]:

$$\frac{S}{\rho} = -\frac{\mathrm{d}E}{\rho\,\mathrm{d}x} = 4\pi N_{\mathrm{A}} r_{\mathrm{e}}^2 m_{\mathrm{e}} c^2 \frac{Z}{A}\frac{z^2}{\beta^2}\left[\ln\frac{2m_{\mathrm{e}}c^2\gamma^2\beta^2}{I} - \beta^2 - \frac{\delta}{2} - \frac{C}{Z}\right]. \tag{2.3}$$

The variables are defined as: Avogadro's number N_A; the radius r_e and mass of the electron m_e; the atomic number Z, relative mass A and the mean excitation potential I of the absorbing material; the charge z and velocity v of the incident particle where $\beta = \frac{v}{c}$, with speed of light c; the Lorentz factor $\gamma = \frac{1}{\sqrt{1-\beta^2}}$; density corrections for energy losses due to electron shielding δ as applicable at higher energies and the shell correction C at low energies. The behaviour of the energy loss from the different interactions for a proton in water is shown in Fig. 2.1. Electronic processes dominate across the entire energy range and at relevant PBT energies, nuclear interactions have minimal contributions. Water is considered equivalent to tissue in PBT as it is similar in density,

effective Z/A and other attributes. Protons experience corresponding energy losses and interaction processes and as such, water equivalent materials are used for phantoms and in standard dosimetry practice [50].

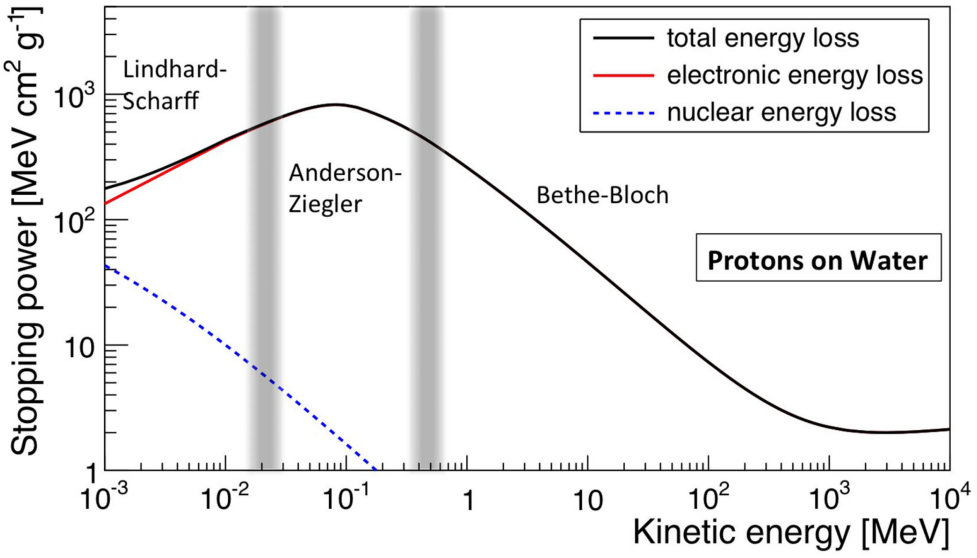

Figure 2.1: Energy loss contributions of different interactions experienced by protons in water. Within ranges for CPT, the energy loss is demonstrated by the Bethe-Bloch formula (Eq. 2.3) [51].

Due to their mass (much greater than electrons), heavy charged particles and particularly protons, travel mostly in a straight line where their rate of energy loss is inversely proportional to the square of their velocities. In tissue, the proton range is almost equal to the projected path length calculated from stopping power data [50]. Deviations are caused by density inhomogeneities of the different biological components within the body and effects from fluctuations in the energies of individual protons are also evident.

2.1.1 Proton Interactions

The main types of interactions which occur can be categorised as *stopping*, *scattering* and *nuclear* [52]:

Stopping: Protons may collide with atomic electrons (in-elastic scattering) if sufficient energy is transferred, resulting in ionisation events which generate secondary electrons. These energy losses continuously slow or stop the protons, contributing significantly to the achievable proton range and variations in the longitudinal profile. These

variations caused by individual differences in the energy lost by collisions are known as range straggling effects [46].

Scattering: Proton collisions with atomic nuclei (elastic scattering) via multiple Coulomb scattering (MCS) result in a change of trajectory. Protons are deflected from their original path which may also generate secondary recoil particles. The scattering mostly observes a theoretically Gaussian distribution and causes the angular, lateral broadening of the beam. In larger beams, this occurs only in the outer edges; protons scatter outward from the central region but this is replaced by particles which scatter back in. In narrow beams, there is less scatter back inside and with depth, the central dose region decreases. For this case, the spread in the transverse plane is estimated to be 5% of the initial range [46, 51]. These are important considerations in passive and active delivery methods.

Nuclear: Protons with sufficient energy to overcome the Coulomb barrier and cross-section may interact further with atomic nuclei (non-elastically). A nuclear reaction results in the absorption of the primary proton, producing secondary protons or other particles such as gamma rays, neutrons, deuterons, tritons, helium or other ions. A reduction in the proton fluence occurs and is compensated by secondaries which can also contribute up to 10% additional dose in high energy PBT treatment [50].

In terms of the energy transfer and its significance to dose, the electromagnetic (EM) interactions dominate. The physics of these collisional events (excitation, ionisation or MCS) which continuously slow, deflect or stop protons, is well understood. In contrast, it is estimated that only 1% of primary protons undergo nuclear interactions and the distributions of secondary particles produced are also more difficult to model. Although these interactions occur less frequently, they affect both the longitudinal and lateral beam profile. Moreover, the additional dose deposited by secondaries can have a noted biological effect [38, 52].

Furthermore, if non-elastic scattering causes protons, nucleon clusters or neutrons to be ejected, they will have lower energies and larger trajectory angles which deposit doses further downstream of reaction sites. Additional secondary particles such as gamma

rays or neutrons, produced from interactions with delivery components or the patient also pose further risks. If irradiating biological matter, secondary fragments containing alphas and residual nuclei may also result [50, 52]. These will have a high stopping power and LET: this is meaningful when examining radiobiological impact and must be accounted for as they have an increased effect in simulations.

2.1.2 The Bragg Peak

Given these interactions, protons lose their energy over a distance, leading to a build up at the BP. This results in a deposition profile with a lower entrance dose and a minimal exit dose as protons achieve complete energy loss. These mechanisms of energy loss can be calculated to model the BP analytically [53, 54] or by using simulation methods (shown in Chapter 5.3.1). As shown in Fig. 2.2, the different interaction processes contribute in varying amounts to the total dose distribution.

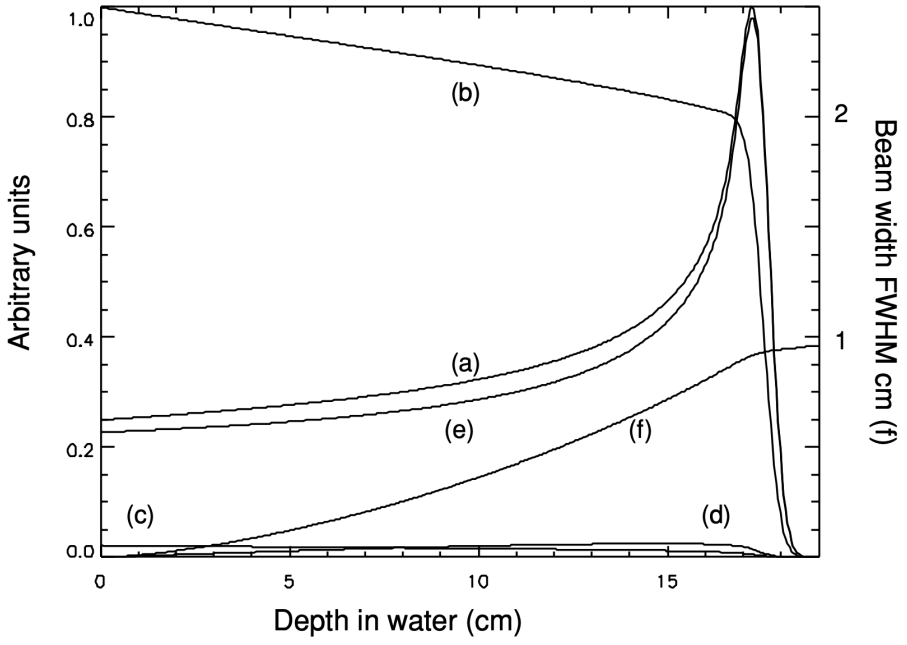

Figure 2.2: Contributions of different processes to the BP and total dose deposition profile (in water) for a 160 MeV PBT beam a) Overall dose profile. b) Primary proton flux. c) Dose from local energy transfer. d) Dose from long range secondaries. e) Dose from primary protons. f) MCS beam broadening [54].

The dose is concentrated at the BP as the number of protons decrease and at this point, most of their energy and momentum has been transferred to other particles; the depth

the BP occurs is defined by the initial beam energy. The contributions from primary protons via Coulombic interactions are significant along the entire range whereas nuclear interactions and secondaries only add to the entrance dose and plateau region. As such, the range is defined as the depth in the medium at which half the protons involved in EM interactions have stopped. Typically, this is assigned to the distal depth in water at 80% maximum dose, after the BP [52]. The slight curve in the fall-off is due to the energy spread and range straggling: these determine the width of the peak.

The dose relates to the amount of energy transfer to the medium. It is a fundamental quantity expressed as:

$$D = -\frac{\mathrm{d}E}{\mathrm{d}m}. \tag{2.4}$$

D is the physically absorbed dose (Gy or J/kg) and E is the mean imparted energy in a medium of mass m. Given Eq. 2.2, for a beam of $\mathrm{d}N$ protons passing through a cross-sectional area $\mathrm{d}A$ with fluence $\Phi = \frac{dN}{dA}$, dose can be further described as:

$$D = \Phi \frac{S}{\rho} = \Phi \frac{S}{\rho} \times 1.602 \text{ [Gy]}. \tag{2.5}$$

As mentioned, when the beam propagates in water, scattering causes particles from the middle of the beam to spread out in the transverse directions. This effectively results in a reduction of the fluence in the central region with depth and is more pronounced for smaller fields and pencil beams. In active delivery methods where there is magnetic steering of a narrow (pencil) beam, i.e. proton pencil beam scanning, this is compensated by using multiple beams or overlaying fields of dose [52]. However, this gives rise to the '*halo effect*', where the secondaries from nuclear interactions results in an excess of dose which surround the primary beam. This appears as a low dose tail along the lateral edges of the beam and cumulatively with multiple beams, can have significant dosimetric impact on the total delivered dose and distribution. This halo effect was originally defined by Pedroni et al. [54] as specific to PBT and in addition, an analogous phenomenon is also a prevalent point of discussion in accelerator physics. As the VELO detector is also often described as a '*halo*' monitor [55], the '*beam halo*' is a key concept in this thesis. This is discussed for context as although these concepts are similar in terminology, each are in fact physically different.

2.1.3 The Beam Halo

In PBT, the halo is defined as the peripheral dose produced from nuclear fragments, scattering inside the patient, phantom, diagnostics (ionisation chambers), components in the beamline (nozzle, range shifter etc.) and also the accelerator. In general, it refers to the region which surrounds the '*core*' of the beam, made of primary protons interacting by EM interactions. The '*aura*' consists of neutral secondaries and loosely, the halo is the wider region [56], as depicted in Fig. 2.3. For further explanation, it is also studied extensively in several other works [57–62].

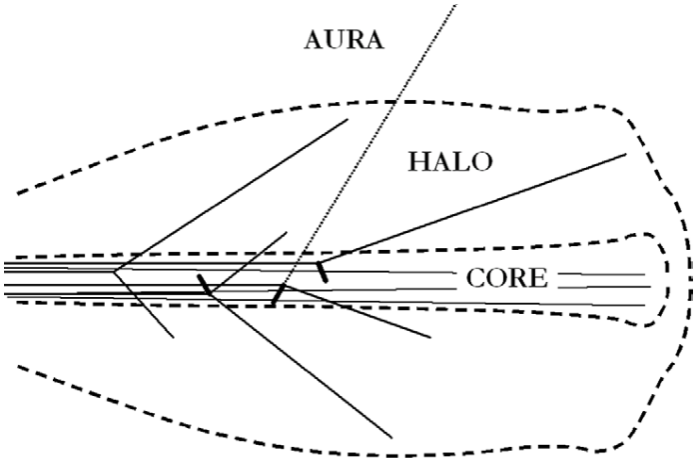

Figure 2.3: The dose components of a PBT beam distribution in water. The halo region encompasses all secondaries which surround the core and aura contributions [56].

As the halo effect is less significant for larger sized beams and given that the VELO monitor provides halo measurements in air (discussed in Section 2.3.3), the halo mentioned in this thesis for this case, is defined differently. The CCC facility operates a passively scattered beam where MCS is utilised to broaden the beam to a field size suitable for treatment (explained in Section 2.2.4). However, as the VELO modules will always remain a certain distance apart from the beam core, the halo is determined by the distance between the sensors: the aperture radius plus separation distance. The part of the beam which is greater than this gap will record hits on the monitor and regardless whether these originate from EM or nuclear interactions, is designated as the halo region. Therefore, MCS interactions from the treatment line delivery elements and in air would mostly contribute to the detected halo: the PBT beam at CCC can be similarly visualised as in Fig. 2.3.

Furthermore, although the halo in PBT is extended to include effects from the accelerator and other components which intercept the beam, in accelerator physics the beam halo has another definition. It can be defined and quantified in several ways [63–67] and is dependent on several factors which differ for the type of machine (i.e. high intensity beams, circular accelerators). For relevance and brevity, the beam halo is broadly described as an intrinsic property of the beam, referring to a lower density distribution of particles surrounding the beam core [68]. The formation of the halo is due to several mechanisms such as space charge effects, scattering with residual gas particles, beam mismatches and particle variations in phase space. Particles oscillate around an ideal orbit but may arrive at different angles and distances and diffuse out from the beam core which can differ from the acceptance of beamline optics. Therefore, it is an important consideration when designing beamlines, the optical elements (i.e. magnet aperture size), diagnostics and optimising machine operation.

In linear machines, the halo is characterised by beam mismatching and space charge forces: EM repulsion within particle bunches and between bunches. For circular machines it arises from asymmetric resonances, collective instabilities and unstable harmonics which are propagated with each revolution. For all machines, the beam halo influences the transverse beam size and most significantly, can result in beam losses. It is also largely correlated with the beam quality: the ability of a beam to be transported and focused into a small region of space while remaining as minimally divergent [69]. This is represented by the '*emittance*', a term which quantifies the elliptical distribution of particles in phase space. This corresponds to the physical size of the beam and is determined by the beam dynamics of the accelerator, discussed later in Chapter 4.

Additionally, to avoid confusion between terms which are defined differently across the fields, the following are considered for this thesis:

$$\begin{aligned} F &= \frac{\mathrm{d}N}{\mathrm{d}t}, \\ I &= \frac{q\,\mathrm{d}N}{\mathrm{d}t}. \end{aligned} \tag{2.6}$$

For a beam, F is the flux for N number particles over time t and I is the intensity or commonly, beam current. The charge q for a proton is 1.6022×10^{-19} C.

2.2 Accelerators

The most utilised types of accelerators for PBT are cyclotrons and synchrotrons. Cyclotrons are much more commonly found, partly due to the early development of this concept of particle acceleration by Ernest Lawrence at LBNL [37]. They have a smaller footprint than synchrotrons and since the introduction of superconducting magnets, the physical size of these machines has reduced, making them cheaper to build and accommodate.

2.2.1 Cyclotrons

The main features of a cyclotron include its ability to generate a continuous beam at a fixed energy and rapidly switch beam intensities. They are mostly used for other applications, at low (10-20 MeV) to medium (∼50 MeV) energies primarily for medical radioisotope production and up to 250 MeV for treatment [70]. For treatment with different particle sources or for imaging capabilities where higher energies (330 MeV) are required, a synchrotron is necessary. As the proton facilities described in later chapters operate cyclotrons, the basic principles of the classical isochronous cyclotron (Fig. 4.5) are outlined.

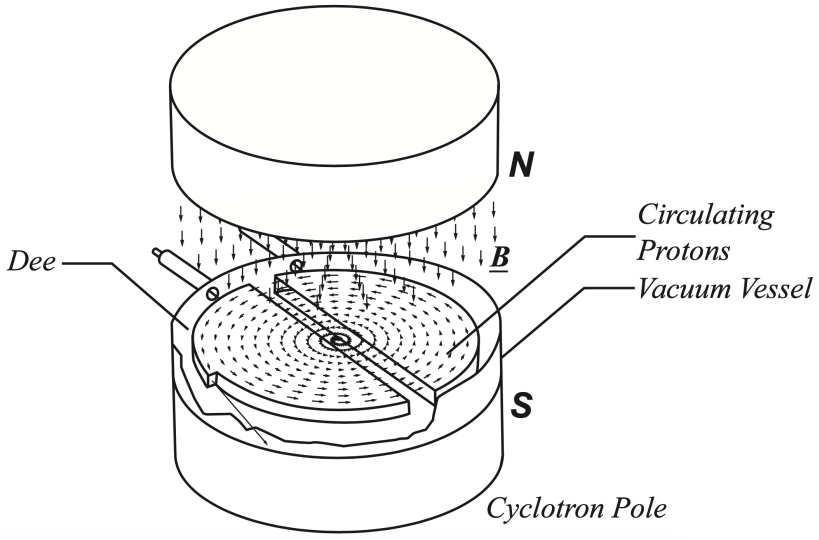

Figure 2.4: Overview of the components and working principles of a cyclotron. An alternating voltage is applied across the two dees where a beam of protons originates from the centre. A constant, perpendicular magnetic field forces the protons to circulate around the vacuum vessel where they continually accelerate with each pass across the gap until their orbit radius increases to a maximum and they are extracted [37].

The principle of acceleration in a cyclotron is governed by the Lorentz force. A charged particle in an electric field will experience a force perpendicular to the field, gaining kinetic energy proportional to half its mass and the square of its velocity. This centripetal force in combination with a uniform magnetic field (also in the perpendicular plane) causes the particle to move in a circular trajectory with a constant rotational frequency:

$$f_c = \frac{qB}{2\pi m}, \tag{2.7}$$

with the cyclotron frequency f_c, particle mass m and charge q and magnetic field B. This equation holds true for a non-relativistic case, corrections are necessary otherwise.

As shown in Fig. 4.5, two D-shaped '*dee*' electrodes are positioned slightly spaced apart laterally, between the pole faces of two large magnets which generate a constant magnetic field in the perpendicular plane. An oscillating voltage is supplied by a radiofrequency (RF) system (with a fixed ∼MHz frequency) to the electrodes: this is the cyclotron frequency and is provided by Eq. 2.7. As the magnetic poles are grounded, this results in a potential difference between the dees. An ion source (typically ionised hydrogen gas) injects a beam of protons from a central point within this gap and gains some energy when it crosses the gap. When there is a positive difference, the protons are accelerated toward the grounded region and if negative, they accelerate towards the gap. The electrodes keep switching polarities and with each crossing, the protons continually gain some acceleration.

As the dees are enclosed within a vacuum vessel, the magnetic field stays constant and the protons will keep circulating with a larger radius as their velocities increase. However, the time it takes for each crossing remains the same. When they reach maximum kinetic energies at the distance equivalent to the pole face radius, protons are evacuated into the beam transport line by an extraction process. The extracted beam consists of bunches of protons which have a distribution of energies across the specified cyclotron energy. The generated beam parameters are dependent on the focusing properties and extraction components of the cyclotron. The beam intensity is determined by the ion source arc current. Several considerations are necessary to maintain orbit stability and to keep the protons circulating; often this can be synchronised by adjusting the RF to be in phase

[71]. The dynamics of the particle beam within the cyclotron is complex and is detailed in [72, 73], however features relevant to CCC are discussed later in Chapter 4.

2.2.2 Synchrotrons

Synchrotrons require much more space and typically consist of several parts including an ion source injection system, RF cavities, linear accelerators, dipole, quadrupole and sextupole magnets and the extraction system. Typically, a linac is used to pre-accelerate particles for injection into the synchrotron ring, consisting of a series of magnets which maintain a fixed orbit radius. As the bend radius is constant, the magnetic fields must vary with the increase in particle velocity; this revolution frequency must synchronise with the RF cavity voltage, where particles acquire energy and are accelerated with each pass. This requires an initial dead time period to ramp up the magnetic field so that sufficient bunches of particles fill the ring until they achieve the required energy for extraction. They are held constant at this energy and are then slowly extracted, resulting in a pulsed beam with a specific repetition rate [71, 72, 74]. An advantage of this acceleration method is the possibility to extract beams at variable energies and with higher magnetic rigidities. This includes beams using other ion sources (carbon ion, helium etc.) and also at higher energies [37]. Additionally, this reduces the need for an energy selection system (ESS) which is used in cyclotron facilities, where absorbers or degraders intercept the beam to lower the beam energy. This has an impact on the quality and physical characteristics of the beam; the production of neutrons also generate some radioactivity. Furthermore, the pulsed time structure of a synchrotron produced beam is comparable to the respiratory cycle and this presents a challenge for certain treatment cases with moving organs [75, 76].

2.2.3 Linacs

Linacs have also been reconsidered for PBT in recent years as new advances have led to much improved accelerating gradients, enabling the possibility for cost and size competitive accelerators. Some benefits include the generation of a beam with a smaller emittance and fast variable energy and intensity modulation capabilities [76]. It is notable that there is a clinic planned for the UK which will uniquely use a purpose built

linac for proton treatments [77–79]. The significance of this new innovation relates to what could be the next frontier of CPT, where fundamental differences to the beam quality, current and delivery could be achievable due to this unprecedented accelerating technology. This development may lead to lower capital costs and also initiate the use ultra high dose-rate ($\geqslant$ 40 Gy/s) '*FLASH*' irradiation [80–82]. Current proton accelerators and conventional clinical linacs (electron mode) can also be modified for these dose rates [83, 84] however the associated challenges in this case are then related to machine specifications, delivery and online dosimetry [85–90].

The rapid irradiation at ultra-high doses per pulse are necessary for the FLASH effect, showing enhanced treatment efficacy by increased tissue sparing. Promising results have been reported for different RT modalities; the use of different particle types are still being explored however the biological mechanism particularly in PBT, is not well understood [91–94]. Nevertheless, this opens up a new realm of research into the needed dosimetric tools in addition to the different chemical and biological responses induced.

2.2.4 Beam Delivery

Given these accelerator types, the choice is contingent on the facility goals and constraints including the cost, geography, throughput, treatment candidates and clinical requirements. Different beam transport and delivery systems must also be considered.

As mentioned, the emergence of superconducting technology has effectively increased the commercial availability of compact cyclotrons and synchrotrons. Single room systems are now offered by leading vendors: a progression from typical multi-room treatments where a single accelerator source produces a beam which can be delivered to multiple beam lines. The beam is likely to pass through several optical elements, diagnostic devices and the ESS system which comprise the beam transport system (BTS), before reaching the gantry or delivery system in the treatment room. The goal is to optimally transport the beam with characteristics sufficient for the prescribed treatment. Several parameters are determined by the BTS including the beam position, size, energy, intensity and overall transmission. The beam transport line is designed to accommodate the desired beam properties for the type of accelerator and facility; more requirements

are discussed in [46, 95, 96]. The presence of a (rotating) gantry also introduces more challenges and optical considerations in comparison to a fixed beamline. For this case, a fixed beam delivery avoids the complexities associated with a moving gantry such as magnetic rigidity, momentum and energy acceptance requirements and positioning uncertainties [97, 98].

The BTS or if no acceleration occurs, the beam transfer line (BTL), consists of a series of quadrupole magnets which focus the beam (in one plane) and dipoles to bend and steer the beam. Beam dynamics concepts are discussed later in Chapter 4; the optics define the resulting beam parameters and properties. In general, a high quality beam with maximum transmission with the applicable beam intensity (i.e. dose rate), transverse distribution (penumbra) and modulation characteristics (range, distal fall-off) for delivery is desired [99]. Some typical objective PBS treatment values derived from accelerator parameters are listed in Table 2.1.

Table 2.1: Objective PBS treatment and beam parameters [100].

Parameter	**Accelerator**	**Clinical**	**Beam**
Dose rate	Beam current	1 Gy/L min	100×10^9 protons/min
Range (in water)	Beam energy	32 cm	226.2 MeV
Penumbra in air	Beam size, emittance	3.4 mm	3 mm σ

These parameters are for a 226 MeV scanned pencil beam and it is noted that the applicable spot size will differ according to the beam energy. As the transverse distribution of the dose exhibits a Gaussian spread, the σ size of the beam can be expressed in different ways, for reference:

$$FWHM = 2\sqrt{2\sigma^2 \ln 2} = 2 \ln 2\sigma = 2.3548\,\sigma. \tag{2.8}$$

This is demonstrated by the full width half maximum ($FWHM$) of the distribution given the particle intensity against position in the transverse plane.

Pencil Beam Scanning

PBS has become the most common method of beam delivery for PBT facilities worldwide. Thousands of individually modulated, small (3-8 mm) beams are scanned across a

treatment volume in both planes and generate a dose distribution (SOBPs) which covers the volume in three dimensions (Fig. 2.5). This results in the delivery of multiple BPs which each deliver a small amount of dose, totalling anywhere between 10,000-50,000 spots and 30-100 slices, over two or more fields. Typically one fraction takes an average of 30 minutes, with a complete treatment course requiring 15-20 daily fractions, varying for the size of the treatment volume and the complexity of the case [31, 101].

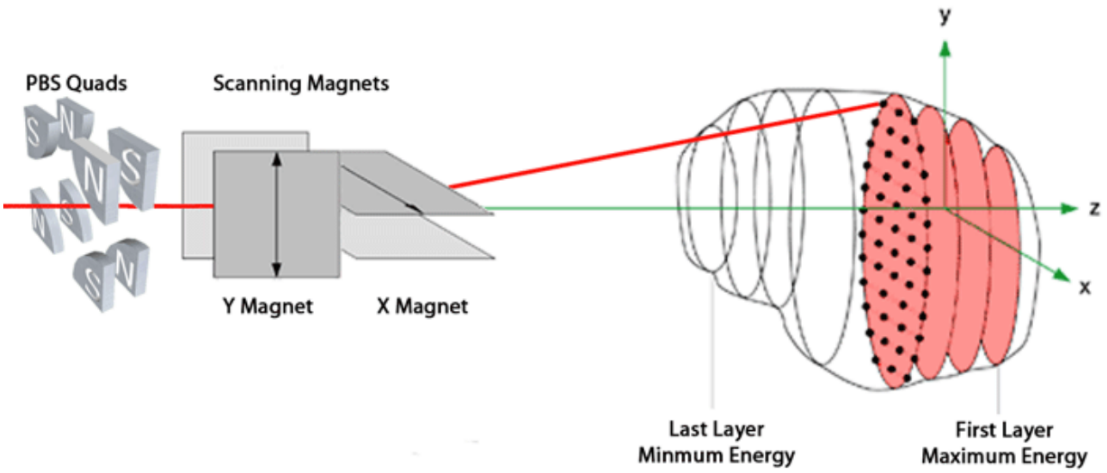

Figure 2.5: Active PBS delivery: scanning magnets are used to deflect the beam which traces across a target volume, superimposed in multiple layers for a conformal 3D dose distribution [102].

This delivery technique enables the beam position, range and intensity to be altered to trace the entire target site and accurately deliver the dose, as prescribed by the treatment plan. The beam itself is magnetically deflected in the transverse plane and movement can also be performed in conjunction mechanically with adjustable collimators, or by also moving the target. However, the time required to switch energies for each layer and the sheer number of spots can be lengthy and rescanning may be required to compensate any underdosage or errors caused by movement [103]. As such, there are several different schemes which can be adopted to enhance the dose delivery and distribution. This includes varying the weights of beamlets, optimising the field coverage and applying biologically weighted factors. PBS is analogous to IMRT and provides a highly conformal dose delivery with protons.

Furthermore, as the beam extracted from the accelerator source will have a small distribution, originally, physical components were used to spread the beam in three

dimensions. PBS overcomes these associated requirements of scattering, modulation or patient specific devices and their limitations. For the case of shallow tumours and in particular ocular treatment (Fig. 2.6), few facilities exist which use the scanning method [104, 105]: these are normally delivered with passive systems.

Figure 2.6: Example of a patient being situated for ocular treatment at CCC [106].

Passive Scattering

Although there is a demand for higher energy beams which can treat a greater range of cancers with conformal techniques and penetrate through to deeper seated tumours, there still remains a need for dedicated ocular treatment beams [15, 107]. Uveal melanomas have the highest incidence rate for adult ocular tumours and although treatment using other methods are possible, proton beam therapy is considered the gold standard treatment modality for these cases [23]. Clinical protocols have been well developed by early facilities such as CCC; although these may vary across centres, the ongoing experience and practised delivery of exploiting the sharpness of the distal edge enables a large volume of patients to be treated effectively.

High energy, multi-room facilities require an ESS in the gantry or further upstream to decrease proton energies to levels applicable for eye treatments. Facilities which operate at close to the maximum machine energy are able to generate a fixed, passively scattered beam with minimal energy or range straggling effects. This makes it possible to produce

a beam with a steep BP fall-off whereas higher energy beams require the presence of a degrader which also decreases transmission. Hence, consistent beam penumbrae and distal-off characteristics can be achieved regardless of the treatment prescription; these parameters remain until the beam is modified for patient specific conditions. Moreover there is no time lost waiting on the ESS to switch between energies and short treatment times are particularly important for the patient experience.

There are several different types of passive scattering systems: a range modulation device can be used to spread the beam longitudinally and a single or double scatterer is used to generate a field broad enough for treatment. The most simple system has a single scatterer (Fig. 2.7a) where the beam passes through a typically high-Z material, spreading the beam before it is collimated to restrict the delivery of only the central region: this enables a uniform dose distribution at the target. More extensive systems have multiple scatterers and collimators to shape the beam. Fig. 2.7b shows a double scattering system with an occluding ring where the overlap of several Gaussian beam distributions generate a large field with a sharp penumbra. The ring attenuates the beam in the central beam axis and further collimation results in a noticeably flat dose distribution.

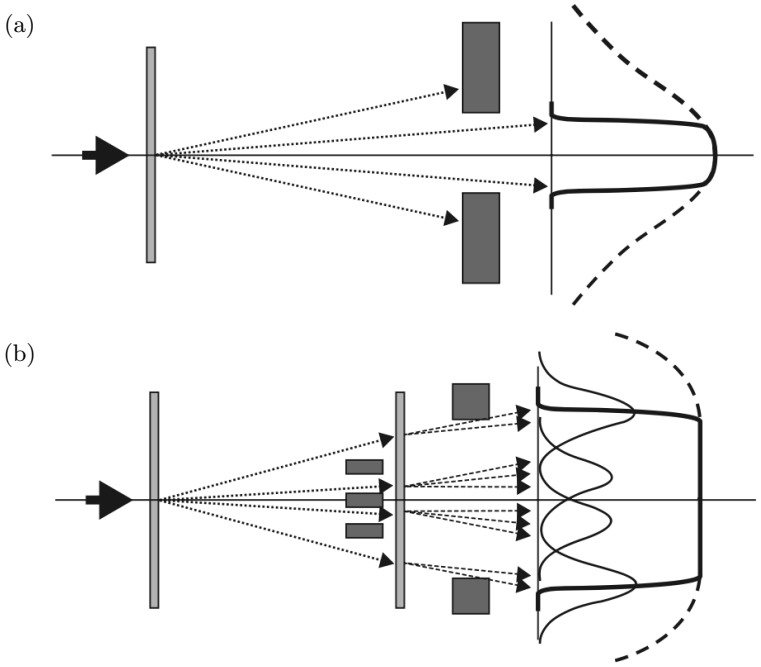

Figure 2.7: a) Single scattering system and b) double scattering system with ring for passive PBT delivery, both form a uniform dose distribution [108].

This double scattering technique is also used at CCC which has two tungsten foils, a brass stopper and a rotating modulation wheel; this is detailed more in Section 3.1.1. Several studies were performed to design the system to produce a beam with ideal treatment characteristics, this mostly involved the materials, arrangements and position of the scattering components [109–112].

However, the rigidity of this shaping technique necessitates additional beam modification devices to modulate and conform the dose delivered for each patient treatment. Customised brass apertures or patient collimators (Fig. 2.8a) are used for lateral shaping while compensators, range shifters or modulation wheels adjust the beam longitudinally. The different gradients in the wheel absorb the beam and shift the BP in depths to generate a SOBP; a modulator used at CCC is shown in Fig. 2.8b.

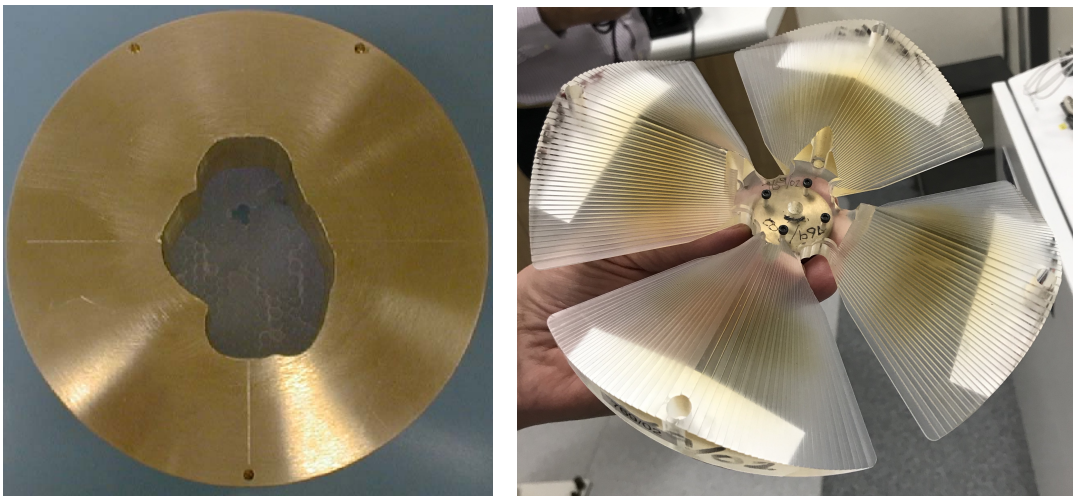

(a) (b)

Figure 2.8: a) Patient specific brass aperture [74] and b) range modulation wheel for passive beam shaping and modulation at CCC.

2.3 Beam Diagnostics

Beam checks and measurements are essential during accelerator operation; for the precision required with PBT, specific instrumentation is needed across all clinical facilities. Beam diagnostics typically refer to the devices which are placed within the BTL however as the systems described in this thesis may be used both in the BTL or the treatment

room, are all considered as beam diagnostics instruments. In clinical environments, the objective of diagnostics are fundamentally for patient safety: to measure and monitor the beam during delivery and to verify the dose distribution. These ensure that the beam is delivered correctly within the standard codes of practice and according to the treatment plan.

2.3.1 Quality Assurance

There are established protocols which provide guidelines for different performance factors such as the beam properties, delivery, dosimetry, treatment planning, imaging and uncertainties. For quality assurance (QA) procedures, this covers dosimetry equipment calibration, TPS, mechanical components, machine and patient QA. With relevance to clinical practice, the diagnostic technologies examined in this thesis relate to machine QA and dosimetry [113, 114]. QA checks involving these are often performed daily or at regular intervals after commissioning in order to maintain performance and adherence of the dose delivered to target volumes within certain margins.

Several systems are commonly used in PBT for beam measurements including the profile, intensity, position, uniformity and current or dose. These are performed by a range of different types of detectors; their uses and properties can be found in [38, 115–118]. There are benefits of using certain instruments for specific tasks however their suitability can be limited due to several operational or technological factors.

Ionisation chambers (IC) are recommended for reference dosimetry in all modalities of EBRT by standard code of practice. Reference measurements are performed in defined, specific conditions to establish the conversion between absorbed dose to water: these involve several corrections and calibration factors [117]. This is necessary to ensure that dosimetry methods are consistent and can be correlated to primary standards provided by national laboratories. Essentially, the ICs measure an amount of dose delivered under reference conditions and this gives an equivalent dose '*monitor unit*' (MU). These are considered as absolute measurements, within precise and reproducible

conditions. For subsequent irradiations under non-reference conditions (relative measurements), the absorbed dose (Eq. 2.4) can then be expressed in MU as proportional to the dose monitor output (i.e. dose per MU) [118, 119].

2.3.2 Dose Monitors

Conventionally, either cylindrical or parallel plane ICs are used as dose monitors and are arranged in pairs within the treatment head on a gantry, or the delivery system in the treatment beamline. Dose monitors are fundamental to the beam delivery as they actively monitor the flux and also the transverse beam size and position. Furthermore, the monitors will interrupt the delivery if beam measurements exceed clinical tolerances [116]. Although different types of ICs are used across facilities and treatment techniques, these detectors provide highly reliable and accurate measurements. They are also LET and relatively energy dependent, however regular and individual calibration is needed as each chamber varies [117].

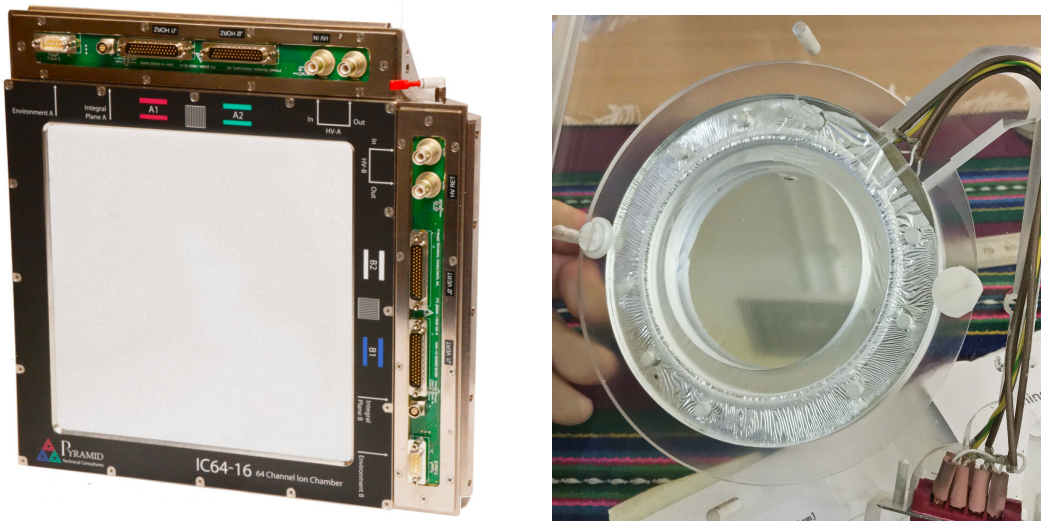

(a) (b)

Figure 2.9: a) Multi-strip parallel plane IC for PBS systems [120] and b) parallel plane IC used at CCC. Both types are used for online dose monitoring during delivery.

To monitor the flux, ICs contain a cavity lined by metal foils (electrodes) placed in parallel at the windows (Fig. 2.9b) or multiple electrodes arranged in pixels or strips (Fig. 2.9a). These chambers are sealed and often contain a gas, where a constant voltage applied creates a potential difference. When the beam passes through, particles ionise

the gas inside creating ion pairs which move toward the electrodes and produce a charge proportional to the number of traversing particles and their stopping power. The applied voltage needs to be high enough such that there is very high collection efficiency (>95%), the measurement time needs to accommodate the ion pair drift time (even up to ∼100 µs) and the readout fast enough (∼ms), which also depends on the beam time structure (pulses can be 1-10 µs). Additionally, the output signal response may not be linear and can be affected by recombination effects where the ion pairs combine before collection by the electrodes, resulting in charge and signal losses. Multi-channel, -wire or -strip ICs are used for monitoring the beam position and size, providing measurements within a resolution of <0.5 mm and 1 mm, respectively [115, 117].

Beam monitors must have a uniform field coverage and be able to provide dose within a 1% tolerance or the allowable limit for the prescribed dose. For X-ray EBRT, ICs are simple and easy to implement. CPT and the new methods of delivery present more challenges: at high beam intensities, the occurrence of recombination increases and their readout systems are insufficient at the currents (µA) anticipated with future accelerators and beam delivery technologies [85]. They will also need to accommodate the changes in the beam structure, including high flux rates, short pulses and fast repetition rates [116]. In general, ICs have a slow response time, low sensitivity and their performance will degrade at high dose gradients. The gas filled cavities also mean that the properties of the active volume need to be maintained (temperature, pressure etc.) and the electrodes protected to prevent leakage current [118]. The ideal capabilities for a beam monitoring system include [115, 121]:

- Linear correlation between the charge collection and beam fluence
- High charge collection efficiency, signal-to-noise ratio and sensitivity
- Linear response independent of charge, temperature, energy or dose rate
- Minimal saturation and radiation hard
- Uniform response across the active volume (<1% deviation)
- Real time measurements
- Beam flux, fluence, position, energy and transverse profile measurements
- High spatial and time resolution

- Minimal beam scattering and interference
- Minimal beam losses and energy deposition in the detector
- Stable and reliable system performance

Although ICs are the gold standard for PBT beam monitoring, a combination of different detectors are necessary to cover these requirements. Improved and new types of monitors have been widely investigated; recent research and developments into silicon based detectors have identified several benefits [122–125]. The use of silicon enables direct measurements by individual particle counting, a fast response time, high sensitivity and increased resolution. As such, the VELO detectors were investigated as an online beam monitor to provide minimally invasive, active measurements during beam delivery. The novelty of this system is related to its technology and design: nothing similar exists for clinical application.

2.3.3 VELO Beam Monitor

ICs can provide several different measurements of the PBT delivery however their mode of operation requires that they are physically interceptive of the beam. Scatter from direct interactions with the detector itself can impact the beam quality and these effects can multiply with each additional beamlet (such as for PBS or with a SOBP). In contrast, the VELO detector modules are considered non-interceptive and comprise position sensitive, silicon detectors surrounding a central aperture (Fig. 2.10a).

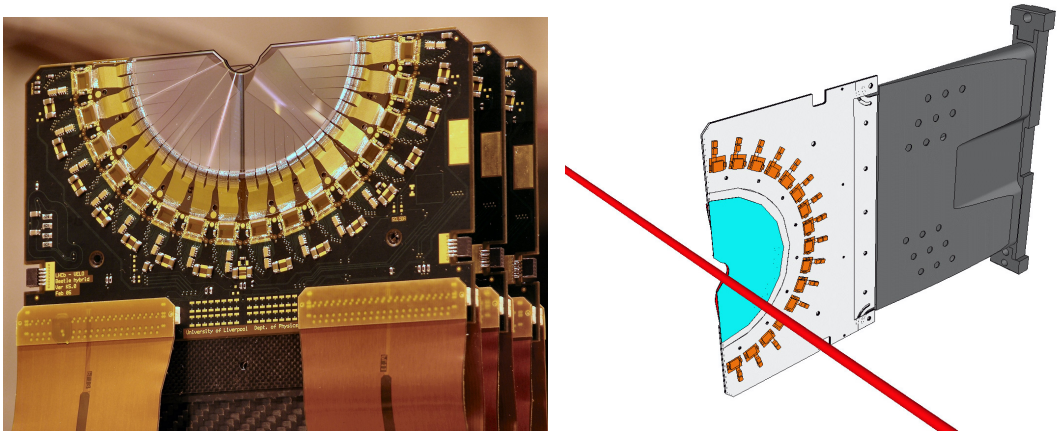

(a) (b)

Figure 2.10: a) VELO sensor hybrid modules; semi-circular silicon sensors surround an aperture [126] allowing b) the beam to pass without interference [127].

Many of these modules were originally built for and used to provide precise track coordinate measurements of secondary vertices originating from collisions at the LHCb experiment at CERN, the European Organization for Nuclear Research. As such, the detection system needed to satisfy specific criteria: high signal-to-noise ratio, an adequate acquisition and readout response and micron scale spatial resolution. As VELO is capable of assessing several beam properties in real time with high resolution, sensitivity and radiation hardness, the detector system also presents as a feasible candidate for clinical beam monitoring.

The advantageous design enables precise measurements of the beam halo (defined in Section 2.1.3) which can provide information about the active delivery of the beam with minimal interference (Fig. 2.10b). The repurpose and adaptation into a standalone beam monitor began from previous work reported in [128]. Initially, the system was aimed at optimisation for implementation into the PBT beamline at CCC however, ongoing developments have since been made to improve several aspects of the system and also to explore its application at other facilities [39, 129].

LHCb VELO Detector Technology

The VELO detector module consists of hybrid semi-circular, radial (R) and azimuthal (φ) sided sensors with multiple silicon micro-strips enabling the full geometrical acceptance of interaction points. Both sides are structurally similar where a semi-circular aperture sits centred along the central, outer edge. When opposing detector halves are positioned together, this geometry permits the sensitive area to approach up to 8.2 mm radially from the beam axis. Built specifically for the beam and conditions of the LHC, the system is well matched to cover the full momentum and angular range of nearby interactions and displaced vertices [130]. Corresponding track reconstruction algorithms are based on a cylindrical polar coordinate system where signal readouts occur at the bunch crossing time of 25 ns, at a frequency of 40 MHz. Due to the nature of these requirements, a cooling system is essential in order to dissipate heat generated from the readout electronics and maintain the sensors at temperatures below 0 °C.

To withstand heavy radiation, the sensors are manufactured from enriched strips of n-type semiconductor material. Each side contains 2048 strips which transmit AC signals via capacitive coupling from a layer of oxidised silicon dioxide through to the readout electronics, around the circumference of the sensors [131]. Each detector module consists of two 300 µm thick p^+ doped silicon sensor halves with an R and φ side each; combined geometrically, they provide sufficient spatial information to resolve and reconstruct the points of interactions. Approximately, both sides have an active area which covers across a width of 84 mm, from the straight edge up to a 42 mm outer radius. The modules can also fully retract up to 60 mm apart laterally. The architecture depicting the distinct sides comprising a module is shown in Fig. 2.11.

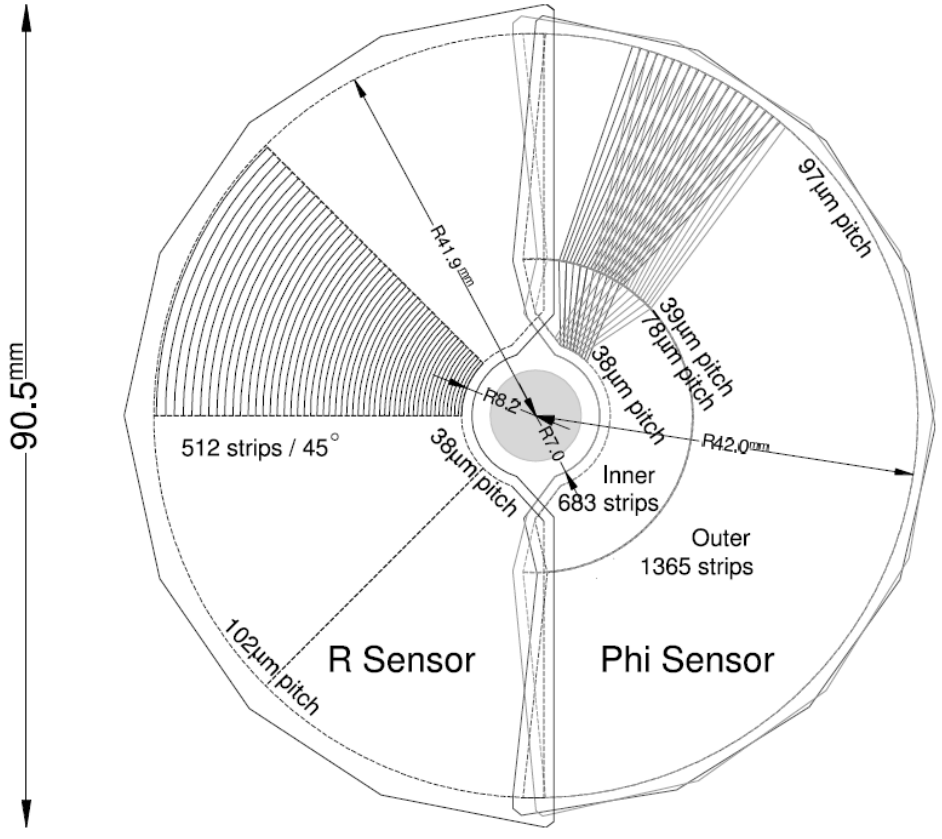

Figure 2.11: Schematic of a VELO module showing the geometry of the r and ϕ sides, as named on each half. Key features and sections have dimensions listed along with partial illustration of the diode strips [131].

The R-side sensor consists of four sectors each split at 45° with 512 diode strips oriented concentrically around the central aperture, through to the circumference. This half provides positioning information relative to the origin of the beam axis. Between the

micro-strips, the pitch increases linearly from 38 to 101.6 µm and charge sharing occurs more asymmetrically across the thinner strips, allowing interactions to be resolved more precisely in the inner regions [132]. The φ-side sensor provides angular positioning information orthogonal to the R-sensor and the azimuthal coordinates. Similar to the R-side, there are 2048 diode strips, however these are split into an inner and outer region, oriented radially from the origin. The inner section comprises 683 strips and the outer has 1365 strips, forming an active area with a marginally larger angular coverage [131].

Structurally, the VELO sensor remains largely unchanged but in order to operate the system as a lone device, several modifications were necessary to migrate the system out of the LHC environment. To be successfully integrated into the treatment line at CCC, the existing technology needed specific amendment for the conditions and restrictions of the medical facility. Moreover, it needed to operate without altering the beam whilst still performing at full functionality. A dedicated cooling and air flow system was designed to preserve the operation of the hybrids below 0 °C and without water condensation: this is below the dew point of air. A Faraday cup (FC) was also built specifically for beam current measurements and to match the CCC beam parameters, along with an assembly to precisely move and position the detector locally. Several modifications were also made to simplify the readout electronics and bypass the pre-existing scheme used for the LHCb experiment, these are detailed in [128].

Standalone Monitoring System

Following first proof-of-principle measurements achieved in 2014 [55], the main considerations for improvement were identified as related to the readout process and synchronisation with the CCC facility. As the LHC has a bunch crossing frequency of 40 MHz, the front-end electronics i.e. readout chips (Beetle chips) needed to be synchronous with the cable delays and (TELL1 board) external triggers for data acquisition (DAQ). The VELO monitoring system is required to match the arrival of proton bunches which are generated by the 25.7 MHz RF frequency of the CCC cyclotron. The internal frequency of the clocks correspond to non-interchangeable quartz crystal and therefore cannot be changed. A solution for this was to inject an external readout trigger for universal clock synchronisation. Improvements to the post readout process were also achieved by

software updates which manage the signal processing and FC readout [39]. The entire system setup with the main components labelled, is shown in Fig. 2.12.

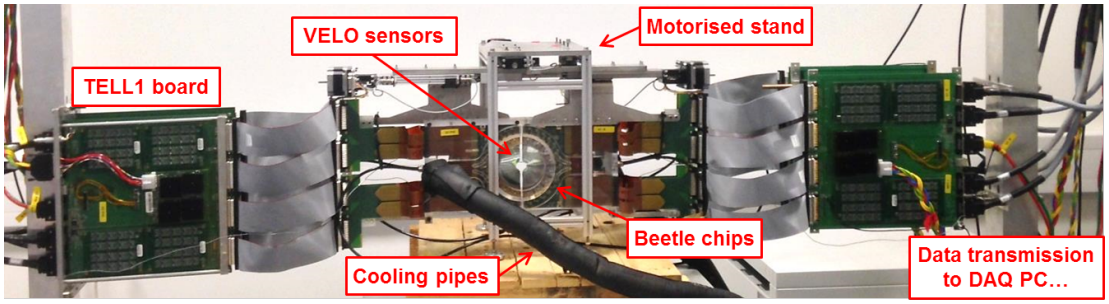

Figure 2.12: The VELO beam monitor system with main components labelled (computers for DAQ processing and storage are not shown).

These initial CCC measurements achieved outputs from the VELO sensors which demonstrated good linearity with FC measurements of the absolute beam intensity. It is anticipated that the combination of measurements obtained with the VELO detector, the beam intensity determined by the FC and knowledge of the dose rate with the CCC beamline, can all be correlated to provide beam and dose information during delivery. These seek to also reduce the time demand required for quality assurance checks in the clinical workflow.

As the VELO sensors are proton counters and register individual charges with each hit, the relationship between the amount of charge induced within the silicon, to absorbed dose can be determined. Fundamentally, this means that fewer conversion factors are needed to determine the MU, in contrast for ICs. The FC is the most direct way of obtaining the beam current and by cross-correlating the total distribution with halo measurements, offers the possibility of online dose monitoring through non-interceptive, relative measurements. The intrinsic properties of this technology also extends its use for potential application in future accelerators and delivery methods.

2.3.4 Radiochromic Film

Another widely used tool for relative dosimetry measurements are radiochromic films. These are commonly used for machine quality assurance and as a visual check of beam characteristics in EBRT. This has led to the development of an industry standard

GAFchromic^{TM} film where the most recent model is EBT3 [41]. The use of EBT3 film is well established in PBT and is commonly used to determine beam performance and quality. The high spatial resolution and low energy dependence enables measurements of transverse dose profiles [115]. For patient specific or machine verification, it is essential to be able to perform checks with high accuracy and reliability, prior to delivering a course of treatment. Film dosimetry allows a visual representation of the beam as well as an analysis of the geometrical beam characteristics (i.e. uniformity, shape and size) and the 3D dose distribution.

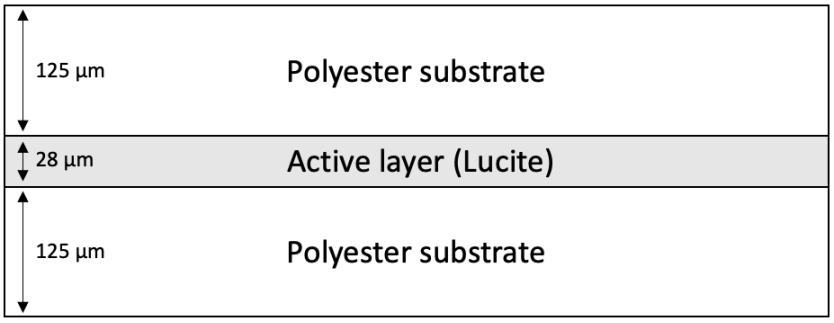

Figure 2.13: Sketch of the composite layers in EBT3 film, a 28 µm active region is surrounded by two thicker substrate layers.

EBT3 film is made of a 28 µm layer of lucite, enclosed by 125 µm of polyester substrate on each side (Fig. 2.13). Exposure to ionising radiation results in polymerisation of free radicals within the active layer, inducing the film to darken [133]. EBT3 self develops and the dark colouring or optical density (OD) is proportional to the extent of irradiation, increasing with absorbed dose. For CPT however, the use of EBT3 film is limited due to quenching effects and saturation at points of high doses, such as the Bragg Peak [134]. It is also noted that there are multiple considerations and sources of uncertainties involved when using film to determine the beam distribution as a function of dose. Calibration measurements must be performed under specific conditions. Established methods and standard protocol have been reported in literature [134–138]; these are further discussed in Section 3.4.1 and were applied for all the film measurements and analysis.

2.4 Summary

The rationale of proton therapy leads from the advantageous dosimetric characteristics of charged particles as they traverse and deposit energy along a path, accumulating to a maximal point as represented by the BP. This enables a high amount of dose to be precisely and suitably distributed to target sites, necessitating the consideration of several factors which influence the properties of the beam. These include the type of accelerator, transport line, delivery system and beam diagnostics employed. Although these aspects differ across facilities as dependent the requirements of the clinic, they ultimately serve the purpose of optimally delivering a beam safely to the patient, for the specific purposes of the treatment prescribed.

Several different parameters and concepts integral to the delivered beam have been overviewed, with a particular focus on the CCC facility. In contrast with modern facilities, CCC has a unique beamline and treatment system which offers an applicable environment for further study and integration of beam instrumentation. Diagnostics are necessary to provide accurate beam measurements to ensure a correct delivery and a high quality of treatment. ICs are typically used to monitor the dose however are interceptive devices and encounter performance limitations, particularly for enhanced CPT beams and techniques. As such, a novel system based on LHCb VELO detector technology was proposed. To support its development and examine the feasibility of other tools, simulation studies, optical modelling and experimental measurements were performed. These are discussed in the following chapters.

Chapter 3

Clatterbridge Beamline Characterisation

Clinical and research proton beams provide opportunities to study different aspects of PBT. With advances in medical accelerator technology and further potential PBT developments, an outcome of this thesis is to explore the capabilities of several silicon detector systems. The VELO online beam monitor is currently being developed to provide measurements such as the profile, current and dose whilst minimally interfering with the beam. This is possible with the novel concept of detecting only the halo where there is no significant impact on the delivery of treatment. However, to resolve these beam properties, measurements must be firstly correlated using some approach which provides knowledge of the entire beam distribution. This can be done in several ways; commonly VELO is calibrated with other beam diagnostic instruments (i.e. an ion chamber, Faraday cup or film). Alternatively this can also be attained by simulating the beam to determine information for relative measurements. Simulation studies are essential for the optimisation and application of the VELO monitor in medical beamlines.

Furthermore, it is valuable to evaluate the beam characteristics and expected detector response before integration into any facility. Simulations allow this possibility without the burden of beamline accessibility. Particularly for clinical facilities, there is often high patient load and other constraints where scheduling beamtime is difficult. This was the case for CCC, where the VELO system was originally adapted for integration into the ocular PBT beamline. Therefore, preliminary simulations were necessary to

investigate the beam behaviour and potential impact, feasibility and performance of the detectors implemented in the treatment line. A model built with the Monte Carlo toolkit, GEANT4 was used to simulate the environment at the CCC PBT beamline.

This chapter provides an overview of the Clatterbridge treatment delivery system and the operational parameters of the beam. These are essential for characterisation of the treatment beam and simulations in GEANT4. The simulation model and fundamental mechanisms of the code are also summarised. Further developments to the model were made and the outcomes of simulation studies are described. To examine the accuracy of the model and results, experimental beam profile measurements with EBT3 film and a Medipix3 detector were performed; these results and several observations about the CCC beam and cyclotron are reported.

3.1 Overview

The Clatterbridge Cancer Centre is one of a few dedicated ocular proton therapy clinics in the world. It operates a fixed horizontal treatment beamline which delivers protons at 60 MeV at isocentre using a purpose built, double scattering system (Fig. 3.1). This produces a conformal beam with a range of 31 mm and a sharp 0.9 mm fall-off, enabling the targeted and precise delivery of uniform dose to tumour volumes.

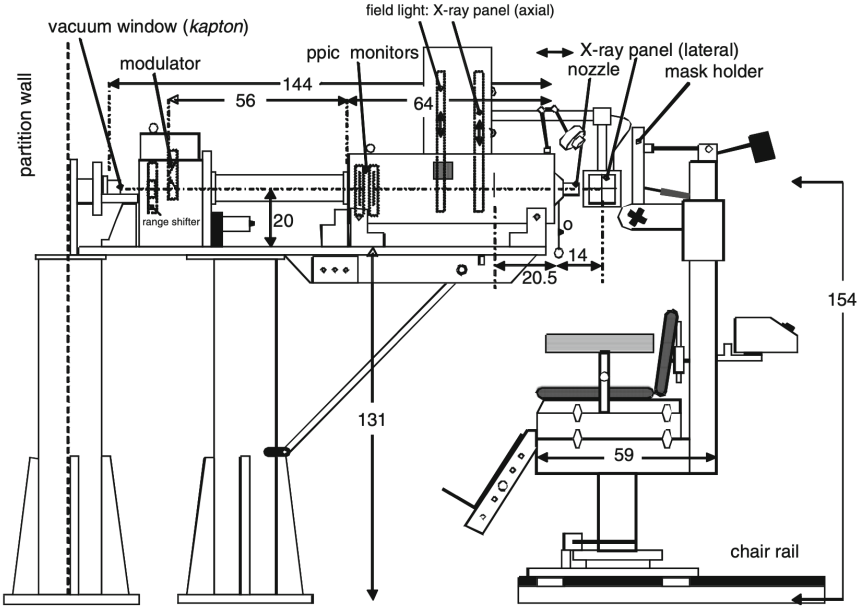

Figure 3.1: CCC delivery system and chair schematic. Dimensions are in cm [15].

Patients are always seated upright in a motorised chair capable of precise alignment (translational in three directions) and wear a custom mask which is attached to a frame at the top of the chair (Fig. 3.2). Each treatment typically lasts 30 seconds and depending on patient requirements, various range shifters and modulators are implemented to adjust the beam energies. Patient collimators shape the field in the transverse plane. Many of these developments were commissioned and are manufactured in-house; these enable the facility to continually provide a well established proton service. As such, high rates of local tumour control, ocular retention and preservation of visual acuity have been achieved and patients with ocular melanoma have been successfully treated for more than 30 years [15, 139, 140].

Figure 3.2: Treatment chair and extent of treatment beamline. The rigid frame (silver) at the top of the chair secures the patient and mask in place.

Facility considerations, delivery approaches and beam requirements for ocular treatments have been discussed in Section 2.2.4. For CCC, quality assurance procedures to maintain typical and local treatment beam parameters are discussed in detail in [139]. A summary is provided in Table 3.1 [†].

[†]Personal communications, A. Kacperek, 2019.

Table 3.1: General treatment beam parameters.

Parameter	**Value**
Dose rate	8-30 Gy/min
Set-up time	10-15 mins
Treatment time	30 s
Verification precision	± 0.2 mm
Field uniformity	<1%
Field diameter	<34 mm
Penetration depth	4-29.3 mm
Fall-off	0.9 mm (90-10%)
Penumbrae	1.1 mm (80-20%)

3.1.1 Treatment Delivery System

The CCC treatment beamline was built during initial neutron therapy trials to provide a clinically useful proton beam as an additional treatment modality. A set of double scatterers, modulation devices, several collimators and custom-built diagnostics combine to generate a uniform beam, whilst also minimising the beam penumbra and energy losses [111]. This is illustrated in Fig. 3.3 where significant components are grouped and denoted with letters.

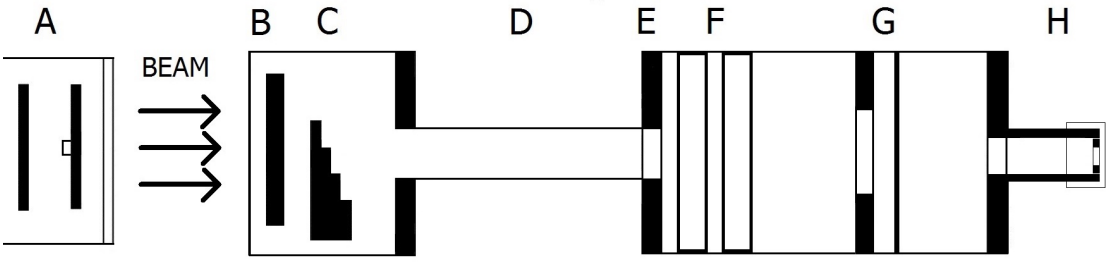

Figure 3.3: Schematic of the beam shaping components of the CCC treatment delivery system. The proton beam originates from the accelerator bunker behind the wall and traverses two scattering foils and beam stopper (A), an optional range shifter and modulator (B & C), drift pipe (D), several collimators (E), two dose monitors (F), cross-wires (G), treatment nozzle and collimator (H).

Details of the cyclotron and generated beam are described later in Section 4.2.1. From the accelerator bunker, the beam (in vacuum) enters the treatment room and traverses through two tungsten scattering foils which spread the beam laterally. There is a central (brass) beam stopper attached to the second foil which significantly reduces the beam fluence such that it attains a uniform transverse profile when it leaves the treatment

nozzle. The beam then exits by a kapton window into air, through an aluminium box containing the modulation devices. Range shifters or absorbers (blocks of PMMA) can be placed here to decrease the maximum proton range and energy at isocentre. A rotating modulator can also be inserted adjacent, to produce a SOBP. This arrangement results in the small lateral penumbra but also increases energy losses in air [15].

An aluminium drift pipe connects the modulation box to the dosimetry box. This section of the delivery system is an important location and is identified as the '*Integration Zone*' from [128]. The pipe can be easily removed to allow sufficient space to situate the VELO monitors. Following this, two dose monitors (parallel plate ionisation chambers) and two tungsten wires arranged in a cross, comprise the QA diagnostics. These are used to routinely monitor the uniformity and performance of the beam. The beam leaves through an end brass nozzle which can be fitted with a cap to secure the last brass collimator. A range of collimators can be fitted here to limit the beam by altering the aperture diameter as dependent on patient requirements.

3.2 Simulation Modelling

At the time of its construction, the CCC treatment beamline was designed to capitalise on the available accelerator technologies and various advantages offered by different delivery approaches [110–112]. As a pioneering facility, the changes to improve the beam delivery were also often self-developed with the equipment built on premises. Several studies were performed to simulate the treatment beamline for further development, examine the performance of different components and for dosimetry [109, 141–143]. Specifically in [142, 143], the Monte Carlo codes MCNPX, GEANT4 and McPTRAN were used to simulate the CCC beam and dissimilarities between the codes were due to differences in the computation of interactions and transport of radiation. Since then, several other codes have been assessed for application in medical physics. In particular, GEANT4 has been benchmarked to clinical data and its capabilities for ocular PBT modelling are well demonstrated [144, 145]. Numerous other facilities have beamline models, the most prominent being '*Hadrontherapy*' [146, 147] which is available with every build of GEANT4 as an example to assist users with developing their own models.

At Clatterbridge, more recent simulation work of the beamline was done by [148] however this was based on the *Hadrontherapy* example where the geometry was adapted from the CATANA, Italy ocular beamline [149]. As the model was not available and previous efforts to validate the geometry were not implemented, the development of an accurate and reliable simulation model of the CCC treatment beamline was pursued. A validated simulation model is essential to investigate the implementation of the VELO detector system and its viability as a candidate for online dose monitoring. This is also highly valuable as CCC supports a wide and diverse scope of experimental work and can benefit the ongoing studies into facility upgrades, integration of other instrumentation and radiobiology. Therefore, an objective was to develop a finalised model and to make the source code and documentation available for wide use as a verified, standard simulation model for all related work performed with the beamline.

3.2.1 GEANT4

GEometry **An**d **T**racking or more commonly known as **GEANT4** [40], is a software toolkit which enables the accurate simulation of the movements and interactions of particles through matter. Originating from CERN initially for high energy physics, an established collaboration of worldwide members provide ongoing developments and user support to maintain and improve capabilities. GEANT4 is written in object-oriented C++ programming language and offers an extensive range of functionalities, visualisation interfaces and approaches to analyse generated results. This flexibility and the open-source accessibility of the code has promoted the use of toolkit for a vast range of applications including particle, detector and nuclear physics, as well as space and accelerator science.

The code utilises Monte Carlo (MC) methods and applies physics models to describe electromagnetic and hadronic interactions from high energies (TeV) down to sub-eV scales. As the nature of radiation events are stochastic in nature, it is necessary to consider particle interactions and physical processes given their probabilistic distributions. GEANT4 utilises random number generation to simulate individual particles on an event-by-event basis, through the geometry of any material. Users can build an application with the toolkit by specifying the particle source, detector properties, tracking

management parameters and selecting packages which implement models of particular physics processes. This is detailed extensively in [150, 151] and the code is fully documented online on [152].

The simulations described in this chapter were performed using a model of the CCC treatment delivery system developed at University College London (UCL)[†]. GEANT4 versions 10.02.p.01 and 10.04.p.02 were used and simulations were executed on the UCL HEP high performance computing cluster. The source code and details of the model are also provided online on [153]. It is noted that the upgrade to the newer GEANT4 version was also accompanied by significant changes to the model, mostly to improve the computational efficiency. Further development was necessary to perform the same tasks as the initial model and also to add capabilities; these specific contributions to the source code are described. As the workings of the toolkit itself are complex, only essential features pertinent to the scope of work in this thesis are overviewed.

Structure & Processes

In principle, GEANT4 will generate a particle, transport and track it through geometries of different materials and record information about physical interactions and processes which occur. Different libraries and classes are utilised for functions to initialise, invoke and process events, define geometry and collect data for analysis and visualisation. Some key classes are: G4RunManager, G4EventManager, G4TrackingManager, G4SteppingManager, G4GeometryManager, G4ParticleGun, G4ProcessManager and G4VisManager. These execute the main features [154]:

- *Run*: A collection of events which occur under identical conditions, with the same beam and detector implemented. The execution of a single run is typically synonymous with and referred to as a simulation.

- *Event*: The units of a simulation where collectively, multiple events constitute a run. An event starts with the generation of a primary particle, tracking these and secondaries completely through the same experimental configuration.

[†]Developed by M. Hentz, 2017.

- *Track*: Represents the movement of particles along a trajectory. It provides details of physical quantities in the current instance and is executed independently of the particle type or physics processes. Tracks are updated after each step.

- *Step*: The distance between two interactions where the process with the shortest interaction length occurs. There are two stages; pre-step and post-step, where particle information can be retrieved at the start, along or end of the step.

- *Geometry*: Objects are constructed by definition given three conceptual layers; solid, logical and physical volume. These describe the dimensions, materials and spatial positioning of geometrical and detector structures.

- *Detector*: Geometry components used to specifically retrieve and record particle information such as the kinetic energy, momentum, time, position and energy deposition. This is attributed at the logical volume level where detector geometries serve as sensitive volumes.

- *Hit*: A physical interaction of a track which has occurred within a sensitive detector. This information can be collected and obtained as outputs.

- *General Particle Source*: Defines the distribution and initial properties of the primary particles generated. This includes the shape, energy, position, spatial and angular distribution of the input source particle.

- *Physics*: Describes the transport and interaction processes of each particle within a material. Different algorithms are needed to model the physics across a wide range of energies or for varying applications; several may be combined to accurately represent the entire domain. These processes are constructed as physics lists which can be user defined, in addition to the several default benchmarked lists available.

- *Visualisation*: Simulations can be executed interactively by graphical sessions to visualise the geometrical and beam components. It is useful to be able to view the model and the beam can be instantiated to generate particle tracks. Several different graphical systems are offered as dependent on the requirements and demands of the visualisation.

3.3 The CCC Treatment Line Model

The model was built to simulate the delivery system and the 60 MeV PBT beam, incorporating information from CCC and older simulations, as shown in Fig. 3.4.

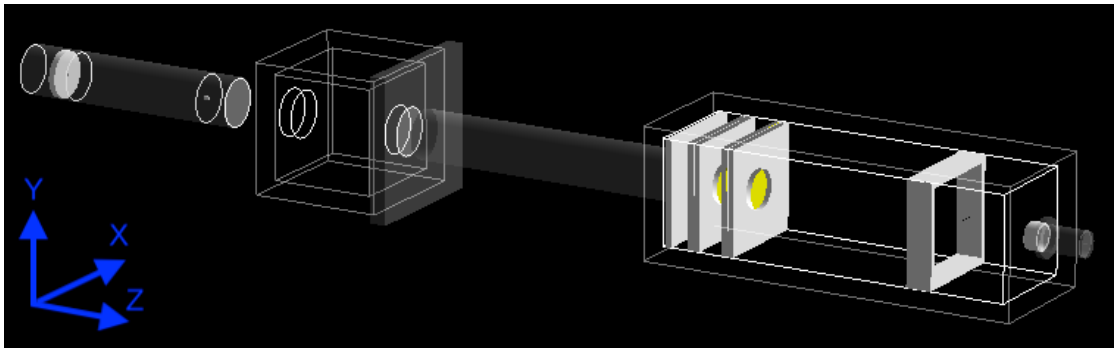

Figure 3.4: Visualisation of the CCC treatment line in GEANT4. Main components (left to right): dual scattering system, modulation box, integration zone, dose monitors, cross-wires and nozzle. Axes (blue): x (horizontal), y (vertical), z (beam propagation).

This treatment line is placed within an '*inner room*', a smaller box representing the treatment room within the world volume which must contain all the components of the simulation. The start of this beamline is positioned at -4200 mm (in the z axis) from the centre of these volumes. Geometries are defined with dimensions as half lengths and their points of origin are at the centre of their mother volume. This is inherent to GEANT4 which uses a hierarchical system so that structures can be defined in relative parameters, using boolean operations and to avoid intersections at the same levels: this is often a common error. However, this can be complicated as components have different mother volumes and thus origin points, so calculations between multiple coordinate systems are needed to determine the correct positions in z. For simplicity, the edge of the inner room where the beginning of the scattering tube is situated will be referred to as the origin of the simulation ($z = 0$). The particle source was rotated and translated to be placed at this point. Beam parameters provided for this model were sourced from unconfirmed or older documentation. Default simulation source settings:

Gaussian distribution of protons

Mono-energetic $\mathbf{62.5 \pm 0.082\ MeV}$ beam

Beam size of $\boldsymbol{\sigma_{x,y} = 4,\ 4.5\ mm}$

Angular spread of $\boldsymbol{\sigma_{x,y} = 2.3,\ 1.2\ mrad}$

3.3.1 Running the Simulation

The simulation is executed in GEANT4 as defined in header (.hh) and source (.cc) files containing mandatory and optional user action classes. All parameters can be directly programmed within these files or run using either of two ways; interactive or batch mode. The interactive mode is executed through a visualisation session using a graphical interface, where individual lines of command must be input to define each parameter (i.e. */run/beamOn 1000* will generate and simulate 1000 primary protons through the model). This is more useful for debugging or visual checks as simulating large numbers of particles this way is computationally taxing. For batch mode, commands are listed instead in a macro (.mac) file where the complete simulation is executed according to these parameters. This mode also makes it easier to set or change different settings or create a customised set of parameters for each simulation.

This CCC model was firstly made available with preset macros to run, visualise and score, as well as with python scripts to analyse and plot simulated data. Shell (.sh) files were also provided to submit parallel versions of the simulation (different seeds) to a queue in the UCL Linux cluster and combine results into new created directories. A summary of the macros and functions of each are provided for context:

- *run.mac*: Set detector geometry and position, activate tracking, call scorer.mac, set physics list, cuts, initialise, set seeds, particle beam parameters, step limits, verbosity, output analysis files, number of protons, call score_dump.mac.
- *scorer.mac*: Create scoring mesh and define size, position, number of bins, quantity scored, close mesh.
- *score_dump.mac*: collect scored quantities, define file and dump data to .txt files.
- *vis.mac*: Open visualisation driver, draw volumes, set axis and viewer style, parameters, zoom, axes, particle trajectory colours.

A pristine BP and the lateral beam profile could be simulated using the primitive scoring method by defining a mesh, collecting the total energy deposition within a number of bins, dumping to a file and plotting (Appendix B.1). Running with the default

simulation parameters achieves a BP at 30.80 mm and a wide, rounded transverse dose profile at isocentre. The beam has diverged from the central axis in air (treatment nozzle is only 34 mm in diameter) however it is expected that the dose deposition here should be more homogenous. In practice, a flat beam is used for treatments such that dose coverage across the target site is uniform. A cause for this difference could be due to a missing collimator between the dose monitors and cross-wires.

More detailed methods were necessary to obtain further information about each particle including the type, position, direction, momentum, kinetic energy. This can be achieved by tracking particles by accessing each step in the simulation and recording relevant parameters at defined points. This is managed by the *G4UserSteppingAction* class which checks for various conditions at the *PreStepPoint* and *PostStepPoint* locations contained in *G4Step* and writes this information as an output. Protons were only tracked if they were inside the components of beamline and ignored if greater than the widest geometries i.e. >100 mm in x or y. The tracking intervals were set given their position in z and steps were counted only if both the pre- and post-step points crossed a boundary. This feature is enabled in the run macro and only particles which completely crossed were recorded. Care must be taken when considering steps and boundaries as this can result in inconsistencies or incorrectly counted steps. These z intervals could be defined in *SteppingAction.hh* (Appendix B.12) where specific information about the beam at any arbitrary position along the treatment beamline could be retrieved.

3.3.2 Beam Study

Simulating protons from the source to isocentre enables different particle quantities to be determined to define the characteristics of the beam. Four main properties are considered; the transverse emittance (in x), beam profiles (in the transverse plane and intensity in x) and the energy spectra, which were all plotted using a python script[‡] (default case in Appendix B.2). Noticeably, a mean energy of 60.15 MeV is obtained with the model which is inconsistent with the measured clinical mean energy of 60.00 MeV. As the simulation was unvalidated, partly due to inaccessible facility information,

[‡]Provided by M. Hentz, 2017.

several assumptions were made about the geometry and input particle source. The following changes were implemented as information was verified or newly acquired[‡]:

Scattering foils:

- Tungsten thickness reduced from 25 µm to 20 µm

Dose monitors:

- Air separation reduced from 3.6 mm to 2 mm
- Guard ring thickness reduced from 1.6 mm to 1 mm
- PMMA layers reduced from 1 mm to 0.5 mm

These changes resulted in slightly different beam characteristics (Appendix B.3); mainly an increase in the resulting energy to 60.25 MeV. This is expected as several layers of material have been reduced, thus there is less attenuation. To investigate the impact of each component and behaviour of the beam through the delivery system, the beam was tracked at 15 z positions. This was defined in lines 35 and 51-53 in the header file (Appendix B.12). Simulations with 100 million primaries were run using the default input beam parameters (see Section 3.3) and the recommended QGSP_BIC_HP physics list for clinical proton beams. Characterisation plots for significant positions are shown in Figs. 3.6-3.11; the remaining are included in Appendices B.5-B.9.

At the start of the treatment line (Fig. 3.5) the beam is fairly sharp: its appearance is indicative of the default parameters. An observation at this point is that by definition, this beam represents the case of a clean, mono-energetic beam with a limited Gaussian spread. The beam then passes through a small aperture (6 mm diameter) and the first tungsten scatterer (Fig. 3.6). The collimation causes a reduction in the beam size and penumbra, removing the surrounding tails. Combined with traversal through the foil, there is a mean energy loss of 0.21 MeV. After passing through the second foil and stopper, the beam distribution and emittance changes considerably (Fig. 3.7). The brass stopper attenuates a significant proportion of the central region of the beam and the remaining lateral protons form a ring. As indicated by the shape of the emittance plot, there is an observable outward spread and a slight halo. The change in flux up to this point amounts to a loss of approximately 94% of initial protons.

[‡]Personal communications, A. Kacperek, 2018.

Source

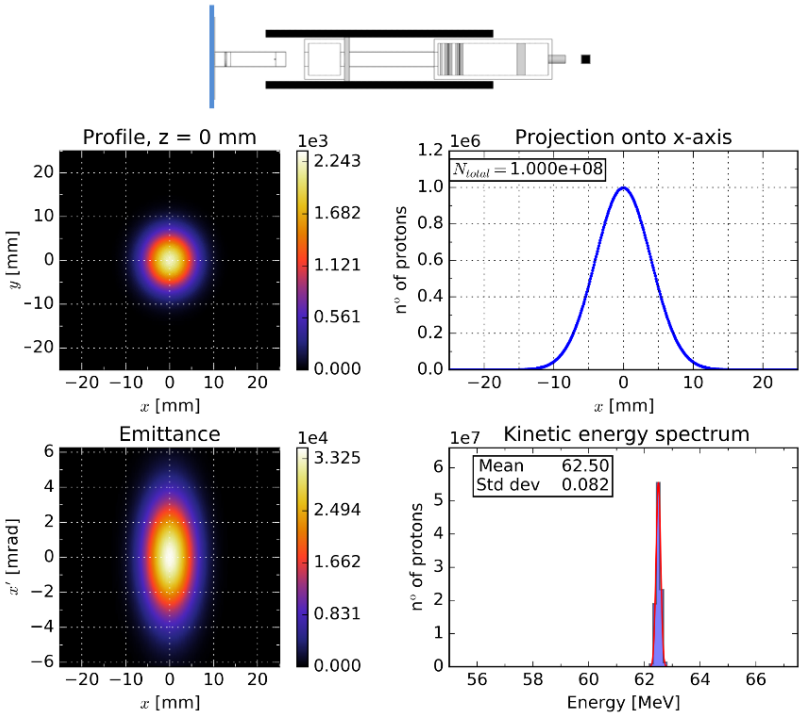

Figure 3.5: Plots of the simulated transverse beam emittance, profiles and the energy spectra at the beam source. The blue line overlayed on the treatment beamline schematic above indicates the tracked position in z.

First Scattering Foil

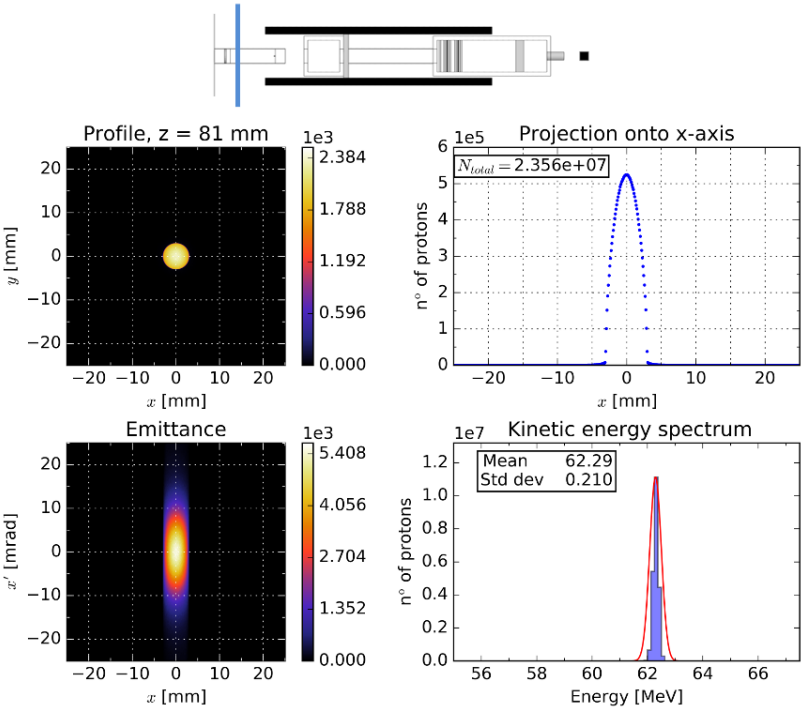

Figure 3.6: A sharper beam emerges from the first collimator and scattering foil with a lower mean energy but greater energy spread.

Second Scattering Foil

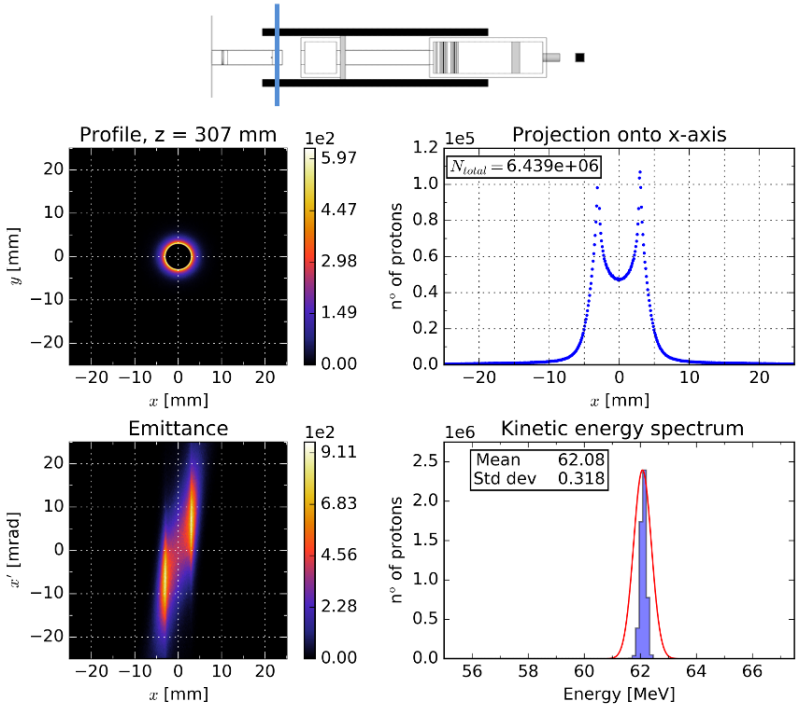

Figure 3.7: The second scattering foil spreads the beam and energy further, the brass stopper results in significant attenuation in the central beam axis.

Now in air, an increase to the spread in the beam profile and emittance indicates that the beam starts to scatter (Fig. 3.8). The dip at the central axis starts to disappear within the integration zone (Appendix B.6) and the particle flux starts to even out by the end of pipe (Fig. 3.9). The lateral extent of the particle distribution is noted here and the beam propagation is examined in more detail later (see Section 3.3.3). After passing through both dose monitors, some energy is lost, the beam widens and the return of the lateral tails are evident (Fig. 3.10). This degradation of the beam due to the dose monitors can be prevented by the use of a non-interceptive measurement method: a benefit of the VELO monitoring system.

After exiting the treatment nozzle, the beam has again been collimated and the distribution is restricted to the size of last aperture (Fig. 3.11). There is a small penumbra and the rotation of the phase space ellipse shows that the beam is diverging. The beam transmission from the source to the end of the treatment beam line is 2.45% with an energy loss of 2.16 MeV (3.5%). The beam also loses another 0.1 MeV in the 70 mm air before it reaches isocentre; the rest of these quantities are listed in Table 3.2.

Start of Modulation Box

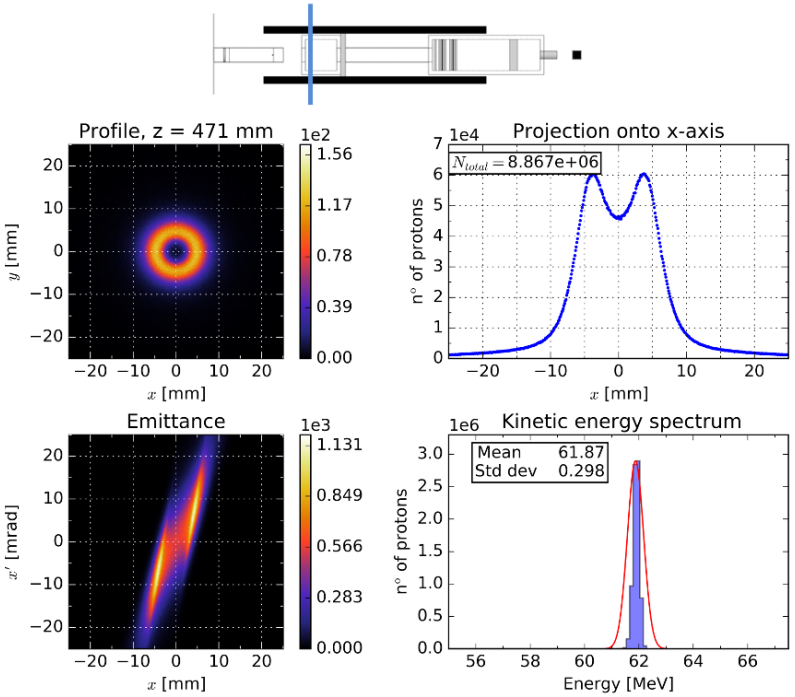

Figure 3.8: Following its departure from the vacuum through the kapton window, the beam starts to diverge at the the start of the box containing the removable modulation components. The central dip also starts to decrease

End of Integration Zone

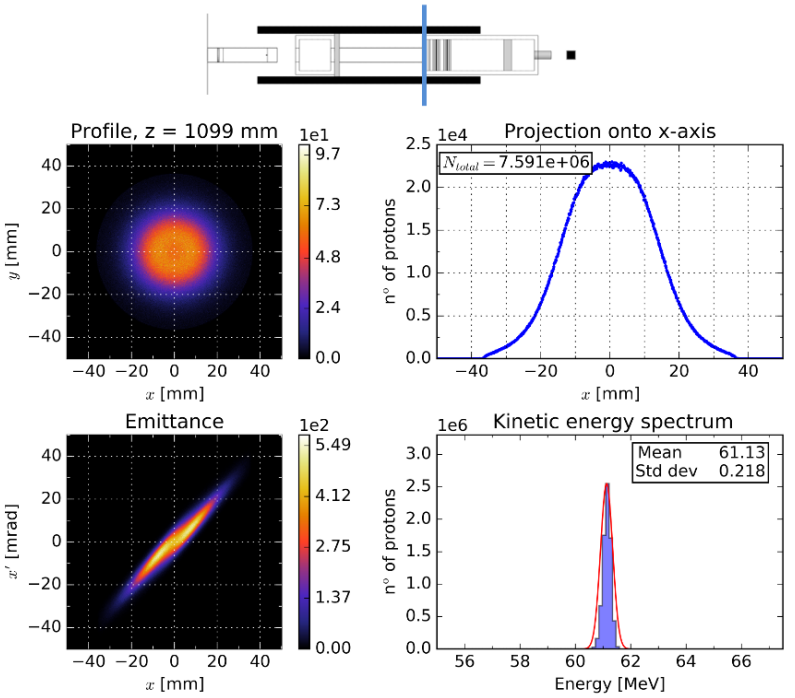

Figure 3.9: The beam shape returns to a Gaussian distribution at the end of the designated VELO integration zone, inside the beam pipe.

After Dose Monitors

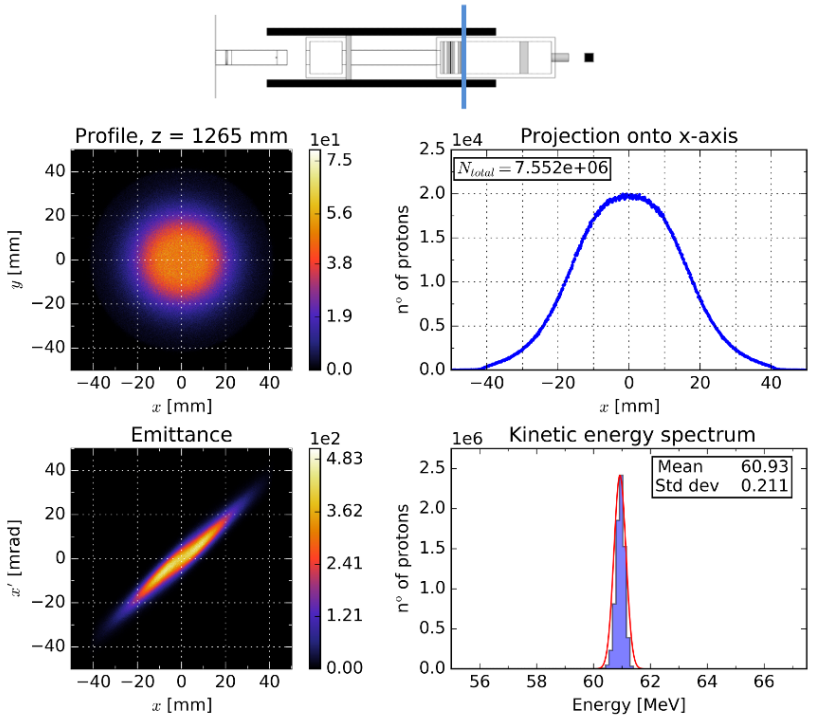

Figure 3.10: Traversal through the dose monitors results in greater spread of the beam.

After Nozzle

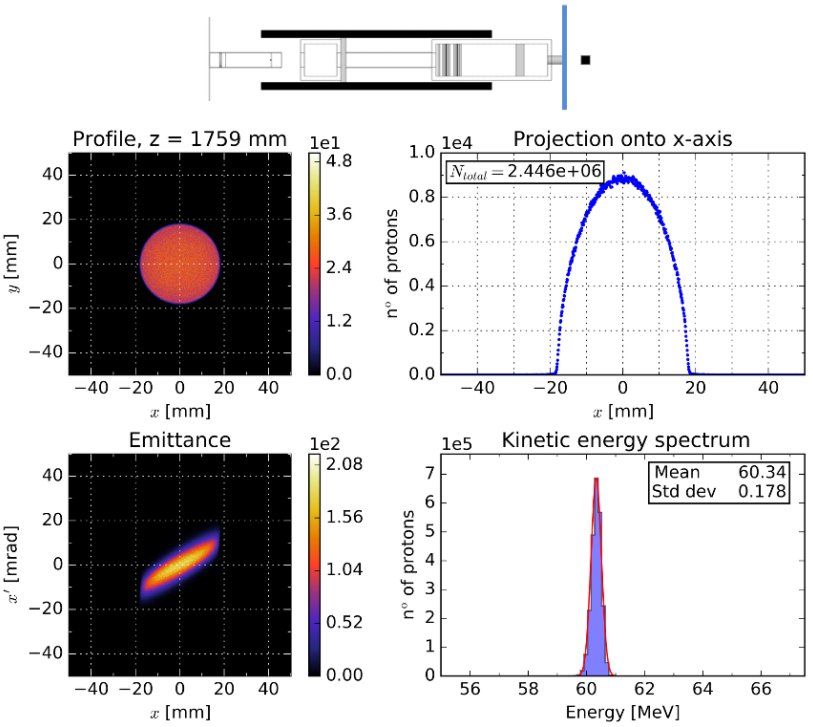

Figure 3.11: After evacuating the treatment nozzle, the beam is noticeably narrow. The collimation also results in a small energy spread

Table 3.2: Simulated particle transmission and energy losses.

Beamline location	***z* position** [mm]	**Transmission** [%]	**Mean energy** [MeV], **Loss** [%]
Source	0	100.00	62.50, 0.00
After foil 1	81	23.56	62.29, 0.34
After foil 2	307	6.44	62.08, 0.67
After kapton window	357	9.28	62.01, 0.78
Start of modulation box	471	8.87	61.87, 1.01
Start of integration zone	676	8.08	61.73, 1.81
Mid of integration zone	900	7.86	61.37, 1.23
End of integration zone	1099	7.59	61.13, 2.19
After dose monitor 1	1195	7.55	61.01, 2.38
After dose monitor 2	1265	7.55	60.93, 2.51
After cross-wires	1577	7.55	60.55, 3.12
After nozzle	1759	2.45	60.34, 3.46
At isocentre	1829	2.45	60.25, 3.60

3.3.3 Integration Zone

The previous simulations and results provide an overview of the beam distribution and transport along the treatment beamline. As the VELO system is to be implemented specifically in the integration zone, the physical impact of the detectors on the beam performance must firstly be assessed. In fact, the beamline at CCC presents a unique case to test the online monitoring system and is thought to be a contributing factor to its conception. Aside from the geographical proximity of Clatterbridge, the beamline offers several advantages for testing and implementation. The cyclotron can produce a beam of protons with relatively high clinical currents (>30 nA, $\sim 10^{11}$ protons/s) over a range of beam sizes using customisable collimators, up to the internal 34 mm nozzle diameter. Typically operating at maximum energy, the fixed components of the treatment line and interchangeable modulators enable delivery of a consistent beam. As a result, the beam should be predictable at any location within known margins. There are minimal differences in accelerator settings for treatment as a sufficient standard at isocentre must be achieved. Moreover, due to the passive scattering system arrangement, the characteristics of the beam within the integration zone should also be consistent. Therefore, evaluating the beam propagation at this location determines the expected beam distribution and halo which would be measured by VELO.

Simulations were performed to obtain the transverse beam profiles and intensity maps across 15 different positions in the integration zone (Fig. 3.12). This is relevant as the VELO sensors are counting detectors and there are several different metrics to correlate with the halo. In Fig. 3.12b, 5 distances are denoted as '*VELO positions*' where the modules were previously placed for measurements in [128].

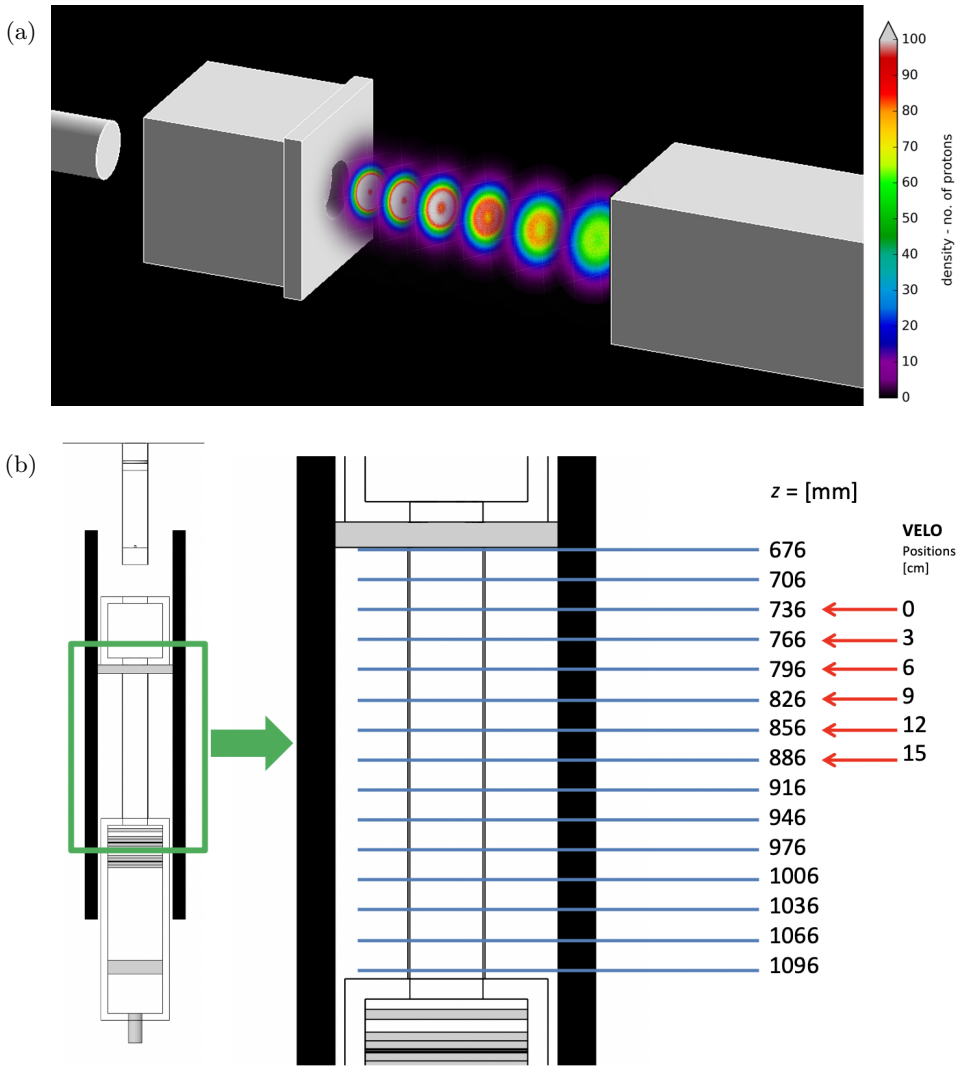

Figure 3.12: a) Projection of intensity maps for 100 million simulated protons. b) Positions of interest across the integration zone.

The pipe was removed in the simulation and negligible differences were found for both simulated cases; in practice the pipe is used as a physical external barrier. The FWHM at each z position was calculated to examine the beam divergence across the integration zone (Fig. 3.13). There is a clear linear trend: the further upstream, the lesser transverse spread, divergence and probability of particles being obstructed by the sensors.

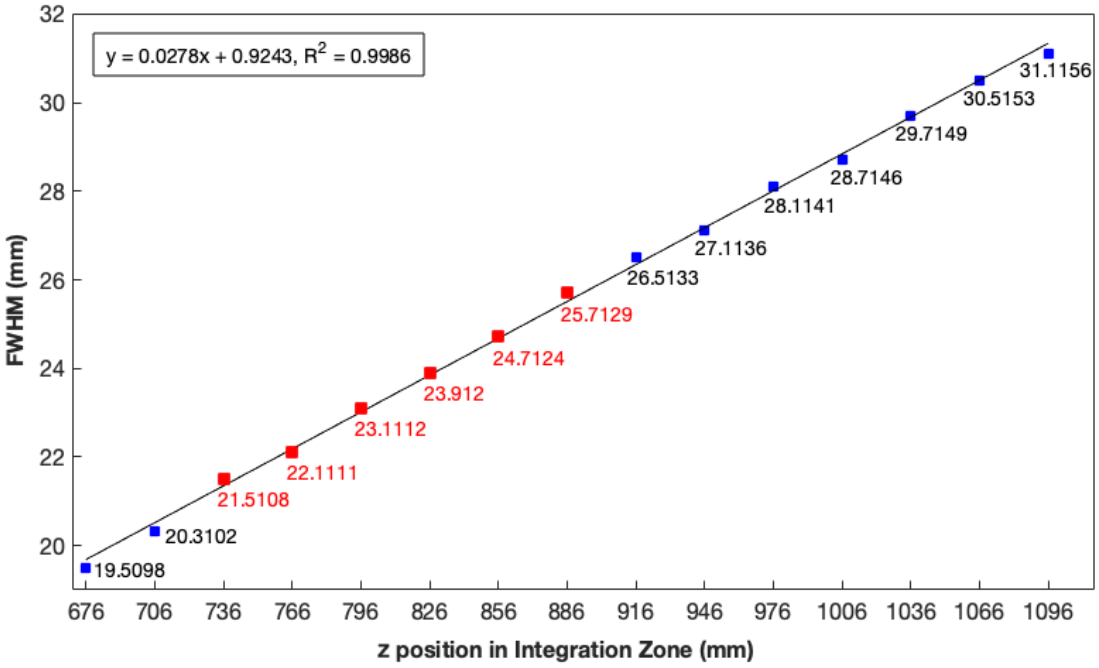

Figure 3.13: Integration zone transverse beam sizes (FWHM) are shown in mm and VELO positions labelled (red). Linear fit (black line) equation above.

Position 0 (z = 736 mm) indicates the most upstream location and therefore the best case to accommodate the modules with minimal interception. Given the dimensions of the VELO modules (Fig. 2.11), a representative 0.6 mm thick silicon disc was placed in the simulation at this position. As a small gap exists between the halves due to the PMMA shrouds, the disc was constructed with an inner diameter of 21 mm and outer diameter of 90.5 mm (Fig. 3.14).

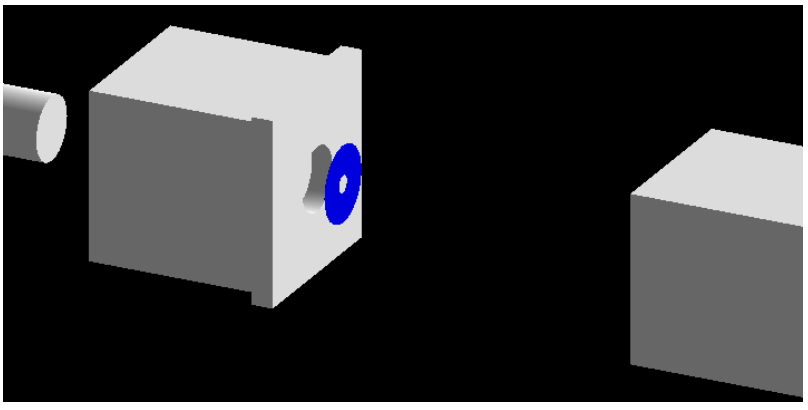

Figure 3.14: Silicon disc placed in the integration zone in GEANT4.

The beam is still slightly larger than the sensor aperture here and a cut-off effect on the beam profiles can be seen as it propagates downstream (Fig. 3.15). The notch along the

lateral sides of the beam is lost by the time the beam leaves the nozzle.

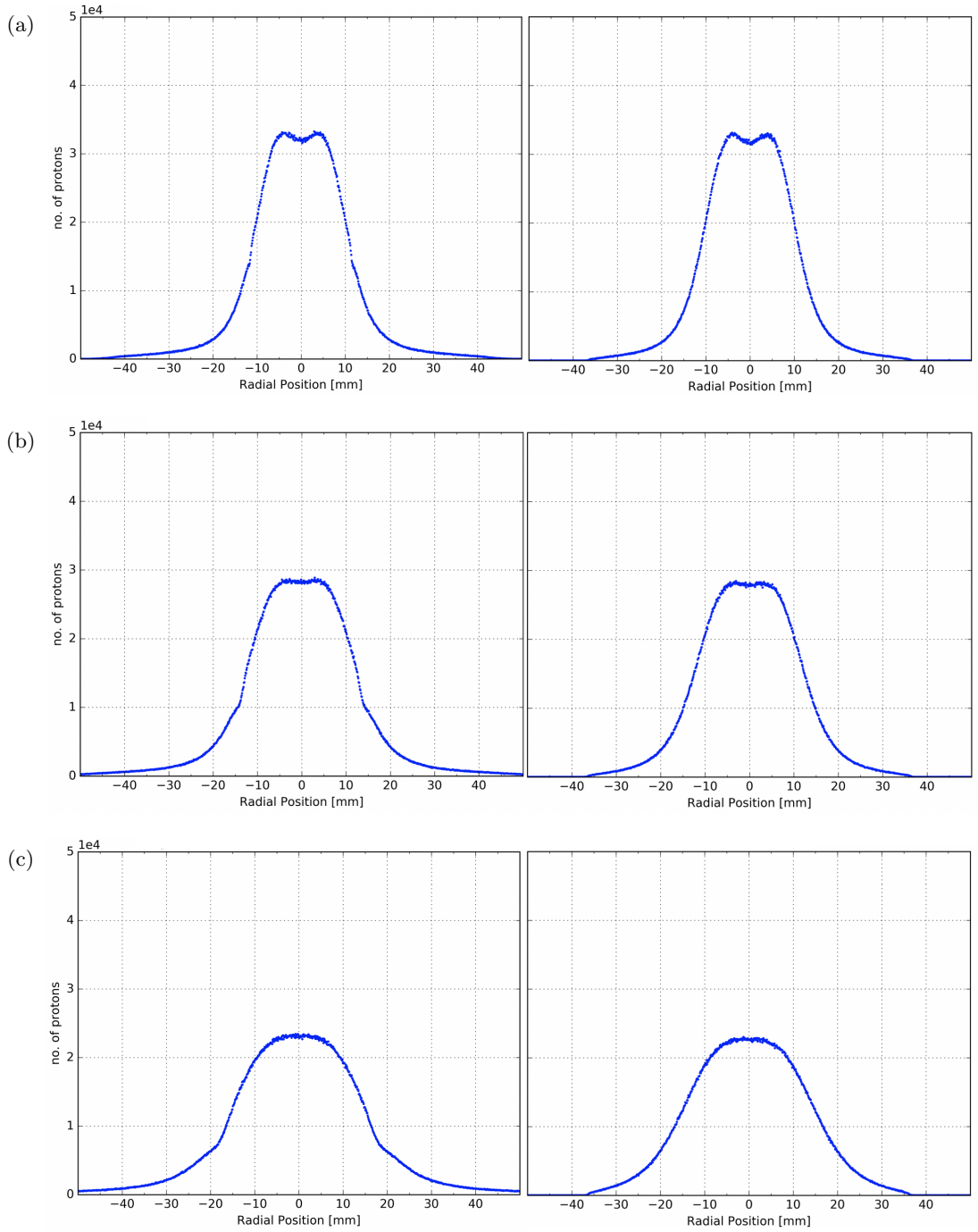

Figure 3.15: Transverse beam profiles in x with sensor implemented (left) and without (right) at z positions a) 766 mm, b) 886 mm and c) 1096 mm.

The impact of the sensors on the beam and energy spectra at isocentre is relatively minimal. A larger total number of particles are recorded and the distortion in the penumbra suggests there may be some forward scattering of protons. There is a greater deviation

of kinetic energies, a very small tail at ∼59 MeV and a resulting energy loss of 0.04 MeV (0.06%) (Appendix B.4). Additional simulations with the disc placed at the other 5 positions caused higher losses, this is detailed in [39]. At these positions there is significant collimation and the beam appears much sharper at isocentre which is impractical for treatment. It is ideal to place the monitors as close to the exit of the modulation box as possible to minimise interactions and changes to the beam. Furthermore, the modules can also be translated laterally to allow the beam to pass through completely. However there must be a balance: the detectors must be able to detect enough particles to register the halo. A threshold for the CCC environment was not established in previous studies and further development is necessary to optimise the VELO monitoring system. First measurements were demonstrated in an experimental proton beamline and are described later in Chapter 6.

3.3.4 Input Source Parameters

For all of these simulations, changes were only made to update the geometry and default beam settings were used, resulting in an increased difference from the expected 60 MeV energy at isocentre. The GEANT4 model continued with the input parameters previously determined in [142] which were back calculated to achieve a BP at 30.80 mm. The differences in the models persist where slight disparities between the simulated BP compared to previously attained QA data[‡], are seen (Appendix B.10). As the shape of the curves are similar, the beam energy and range was matched later, after further updates to the model. However, given that the default parameters were not recently validated, their significance and effect on the simulation were examined. A range of applicable beam energy and spread values were calculated (Table B.1) and simulated to observe if there were any substantial differences at relevant locations: the start of the integration zone and at isocentre. Changes in the input beam energies had insignificant effects on the beam distribution in the integration zone. As expected, a reduction in the input energy resulted in corresponding decreases to the BP range and a larger deviation in the mean energy. In contrast, variations in the beam distribution (sigma size, emittance) led to significant differences and these are summarised in Table 3.3.

[‡]Provided by A Kacperek, 2019.

Table 3.3: Input beam distribution variation on simulated quantities.

Location	**Beam sigma (x, y)** [mm]	**Emittance (x, y)** [mrad]	**FWHM** [mm]	**Change** [mm]	**Particles at peak/s** [1×10^3]
Start of integration zone	1.0, 1.0	2.3, 1.2	23.6473	2.4048	700
	2.0, 2.0	2.3, 1.2	22.0441	0.8016	600
	4.0, 4.5	**2.3, 1.2**	**21.2425**	**0**	**200**
	4.0, 4.5	5.0, 5.0	22.8457	1.6032	200
	10.0, 10.0	2.3, 1.2	21.2425	0	400
Isocentre	1.0, 1.0	2.3, 1.2	39.6794	3.2065	120
	2.0, 2.0	2.3, 1.2	38.0762	1.6033	120
	4.0, 4.5	1.0, 1.0	36.4729	0	45
	4.0, 4.5	**2.3, 1.2**	**36.4729**	**0**	**45**
	4.0, 4.5	5.0, 5.0	38.0762	1.6033	45
	10.0, 10.0	2.3, 1.2	36.4729	0	10

Modifications to the default input parameters (boldface font) in Table 3.3 resulted in noticeable differences to the FWHM determined at both of the beamline locations. The beam sigma has a direct effect on the transmission (particles at peak/s); if a geometrically smaller beam is delivered then more particles are recorded. This results in a larger FWHM at both locations but remains unchanged even with a larger input beam. Changing the emittance appears to have no influence on the transmission but a higher emittance results in a larger beam spread in both directions and thus an increased FWHM. The FWHM was calculated by using the same script to fit a Gaussian distribution to each beam profile and although the differences equate to a few mm, this is consequential for VELO. The variations especially at the integration zone demonstrate that the input parameters are significant: inaccuracies at the source will propagate along the beamline and scale with beam current. Therefore, the beamline must be characterised and each of the input beam parameters (beam energy, spread, size and emittance) must be precisely known in order to optimise the detectors for CCC.

Phase Space Scoring & Tracking

Subsequent major improvements to the model were implemented by the developer. These improved the tracking capabilities and enabled more detailed particle quantities to be retrieved with less computational demand. As mentioned in Section 3.3.1, particles

were tracked if their spatial coordinates met certain conditions. A different approach is required in order to track particles independent of their material and boundaries, thus a parallel world was introduced. This world remains separate from the mass world and they do not overlap or interact. Constructing geometry in a parallel world enables scoring at any arbitrary position by placing multiple sensitive detectors along the beamline. Particle information is recorded using the *SensitiveDetector* class where different quantities (i.e. parentID, particleName, *x, y, z*, momentum in *x, y, z* and kinetic energy) can be collected and the registered hits are processed by *PhaseSpaceSD.cc*. As this significantly changed the way which relevant quantities were scored, several adaptations and further improvements to the simulation were required. The following changes made to the source code (Appendices B.13-B.15) are summarised:

Enable option to track across '*all*' positions at defined intervals

- Construct a *ParallelContainer* large enough to contain the entire beamline and phantom.
- Place it in the parallel *GhostWorld* (duplicate of mass world) at z = -2340 mm relative to the mass world, this centres it relative to the beamline.
- Parameterise it to contain thin boxes to track along 1 nm slices in *z*.
- Define new variables to convert the coordinate reference frame from the *GhostWorld* to relative to the beamline (GPS source $z = 0$).
- Link this such that the position, length and slice can be defined in *proton.mac*.

Modify the *ParallelContainer* length to score within a '*detectorvolume*', specifically to obtain a BP

- Construct a *detectorvolume* component within the *ParallelContainer*.
- Introduce new variables to convert the coordinate reference frame from the *ParallelContainer* to be relative to the beamline *z*.
- Link this so parameters can be defined in *proton.mac*.

Enable option to score the energy deposition in an arbitrary phantom

- Retrieve the total energy deposited as hits in *PhaseSpaceSD* when the start of each step is on a boundary (G4double energy = step->GetTotalEnergyDeposit();).
- Change the layer thickness to match its mother volume.
- Link this so the dimensions can be defined in *proton.mac*.
- Dump eDep in each layer to a .txt file.

Modify *ParallelContainer* length to score within a *detectorvolume*, as a thin slice for interchangeable components

- Construct *detectorvolume* for components as defined in *proton.mac*.
- Place additional components but with z positions relative to *ParallelContainer*.
- Dump phase information to a file defined by beamline z position in *proton.mac*.

As each phase space file contains a considerable amount of data (hundreds of millions of particles), further analysis was required and additional scripts were written to merge the data and extract meaningful information [155]. All of these developments enable further possibilities to study different aspects of the delivery system and facility. However, the focus of the model for the remainder of this project was mainly to evaluate the performance of the simulation and examine how closely it was able to predict measured beam quantities. As such, measurements of the lateral beam profiles along the delivery system were performed to validate the model and to support the complete characterisation of the CCC beamline.

3.4 Experimental Measurements

Beam measurements were performed at multiple locations along the treatment line using two different methods to determine the transverse beam distribution: with EBT3 gafchromic film and a Medipix3 detector. The transverse beam profiles, beam divergence and lateral spread indicate the accuracy of model parameters.

3.4.1 Film Irradiation

EBT3 film provides the geometrical beam distribution as a function of the dose, evaluated by converting the grey value of each pixel to an OD value. The OD is dependent on the extent of irradiation and thus each OD value results in a corresponding dose (Gy). The dose at this location is determined by establishing a correlation with known quantities of radiation. This is done by exposing a calibration set of film to well defined quantities of radiation under standard conditions, with reference to the dose measured by the ion chambers. A calibration curve can be obtained which enables dose conversion across the full dose range, taking into account any corrections for minor deviations in

grey values and saturation effects. This process is prone to several uncertainties discussed later. Nevertheless, as the OD is fitted to a calibration curve, net OD is used to represent the film response to measured dose. This is expressed as the difference between transmission intensities [136]:

$$net\,OD = OD_{exp} - OD_{unexp} = \log_{10}\left(\frac{I_{unexp} - I_{bckg}}{I_{exp} - I_{bckg}}\right), \tag{3.1}$$

where *exp* refers to whether the film was irradiated (*unexp*, unexposed) and *bckg* is the zero-light transmission quantity. This is the pixel value related to the white light value of the scanner used. I is the respective intensity value and is taken across each colour (red, green, blue) channel. The possible errors and uncertainties are calculated by:

$$\sigma_{net\,OD} = \frac{1}{\ln(10)}\sqrt{\left(\frac{\sigma^2_{unexp} + \sigma^2_{bckg}}{(I_{unexp} - I_{bckg})^2} + \frac{\sigma^2_{exp} + \sigma^2_{bckg}}{(I_{exp} - I_{bckg})^2}\right)}. \tag{3.2}$$

Eight pieces of film were placed along the treatment line and irradiated under standard conditions simultaneously (Fig. 3.16); 4 Gy at isocentre for ∼30 s with a 43 mm nozzle collimator at ambient room temperature (24.2 °C) and pressure (1016.8 mbar). The film was cut into equivalent and sufficiently large pieces to contain the complete beam spots and labelled to ensure that the direction and orientation remained consistent.

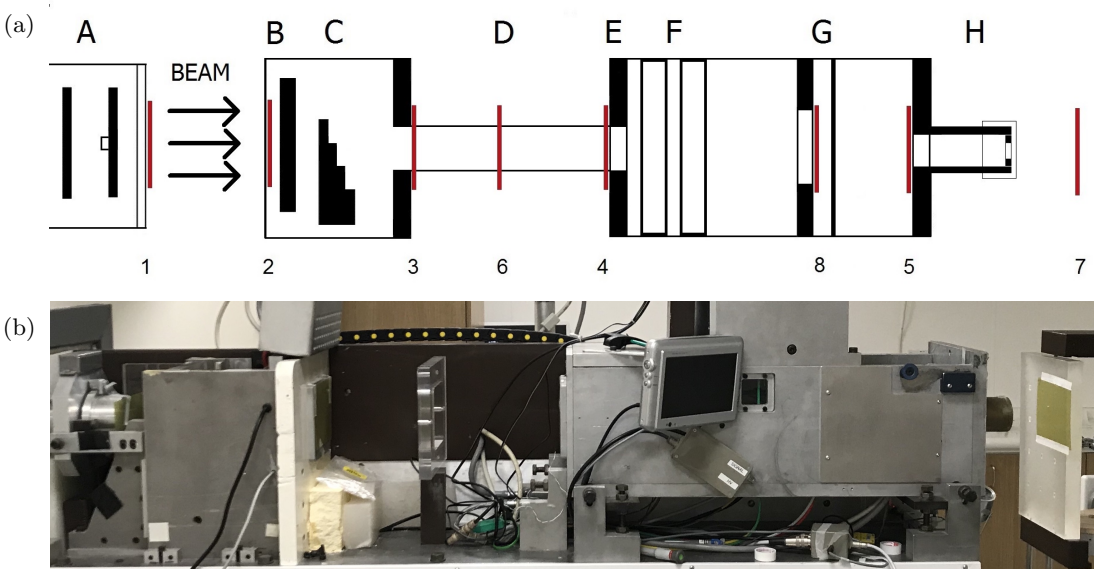

Figure 3.16: a) CCC beamline sketch with positions of film (red).
b) Pre-irradiation photo with films 1, 3, 6, and 7 visible.

A calibration set consisting of 12 pieces of film (2 control) were irradiated individually at isocentre with doses ranging from 4-60 Gy (Fig. 3.17).

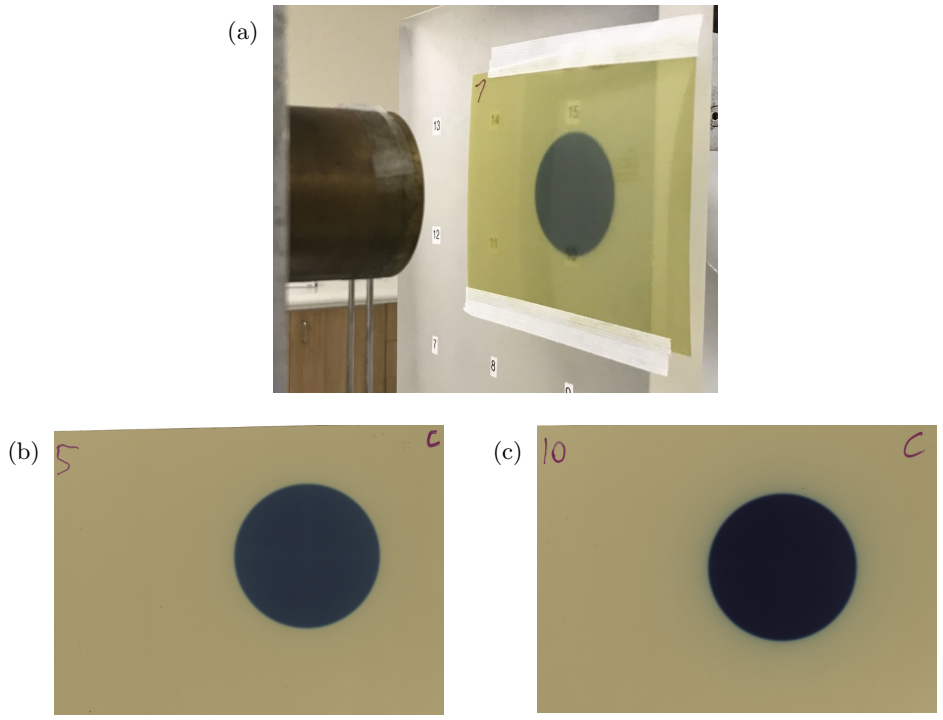

Figure 3.17: a) Film 7 irradiated at 4 Gy at isocentre. Calibration films were also positioned here and irradiated at b) 20 Gy and c) 60 Gy. The appearance of the beam spots are darker with increasing dose.

3.4.2 Analysis

Following complete development (>24 hours), the irradiated film pieces were scanned using an EPSON 750 scanner and saved as 48-bit .tif images with no colour corrections at 150 dots per inch (dpi). All film analysis was done using the image processing software ImageJ [156]. A circular region of interest (ROI) was selected such that it was encased inside each beam spot and duplicated for each film. ImageJ generates a plot of the grey values per pixel against distance which gives a simple indication of the beam profile and a way to check the suitability of the ROI. The software measures the ROI intensity metrics for each film, for each colour channel. The net OD values can be determined using Eq. 3.1 and are plotted against the corresponding irradiated doses with the error bars given by Eq. 3.2. Plots for each colour channel constitute the calibration curves and given standard protocol, the red channel is used to generate a fitted curve to correlate the net OD to dose (Fig. 3.18).

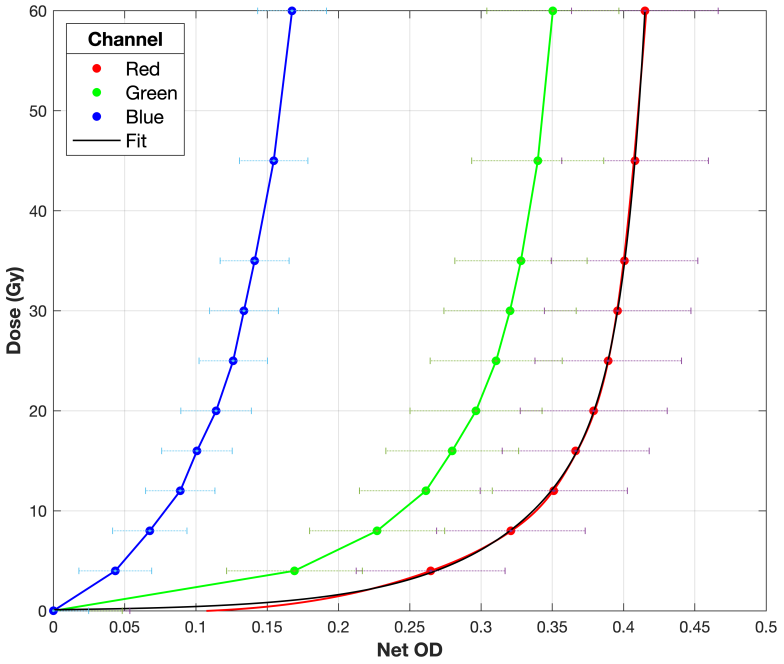

Figure 3.18: Calibration curve to determine dose from net OD values.

The exponential (or double exponential function) fit is used to calculate the dose from the net OD for each pixel value. The position along the horizontal axis for each pixel is found by converting from dpi to mm. Therefore the transverse beam profile can be obtained by plotting the dose against position. For comparison, a Gaussian function was fitted to each profile with the calculated FWHM. This entire process was written into several Matlab scripts which automate the generation of the calibration curve, fit and beam profile plots for each film. This material has been fully documented and developed into a package for self-directed use at CCC. The authored guide and code is included in Appendices C.1-C.5; it can also be used for general film analysis elsewhere or for other applications. Any settings specific to the facility (i.e. scanner dpi, zero value and pixel range) can be easily modified within the code.

3.4.3 Results

The estimated dose for each beam spot was determined by calculating the net OD from the mean pixel values over the total ROI area. Although each ROI is uniform, this gives only an approximated dose as the uncertainties associated with each piece of film are not individually corrected for. The control provides a single baseline value for the background OD: negating the background OD doesn't account for the more significant

changes at higher doses due to the exponential fit. A resulting 4.59 Gy was obtained for the film 7 beam spot which is slightly larger than the expected 4 Gy. However as there are large associated uncertainties, the mean dose was scaled to 4 Gy and similarly calculated for the other pieces of film to provide the dose ranges along the beamline (Fig. 3.19). This is useful to estimate the anticipated dose upstream of the ion chambers as there are no diagnostics to obtain this otherwise.

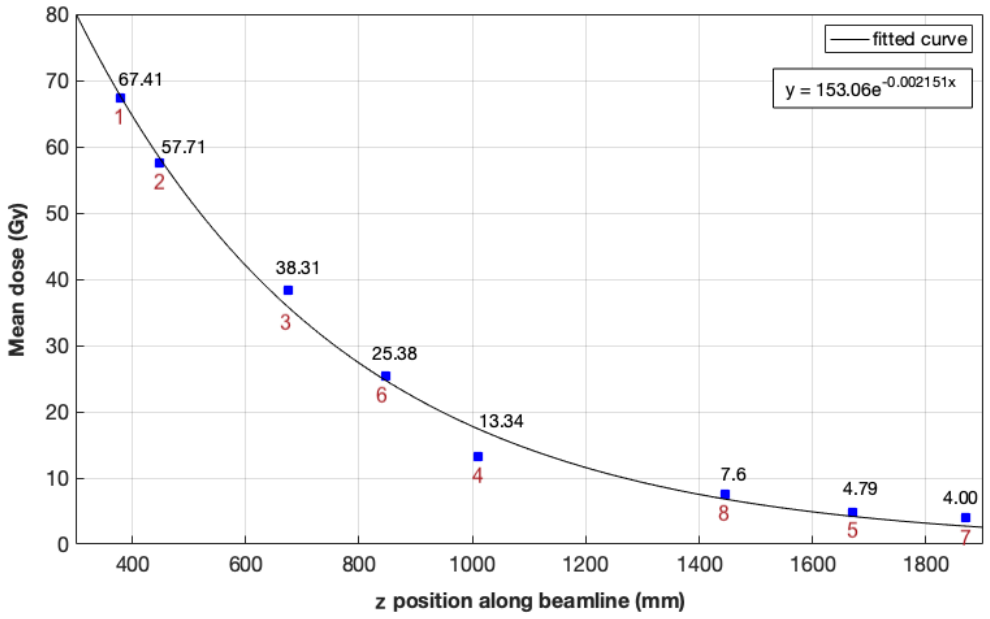

Figure 3.19: Mean dose for each film (red) in order along beamline: 1, 2, 3, 6, 4, 8, 5 and 7. z positions differ slightly to correspond with the updated simulation model.

The beam profiles obtained for each film are shown in Fig. 3.20.

(a)

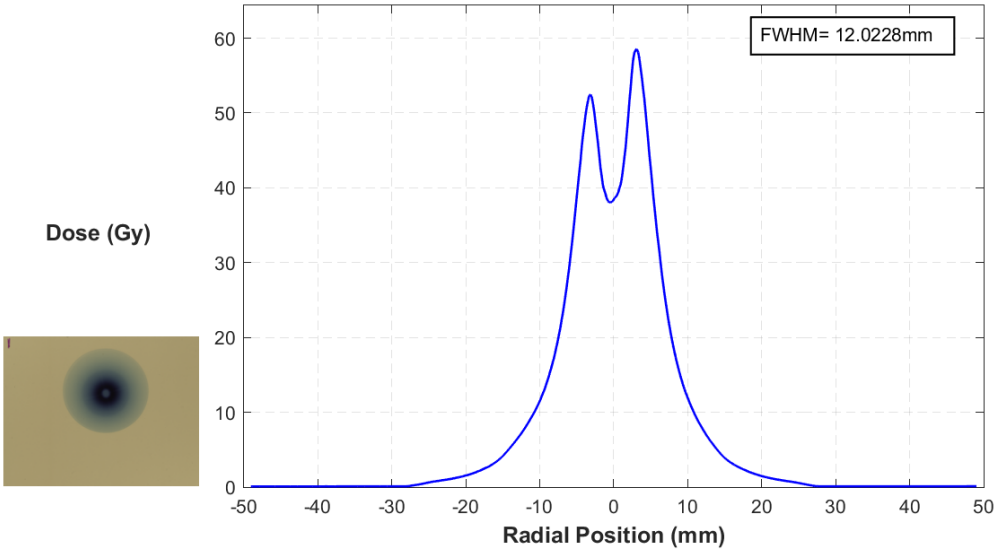

(b)

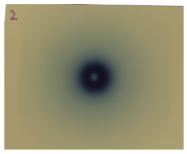

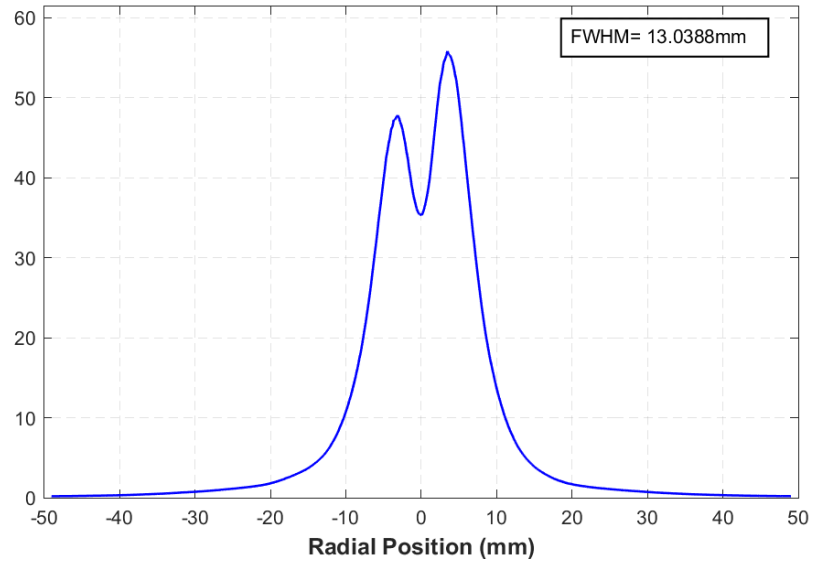
FWHM= 13.0388mm
Dose (Gy)
Radial Position (mm)

(c)

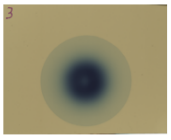

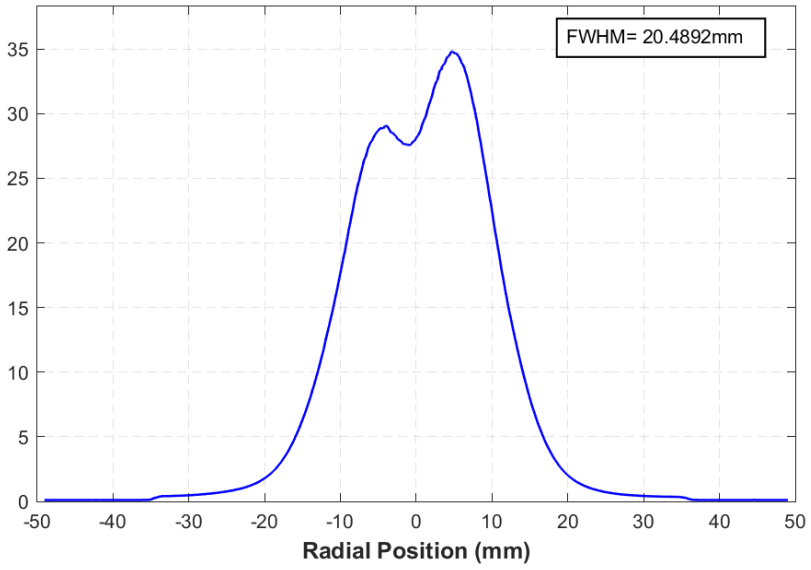
FWHM= 20.4892mm
Dose (Gy)
Radial Position (mm)

(d)

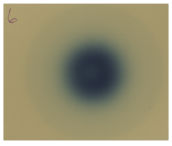

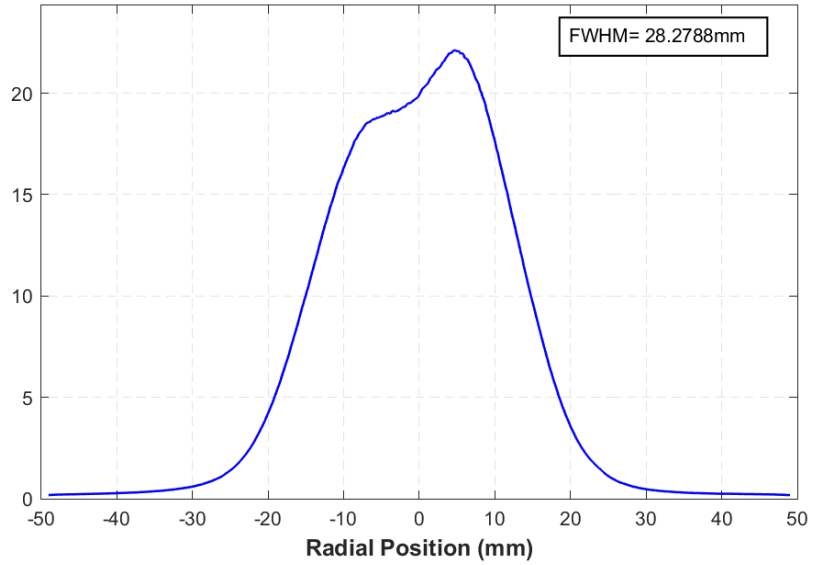
FWHM= 28.2788mm
Dose (Gy)
Radial Position (mm)

(e)

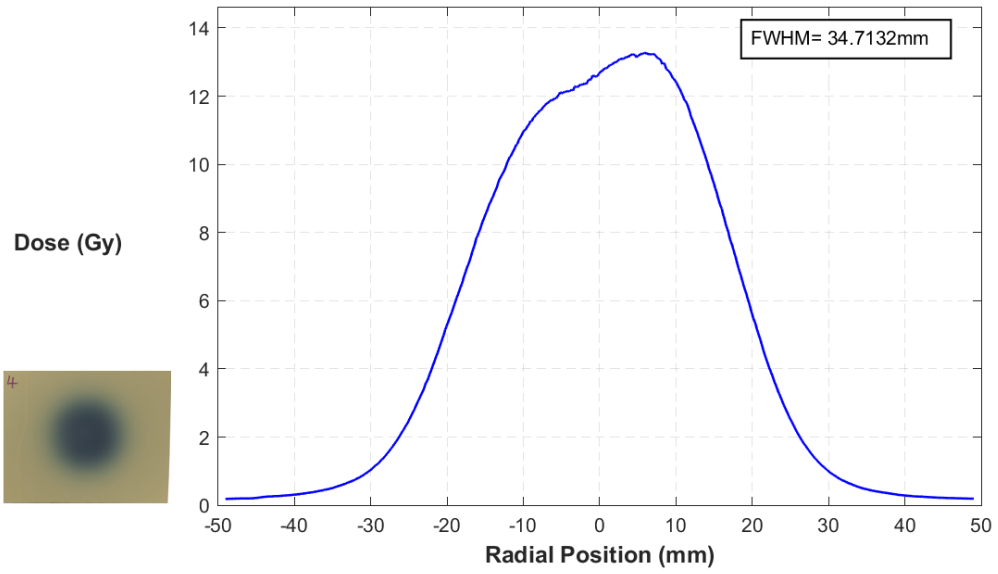
FWHM= 34.7132mm
Dose (Gy)
Radial Position (mm)

(f)

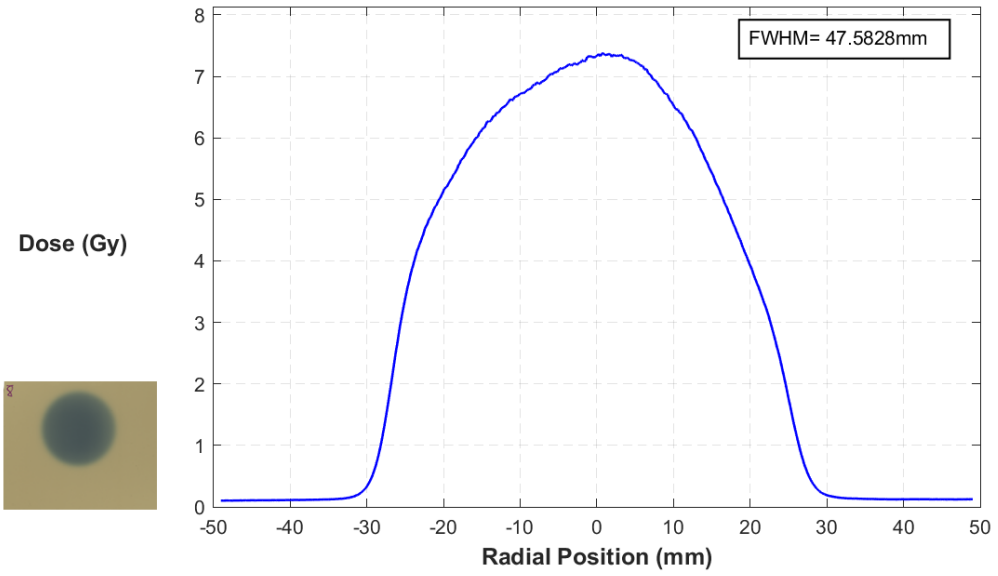
FWHM= 47.5828mm
Dose (Gy)
Radial Position (mm)

(g)

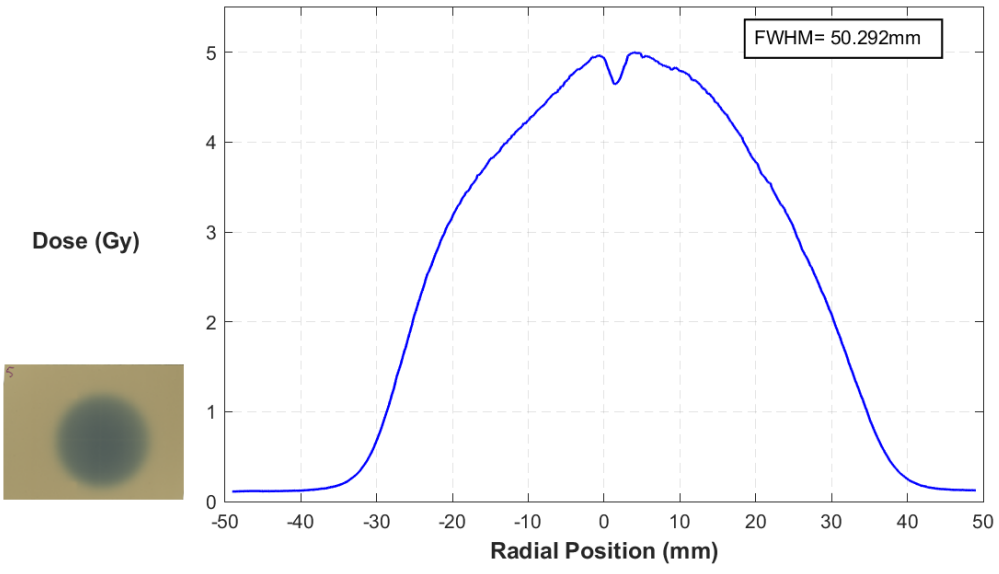
FWHM= 50.292mm
Dose (Gy)
Radial Position (mm)

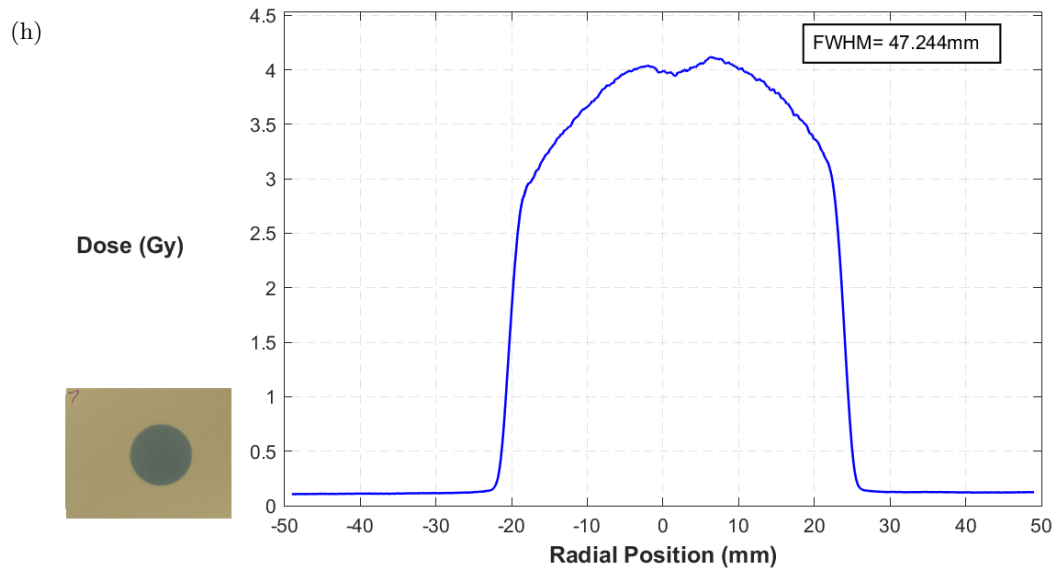

Figure 3.20: Beam profiles for each film in order along beamline a) 1, $z = 380$ mm. b) 2, 449 mm. c) 3, 676 mm. d) 6, 846 mm. e) 4, 1009 mm. f) 8, 1446 mm. g) 5, 1671 mm and h) 7, 1871 mm. Corresponding scanned film images and calculated FWHM are also shown.

There are clear non-uniformities for all the generated plots indicating a beam tilt in the positive x direction (right, in the reference frame of the direction of beam propagation). As this is consistent throughout, it suggests that it is correlated with the beam itself rather than misorientation of the film. Although, film 6 (Fig. 3.20d) was free standing and may not have been exactly perpendicular to the beam. In addition, the possibility that the beam stopper may actually be angled slightly (left, where more of the beam is attenuated) was mentioned in the past. Given these considerations, the FWHM between the film and simulated beam profiles was compared quantitatively (Table 3.4). Simulated beam profiles are included in Appendix B.11 for reference.

Table 3.4: Film and simulated FWHM comparisons.

#	**Film** [mm]	**Simulation** [mm]	**Difference** [mm]	**Difference** [%]
1	12.02	11.62	-0.40	-3.32
2	13.04	14.03	0.99	7.59
3	20.49	21.24	0.75	3.68
6	28.28	26.85	-1.43	-5.04
4	34.71	32.46	-2.25	-6.48
8	47.58	46.09	-1.49	-3.13
5	50.29	55.71	5.42	10.78
7	47.24	36.47	-10.77	-22.80

The differences between the two cases increase with distance and significantly, the simulated FWHM is ∼11% larger than the film just before the beam exits the nozzle (film 5). This is again partly due to the absence of a (90 mm) collimator before the cross wires in the updated simulation model. At the isocentre, the FWHM drops to much less than the film spot size which has diverged slightly from the 43 mm (radiobiological) nozzle collimator used for these measurements. Similarly with the effects observed in Table 3.3, the severe collimation by the nozzle restricts the transmission and there is also slight divergence from the 34 mm nozzle opening. These differences are reasoned as the nozzle itself was different than in the simulation model.

It is also observed that a central dip appears in film 5 (Fig. 3.20g) which indicates attenuation caused by traversal through the cross-wires. This almost recedes by the time it reaches isocentre (Fig. 3.20h) however a decrease at $x = 0$ mm can be seen. The dose distribution here is also not uniform which suggests limited beam uniformity and performance on the day.

Uncertainties

The calibration and response of film is generally affected by a multitude of uncertainties which can arise at almost every step during analysis. The errors represented within the error bars in Fig. 3.18 indicate the overall uncertainty, accounting for variations in the measured transmission and standard deviation of the grey pixel values. Although these quantities are defined by the ROI and scanner used, results are largely dependent on the post-processing protocol and its extent of reproducibility. Images of the film were provided afterwards by the facility where attempts had been made to scan each piece consistently (same approach, settings, orientation, position, time, environmental conditions etc.). It was discovered later that more extensive procedures [136, 138] could reduce the uncertainties however these were not repeated. Moreover, these appear to be exacerbated by the spatially non-uniform beam delivered. This was unpredictable as the beam is optimised for clinical treatments but these measurements were performed after biological experiments during research beamtime. Several other aspects and inconsistencies which impacted these results were also identified.

Firstly, due to the composition of the film (each sheet of film also differs slightly), its physical characteristics are important. The orientation must remain the same as the grain size and positioning can affect the polymerisation process. The beam must pass through the film on the same side and this exposure must be done under the same conditions and environment. The film must be adequately stored before and after irradiation and scanned at the same time.

For the analysis, the selection of the ROI was significant. The size and shape was found to affect the resulting transverse beam profile and therefore the FWHM. The ROI must contain enough pixels for sufficient statistics to obtain a smooth profile with acceptable resolution. However, if the ROI is too large then the profile gets smeared out and the characteristics of the distribution are not obvious. A circular ROI was used for the calibration set but as the beam spots size and shape differed too much for films 1 to 7 (Figs. 3.20a-3.20h), a rectangular ROI was used (see Appendix B.23). As a result, it was unclear whether it was reasonable to match the simulated profiles to approach the film profiles or if simulations should be more appropriately used as a benchmark. One approach is if both profiles were able to resemble each other and agreement was reached within a certain percentage of uncertainty (i.e. clinical criteria states a 2% dose uncertainty [138]). To examine this further, measurements were performed with a Medipix3 detector and compared with film.

3.4.4 Medipix3

The Medipix3 is a hybrid pixel detector which comprises a single quantum counting chip and a SPIDR readout system. This technology was initially developed for particle tracking at the LHC, evolving to radiation imaging. Medipix was firstly used for X-ray detection however the newer generations have supported its developments specifically for medical applications [42, 157]. The chip consists of a 500 µm silicon sensor with an active area of 28×28 mm^2. This collects the charge deposition of protons passing through the sensor and registers individual hits as pixels on an event-by-event basis. The chip is capable of detection at large flux rates however this was the first time its performance was tested within a clinical, high proton flux environment. The objective

of these measurements were twofold: to benchmark the film with an absolute detection method and to investigate the applicability of Medipix3 for absolute proton therapy dosimetry.

3.4.5 Method

The Medipix3 detector was placed at three locations throughout the treatment beamline and irradiated under varying beam conditions (Fig. 3.21). Sections of EBT3 film were also positioned in front of the detector and irradiated simultaneously in order to directly compare performance. A summary of the experiment is described in [158]; for relevance to this thesis, only the main methods, results and other supplementary observations are discussed[‡].

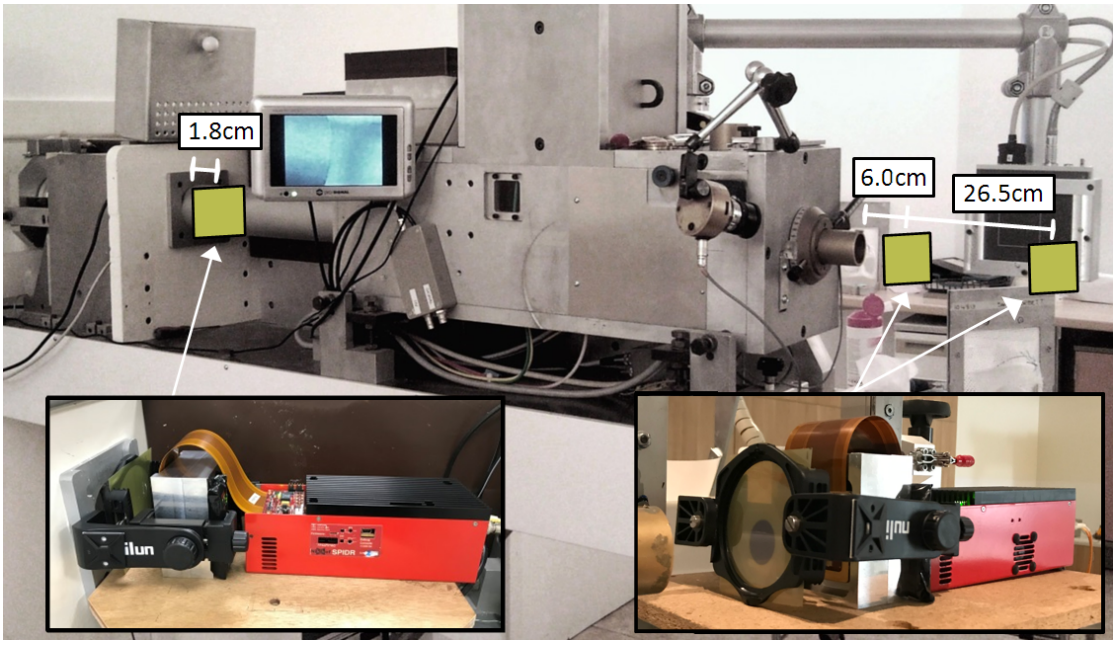

Figure 3.21: Experimental setup with irradiations performed at three different positions (integration zone and after the nozzle) with the Medipix3 detector and EBT3 film.

The sensor itself was held in an aluminium cooling block and connected to the readout system by fibre cables (Fig. 3.22a). A small assembly was designed to securely hold a piece of film 3.5 cm in front of and parallel to the sensor and was clamped onto the edges of the block (Fig. 3.22b).

[‡]All detector related hardware modifications, operation and analysis was done by N. Bal.

(a)  (b) 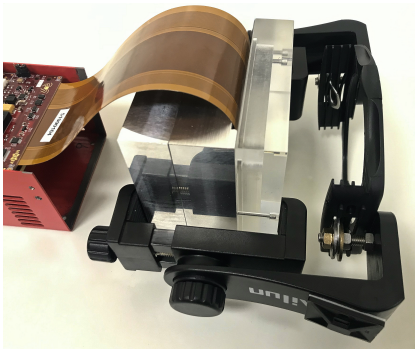

Figure 3.22: a) Medipix3 chip affixed within an aluminium cooling block with the SPIDR readout system (red). b) Clamp assembly to attach film, the adjoining plastic shield was built as protective casing for transport.

Prior to the experiment, the expected dose (Fig. 3.19) and estimated fluence was calculated to estimate the possible range of measurements and registered events. Similar to VELO, the Medipix3 chip can withstand high amounts of radiation and hence was also situated in the beginning of the integration zone. At this position, the beam FWHM was expected to be smaller than the sensor sensitive area (Table 3.4) however a 20 mm collimator was needed for the nozzle.

On the day, the lowest stable beam current of 0.012 nA was attained and then was ramped up to 1.97 nA for the different runs. These readings were provided by an electrometer connected to the second scattering foil as the dose monitors could not be used with the detector in the integration zone. The foil currents have a linear relationship with the dose monitor MU.

3.4.6 Results

Images obtained with the detector were directly compared with film using the procedure described in Section 3.4.2. An additional set of 5 films were irradiated from 4-25 Gy to generate a calibration curve (Appendix B.22) to convert the film to beam profiles. The Medipix3 images were generated by integrating over all frames where some post-processing was required mainly to normalise detector caused effects (Appendix B.23). Small artefacts in the centre are observed from the join between the sensors as the sensitive area combines 4 sections. Changes for the different grey pixel range and dpi were also made.

As the selection of the ROI is significant, total horizontal beam coverage with sufficient vertical height was ensured in order to generate a smooth profile. Consistent ROI selections were used for each film and corresponding Medipix3 image; the resulting profiles at 9.5 cm and 30 cm after the nozzle at the same beam current are shown in Figs. 3.23a and 3.23b.

(a)

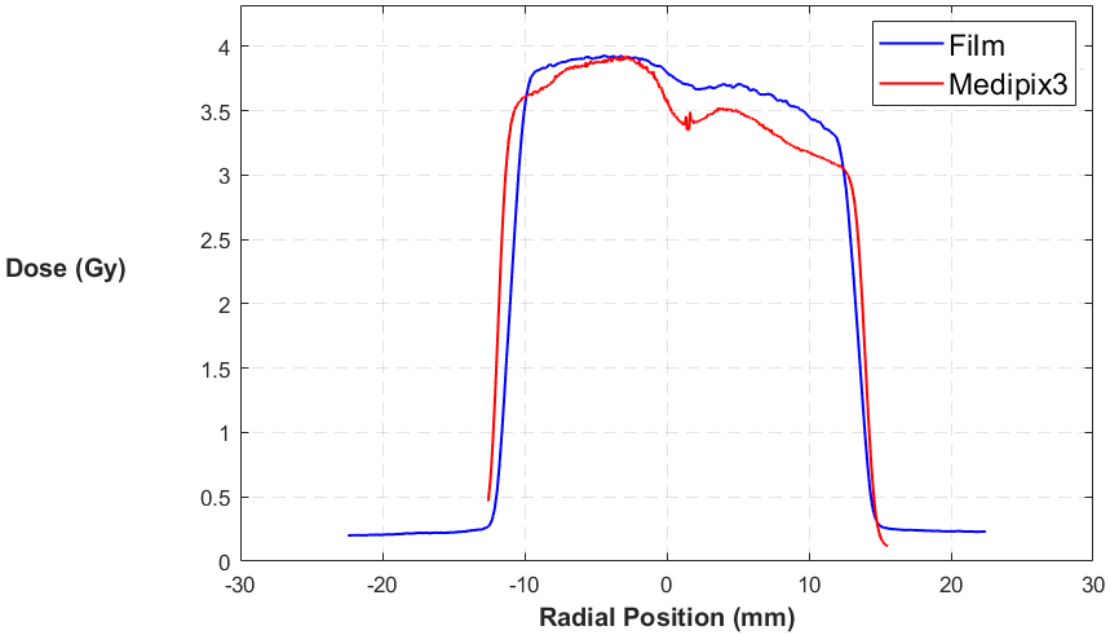

(b)

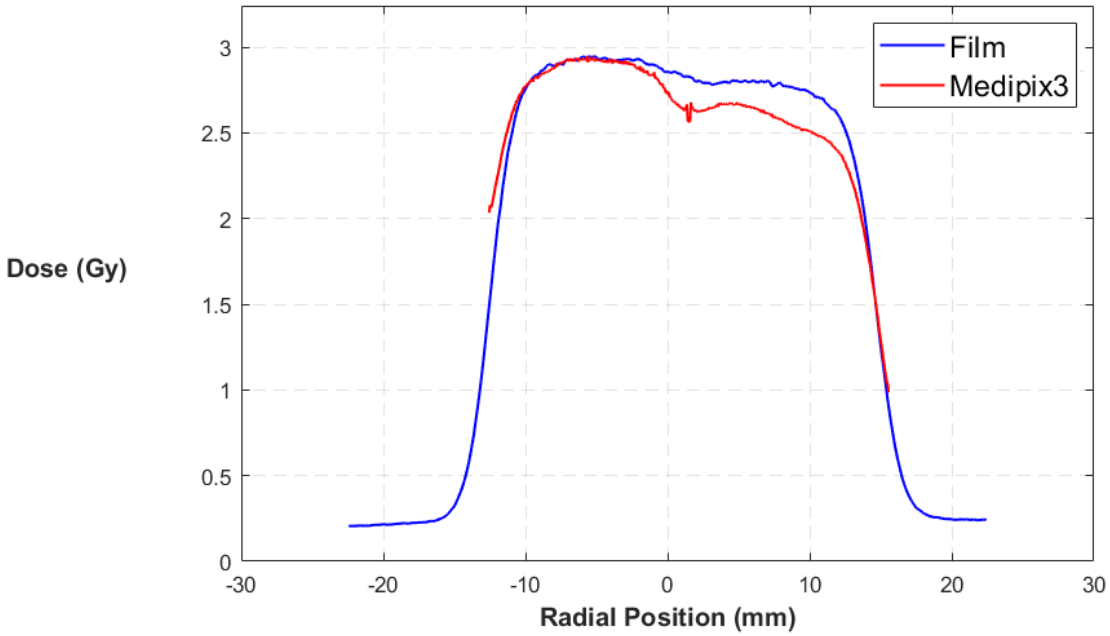

Figure 3.23: Film and Medipix3 beam profiles at a) 9.5 cm and b) 30 cm after the treatment nozzle.

For these cases, correspondence between both methods was achieved, particularly at the lateral penumbra. Slight translation (in the positive x direction) for both plots suggest that the detector was not precisely aligned at the centre of the beam axis. Nevertheless, a linear response was observed across the full current range and the high doses were detected right through to the edges of the sensor. The observable differences at the highest points of dose are likely to be related to the image analysis and also due to fundamental differences between the detection processes.

The beam fluence recorded by Medipix3 was directly converted to dose by scaling the pixel values to the film irradiated at the same experimental location. This preserves the linearity of the grey values (grey pixel intensities would correspond to numbers of hits) and also correlates the magnitude of hits to a determined quantity: dose. The dose was not calculated from hits or the resolved beam current recorded by Medipix3 due to the uncertainties with the electrometer. These were further perturbed by beam instabilities, particularly at the low currents during moments where there was a complete loss of beam. This was presumed to be caused by a dropout in the RF supplied to either one of the dees of the cyclotron, resulting in a loss of the accelerating field between the two electrodes and therefore a disruption to the beam. It was also mentioned that it may be related to issues with the deflector which has deteriorated with use or from changes to the ion source (discussed later in Section 4.2.1). Furthermore, maintenance cleaning of the cyclotron tank can also influence the beam operation, resulting in changes to the beam characteristics.

Although the beam operated reliably at higher currents and particularly at clinical rates, several other observations about the accelerator and general beam were realised from the measurements with Medipix3. Recurring jitters were seen in the data where variations in the count rate over time appeared as small amplitude waves. At a higher time resolution and deconvolved, these seemed to comprise of sets of periodic waves at low (few ms) and higher (order of hundreds of ms) frequencies. One set was presumed to be related to the mains electricity however it is unclear if the second was associated with the cyclotron or detector. This was not experienced during previous detector tests with X-rays nor supposedly seen with any other measurements at the beamline. This

is possibly because Medipix3 is capable of measuring the beam current by detection of individual protons with high temporal resolution: this is not commonly achievable with typical instruments.

The significance of these rapid oscillations may be meaningful as they demonstrate something otherwise unforeseen which may have an impact on beam performance. When the beam is modulated with a rotating wheel to generate a SOBP, the graduations determine the longitudinal distribution of dose. If there are variations in the beam currents, there could be asynchronicity with the rotational frequency of the wheel and may cause aberrations in the dose delivered at each step.

If the oscillations are present in regular operation, these sorts of measurements may indicate an underlying aspect of the cyclotron. An irregularity in the structure or accelerating process can influence the beam dynamics (orbit, stability, focusing effects from magnetic field etc.) of the circulating protons and therefore the extracted beam quality (energy spread, emittance, dispersion etc.). These are likely to be caused by a combination of different factors including the design, changes to the ion source and aged components. It is unknown if or how the beam is adjusted upon extraction. If there is a collimator at the exit then some properties of the beam would be regulated, such as the beam distribution in the transverse plane. Nonetheless, these observations suggest the tendency of the parameters of the beam to change based on the operation and changes to the cyclotron over time. Differences from originally documented beam parameters would be reasoned: this is an important finding and is discussed in greater detail in Chapter 4.

3.5 Summary

Simulation modelling is essential to investigate the implementation of the VELO detector system; to examine the behaviour of the beam and to establish a correlation between the entire beam distribution and halo. The CCC facility, treatment delivery system and previous efforts to simulate the beamline are overviewed, facilitating the development of a new and improved simulation model in GEANT4. The structure of the toolkit, its

classes, processes and how the CCC model runs from its source and macro files have been detailed. Default input parameters were used to characterise the beam along the entire treatment line and examine the beam divergence within the integration zone. These were found to significantly affect the transverse distribution and therefore the beam must be well defined for the integration of the VELO detectors. The VELO beam monitor has a limited impact on the resulting beam and can be a suitably accommodated in the facility due to the arrangement of the delivery system components. Nevertheless, several developments were needed to enable accurate measurements and simulations; the code was modified for better modelling capabilities and analysis scripts are provided.

The GEANT4 model was assessed by quantifying differences in the FWHM between the simulation and film obtained transverse beam profiles. Measurements with EBT3 gafchromic film required an extensive process of analysis and scripts were written to automate the conversion from OD to dose, obtaining plots of the 3D dose distributions at different locations throughout. To explore the accuracy of the film profiles, simultaneous measurements were performed with a Medipix3 detector. Good agreement with the irradiated film provided an absolute representation of the spatial spread of the beam. Both methods contribute meaningfully to the benchmarking, development and validation of the simulation model as necessary to completely characterise the CCC beamline.

Chapter 4

Clatterbridge Beam Dynamics

There has been a rapid emergence of clinical ion beam facilities worldwide especially in recent years, due to significant advancements in accelerator technology. For proton therapy, the majority of facilities in operation treat with higher energies (i.e. >160 MeV) and encompass a variety of different beam delivery methods and arrangements of beamlines, gantries, cyclotrons, synchrotrons or synchrocyclotrons.

Modern facilities constructed by major turnkey vendors often feature the same or related designs, systems and commissioning procedures to enable higher consistency with day-to-day operation. Although each facility or individual machine may be different (as mentioned in Chapter 2), minimal requirements and standards of performance must still be met before initial or regular clinical operation. Acceptance and commissioning tests are performed to study, verify and characterise the beam; necessary performance and beam quality is maintained across the lifetime of the equipment. However, this can differ across facilities, particularly for centres which were developed much earlier and have been longer established. The extent of characterisation and study may be limited and as for this case, they are most often unique facilities.

As described in Chapter 3, Monte Carlo codes can be used to extensively simulate the beam delivery and particle interactions. However, in order to have a complete understanding of the facility, it is essential to also examine the transport of the beam. It is expected that accurate modelling of the beam dynamics are employed in the design process for modern builds yet this is less certain for older facilities. These methods may be studied only for relevant research and development purposes. For the implementation

of the VELO detectors, it is crucial that the distribution and divergence of the beam is completely and precisely known in order to correctly correlate the halo region with the total beam. As discussed, there are several factors which affect the resulting beam profiles and thus an alternative approach was devised: to model the CCC beam optics to determine applicable beam input parameters for simulations. Simultaneously, this also contributes to complete end-to-end characterisation of the CCC beamline. This serves as a basis for future upgrades, optimisation, testing and integration of diagnostics. This method of characterisation and modelling can also be applied for similar facilities. This chapter covers the fundamentals of beam dynamics as relevant to study the optics of the Clatterbridge beamline.

4.1 Transverse Beam Dynamics

Beam dynamics are fundamental to accelerator physics, representing the theory and physical concepts to describe the movement of charged particles. As particles travel at high velocities, their paths are affected by focusing and bending fields in an accelerator. Electromagnetic fields are designed to guide and direct their trajectories along an intended path. In practical terms, this enables the beam of particles to be defined and also to determine certain beam properties. As the work in this chapter relates to the geometrical implications of the beam trajectory, the specifics of fundamental derivations are not shown. Instead, key beam dynamics concepts are summarised. A more complete review of accelerator beam dynamics can be found in [159–161].

Co-ordinate System

The transverse motion of a single particle within an accelerator or transport line can be visualised given a reference coordinate system, as shown in Fig. 4.1. In this transverse plane, the particle (red circle) traverses some distance along s with deviation shown by the tangential z-axis, with horizontal co-ordinates in the perpendicular x-axis and vertical co-ordinates in the also perpendicular, y-axis.

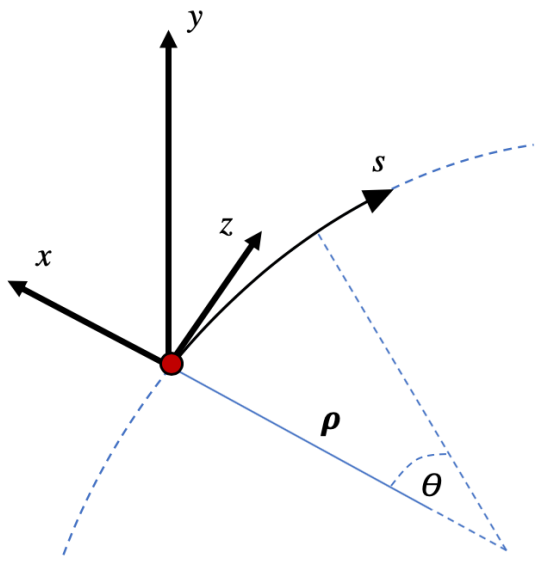

Figure 4.1: Reference frame for an ideal particle.

This represents the path of an ideal particle with 'perfect' conditions and is named the reference, design orbit or closed orbit (for a storage ring). Under electromagnetic fields, particles will follow a circular path given an angular rotation θ around the x-axis with a local radius of curvature ρ.

Magnetic Fields

The trajectory of particles with charge q is influenced by electromagnetic forces as governed by the Lorentz force and this radius of curvature ρ is dependent on the particle momentum p and strength of the field B. Accordingly, magnetic elements such as dipoles and quadrupoles are used to constrain and guide the beam of particles in an accelerator. The sequence of these are commonly referred to as the '*optical lattice*' and vary according to the design and warranted beam properties of the accelerator. Dipoles are used to steer the beam and particles passing through a magnetic field will experience a bending effect described by:

$$B\rho = \frac{p}{q}. \tag{4.1}$$

B is the magnetic field strength and when multiplied by ρ, is known as the magnetic beam rigidity. This represents the resistance of a particle to move along a curved path and is an important quantity to consider when optimising and designing for the required field strength and length of dipoles.

Quadrupoles have four poles with zero field in the central axis (x, $y = 0$), resulting in opposite effects in two different planes: focusing or defocusing. A conventionally focusing quadrupole (Fig. 4.2) will correct particles which deviate from the horizontal axis but defocus the beam in the vertical axis. This is the opposite for defocusing quadrupoles, where the particles are focused in the vertical plane and defocused in the horizontal plane.

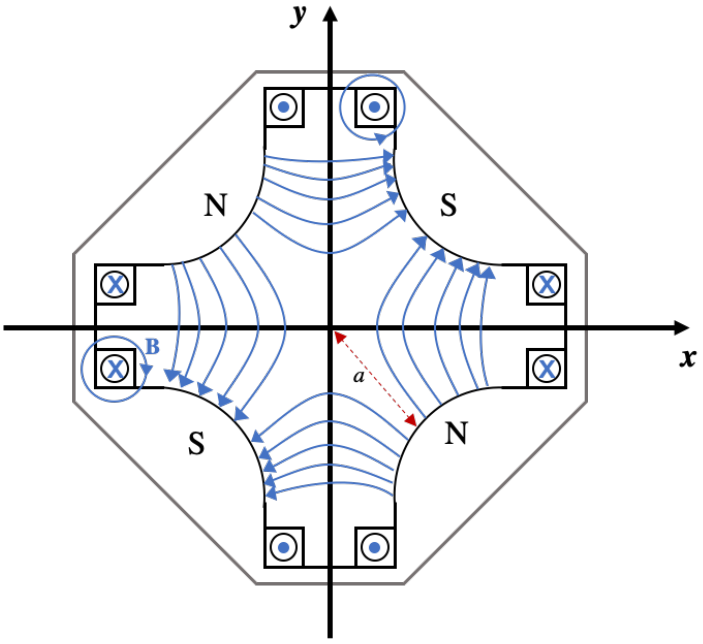

Figure 4.2: Sketch of a conventionally focusing quadrupole (particle travelling out of the page). The field lines (blue) are spaced closer toward the edges of the yoke indicating a stronger field. The pole tip radius (red dotted arrow) and the direction of the (**B**) fields generated by current passing through wrapped around coils, are also shown.

As the field changes along either axis, the strength of the quadrupole field is defined as a constant quantity k where the field gradient $g = \frac{\partial By}{\partial x}$. This is also commonly described as the '*normalised gradient*', '*normal quadrupole strength*' or '*normal quadrupole coefficient*'. This can be determined by using Eq. 4.1 and taking g over magnetic rigidity or given the physical specifications of the quadrupole magnet:

$$k = \frac{g}{B\rho} = \frac{\frac{\partial By}{\partial x}}{B\rho} = \frac{\mu_o g}{B\rho a}. \tag{4.2}$$

The gradient is related to the nominal current I by $g = \frac{2NI}{a}$ with N number of turns of wire about each pole face for the coils, μ_o is the magnetic permeability in vacuum and a is the quadrupole pole tip radius.

There are also higher order magnets such as sextupoles (six poles) and octupoles (eight poles) which are used to correct optical aberrations or for further beam manipulation. However, a study of non-linear optics is beyond the scope of this thesis and this work is limited to just the linear optics.

4.1.1 Particle Motion

For these linear fields, as only an idealised particle follows the design orbit, the actual motion of a particle can be determined by considering the deviation or oscillation from this reference path. The sets of equations which describe this are derived from Hill's equations [159], where solutions provide several expressions and optical parameters. Given that the facility has a straightforward lattice: a fixed horizontal transfer line with a slight bend, no ESS and is without sextupoles or higher order considerations, only the following few terms are discussed.

Equations of Motion

Given the focusing effects as particles traverse through dipole and quadrupole fields, the equations of motion are developed into differential equations representing the deviation from the design orbit in both the horizontal (x) and vertical (y) planes (Eq. 4.4). The periodic functions in Eq. 4.3 describe the focusing properties of the lattice; these are derived in full in [159]:

$$\begin{aligned} K_x(s) &= \frac{1}{\rho^2} - \frac{\frac{\partial B_y}{\partial x}}{B\rho}, \\ K_y(s) &= \frac{1}{B\rho}\frac{\partial B_y}{\partial x}. \end{aligned} \tag{4.3}$$

Considering only the linear terms and assuming several conditions, including that k and ρ are constant, provides the equations of motion in x and y:

$$\begin{aligned} x'' + K_x(s)x = 0, \\ y'' + K_y(s)y = 0. \end{aligned} \tag{4.4}$$

These illustrate that the path of a particle changes with the strength of the field as dependent on s and in fact, exhibits motion with a periodicity as similar to a harmonic

oscillator. The transformations and further steps are detailed in [162–164] where a solution to Eq. 4.4 will yield the following expression for the particle's position, for x:

$$x(s) = \sqrt{\varepsilon\beta(s)}\cos(\psi(s) + \psi_0). \tag{4.5}$$

Where ε is the emittance related to the beam area, β is an amplitude term and ψ is the phase component and both vary according to s. Taking the derivative of Eq. 4.5 to determine the particle's divergence (x') gives:

$$x'(s) = \frac{-\sqrt{\varepsilon}}{\beta(s)}\Big(\sin(\psi(s) + \psi_0) + \alpha(s)\cos(\psi(s) + \psi_0)\Big). \tag{4.6}$$

It is important to note the beta (β) term here again as it relates to the amplitude and is an important quantity which is strongly associated with the beam envelope and therefore the physical geometrical size of the beam. It is also known as the betatron or beta function (β_x or β_y for each plane) and varies along s, as dependent on the focusing properties of the magnetic elements in the optical lattice. Similarly, ε is another important parameter which relates to the beam envelope and physical size of the beam.

Twiss Parameters

Ideally, the emittance should be considered as an invariant (Liouville's theorem [159]) and is rearranged to obtain the following (Courant-Snyder) expression:

$$\varepsilon = \gamma(s)x^2(s) + 2\alpha(s)x(s)x'(s) + \beta(s)x'^2(s), \tag{4.7}$$

where ε represents the area the beam occupies in phase space (position against angle) and allows all 3 optical terms (α, β and γ) to be specified:

$$\begin{aligned} \alpha(s) &= -\frac{1}{2}\beta'(s), \\ \gamma(s) &= \frac{1 + \alpha(s)^2}{\beta(s)}. \end{aligned} \tag{4.8}$$

These are known as the Twiss parameters and describe the transverse beam phase space at any point along s. For the horizontal plane, these can be referred to as α_x, β_x, γ_x for x and similarly as α_y, β_y, γ_y for y.

4.1.2 Beam Ellipse

Accordingly, in a beam of particles, several particles with the same energy will exhibit oscillatory motion in this elliptical shape described in another co-ordinate system aforementioned as phase space ($x-x'$). A plot of Eq. 4.7 depicts this parametric coverage by particles, as the beam travels along s. The ellipse will vary in shape around the origin of the reference axis however the emittance is independent of the lattice focusing properties. The area remains constant according to the Liouville theorem for a Hamiltonian system: the density in phase space is conserved in the absence of acceleration, collisions or dissipative forces.

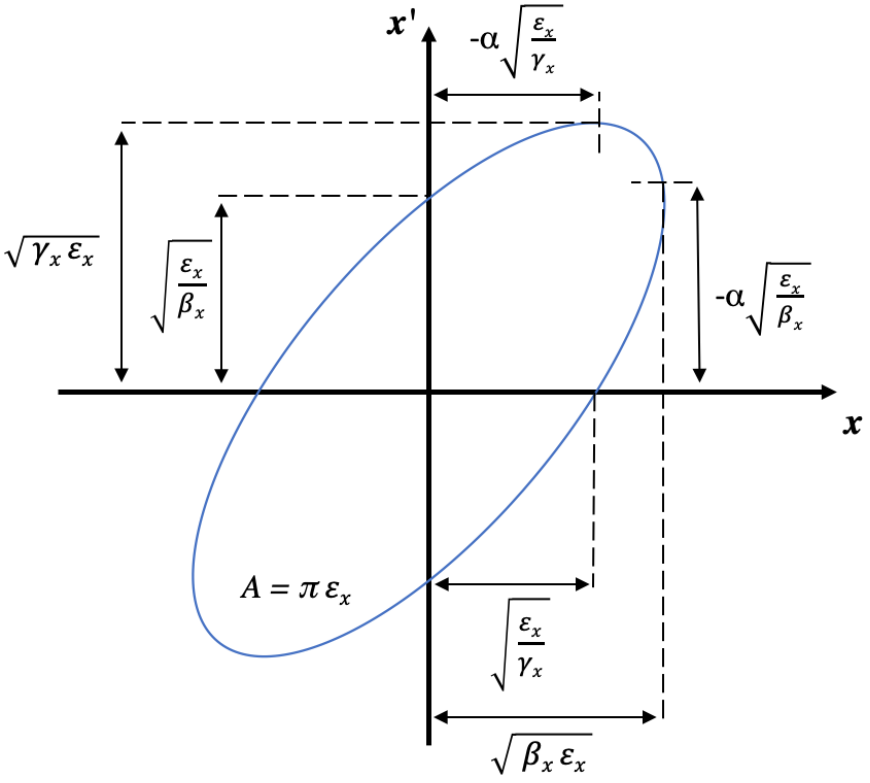

Figure 4.3: Twiss parameters and the beam ellipse in the horizontal phase space.

Each particle can be defined by the 6 phase space variables (x, x', y, y', z, z'), giving their position, momentum and angle:

$$\begin{aligned} x' &= \frac{dx}{ds} = p_x, \\ y' &= \frac{dy}{ds} = p_y, \\ z' &= \frac{\Delta p}{p_0} = \frac{p - p_0}{p_0} = \delta, \end{aligned} \tag{4.9}$$

where δ is the relative momentum offset in the longitudinal plane as the z-axis is parallel to the reference frame trajectory.

Dispersion

A beam will consist of particles with different positions (in the x and y transverse planes) however they will all not have the same energy or momentum. This momentum spread δ results in some deviation as the beam passes through magnetic fields. A correction for this can be rewritten for Hill's equations (Eq. 4.4) to determine the particle's position again:

$$x(s) = x_\beta(s) + D_x(s)\delta, \tag{4.10}$$

where *D(s)* is known as the dispersion, representing the position offset (in x or y) due to the change in momentum. Particles with higher momentum will have a higher bending rigidity and therefore bend less given the same field; this holds true for the opposite. Similarly, particles will trace out another orbit as related to the differences in momentum, represented by this dispersive term.

Emittance

A particle with an ideal trajectory will have no difference in momentum and zero divergence from the design orbit and therefore zero emittance. In reality, a beam will contain a spread of particles in phase space and therefore this area is a significant indicator of accelerator performance. The emittance is important for the design and optimisation of the beam optics as it is closely linked with the Twiss parameters and the beam size. The emittance can be defined in several different ways depending on how the particle distribution is chosen; for the work in this thesis, the transverse root mean square (RMS) emittance is considered:

$$\varepsilon_{rms} = \sqrt{\langle x^2 \rangle \langle x'^2 \rangle - \langle xx' \rangle^2}. \tag{4.11}$$

As shown in Fig. 4.3, the occupied phase space is $\pi\varepsilon$. The emittance ε_{rms} is usually given in units of π mm mrad and considers the distribution of particles in an equivalent ellipse in phase space, within one standard deviation (of $x = 0$). The brackets $\langle\ \rangle$ indicate an average value.

The transverse emittance can be measured using many different methods [69, 165] as dependent on the type of facility, properties of the beam and the extent of disturbance on the beam. Several limitations meant that a scheme for these measurements needed to be tailored to the specifications of Clatterbridge; this is discussed later in Section 4.4.1.

4.2 The Clatterbridge Facility

A few studies were done previously at Clatterbridge involving the transport line and accelerator. The feasibility of an upgrade to increase the maximum proton energies by incorporating a linac at CCC was explored in [166, 167] and measurements of the extracted beam and cyclotron were performed [168]. As there have been several changes over the years, further work into the optical modelling and beam emittance was also done by [128, 169]. However, these results were inconclusive and there has been little attempt since to combine all findings and understanding of the beam optics for practical use. Consequently, as there is no pre-existing optics beamline model for CCC, a comprehensive review of the facility was firstly needed for modelling of the beam dynamics.

All relevant documentation over the lifetime of the facility that was still in record and accessible was reviewed (Appendix A). Historical information of the cyclotron and beam properties (Appendices A.2-A.4) only originate from the period of time prior to and surrounding the beamline conversion, thus only pertain to its initial operation for neutron therapy. During the commissioning phase, studies were done in [110, 111] to design a delivery system based upon considered specifications to generate a clinically applicable beam. Since then, there has been an absence of functioning diagnostic systems upstream of the treatment room and as a result, the beam transport upstream of the delivery system is not well understood. Despite this, the beam requirements for treatment fall within defined ranges (Table 3.1); the operation of the accelerator and beamline remain consistent as performance is maintained with routine checks.

In modern facilities, multiple beam instrumentation devices are commonly placed along the transport line to provide measurements including the current, profile, emittance, position, dose or energy losses [170]. These parameters are available either actively

online or during downtime checks which can be used to examine the beam and to define the beam behaviour. In the case of CCC this was not possible: it is difficult to accurately model the treatment beam without knowing the characteristics and distribution of the beam generated between the delivery system and the exit of the cyclotron. Nevertheless, a retrospective study is a practical method to overcome this and model the beam optics of an established proton therapy facility given the arrangement of the beamline, components, cyclotron settings and magnetic parameters. This study has also been reported with some modifications in [171].

4.2.1 Bunker Overview

Housed in the Clatterbridge Cancer Centre, Wirral in the North West of England, the Douglas cyclotron and beamline was built and commissioned in 1984 initially for fast neutron therapy trials. Further construction was required to accommodate a supplementary treatment room for the proton therapy service [15, 111]. Parts of this early beamline are still contained within the cyclotron bunker however are no longer in use, along with several other components displayed in the layout below (Fig. 4.4). This includes flip screens (FS), stray beam detectors (SBD) and beam profile monitors (BPM) which are shown in the layout but have been removed. The BPMs were last used more than 10 years ago and wire scanners were no longer used as a much higher current was needed to generate signals with sufficient resolution[†].

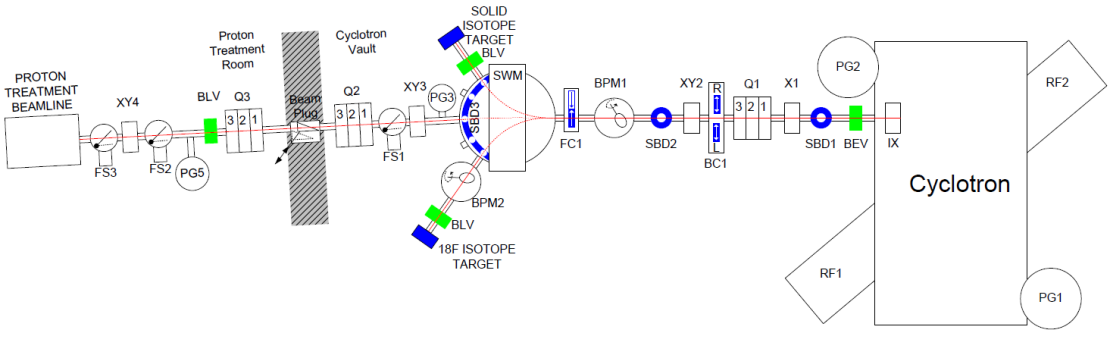

Figure 4.4: Original layout of the complete CCC beamline. Within the vault, the cyclotron produces the proton beam (red line) which passes through the transport line comprising various components and magnets, to the treatment room area. Notable beamline elements; quadrupoles (Q), dipoles (X), switching magnet (SWM) and beam collimator (BC1). Full listing can be found in Appendix A.1.

[†]Personal communications, I Taylor, 2018.

The Scanditronix MC-60 PF isochronous cyclotron (Fig. 4.5) generates a 62 MeV beam of protons transported through nine quadrupoles arranged into three triplets, a switching magnet and collimators before leaving the bunker and onto the passive delivery system in the treatment room (Fig. 4.6). Adjustments were necessary to change the produced beam from neutrons to protons, particularly to limit the extracted beam current from 50 µA to 30 nA and to therefore also decrease the resulting dose rate. This required installation of another ion source power supply which restricted the arc current [111]. The affect of this change on the beam quality is not quantified however several observations are discussed in Chapter 3 which are thought to be strongly associated with the cyclotron repurpose.

Figure 4.5: Scanditronix MC-60PF cyclotron. The first quadrupole triplet is partially visible and located just after beam extraction upstream of a dipole which steers the beam onward to the switching magnet.

The beam enters the treatment room through a beam pipe in the wall and traverses two scattering foils before it leaves the vacuum pipe through a kapton window. Cross-wires and an ionisation chamber in the box just upstream of the nozzle are used to monitor the uniformity and performance of the beam.

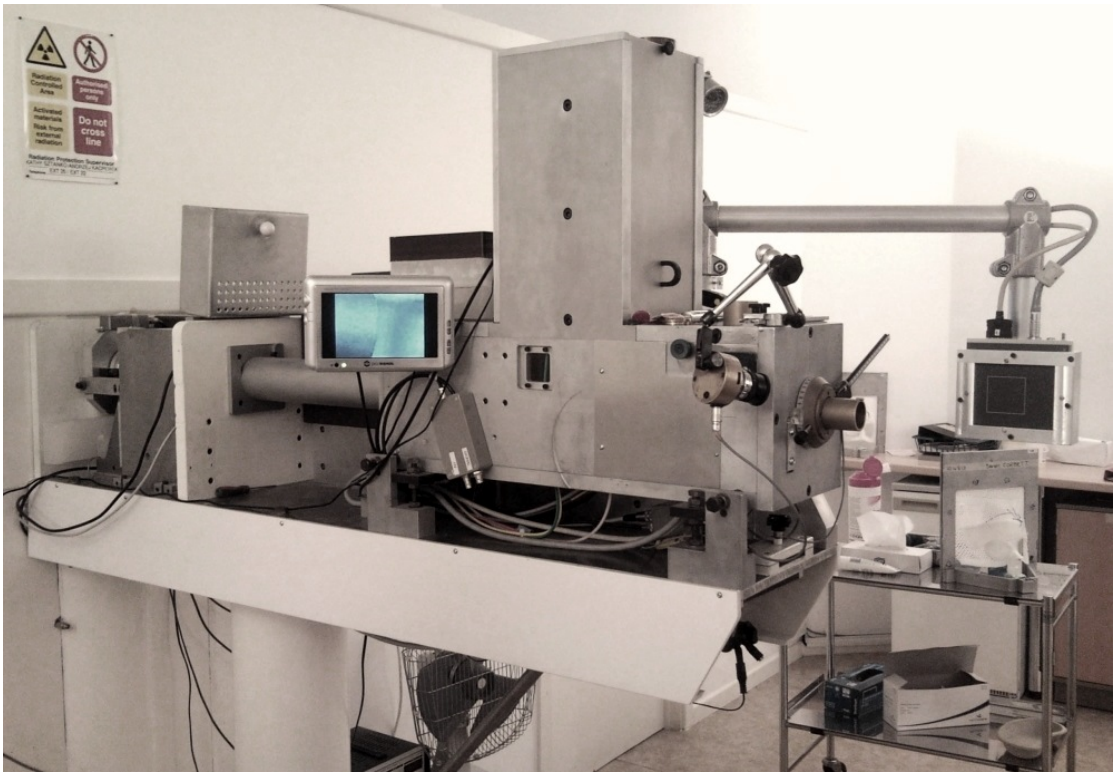

Figure 4.6: The treatment room beamline. The proton beam originates from the accelerator bunker behind the wall and passes through the delivery system before exiting through the brass nozzle and last collimator.

Functional parameters of the cyclotron and proton beam are listed in Table 4.1. These are typical values considered for current practice and as noted, differ from those provided by the manufacturer and as measured in past studies.

Table 4.1: Cyclotron and beam parameters.

Parameter	**Value**
Ion type	p^+
Ion max kinetic energy	62 MeV
Beam current (treatment)	1-30 nA
Number of ions	3.12×10^{10}
Energy spread	0.10 %

Accelerator Parameters

In order to generate an optical lattice of the facility, knowledge of fundamental beam properties such as the Twiss parameters and the emittance at the source point or exit of the cyclotron are necessary to define the input beam source for simulation codes. This

information was either unknown, inconsistently documented or irretrievable. All relevant historical documentation was extensively reviewed, salvaged and collated. Several values of emittance were found mentioned and are listed in Table 4.2.

Table 4.2: Documented emittances.

ε_x **[mm mrad]**	ε_y **[mm mrad]**	**Source/s**
<15	<15	T. E. Saxton [172], Appendix A.4
4.2	6.6	J. Ahlbäck, >1986[†]
<2-3π	<2-3π	J. Clarke [168]
2	1.5	H. Owen, 1998[†]

As these are inconsistent, the more recent work done by [128] was further examined. Similarly described in [169], a set of quadrupole variation scans (QVS) were done to determine the transverse emittance and Twiss parameters at the entrance of the first quadrupole. A set of Twiss parameters at the beginning of Q1 were obtained (Table 4.3) and these are assumed to be equivalent to the extraction point of the cyclotron. This study encountered several difficulties; uncertainties associated with the beam tails were reported however accommodations were made to appropriately analyse and model the beam. Although these values did not agree specifically with those in Table 4.2, it is recognised that the emittance would differ given the changes to the cyclotron and facility over time (discussed previously in Section 3.4.6). As these are the most recently reported values, were retained as input parameters for these beamline simulations.

Table 4.3: Reported Twiss parameters, dispersion and RMS (1-σ) emittances at the cyclotron exit and nominal input parameters for this study [128].

Parameter	**Horizontal (i=x)**	**Vertical (i=y)**
Twiss Alpha (α_i)	0.8600	0.2685
Twiss Beta (β_i)	1.9897	1.0629
Dispersion (D_i)	0	0
Transverse Emittance (ε_i)	5 mm mrad	1 mm mrad

[†]Reported in records of previous personal communication.

4.2.2 Quadrupole Parametrisation

An accurate description of the beamline components are needed to model the beam in any simulation code and specifically, it is necessary to define the parameters of the magnetic elements which comprise the optical lattice.

Geometrical measurements were taken across the entire beamline (Table 4.4) for all relevant components in both the demarcated bunker and treatment room areas. As the beamline is permanently fixed in place and the beam pipe passes through a concrete wall, measurements were also checked against original floor plans for accuracy [173]. The measured layout and determined lengths of the beamline components are shown in Fig. 4.7. The process to define these quadrupole parameters is described in detail in the following sections.

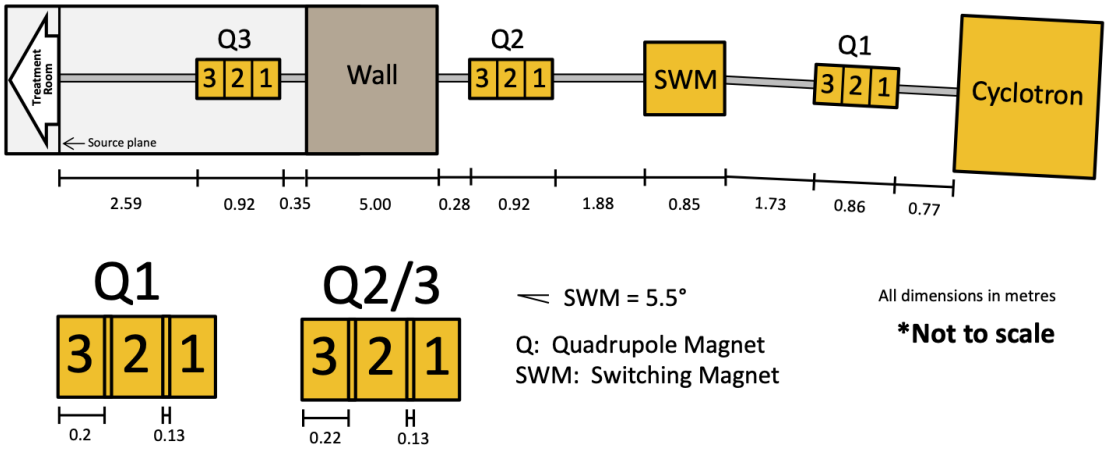

Figure 4.7: Beam transport line from the cyclotron to the treatment room. The origin point for all treatment delivery simulation models is indicated (source plane) at the start of the treatment room. Dimensions are provided in m but are not to scale.

For the magnets, defining the physical dimensions was more problematic as the quadrupoles were grouped into triplets with their individual yokes and coils obscured from view (Fig. 4.8a). Schematics were only available from initial neutron therapy line designs and it is not feasible to move or disassemble any elements. Therefore, dimensions were inferred by checks against original manufacturer drawings and the geometry for the second and third quadrupole were extrapolated from Q1. The SWM (Fig. 4.8b) has a deflection angle of 5.5° which has only a slight influence on the beam optics.

(a)

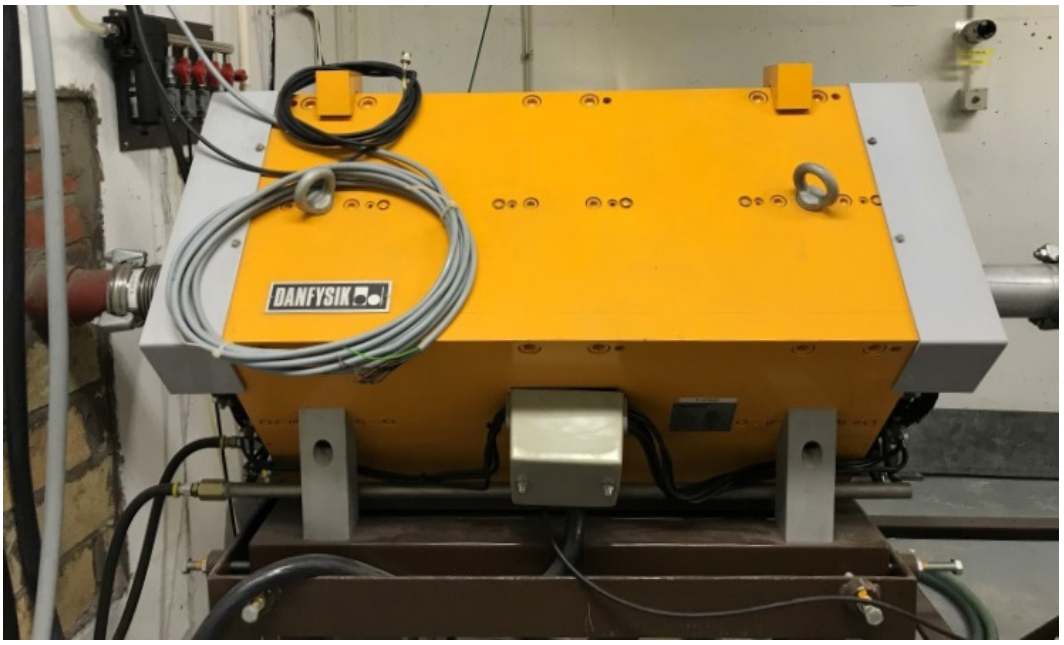

(b)

Figure 4.8: a) Close up of the second quadrupole triplet (Q2). Groups of bolts on the upper half of the external enclosure indicate the locations of the coils and poles belonging to each quadrupole. b) The switching magnet (SWM) coils are visible leading onto an upstream pressure valve.

Fields

Magnetic fringe fields can also be modelled in the simulation code and this relates to the difference between the physical and effective lengths. Fringe fields are the regions

on the edges of a magnet where the field reduces to zero. For realistic simulations, field maps or models can be implemented to account for the changes in the field.

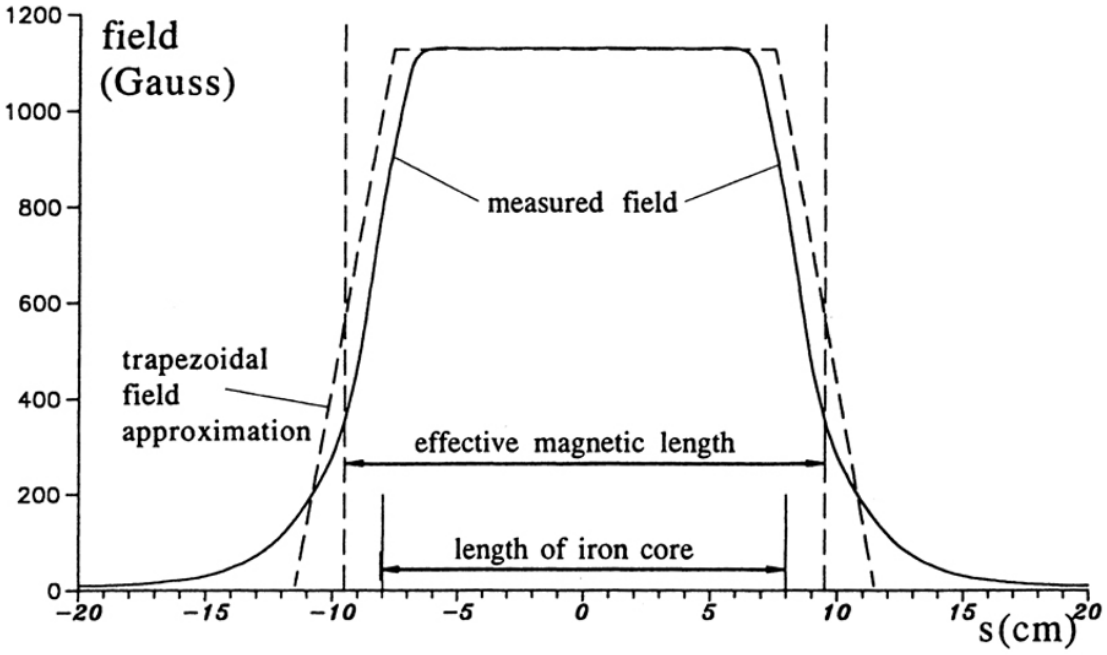

Figure 4.9: Different regions and changes in the magnetic field across the physical and effective lengths. The outline for a field approximation to model a dipole fringe field is shown [174].

Due to the lack of information and accessibility, drift distances (exterior to the iron core length) between the quadrupoles for all the triplets had to be estimated. As the exterior magnet dimensions were known from physical measurements, this total length (of a triplet) accommodates multiple drift spaces and effective lengths, which must be compensated equally by each quad. A range of lengths were simulated and smaller gaps were observed to cause blow ups in the optics further downstream, hence maximum drift lengths of 0.13 m were designated for each triplet. For simplicity, fringe field effects were discounted by equating the total effective lengths to physical lengths, as displayed in Table 4.4. In the event that more precise information is determined in the future, the optical lattice can be matched by modifying the relevant parameters.

It is also important to describe each quadrupole in terms of their magnetic strength or field gradient. This presented complications, requiring that the limited information provided by the manufacturer and any legacy control system data be converted into relevant quantities.

Accordingly, each quadrupole triplet had recommended operational parameters stated for each magnet and these were scaled and optimised for practicality. As the field coverage was approximated to the effective length of each quadrupole, a linear correlation was assumed to calculate the normalised quadrupole gradients K_I. This is based on the listed field gradient and nominal current for each quadrupole, multiplied with the programmed currents. This provides an estimate of each field gradient: the generated field gradient $G = I \times K_I$, where I is the supplied current. The normal quadrupole strength is determined by taking this field gradient over the beam rigidity (i.e. substitute G for g in Eq. 4.2). Corresponding nominal values are also listed in Table 4.4. The treatment line is indicated to begin 2.59 m downstream of Q3 and combined with the beam transport line, amounts to the total beamline length from the exit of the cyclotron to the treatment nozzle.

Table 4.4: Nominal parameters and lengths of beamline elements.

Element	**Physical Length** [m]	**Effective Length** [m]	**Normal Quadrupole Strength** [m^{-2}]
Q11	-	0.20	-11.93
Q12	-	0.20	7.35
Q13	0.97	0.20	-6.40
Q21	-	0.22	4.14
Q22	-	0.22	1.21
Q33	0.92	0.22	-4.14
Q31	-	0.22	5.89
Q32	-	0.22	-10.92
Q33	0.92	0.22	5.89
SWM	1.13	0.85	-
Transport line	16.15	-	-
Treatment line	1.77	-	-
Cyclotron to Nozzle	17.92	-	-

Given all these considerations, two codes: **M**ethodical **A**ccelerator **D**esign (**MAD-X**) [43] and **B**eam **D**elivery **Sim**ulation (**BDSIM**) [44] were used to model the CCC beam optics.

4.3 Optical Modelling

4.3.1 MAD-X

MAD-X was originally developed and is currently maintained by CERN, used to describe alternating-gradient accelerators and transport lines. It performs beam dynamic calculations of charged particle accelerators and is particularly useful for optics studies, including design and optimisation. For this work, the CCC beamline was defined in MAD-X using the optical components and lattice of the transport line combined with nominal parameters (Tables 4.1, 4.3 and 4.4). By providing a description of the beam source and a sequence of magnetic elements, it is possible to obtain the Twiss functions which describe the beam envelope throughout the beamline. The tool performs beam dynamic calculations to determine the beam ellipse at a point which can also be transported to various locations. As a result, the beam phase space can be determined at any arbitrary position which allows the flexibility to match components and parameters to generate outputs as necessary.

As mentioned in Section 4.2.2, the normal quadrupole coefficients listed in Table 4.4 were approximated and as such, a process of optimisation was necessary to obtain results with minimal beam sizes and higher transmission. This was performed by applying a range of factors to further scale the strengths of each quadrupole triplet and resulting effects on the optical functions, transmission and calculated beam sizes along the transport line were assessed. The values quoted in past work [169] were also examined. For context, the resulting changes to the Twiss functions are also shown as additional plots in Appendix B.16.

As the physical beam properties are primarily dependent on the extent and evolution of the beam envelope, the Twiss functions were optimised to reduce erratic or large fluctuations such that outputs within beamline constraints could be achieved. This process is discussed later in Sections 4.3.3 and 4.4.3. Q1, Q2 and Q3 were finally scaled by 0.3, 0.8 and 0.8 respectively, obtaining the optimised set of simulated Twiss functions (Fig. 4.10). The code describing the optimised CCC optical lattice is included in Appendix B.17.

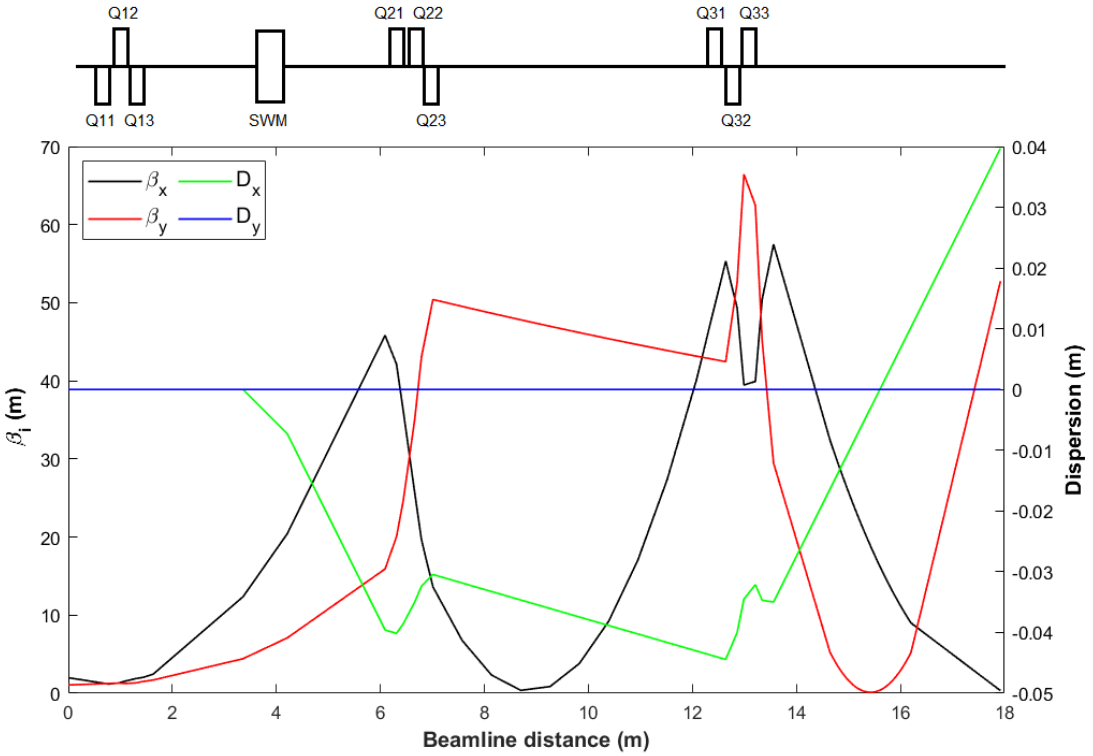

Figure 4.10: Twiss functions (Twiss beta β_x, β_y and dispersion D_x, D_y) for the nominal case, across the entire beamline starting from the cyclotron exit to the nozzle. The magnetic elements are displayed above the plot.

The green line shows an increase in dispersion in the negative direction (across the x plane) beginning around the switching magnet but remains constant at 0 in the y plane as the magnetic field generated by the dipole bends the particles in the beam only across one plane. The switching magnet was originally responsible for diverting the beam to the different beamlines but now just deflects the beam slightly, hence only has a small dispersive effect.

The betatron functions β_i are dependent on the fields produced by the quadrupoles and describe the orientation and divergence of the beam. The beta functions converge following passage through the first and second triplets, however the overall changes to the optical functions show a clear increase from initial beam parameters. To examine practical conditions, the Twiss functions are examined for the extent of their physical implications, specifically to determine RMS transverse beam sizes.

4.3.2 Transverse Beam Size

Knowledge of the divergence and size of the beam is essential when considering the geometrical constraints of equipment. This includes the beam pipe and collimators; also if integrating any instrumentation into the beamline either in the transport line or further downstream. Therefore, beam sizes at several important locations were evaluated using the following equation:

$$\sigma_i = \sqrt{\beta_i \varepsilon_i + {D_i}^2 \left(\frac{\triangle p}{p}\right)^2}, \tag{4.12}$$

where σ_i is the transverse RMS 1-sigma beam size and i denotes the horizontal (x) or vertical (y) direction. This is determined by the Twiss beta β_i, transverse emittance ε_i, dispersion D_i and the square of the relative RMS momentum spread $\frac{\Delta p}{p}$. Furthermore, as the beam is (slightly) relativistic, a correction was required to account for the spread in kinetic energy and momentum:

$$\frac{\triangle p}{p} = \frac{\gamma}{\gamma + 1} \frac{\triangle E_k}{E_k} \simeq 0.5160 \times \frac{\triangle E_k}{E_k}. \tag{4.13}$$

In this case, $\frac{\Delta E_k}{E_k}$ is the kinetic energy spread of the Scanditronix cyclotron (Table 4.1) and γ is the Lorentz factor which is determined by:

$$\gamma = \frac{E}{m_o c^2} = 1.066. \tag{4.14}$$

The calculated transverse RMS sigma values are plotted against distances along the beamline and displayed in Fig. 4.11. To examine the reliability of the nominal emittance (red), two other emittance values were also used to calculate beam sizes as reported by Clarke (blue) and the manufacturer - Ahlbäck (green), as listed in Table 4.2. A diagram of the magnets has been overlaid for approximate comparison.

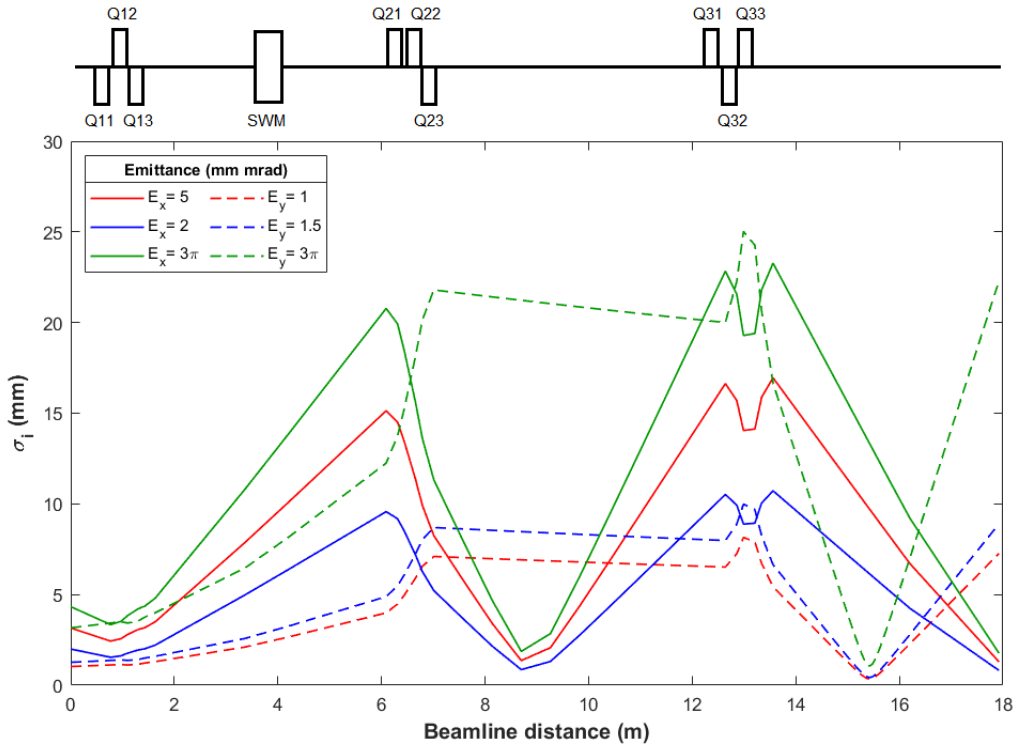

Figure 4.11: RMS beam sigma values for x (solid line) and y (dashed line) for different emittances. The nominal emittance (red line) is utilised for this study.

This plot illustrates the physical changes in the transverse beam sizes. As σ_i is largely dependent on the optical Twiss functions, the plots follow the distribution of the beta curves in Fig. 4.10. The lattice is designed such that the beam is delivered with qualities to fulfil its operational purpose; for operation at CCC this mostly involves altering the magnetic fields to transport a small and flat beam (uniform transverse distribution) through the treatment nozzle. A smaller beam is desired to maximise transmission, to avoid losses from interactions with the beam pipe wall or parts of components which may obstruct the beam path. This was achieved by the geometrical arrangements of quadrupoles into triplets and by the varying quadrupole field strengths or polarities, resulting in stronger or weaker focusing in one, or the opposite plane.

4.3.3 Optimisation

Given the range of σ_i obtained by using these nominal parameters, in practice the upper limits would not be possible as the beam would be too large for the beam pipes thus resulting in large losses. Physical measurements of the vacuum beam pipes were made however the outer diameters were not uniform and it is unclear if this is due to changes

in the thickness of the pipe walls or if the inner dimensions also change. The minimum inner radius was determined to be 30 mm and this was assumed for the simulations.

Furthermore, it is possible that other elements in the beamline may also affect the transmission. It is also mentioned in [128] that BC1 (Fig. 4.4) is an actuated collimator and when it was replaced with a scintillating screen to image the beam experimentally, the appearance of a trailing tail in the horizontal plane was detected. It is thought that BC1 was installed to remove the beam halo or tails [175] which skew the shape of the beam asymmetrically, accounting for the larger horizontal emittance. The collimator minimises the beam spread and dispersion of the beam envelope specifically as it enters the switching dipole where the magnetic field results in the separation of particles, horizontal beam growth and a magnified tail further downstream. BC1 is presumed to mitigate radiation losses and improve the beam quality for treatment.

Given the uncertainties and to keep the lattice straightforward, smaller apertures or collimators were not included. In reality, the beam should be less than the minimum 60 mm pipe diameter to be able to traverse the vacuum pipe at the beginning of the treatment beamline (>16.15 m) with sufficient transmission. Ideally at this point the beam size should be small enough as the pipe contains a first collimator (6 mm diameter). At this stage the beam sigma has doubled in comparison to the start of the transport line. Additional beam sizes, corresponding betatron values at significant locations and potential positions for diagnostics (P1-P4) are listed in Table 4.5.

Table 4.5: Optimised lattice beam sizes and betatron values.

Marker Location	**Distance** [m]	σ_x [mm]	σ_y [mm]	β_x [m]	β_y [m]	D_x [m]	D_y [m]
Cyclotron exit	0	3.15	1.03	1.99	1.06	0.00	0.00
After SWM	6.09	15.13	3.99	45.81	15.91	-0.04	0.00
End of Q3	13.56	16.95	5.43	57.48	29.47	-0.03	0.00
Diagnostics P1	14.65	12.73	2.29	32.42	5.25	-0.02	0.00
Diagnostics P2	14.81	12.10	1.82	29.26	3.33	-0.01	0.00
Diagnostics P3	14.97	11.46	1.36	26.27	1.85	-0.01	0.00
Diagnostics P4	15.14	10.83	0.91	23.44	0.82	-0.01	0.00
Treatment line start	16.15	6.89	2.14	9.52	4.59	0.01	0.00

Experimental measurements are necessary to benchmark this lattice as these values are contingent on the reliability of information and the assumed parameters used in the simulation. Moreover, as the quadrupole specifications cannot physically be checked and have been approximated to their best degree, one approach is to modify the normal quadrupole gradients to match actuality. This optimisation was performed in MAD-X where the normal quadrupole strengths (Table 4.4) were scaled for all triplets and a corresponding set of σ_i was generated. Fig. 4.12 illustrates the wide range of possible beam sizes; minimum or maximum σ_i are denoted by either a marker or line to indicate the boundaries at either extreme, anywhere along the transport line. Each marker or line type represents a set of either σ_x (red) or σ_y (blue) values which have been generated by applying a scaling factor to the nominal quad strengths. For clarity, only the sets pertaining to the outer boundaries have been individually displayed and the remaining series of σ_i pairs are contained within the shaded region. The beam sizes determined for the nominal, optimised case is specified by the solid lines.

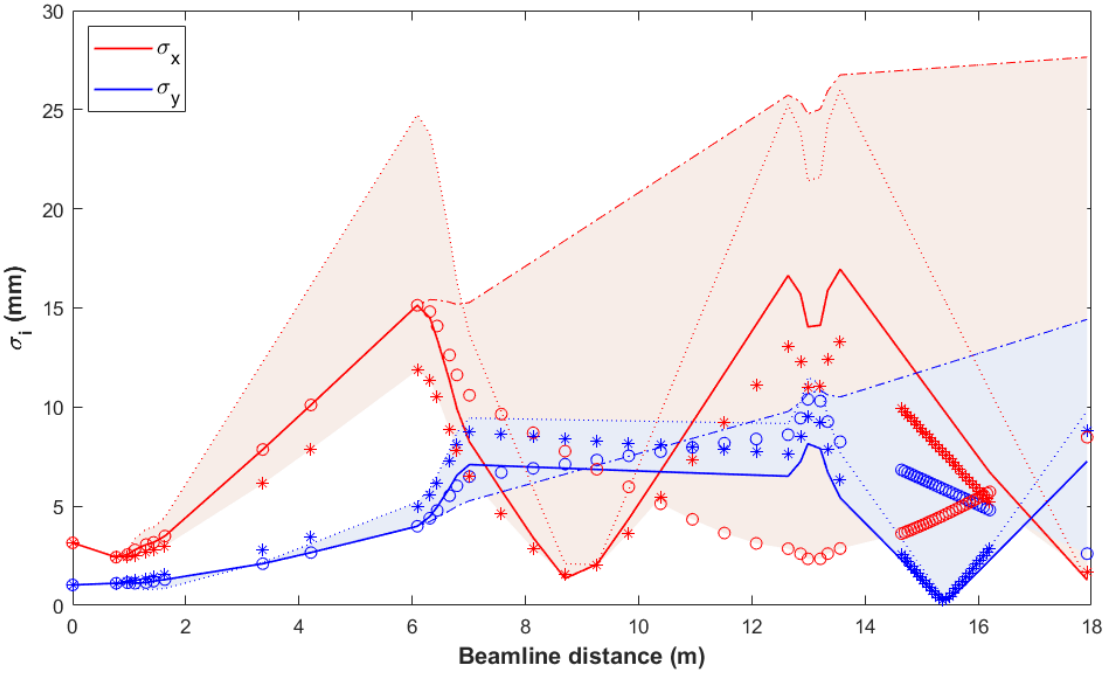

Figure 4.12: Ranges of possible transverse RMS beam sizes by varying the quadrupole gradients. The non-solid lines and markers correspond to the sets with maximum or minimum σ_x (red) and σ_y (blue) values. All other σ_i sets are contained within the shaded regions and the optimised case is indicated by the solid lines. As distances between 14.5-16.2 m are meaningful, there is smaller interpolation between these points.

This plot indicates that varying the magnet settings results in a large range of beam sizes. This is most significant at >12 m, where knowledge of the beam parameters is most important. Experimental measurements are necessary to verify the precision of this model and can be benchmarked by determining the emittance or transverse beam profiles under standard or defined accelerator settings.

4.4 Model Verification

Active verification measurements are straightforward for modern facilities which already have diagnostics devices [170, 176–178] installed in their transport lines. As such, two approaches to verify the model experimentally were developed, as CCC would require a system be designed and integrated into the beamline. In terms of both the physical design and optics, locations P1-P4 were identified as the most ideal sites for system integration for experimental measurements. These can be done using several different methods, most suitably either pepper pot, quadrupole variation scans (QVS) or multiple profile measurements [69, 165, 179]. As past difficulties were encountered using a scintillating screen and camera to capture the beam, a more flexible and robust method is needed. Therefore, a combination of multiple profile and QVS measurements with a scanning fiber system [180] was pursued. It was aimed that measurements with this system using multiple methods will yield the Twiss parameters, emittance and also allow simultaneous characterisation of the quadrupoles.

4.4.1 Proposed Emittance Measurement Campaign

The ^{4}PrOBεaM (4-Profiler Online Beam Emittance Measurement) [181, 182] is an efficient system which measures the transverse RMS beam emittance by scanning a doped silica fiber across the beam. The short acquisition time and compact size of the system enables integration in medical beamlines, capable of providing fast and accurate measurements of the beam size, shape and position. This allows the transverse emittance to be studied as a function of both the accelerator and beam, across a wide range of beam intensities. The technical specifications and concept of measurement is found in the mentioned sources. The system comprises of 4 UniBEaM detectors (Fig. 4.13a)

connected by KF-40 flanges for a total length of 54 cm, for simple integration into a beamline.

(a)

(b)

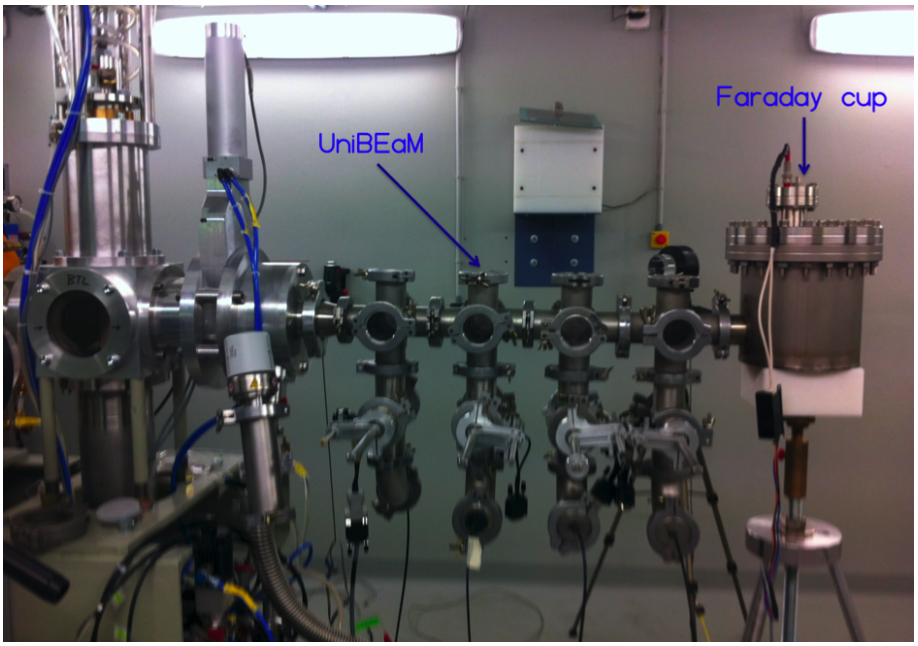

Figure 4.13: Single UniBEaM detector. The beam traverses horizontally through top (open) pipe and fiber originates from bottom tubing. b) ^{4}PrOBεaM detector system installed at the Bern cyclotron [180].

To incorporate the system into the CCC beamline, several parameters needed to be met, including: enough space (horizontally and vertically), suitable optics (visible beam waist), positioned further downstream of the cyclotron, sufficient distance after a quadrupole and preferably close to the start of the treatment line. Therefore, P1-P4 (Fig. 4.14a) presented as the most suitable location and an experimental scheme was developed (Fig. 4.14 with equipment listed in C.6).

(a)

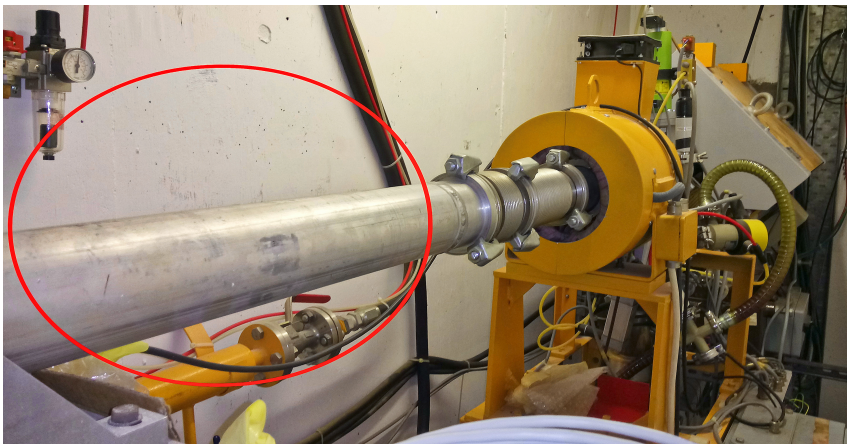

(b)

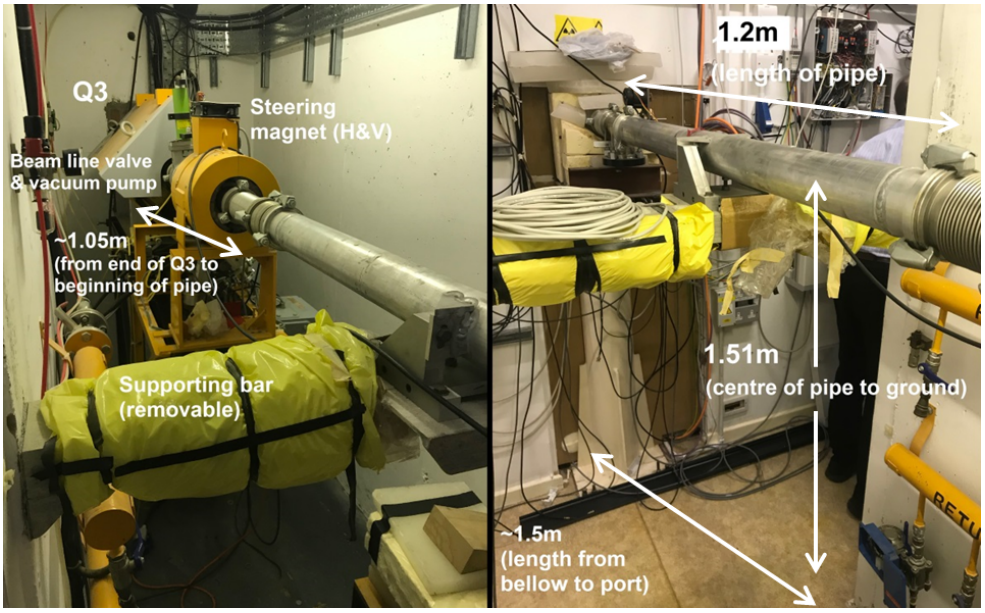

(c)

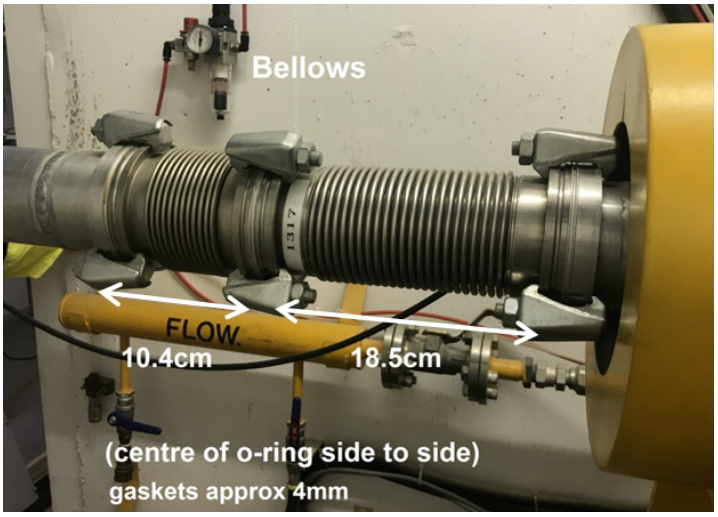

Figure 4.14: a) P1-P4 positions (red circle) along the beam pipe after the last quadrupole triplet Q3. The left side of the photo leads onto the start of the treatment room. b) Labelled diagram with dimensions of beamline and components. c) Close up of bellow closest to Q3.

Although temporary, the integration of any diagnostic devices requires destructive interference with the beam pipe and components. For this system, beamtime over a few days was required to allow for sufficient set-up, calibration and measurements. This presented significant difficulties as Clatterbridge operates a busy treatment schedule and among other operational uncertainties, time and resource restrictions meant that this experimental campaign was no longer feasible. Therefore, as an alternative approach to this issue and moreover as a baseline check of the optics, a measurement of the transverse beam profile at the beginning of the treatment line was performed with EBT3 Gafchromic^{TM} film.

4.4.2 Beam Profile Measurement

The start of the treatment line is indicated to begin at 16.15 m (Table 4.5), which is also defined as the location of the beam source plane for particle tracking simulations. The significance of this location is also associated with the close proximity to P1-P4, where measurements performed here may also have additional uses secondary to the beam optics by providing a direct determination of the beam profile. However, the closest accessible location to non-destructively measure the beam is 36.3 cm downstream of this point, where the beam exits the vacuum sealed scattering pipe (Fig. 4.15a) and enters the treatment room. As such, EBT3 film was attached to the downstream face of the kapton window and irradiated to obtain relevant information to resolve the beam profile. A close up of the kapton window attached to the end of the scattering tube, affixed film and obtained beam spot is shown in Fig. 4.15.

(a) 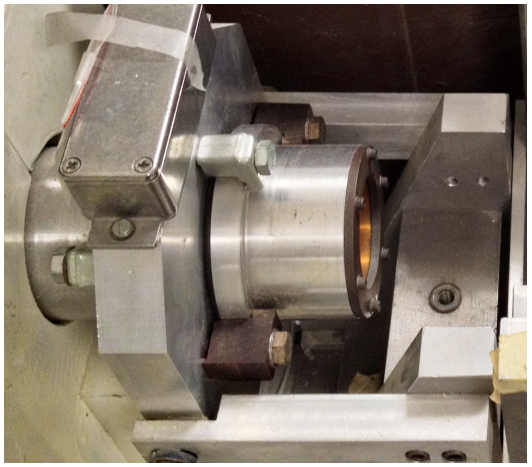

(b) 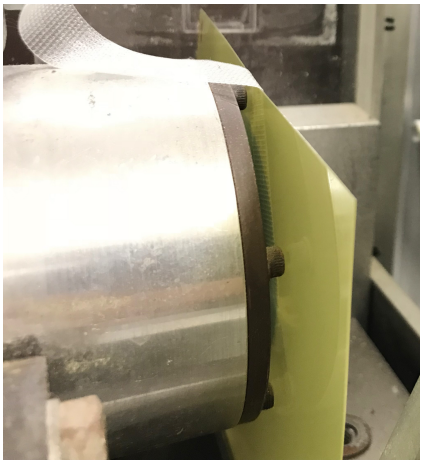

(c)

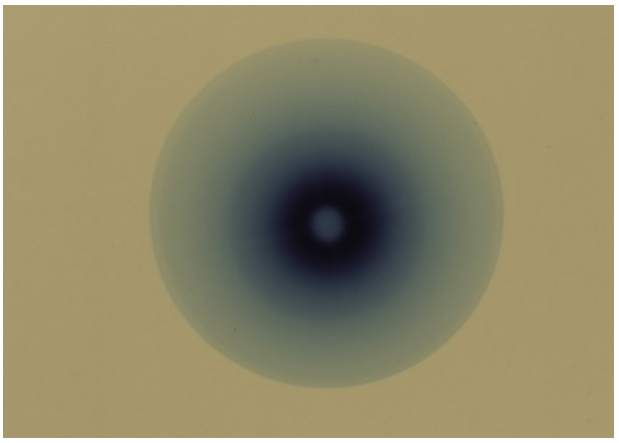

Figure 4.15: a) Scattering tube protruding from the wall separating the cyclotron bunker. The beam exits the kapton window (orange hue) and enters into the treatment room. b) Film setup. c) Beam spot on film after irradiation and self development.

The film was irradiated, calibrated and evaluated using the procedure described in Section 3.4.2 to determine the transverse beam profile at the designated point (Fig. 4.15b). Moreover, at this point the beam has passed through several components (two tungsten scattering foils and a brass beam stopper, Fig. 3.3) which alter the shape and spread of the beam. This is observed in Fig. 4.15c) by the distinctive void in the central area of the beam spot, as intended by the delivery system design [110, 111]. Primarily due to the presence of the brass stopper, the proton fluence here is substantially reduced such that the beam distribution will be flat and uniform at isocentre (70 mm after the end of the treatment nozzle). As the beam here has a modified shape and distribution, the optics calculations alone are insufficient to determine the corresponding size of the beam. Therefore, particle tracking simulations were necessary to reverse engineer the expected input beam size at the designated start point of the treatment beamline.

GEANT4 Simulation

Simulations were performed using the GEANT4 beamline model described in Chapter 3.3, where outcomes of this beam dynamics study contribute to efforts to verify and validate this and other related models of the Clatterbridge facility. As discussed, several beam parameters must be inferred, thus the input particle source used for the simulation (at the source plane) was defined from known beam quantities and those derived from beam dynamics calculations (Tables 3.1, 4.5). A beam of 100 million primary protons was generated and tracked at the same position as the film. The particle fluence

distribution was scored in the x and y directions and plotted against position in each plane, representing corresponding beam profiles. These were compared to the transverse profiles obtained from film measurements (Fig. 4.16).

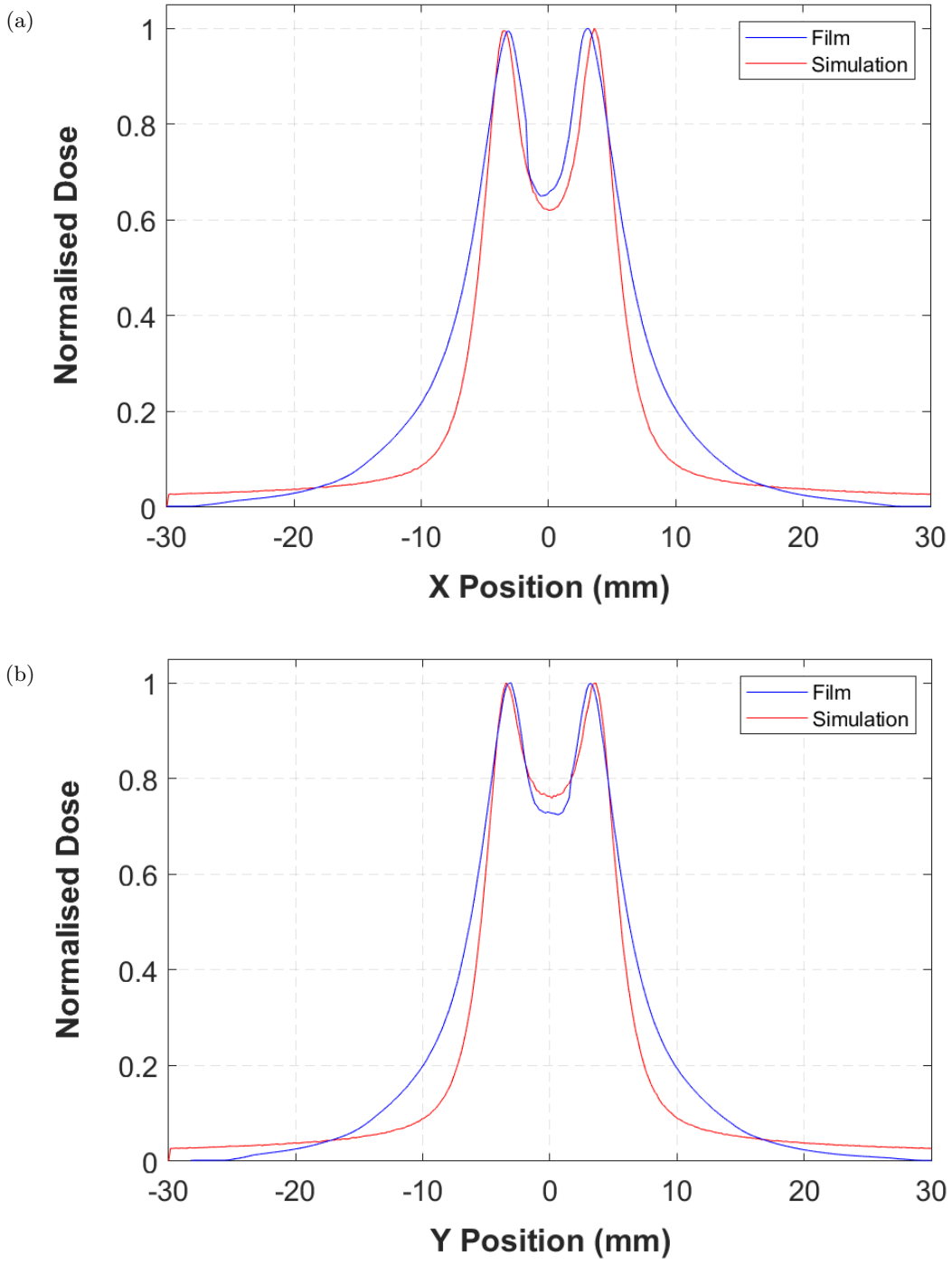

Figure 4.16: Transverse beam distributions in the a) X and b) Y direction. Film measurements (blue) are normalised to maximum doses obtained by conversion from optical density by standard irradiation calibration protocol. Simulated profiles (red) have been normalised to maximum doses for comparison.

In order to directly compare the two methods, plots were normalised to maximum values. As the film was also found to have a slight tilt in the positive x direction, an adapted normalisation factor was applied to adjust for the non-uniformity. Furthermore, at this location the dose is a relative value (correlated to ion chamber further downstream) and the beam current would also be similarly approximated. As the fluence is dependent on the beam current but directly proportional to dose, the simulated results were also normalised to maximum dose and plotted according to position along the axis.

In Fig. 4.16, the profiles follow a similar distribution however the film plots have a larger penumbra for both cases, with slight deviation in the central aperture regions. This is partly attributed to the process of conversion from net OD, where higher uncertainties were associated with smaller dose or net OD values. Furthermore, the exponential nature of the calibration curve mean that at this lower end, marginal variations in ODs may result in augmented doses. Additional scatter and interactions within the multiple layers of the EBT3 gafchromic film contribute to the lower dose tails and disagreement here also originates from differences with the scattering system geometry. These simulations were run with the preliminary GEANT4 model and precise revisions of the collimation geometry and specifications of the film were not yet implemented. This was corrected in later work and better similarity was achieved, as reported in [171].

Good agreement between the simulation and experimental profiles is observed at the highest regions of dose. While testing the model with different input source parameters, it was also noted that the beam distribution remained mostly unchanged except for the extent and elevation of the centre dip. However, as all factors influence the beam shape, it was unclear which (beam size, angular spread etc.) had the most significant effect. The differences between the two graphs are also evident of this, as the brass stopper has the same radius and extrusion in either direction but there is less attenuation in y. Both the beam size and emittance are smaller in y, indicating less spread, a slightly smaller beam width and less reduction to the apex.

Nonetheless, the agreement between these distributions suggests the applicability of the optical study derived parameters to simulate a physically similar beam. It is clear that at this point the beam divergence and distribution are influenced by the input beam

parameters. These results yield initial coherence with actual measurements which can be further validated with experimental beam emittance and profile measurements.

4.4.3 BDSIM

The optical lattice was also defined in BDSIM to look at other aspects of the beamline and for inclusion into a complete end-to-end model. Based on several codes, BDSIM also utilises the GEANT4 toolkit to simulate the beam distribution, transport, particle losses and has the capability of building detailed 3D geometries.

The lattice is defined in similar syntax to MAD-X; developers have provided several python utilities to ease the conversion process, usage between different codes and also to analyse results [183]. The necessary information describing the beam and lattice is split into several .gmad text files where a single file is executed to run the simulation. The main CCC lattice files are listed in Appendices B.18-B.19. Outputs from BDSIM can also be visualised and analysed using the provided tools in ROOT and python.

For the scope of this study and specific applicability for the facility, BDSIM was used to benchmark the MAD-X beta functions (Fig. 4.17) and analyse the beam transmission (Fig. 4.18) for lattice optimisation. The beam distribution (Fig. 4.19) at the beginning of the transport line was also visualised in the code.

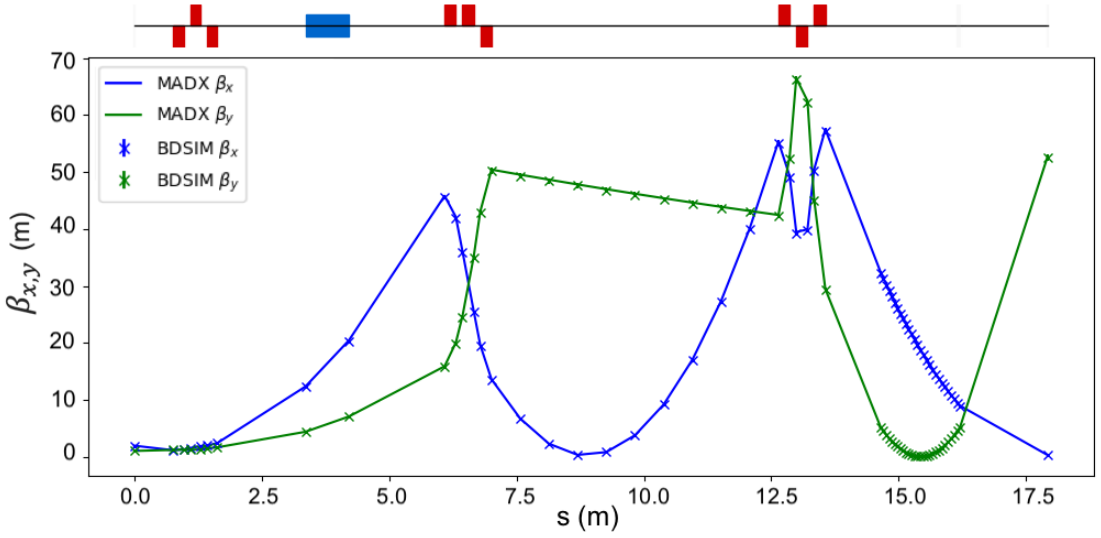

Figure 4.17: Comparison of Beta function plots between MAD-X (solid line) and BDSIM (markers) in the x and y direction for 10,000 primaries.

Although the optical functions are calculated differently, BDSIM was found to be consistent with MAD-X as both codes are observed to agree well (Fig. 4.17). As discussed before, BDSIM was also used to optimise the lattice by calculating the transmission. The optimised transmission from the extraction point of the cyclotron to the end of the treatment line is shown in Fig. 4.18.

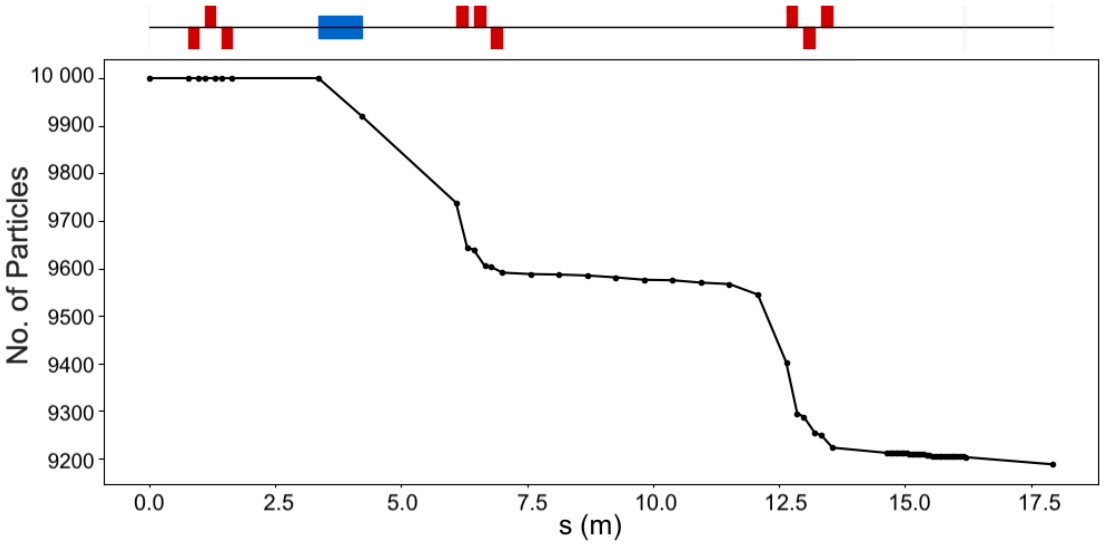

Figure 4.18: Particle losses across the beamline for 10,000 simulated primaries.

Fig. 4.18 shows a transmission of 92% from the exit of the cyclotron to the end of the treatment line. This suggests that minimum beam losses of 8% are expected with this optical lattice arrangement and nominal parameters. Large numbers of particles are lost after the SWM as the growth in dispersion here causes an increase in the beam σ_x. Significant losses occur where there is high dispersion, as seen at points of entry to Q2 and Q3. Once the beamline and quadrupoles have been characterised, it could be possible to improve the actual transmission efficiency.

Low losses across the transport line are ideal because once the beam enters the treatment line, transmission dramatically reduces to a few percent. This is caused by beam traversal through multiple components in the delivery system or gantry to shape and correct the beam as dependent on the needs for treatment. The scattering system and shaping components collimate and modify the distribution to such an extent that the beam delivered for treatment will remain consistently within specified constraints. As a consequence, at this point the uncertainties associated with the optical model and

its representation of the actual treatment beam and quality achieved at isocentre, has a limited and unforeseen impact. Nonetheless, the resulting aim is to determine the distribution and size of the beam as a basis for beam parameters at the start of this treatment line.

End-to-End Model

BDSIM can be used to visualise and determine the beam size at any given point throughout the beamline which is useful for beam characterisation (Fig. 4.19).

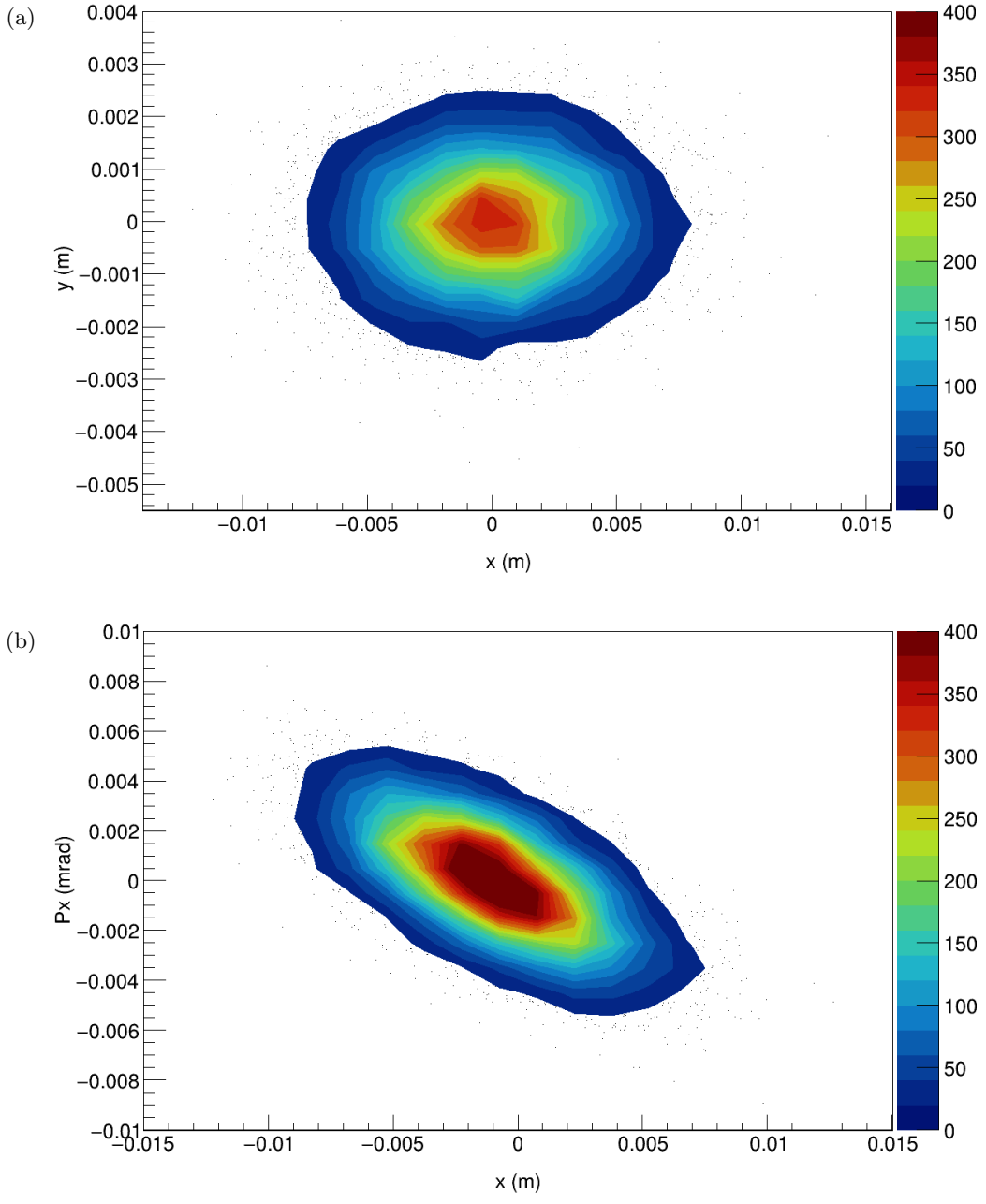

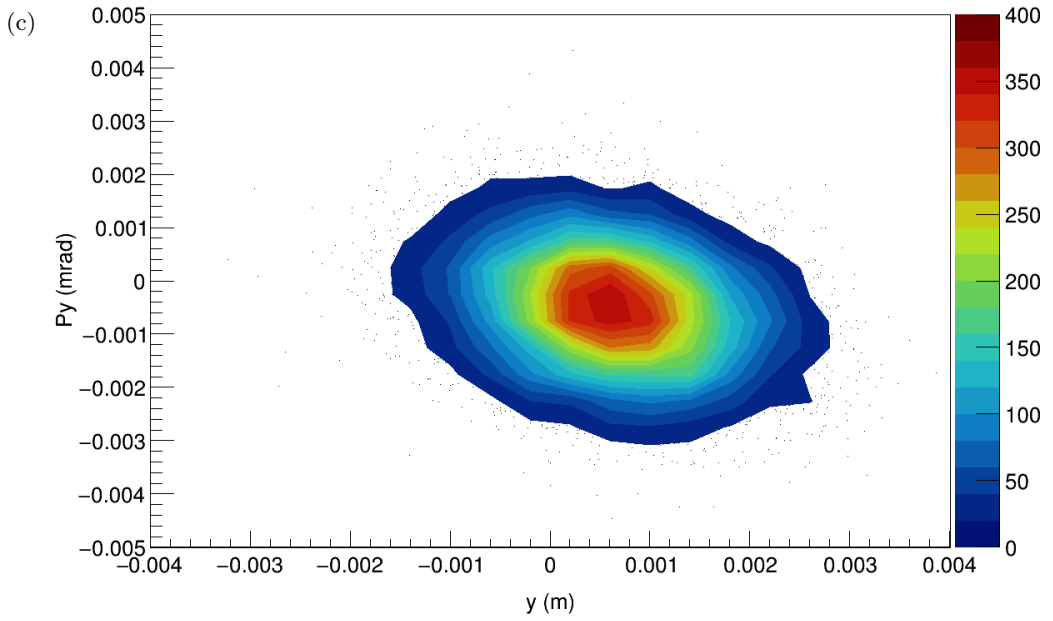

Figure 4.19: a) Beam distribution at the exit of the cyclotron in the transverse plane. Phase space ellipses in the b) x and c) y direction.

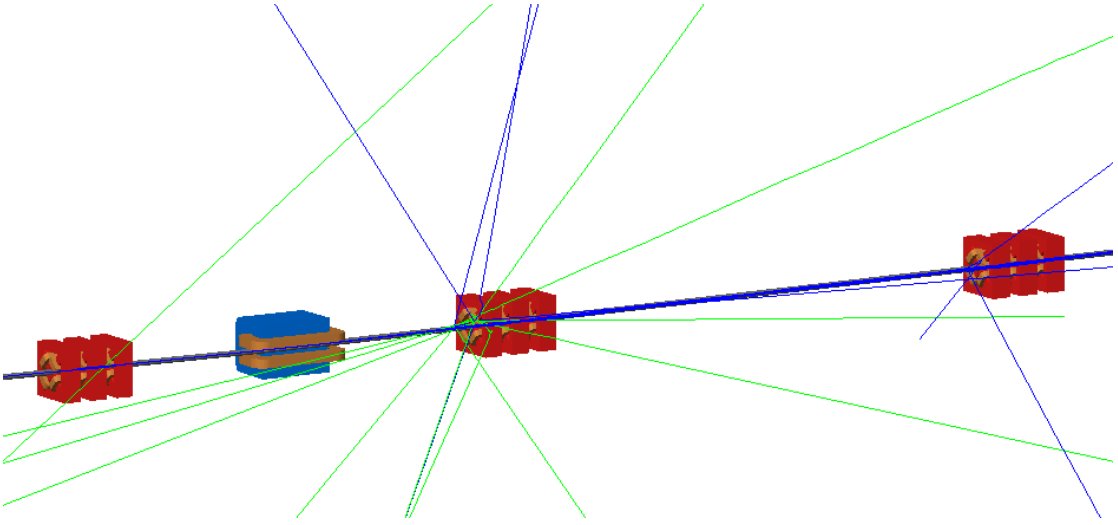

Figure 4.20: CCC transport line modelled in BDSIM displaying trajectories of protons (blue) and secondary particles (green). Beam goes from left to right, through Q1 to the SWM to Q2 and Q3.

The code has the capacity to import detailed geometry and as an additional capability of the model, realistic Computer Aided Design (CAD) models of the treatment beamline were imported (discussed later in Chapter 5.2.2) to achieve a complete end-to-end model of the Clatterbridge beamline. The complete geometry was implemented as an individual element in the components file. Several other aspects of the facility are able to be

studied and the beam can be simulated anywhere from the extraction point of the cyclotron all the way to the clinical nozzle (Fig. 4.21). This is an interesting concept as complete models are uncommon; typically the accelerator and treatment line are individually built as these areas of study do not overlap. BDSIM is a flexible code where further developments for medical applications are anticipated. A potential avenue for this would be to generate these beam distributions as an output file for incorporation into simulations of the particle beam source for the treatment delivery line.

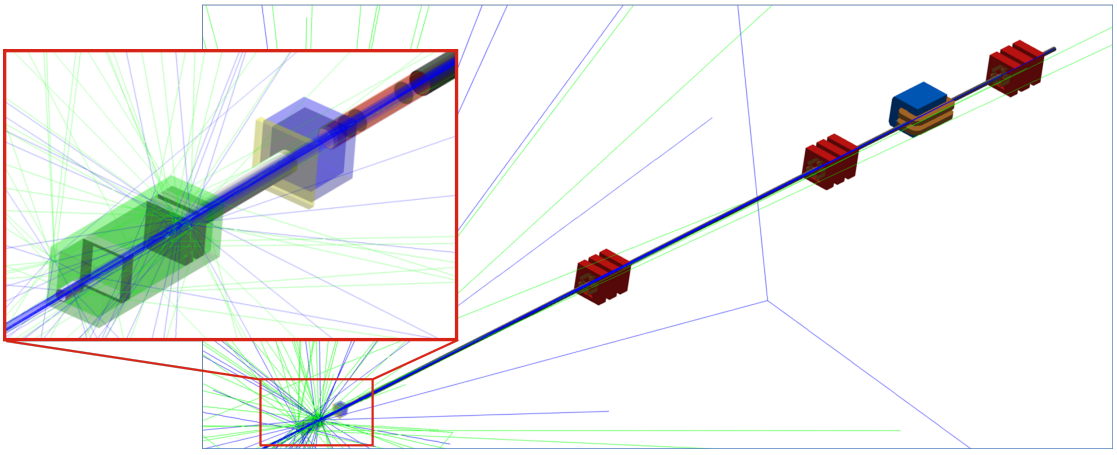

Figure 4.21: Complete end-to-end beamline model visualised in BDSIM with close up of treatment line geometry. Beam originates from the right. The different components are denoted: beam pipe (red), modulation box (blue), dosimetry box (green).

4.5 Summary

As a step toward the full characterisation of the Clatterbridge Cancer Centre proton therapy beamline, a detailed overview of transverse beam optics has been described in this chapter. Following the changes over the years, this chapter provides the first comprehensive overview of the beam dynamics of the CCC facility.

Treatment requirements and present day conditions of the facility and transport line provided constraints to define a model of the beamline simulated in both MAD-X and BDSIM. All existing beamline information was reviewed and the quadrupole parametrisation, simulated optical functions, RMS transverse beam sizes and transmission efficiency was investigated. The developed optical lattice can be modified to match

arbitrary parameters but given discussed limitations, an optimised case was studied. The resulting optimised quadrupole and beam parameters are summarised in Table 4.6.

Input beam parameters derived from optics calculations were used in GEANT4 simulations to generate beam profiles and these simulated beam distributions were checked against EBT3 Gafchromic film measurements. Similarities suggest the applicability of utilising parameters as determined from the developed optical lattice. It is expected that the model can be improved further with experimental measurements. An additional end-to-end model of the beamline was developed in BDSIM and can also be used for future studies.

Table 4.6: Summary table of optimised quadrupole settings and determined beam parameters for the start of the treatment line.

	Parameter	**Value**
Quadrupoles	Q11	3.58
[Normal quadrupole strength m^{-2}]	Q12	-2.20
	Q13	1.92
	Q21	-3.31
	Q22	-0.97
	Q23	-3.31
	Q31	4.72
	Q32	-8.74
	Q33	4.72
Twiss Parameters	β_x	9.52
[m]	β_y	4.59
	D_x	0.01
	D_y	0.00
Beam size	σ_x	6.89
[mm]	σ_y	2.14

Chapter 5

TOPAS Model

In previous chapters, different computational and experimental approaches were demonstrated to model the facility in several simulation codes as accurately as possible. In order to completely characterise the CCC facility, this chapter details a successive model of the CCC treatment line resulting from the work discussed in Chapters 3 and 4.

As mentioned in Chapter 1, CCC is part of the quickly growing PBT community in the United Kingdom and therefore it is highly valuable to have a publicly accessible, comprehensive and validated simulation model of the facility. For this purpose, an improved version was created using the **To**ol for **Pa**rticle **S**imulation (**TOPAS**) [184] code to extend the model for user ease, added capabilities and radiobiological applications.

This chapter describes a simulation of the CCC treatment line built in TOPAS and the improvements and developments from the previous GEANT4 model. As this code facilitates work into radiobiologically relevant quantities, studies into LET and further applications were explored. Experimental measurements to benchmark the model with a MiniPIX-Timepix detector are also detailed.

5.1 Introduction to TOPAS

TOPAS is a Monte Carlo code extended from the GEANT4 toolkit and was developed as a simulation platform specifically for research and clinical use in PBT. It was created as a means to exploit the capabilities of GEANT4 without needing proficiency with C++; to promote the ease of use of Monte Carlo simulations in medical physics research and in the clinic. As Monte Carlo techniques are becoming more prevalent in clinical environments, the tool enables users with ranging levels of experience and knowledge to utilise the code. The CCC beamline was redeveloped in TOPAS to take advantage of this, in addition to its other functions such as the TOPAS-nBIO extension [185]. This allows simulation modelling at the biological scale: radiobiological effects from individual and low energy interactions at the sub-cellular level, mechanistic DNA repair kinetics and chemical responses with geometry of specialised cellular components. The code also enables a platform for future biological work at the facility. At present, the TOPAS model provides relevance for cell studies with the North West Cancer Research (NWCR) centre and for further radiobiological and biophysical modelling with the Department of Oncology, University of Oxford.

For the work covered within the scope of this thesis, the context of dose and implications in treatment are considered through modelling of the LET. The significance of this parameter is that it is a physical and measurable quantity of energy deposition and can be related to radiobiological effects. The architecture and various functions of the TOPAS code are described next, as relevant to the CCC model, however full documentation of the code can be accessed from [186].

5.2 Simulation Environment

While the GEANT4 environment is governed by source code written in C++ to initialise and specify parameters in user action classes, TOPAS operates much differently. TOPAS still takes advantage of the extensive capabilities of GEANT4 such as incorporating its libraries, materials and physics lists, however employs a more modular framework to assemble and execute a simulation. This provides a more user friendly system while

ensuring sufficient flexibility for advanced users who also have the option of hard coding new classes or amending the TOPAS base classes, similar to GEANT4.

Instead of executing applications based on macro files, TOPAS uses a parameter system to firstly check and prevent errors, seeking reliability and repeatability in avoidance of dependency and other issues commonly encountered with GEANT4. Furthermore, lines of code do not need to be in a particular sequence as TOPAS does not enforce strict order dependence.

Parameter Control System

Parameter files must be written and read in plain text format and their functions are specified given the following command structure:

```
1    Parameter_Type : Parameter_Name = Parameter_Value
```

The *Parameter_Type* is the declared object type: string (s), integer (i), boolean (b), unitless double (u), dimensioned double (d) or a type of vector i.e. integer vector (iv). The *Parameter_Name* is a sequence of a prefix related to functionality (i.e. Ge: Geometry), the object name and property:

```
1    Parameter_Name = Ge/Phantom/Material
```

The *Parameter_Value* will be expressed according to object type and if appropriate, must also be followed by the unit. Settings can also be specified with respect to other parameters however acceptable boolean operations are limited (line 4). Some examples of different parameter lines:

```
1    d:Ge/Phantom/HLX = 40. mm
2    b:Sc/DoseScorer/Active = "True"
3    sv:Ph/Default/Modules = 1 "g4em-standard_opt0"
4    d:Ge/RoomWall/HLX= Ge/DeliveryBLineBox/HLX - 0.5 mm
```

These prefixes are one instance where the predefined vocabulary and syntax provided by TOPAS allows uncomplicated user specification. These enable different things to be controlled with a single line command, including options controlling the physics (Ph),

scoring (Sc) particle source (So), material (Ma) and graphics (Gr). This is not the full list but are the most commonly used; several more prefixes are mentioned in this chapter and their functionality will become apparent.

File Chain Structure

As more complicated applications require hundreds of parameter lines, it is logical to split up the code into several parameter files. A file will inherit and execute all lines from other files which are called by the following statement:

```
includeFile = anotherParameterFile.txt
```

It can be useful to also call another file from within the secondary parameter file where it then becomes a parameter file chain. This allows the application to be organised and managed as essentially separate modules: a supportive feature for collaborative work or developing different aspects of a simulation model. Parameter file chains can span horizontally as well as vertically, however the hierarchy structure must be considered as the order is important in this case. Parameter lines higher up in the chain will take precedence over the same commands further down. Moreover, to handle all the different parameters, TOPAS does not allow settings belonging to the same object to be changed in a separate chain. Two different files are not able to modify the same parameter. Similarly, all components which are given the same geometry or the same scorer must be contained in the same vertical chain.

Fundamentally, the main or default parameters should be defined in the initial file and then everything else that utilises these conditions should be written into adjoining files. A mostly linear hierarchical structure was adopted for the CCC model with interchangeable files for the scoring and this is illustrated in the diagram in Fig. 5.1.

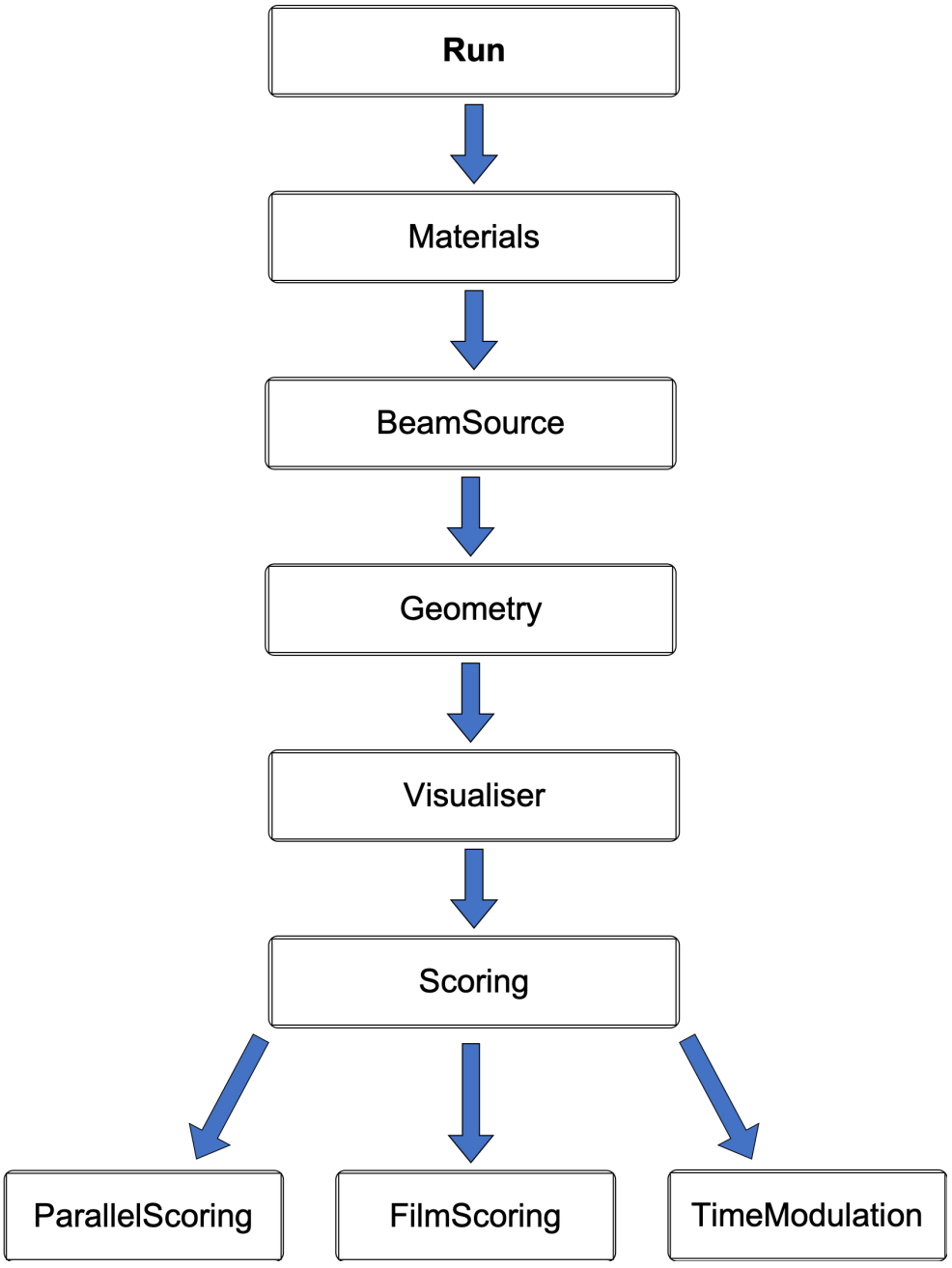

Figure 5.1: Parameter file chain. The initiating **Run** file is shown at the highest position, through a single chain to the multiple parameter files, responsible for the scoring.

Some of these have files been included in the Appendix (B.20-B.21) for reference and several important parameter files are discussed in the following sections. The full source code has been made available on [153]. Ongoing developments will be updated and documented as it is hosted on the GitHub repository and can be accessed from [187].

5.2.1 Particle Source

The particle source is defined in TOPAS by specifying various parameters of the beam such as the particle type, energy, shape, size, distribution and angular spread. By default, the beam is placed at the centre of the world volume. This ensures that the particle source is positioned at the origin of each axis. In TOPAS, each generated primary particle is termed as a history.

The CCC beam is defined in a parameter file (Appendix B.21) as a Gaussian beam and as a second option, a more realistic beam is described by Twiss parameters (summarised in Table 4.6). Both of these approaches correspond to the optical beam properties determined at the mentioned start of the treatment line '*source plane*' in Chapter 4. This is the point of overlap between the two models and for the rest of this chapter, will be referred to the starting point of the simulation; all the following TOPAS parameters will also be detailed as specifically implemented within the CCC model.

For clarity, a purple box was created to visualise the source plane and placed equivalent to the particle source position (Fig. 5.2).

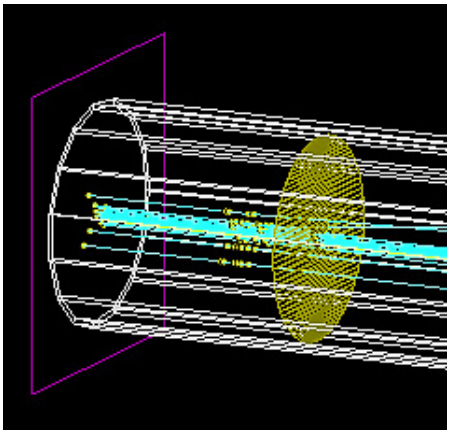

Figure 5.2: Particle beam origin at source plane. A beam of a small number of protons (cyan) is shown traversing through the beginning of the vacuum tube and the first scattering foil (gold), neutrons (yellow) are also visible.

The position of the source and the '*PlaneAtBeamPosition*' box are both defined as geometry components. Similar to GEANT4, geometries must be specified in relation to their mother volume and overlaps must be avoided as they cause errors which often break and stop the execution of the simulation.

5.2.2 Geometry

In general, TOPAS geometry can be described in different ways: essentially the dimensions and position must be specified with respect to the centre of their parent volume. The component name is included in each line with the stated type (shape), parent volume and material. Translational and rotational *X, Y, Z* parameters are assigned for positioning of the component within its mother in x, y and z. The orientation however will depend on the type of component and additional parameters may be required. Furthermore, the size (length) of the component is defined as a half length in the 3 orthogonal axes. A box symbolising the '*Room*' component: the CCC treatment room, is defined with the following lines:

```
1  s:Ge/Room/Parent = "World"
2  s:Ge/Room/Type = "TsBox"
3  s:Ge/Room/Material = "Air"
4  d:Ge/Room/HLX = 4. m
5  d:Ge/Room/HLY = 2. m
6  d:Ge/Room/HLZ = 5. m
7  d:Ge/Room/TransX = 0. m
8  d:Ge/Room/TransY = 0. m
9  d:Ge/Room/TransZ = 0. m
```

In GEANT4 these properties also define the component geometry but require multiple lines to construct the conceptual volume layers. Evidently, it is much easier to define objects using the TOPAS parameter syntax.

A collection of predefined generic components also exists and users can implement these individually or as a combination of components. Additionally, there is a TsCAD import feature which enables the conversion of any geometry created using CAD software into TOPAS geometry from Stereolithography binary (STL) or Polygon ASCII format (PLY) format. In order to preserve precise details of the treatment line system, the majority of the components were imported as STL files using this method. The

remaining components needed to be individually user defined. They were unable to be correctly imported and presented issues or difficulties due to the nature of their shapes.

STL files describe geometry only by their surfaces, a tessellation of triangular and quadrangular faces which approximate the volume. Although other file formats (i.e. GDML) may intrinsically include different properties such as materials or colour attributes, TOPAS does not interpret this information.

Therefore, given some missing elements and discrepancies which were noticed in the GEANT4 model (see Section 3.4.3), each component in the treatment line was physically remeasured within ±0.5 mm precision. Photos and schematics from this effort are extensively documented on the UCL website [173]. Following this, most of the components were implemented as a CAD design in GDML and STEP format[‡] (Fig. 5.3). This same model was also previously imported into BDSIM (see Section 4.4.3) but in this case the entire treatment line could be imported into BDSIM as a single entity. A GDML format was used and thus the material of each component could be preserved.

CAD Model

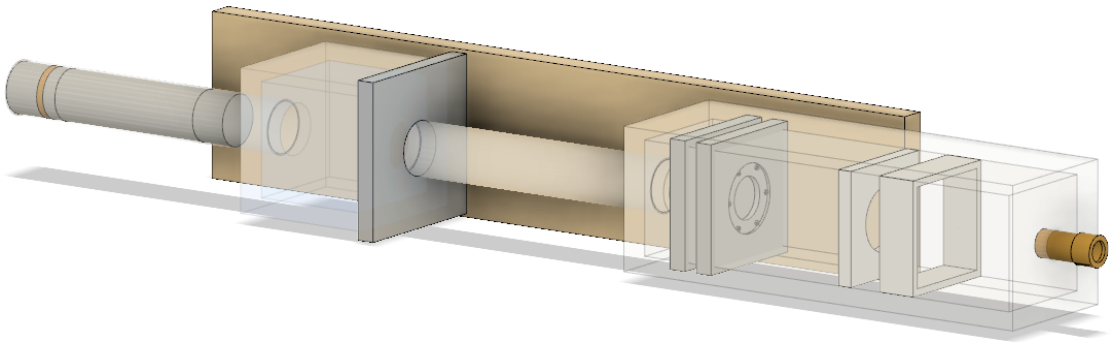

Figure 5.3: CAD rendering of the CCC treatment line with updated geometry following the rechecking of physical measurements.

As TOPAS does not offer such capabilities, each component (with their elements grouped by material) needed to be exported from the model as an individual STL file. This was a rigorous task as each component could have been created with its own respective axis within the world coordinate system, which is retained during export. TOPAS does not automatically determine this origin point and therefore may randomly place the

[‡]Provided by O Mayenin, 2019.

imported component either at the centre or the edge of the mother volume. As such, this meant there were several coordinate systems at play and final adjustments required additional rotation or translation using parameter lines. These were also checked against a list of z positions determined for every single element as relative to the treatment line coordinate system (Appendix C.7).

The CAD model (Fig. 5.3) was accessed using Autodesk Fusion 360 [188] and several more amendments were made in order to successfully import the components. As TOPAS does not allow overlaps, clearances were built between each adjacent surface to provide a 0.05 mm tolerance between each component. Several other modifications were also made to the original CAD design to improve the model and bring it closer to reality. The first aluminium (scattering) tube was extended to exceed the kapton window. The tungsten cross-wires in the dosimetry box were positioned more accurately. The dose monitors were reworked such that all of the pieces could be imported. Slightly larger clearances were needed between pieces; similar parts were grouped (bolts, foils, guard ring, PMMA exterior) and exported as separate STL files. These updates and all corresponding dimensions are displayed in a complete schematic of the treatment line in Appendix C.8.

CCC Treatment Beamline

The CCC treatment line is described in TOPAS realistically, as based on the exact geometrical measurements of each component. The entire delivery system is represented in Fig. 5.4. This starts with the vacuum tube containing the double scattering foils, through the modulation and dosimetry box and past the patient nozzle. All the simulated components are shown in Appendices B.34-B.38.

(a)

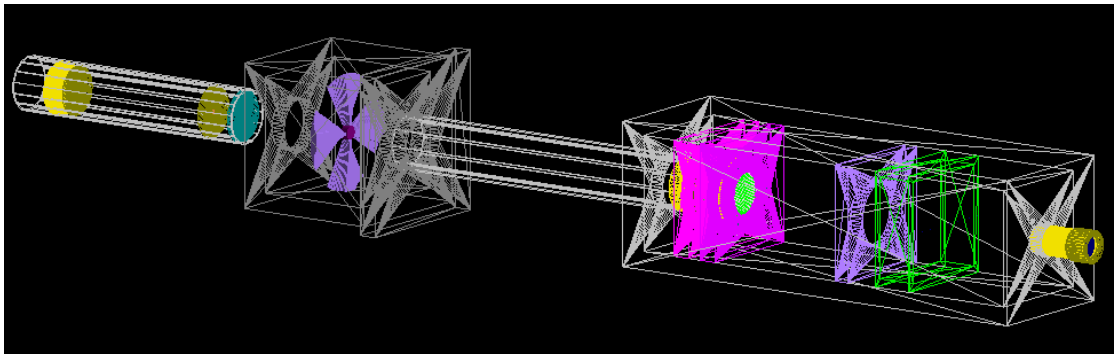

(b)

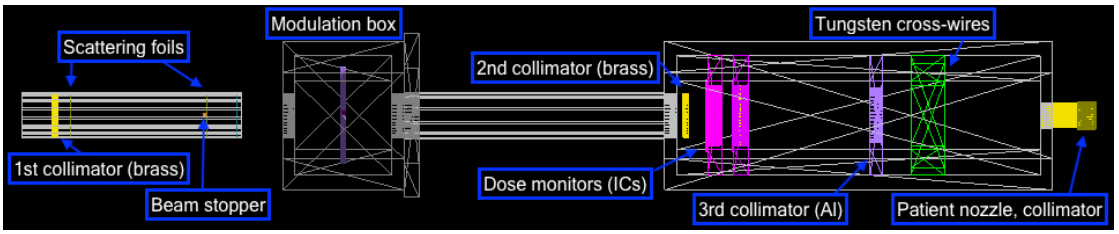

Figure 5.4: a) CCC treatment beamline model in TOPAS. b) Birds eye view with major components labelled.

Time modulation features in TOPAS also enable a SOBP to be generated based on a specified rotational rate, steps, repetition intervals and timeline. Additionally, schematics were obtained and used to model the components which were not able to be physically measured (i.e. dose monitors). These can be found with numerous photos of every component on [173].

5.2.3 Scoring

TOPAS scores particles using two main scoring classes: volume and surface scorers. Several preset scoring types are provided and enable scoring for certain quantities; these must be called upon as a *Parameter_Value*. There are also other extended scorers available including an RBE scorer and it is also possible for users to write their own.

Quantities such as the dose, energy deposition, fluence, charge and LET can be determined for different components and materials. There are more scoring options for volumes and often the same information can be obtained (although may be output in a different form) by using different scorers with the appropriate settings or filters.

To score the dose deposition and generate a BP, a $40 \times 40 \times 40$ mm^3 water phantom was created (Appendix B.38) at isocentre. Scored quantities are contingent on the geometry of the applicable component and the resolution is designated by the number of bins in the respective axis (lines 10-12):

```
1    s:Ge/Phantom/Type          = "TsBox"
2    s:Ge/Phantom/Parent        = "DeliveryBLineBox"
3    s:Ge/Phantom/Material      = "G4_WATER"
4    d:Ge/Phantom/HLX           = 20.0 mm
```

```
5  d:Ge/Phantom/HLY          = 20.0 mm
6  d:Ge/Phantom/HLZ          = 20.0 mm
7  d:Ge/Phantom/TransZ       = 1863.4 mm
8  s:Ge/Phantom/Color        = "lightblue"
9  s:Ge/Phantom/DrawingStyle = "Wireframe"
10 i:Ge/Phantom/XBins        = 1
11 i:Ge/Phantom/YBins        = 1
12 i:Ge/Phantom/ZBins        = 400
```

A volume scorer was used to obtain the dose accumulated in each 0.1 mm slice of the water cube:

```
1  s:Sc/DoseInPhantom/Quantity          = "DoseToMedium"
2  s:Sc/DoseInPhantom/Component         = "Phantom"
3  s:Sc/DoseInPhantom/OutputFile        = "Data/DoseInPhantom"
4  s:Sc/DoseInPhantom/OutputType                = "csv"
5  b:Sc/DoseInPhantom/OutputToConsole           = "False"
6  s:Sc/DoseInPhantom/IfOutputFileAlreadyExists = "Overwrite"
7  s:Sc/DoseInPhantom/Visualize                 = "TRUE"
```

The LET could be determined using the prebuilt '*ProtonLET*' scorer, weighted by either the average dose or track (line 3). TOPAS implements the approach developed by [189]; the energy deposition from both primary, secondary protons and electrons are taken over each step.

```
1  s:Sc/LETScorer/Quantity                  = "ProtonLET"
2  s:Sc/LETScorer/Component                 = "Phantom"
3  s:Sc/LETScorer/WeightBy                  = "Dose"
4  d:Sc/LETScorer/MaxScoredLET              = 100 MeV/mm/(g/cm3)
5  d:Sc/LETScorer/UseFluenceWeightedBelowDensity   = 0. g/cm3
6  b:Sc/LETScorer/OutputToConsole                  = "False"
7  s:Sc/LETScorer/OutputFile                       = "Data/LET"
8  s:Sc/LETScorer/OutputType                       = "csv"
```

```
9  s:Sc/LETScorer/IfOutputFileAlreadyExists        = "Overwrite"
10 b:Sc/LETScorer/PreCalculateStoppingPowerRatios  = "True"
```

Surface scorers were useful to quickly check that the simulation and scoring was functioning correctly. As such, these were assigned at key locations in each section as checkpoints throughout the beamline. Quantities could be scored according to transmission (in any direction) through a single surface and also as a phase space file. The phase space output provides detailed information about particles at that exact plane, scoring for multiple quantities including the position (in x, y, z), divergence, energy, time and particle ID. The other scoring and parameter files can be accessed from [187].

5.2.4 Physics Settings

The default physics processes in TOPAS correspond to a physics list used in an earlier version of GEANT4 which has been validated for proton therapy research at MGH. Although it is possible to create a whole new physics list, TOPAS provides two general methods of customisation: reference and modular lists. The first option applies a complete, preset GEANT4 list and the latter allows users to select different modules to construct a list.

Parameter lines are used to specify the type of physics processes chosen and to define cuts for different particles, energy thresholds and geometric ranges. As previously discussed (see Chapter 3), the step size can be a consequential factor in tracking particles. TOPAS tries to account for this automatically so that it doesn't need to be initiated by the user but can be changed if necessary.

A second set of QA Bragg peak measurements[‡] were used to benchmark the model. As this model implements the final revised geometry, several parameters were adjusted to match the obtained BP with actual data. The lack of definitive and verified input beam parameters (input energy, energy spread etc.) permitted this flexibility.

In order to match the simulated BP with the CCC BP, the most significant parameters are related to the beam energy. The energy spread mostly affects the shape of the

[‡]Provided by A Kacperek, 2019.

peak however also influences the depth of the BP and the steepness of the fall-off. Therefore, a balance between all these characteristics is necessary. A range of input settings were tested to modify the BP to replicate the CCC BP curve. Moreover, physics models which most appropriately represent the data best must also be selected. The type of physics lists and cuts also have a further impact on the BP, particularly in the build up region: the dose here is mostly contributed by nuclear interactions and secondaries. The differences between some chosen physics lists and options are shown with simulated BPs in Fig. 5.5. In addition, the impact of these differences were assessed by scoring LET_d (Appendix B.39) however, limited variation was observed.

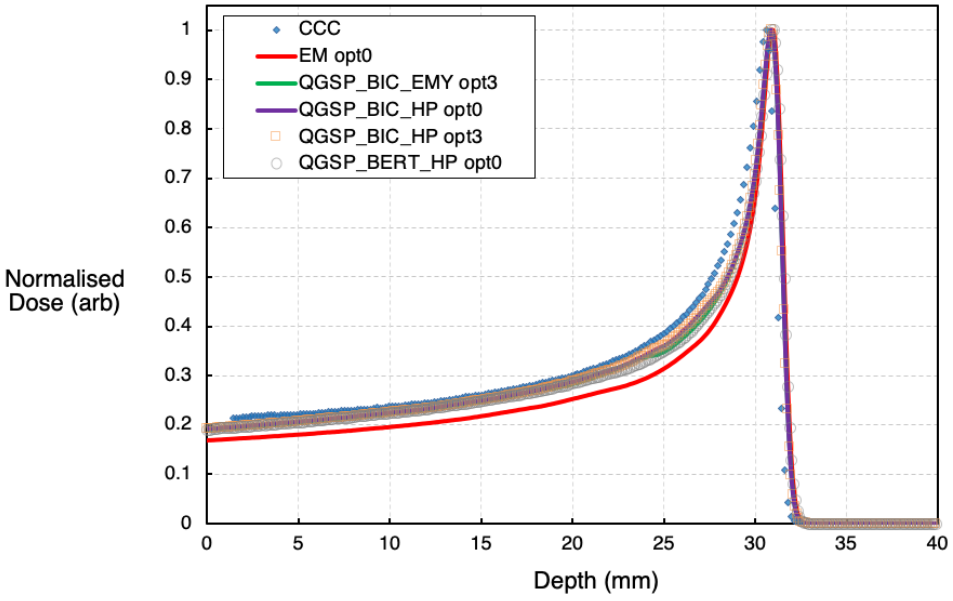

Figure 5.5: Pristine BPs simulated using different physics options against CCC data.

After numerous iterations of these adaptations, the best match was achieved with the following beam settings (Appendix B.21):

```
d:So/BeamSource/BeamEnergy = 62.2 MeV
u:So/BeamSource/BeamEnergySpread = 0.53
sv:Ph/Default/Modules = 2 "g4em-standard_opt3" "g4h-phy_QGSP_BIC_HP"
d:Ph/Default/CutForElectron = 0.01 mm
d:Ph/Default/CutForProton = 0.01 mm
d:Ph/Default/CutForGamma = 0.1 mm
d:Ph/Default/CutForPositron = 0.1 mm
```

Notably, the complexity of the chosen physics lists and the size of the cuts have varying computational demands. All the simulations were tested and executed on a single, quad core computer. As a consequence, a compromise between the combination of these settings were necessary: the number of modules and cuts were limited to those shown (lines 3-7).

5.3 Results

Simulations were run using TOPAS 3.2.p1 with a beam of 10 million protons and scored across the length of the water phantom to obtain a proton depth dose profile and corresponding LET_d values. The nozzle collimator and cap were removed in order to attain a pristine BP (Fig. 5.6). A phase space scorer was placed after the nozzle to determine the number of particles and the total transmission was found to be ∼5%.

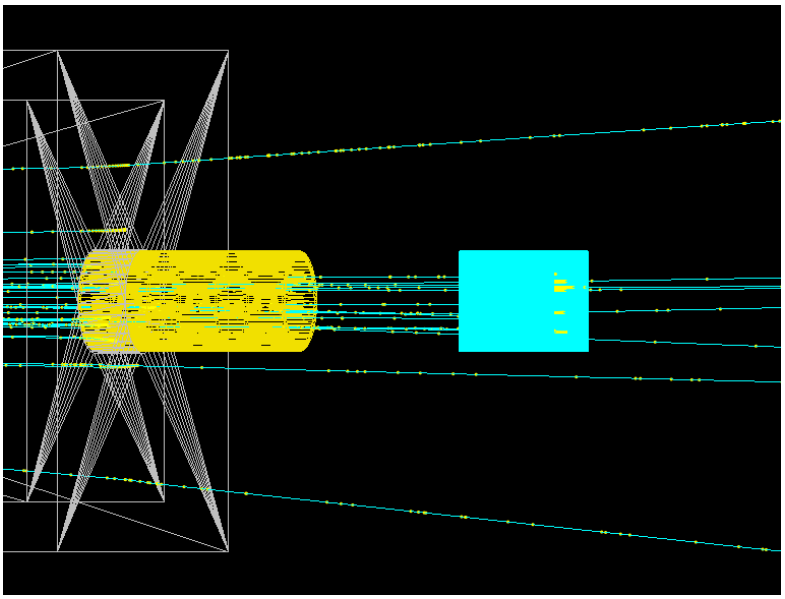

Figure 5.6: TOPAS visualisation of dose deposition in the phantom. Only protons (cyan) and neutrons (yellow) are visible.

5.3.1 Simulated CCC Dose Profile

The dose deposition was normalised to the maximum dose as the beam parameters for the QA measurement were not clear. The simulated BP and LET_d is compared against the measured CCC BP in Fig. 5.7.

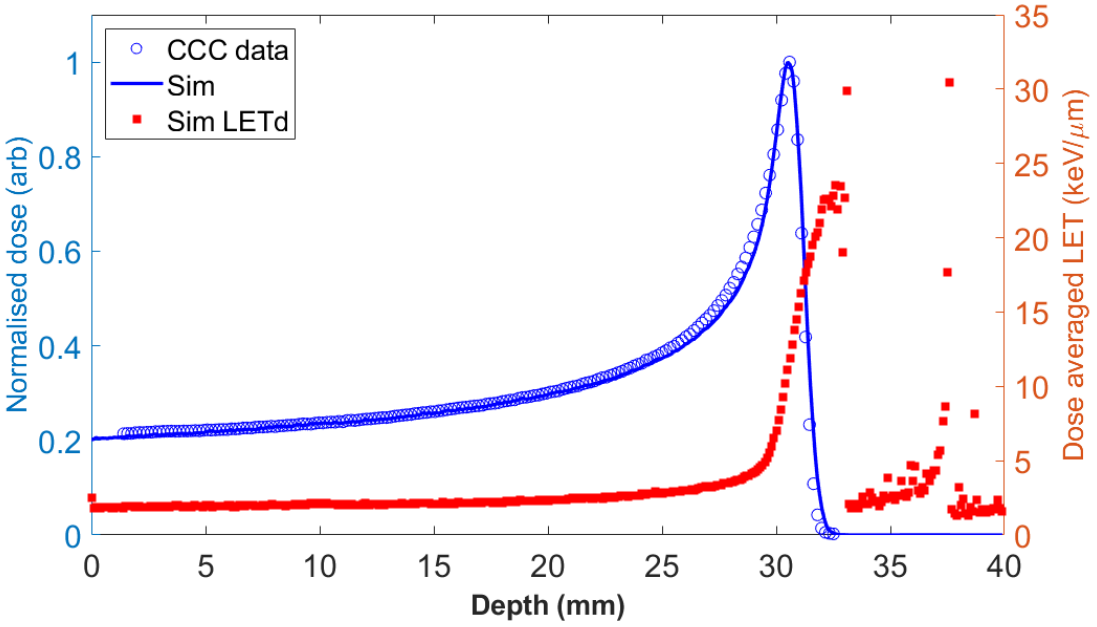

Figure 5.7: Simulated CCC BP and LET_d in water.

The maximum dose is observed at a depth of 30.59 mm for CCC and 30.50 mm with TOPAS. There is a slight margin of difference here as the CCC data was measured in graduations of 0.175 mm in depth. The entrance region agrees well however an under dose at the base of the BP is observed. Instead, the additional dose is displaced to the edge of the fall-off region where the simulated data is not as steep. These are both influenced by the shape of the peak, indicating minor differences in the energy characteristics of the input beam.

5.3.2 Transverse Beam Profiles

As discussed in Section 3.4, the distributions of the beam in transverse plane can illustrate the accuracy of the simulation model. Multiple pieces of EBT3 film were defined in the model (Fig. 5.8) with an area large enough to reproduce the majority of the beam distribution. The dose deposition was scored in 0.1 mm slices across the transverse x plane within a 28 µm sensitive (lucite) layer. Given the previously mentioned uncertainties with the beam current and computational limitations, 10 million primaries were simulated and normalised to the maximum dose for each film.

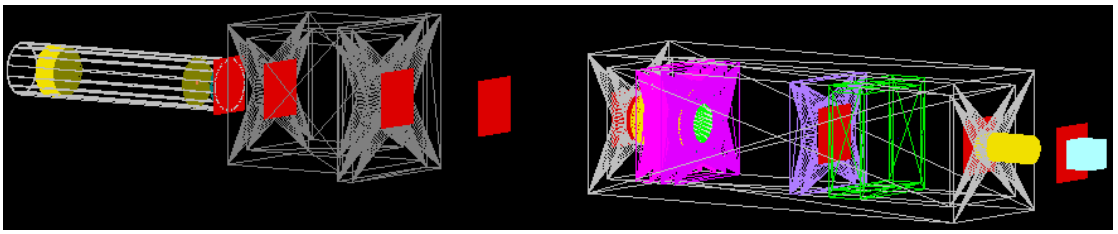

Figure 5.8: Eight pieces of EBT3 film (red) simulated in TOPAS to obtain transverse beam profiles in x.

The same film comparisons as Section 3.4.3 were made to examine the transverse beam distributions in the x plane at the eight locations (Fig. 3.16). Additional scaling and correction factors were applied to correct for the asymmetries and non-uniformities seen with the film. Comparative plots are included in Appendix B.24 and similarly, quantitative differences between the film and simulated beam profile FWHMs are shown in Table 5.1.

Table 5.1: Film and TOPAS simulated FWHM comparisons.

#	**Film** [mm]	**Simulation** [mm]	**Difference** [mm]	**Difference** [%]
1	12.05	10.40	-1.65	-13.66
2	14.05	14.20	0.15	1.03
3	22.86	23.20	0.34	1.49
6	29.73	30.80	1.07	3.61
4	37.42	40.80	3.38	9.02
8	43.49	53.20	9.71	22.34
5	51.45	63.60	12.15	23.62
7	43.45	38.20	-5.25	-12.09

The transverse profiles obtained with TOPAS have an improved agreement over GEANT4 and this is seen in the first 4 plots (Appendices B.24a-B.24d). The later positions have noisier data points (limited statistical number of particles) as the beam transmission decreases and as a result, each plot shows the simulated hits with a fitted curve to illustrate the general trend. Inconsistencies between the distributions are visible starting from film 4 (Appendix B.24e). From this location onward, the deviations between the simulated and film profiles start to propagate. At the next position (Appendix B.24f), the simulation still shows a dip in the central axis even after traversing through both the multi-layered dose monitors. The effect of this results in further scatter particularly along the higher dose regions and continues onto isocentre.

In contrast, this does not show up on the film, which has a rounded profile and is ∼22 mm smaller than the simulated FWHM. After passing through the tungsten cross-wires, a notch in the centre is present in the film which is inconsequential in the simulation. The beam then passes through the 43 mm collimator where it appears to converge at isocentre (Appendix B.24h). These deviations indicate that: inaccuracies in the simulation become magnified further downstream; the film measurements are susceptible to beamline variations and experimental conditions; dissimilarities with the beam distributions after the integration zone are related to the model.

The observed agreement at the beginning of the treatment line suggests that the input beam source parameters are applicable to a certain extent. However, this changes dramatically after the integration zone. As discussed in Section 3.3.4, variations in the parameters which describe the source will impact the beam distributions downstream; these are potentially magnified with the propagation distance as the beam is free to move through the air uninterrupted until it passes through the dose monitors. After this, the simulations register minimal effect and profiles still show the central dip from the beam stopper. On the other hand, the film shows a rounded profile with maximum dose centrally and a much smaller FWHM. This suggests that in reality, the dose monitors actually do have a more significant effect on the beam which hasn't been sufficiently modelled in the simulation. The differences in the shape at these downstream locations may also allude to differences in the geometry of the beamline at this point; the dosimetry box was enclosed and therefore access was physically restricted. Moreover, the dose monitors themselves are also difficult to model as they were developed at CCC and contain multiple layers and components.

A uniform and flat beam profile is expected at the isocentre however this was not obtained with the film or simulations: the slight decrease in the centre indicates that the quality on the day was not ideal. Uncertainties with this batch of film and analysis have been previously detailed in Section 3.4.3. Aberrations can be augmented especially at the points of high dose and the sensitivity of the film is exhibited after the cross-wires (Appendix B.24g). Additionally, at this point the large spread means the beam undergoes considerable collimation before it exits the nozzle and consequently, is still

converging at the isocentre. Some of these discrepancies may decrease with higher statistics by simulating much larger numbers of primaries and certainly also with verification measurements (see Section 4.4.1).

Nevertheless, it is inferred that these identified issues do not have any considerable significance on the resulting dose distribution: it is offset by the low beam transmission and prevalence of particles at the central axis. It is also very much dependent on the measured and on the day performance. However, in practice these beam deviations would be negated by clinical requirements and QA practices. As the simulation model has been matched to the CCC dose profile, simulated LET quantities achieved with the model were further examined.

5.4 Linear Energy Transfer

The LET is macroscopic quantity and is similar to the stopping power (Eqns. 2.1 and 2.2) however instead of the mean energy loss, it describes the energy deposited ($\mathrm{d}E$) by a particle per unit of its interaction track length ($\mathrm{d}l$) given in [keV/µm]:

$$LET = \frac{\mathrm{d}E}{\mathrm{d}l} \tag{5.1}$$

LET is synonymous with the restricted linear electronic stopping power as the energy deposited by the incident particle may produce secondary scattered electrons; these form individual tracks and carry sufficient energy for subsequent ionisations to occur further from the primary path. The restriction in this case refers to an omission of energy contributions from liberated electrons which have a greater initial kinetic energy than a specified threshold (i.e. 100 eV) [49]. This limits it to the local energy absorbed within the medium and is defined in terms of the energy rather than as a range cut-off.

LET is often used to describe the radiation quality of different RT modalities. It is a function of particle type where charged and heavier particles possess higher values resulting in a better possibility of inducing detrimental effects at a cellular level. Qualitative radiobiological differences in track structure and the lethality of lesions have been shown as related to the repair, fractionation, dose-rate and chemical modifiability

[190]. As dose is delivered primarily by the interaction of primary particles with electrons, a larger LET arises from a greater number of interaction events across the same path length. The increase in direct ionisation events and the concentration of interaction sites translates to significant damage to the cell nucleus: the enhanced relative biological effect seen in CPT.

In general, cell damage occurs due to direct or indirect action by single (SSB) or double strand breaks (DSB) within the double helical DNA structure. Single radiation tracks may induce SSBs which occur sparsely and can be easily repaired. In contrast, DSBs have a much lower possibility of repair due to the increased complexity, clustering and prevalence of errors during the repair process. The pattern and occurrence of these events is dependent on the LET: higher LET has been demonstrated experimentally to correlate to greater cell damage as the dense ionisations clusters are distributed inhomogeneously, causing multiple breaks which are more difficult to repair [21, 190].

For CPT and as also shown in Fig. 5.7, the LET remains relatively constant along the path of the particle towards the end of its range before increasing rapidly to a maximum and extending past the terminal end of the BP fall-off. The higher LET values associated with particle beams represent the radiobiological impact of the BP and possibility to achieve better treatment outcomes with PBT. However, LET is a quantity indicative of the track structure and the physical energy deposition: there are many complexities in defining a casual relationship with the biology and RBE effects [20, 191]. These are not discussed in this thesis however there are extensive studies which model the radiobiological effects for clinical applications of LET [192–196].

As such, several definitions of LET exist in order to adequately calculate and score the quantity either analytically or with MC methods [189, 197–202]. In practice, a particle beam is not monoenergetic and therefore the LET is averaged for the weighted dose contributions of individual particles. This is the dose-averaged LET ($\mathrm{LET_d}$) and can include contributions from both primary and secondary particles. $\mathrm{LET_d}$ is widely considered as an indicator of biological effects and has been examined for use in TPS [203]. As the $\mathrm{LET_d}$ can be obtained by MC simulations with TOPAS, it also provides a meaningful link to the radiobiological work performed at the CCC beamline.

5.4.1 LET Studies and Radiobiological Applications

As mentioned in Chapter 3, the CCC beamline has been simulated several times. In [204], a BP and SOBP was simulated under standard conditions at 6 positions to determine the LET and examine the RBE dependency as relevant for radiobiological cell studies (Table 5.2).

Table 5.2: LET values for studies performed in [204].

Positions	**Depth** [mm]	**LET** [keV/µm]
P1	1.69	1.11 ± 0.03
P2	28.21	4.02 ± 0.16
P3	29.28	7.0 ± 0.9
P4	29.76	11.9 ± 1.5
P5	30.24	18.0 ± 1.4
P6	30.72	22.6 ± 1.2

The scope of this work preceded what is currently being investigated with the beamline by the NWCR group [205–208] and similarly, one objective of the TOPAS model is to determine the LET_d for relevance in these studies. For comparison, the LET_d obtained with the TOPAS model and differences with the previous study are listed in Table 5.3. The uncertainty values are calculated based on interpolated deviations in depths.

Table 5.3: TOPAS simulated LET_d at corresponding experimental study depths.

Depth [mm]	**LET_d** [keV/µm]	**Difference** [keV/µm] (%)
1.70	2.34 ± 0.01	-1.23 (-111.82)
28.20	4.30 ± 0.01	-0.28 (-6.96)
29.30	6.14 ± 0.07	0.86 (12.29)
29.80	8.99 ± 0.28	2.91 (24.45)
30.20	12.13 ± 0.29	5.87 (32.61)
30.70	15.71 ± 0.12	6.89 (30.49)

The earlier work by [204] utilised a GEANT4 model which was based on the Hadrontherapy example [209] and adapted for the CCC beamline. The model was checked against ionisation and film measurements; the only major modification involved implementing the CCC modulation wheel specifications. The simulations were run with an input proton beam energy of 62 MeV and 0.3 MeV sigma. LET values were scored within a water

phantom using a standard approach (energy deposited in each step as a ratio of the step length) to determine the dose-weighted LET in each voxel[†]. This quantity is equivalent to the LET_d however values here are referred to as LET.

As this was essentially a different model with generic geometry and different beam parameters, it is reasonable that the obtained LET values would differ. On face value there is good similarity with the study's simulated LET and BP curve: LET values are within expected ranges (maximum at 25 keV/µm). However, at the small increments where the LET increases quickly (P3-P6 $\approx$ 29.30-30.70 mm), the deviation is clear as the positioning of the BP differs. It is also noted that TOPAS scores the LET using a more rigorous method: this would also result in differences to the achieved LET curve.

In Fig. 5.7 the BP falls off sharply and the dose is shown to drop back to 0 keV/µm at approximately 33.20 mm. After this point the LET (red markers) are inferred to be spurious due to low statistics but are included for completeness. Physically, negligible energy transfer would occur past this point and these points are thought to be a by-product of the simulation: presumably these would diminish if simulations were run with larger numbers of primaries.

Experiments to measure the LET spectra were pursued to provide an empirical value of the physical energy deposition as the TOPAS model can also determine the anticipated and corresponding LET values under the experimental conditions. However, these do not provide any information about the induced biological or chemical responses resulting in the measured biological outcomes or endpoints. In compliment, the NWCR group investigates the impact of proton irradiation under different LET conditions, assessing the DNA damage and repair mechanisms of different cell lines. Furthermore, by analysing the energy spectra and deposition, it is possible to establish relevance in this direction. This also facilitates further collaborative work to model DSB induction and damage as biological factors for application in treatment planning [210].

However, it is fundamentally difficult to measure the LET due to several performance requirements which exceed typical capabilities of commonly used methods of detection.

[†]Personal communications, S McMahon, 2018.

In particular, the position, charge and distribution of tracks deposited by individual particles must be able to be recorded rapidly and resolved with very high spatial resolution. Given the previous experiments with Medipix3 (see Section 3.4.4), the MiniPIX-Timepix imaging system[‡] was identified as a suitable device for measurements.

5.5 Experimental Measurements

5.5.1 The MiniPIX-Timepix Detector

The Timepix chip [211] was developed at CERN, proceeding from developments made by the Medipix Collaboration. Among other capabilities, the chip has a time-over-threshold (TOT) feature which allows individual events to be counted independently in each pixel according to their arrival times. The capacity of Timepix to measure LET has been demonstrated in different radiation environments [212–217] and techniques for application in ion beam therapy have been explored [218–221]. As such, this technology was utilised for measurements at the CCC clinical proton beamline to determine the LET and relevant quantities applicable for simulation studies and radiobiological work.

The MiniPIX-Timepix detector is a compact, hybrid semiconductor pixel detector which has a Timepix chip with a 300 µm thick silicon sensor, 55 µm pixels and a 14 × 14 mm^2 active area (Fig. 5.9). This encompasses a 256 × 256 pixel array with 65,536 independent channels and readout via USB at up to 45 frames per second (FPS). An approximately 1 mm aluminium slider covers the chip sensitive window [45].

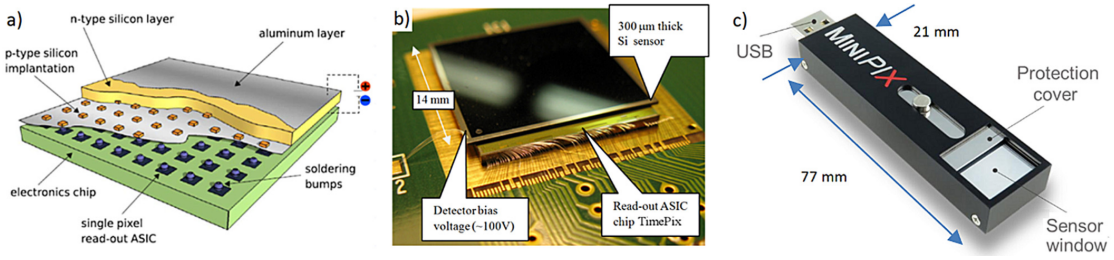

Figure 5.9: a) Labelled illustration and b) photo of the Timepix chip. c) Miniaturised MiniPIX-Timepix detector system [45].

[‡]Provided by collaborator Advacam s.r.o, Czech Republic.

5.5.2 Detector Setup

In order to securely support and rotate the detector, a 3D printed case was designed and built for attachment to a remotely controlled, motorised rotating stand (Fig. 5.10).

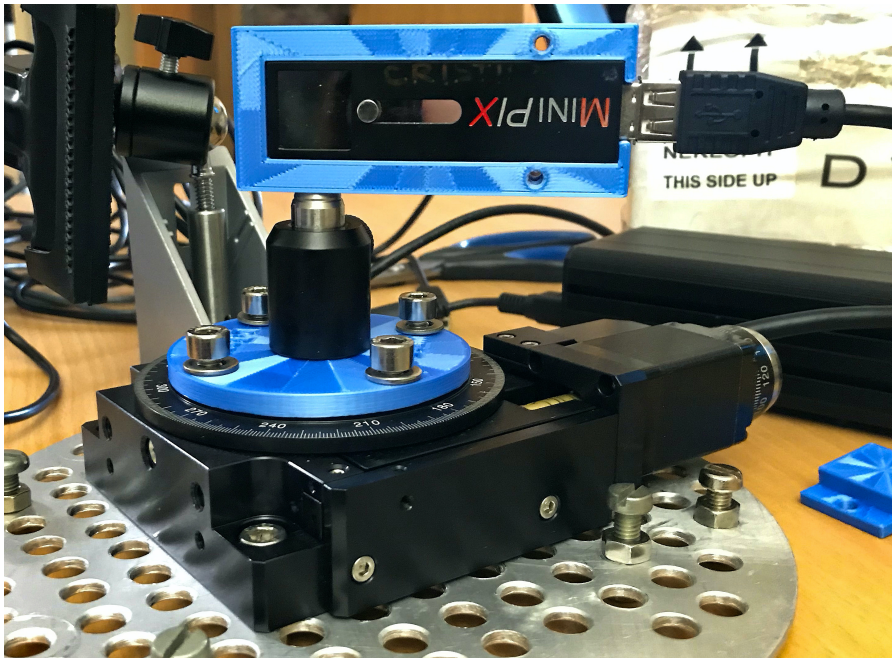

Figure 5.10: The MiniPIX-Timepix detector casing (blue), the centre of the chip is positioned at the the origin of the rotational axis. The stand is affixed to a metal plate and was clamped into position to the upper fixtures of the treatment chair.

At CCC, typical treatment beam settings achieve flux rates of up to 10^{10} protons/s however MiniPIX operates optimally within a range in the orders of 10^3-10^4 protons/s/cm^2 and an upper limit of $\sim 10^6$ protons/s/cm^2. As several beam current related challenges were encountered during the Medipix3 measurements (see Chapter 3), the beam current needed to be heavily reduced to prevent damage to the sensor. As it was uncertain if this could be done reliably with the cyclotron, preliminary simulations were necessary to gauge an alternative approach.

As seen previously, the lowest approximate beam current achieved at CCC was 0.012 nA, corresponding to $\sim 7.5 \times 10^7$ protons/s. The beam current (event/s) detected by Medipix3 was used to calculate the fluence specifically for the MiniPIX sensor area at each current (Table 5.4).

Table 5.4: Estimated proton fluence rates for MiniPIX at CCC

Current [nA]	**Fluence** [Protons/s/cm^2]
0.012	3.82×10^7
0.052	1.66×10^8
0.350	1.11×10^9
0.690	2.20×10^9
1.350	4.30×10^9
1.970	6.27×10^9

Therefore a reduction by an order of at least 10^3 protons/s is necessary. As simulation results were demonstrated to trend linearly based on the number of primaries (see Chapter 3), various conditions were simulated with up to 200,000 initial protons. Some common solutions include using a target, filter or mesh placed between the beam and sensor. In this case, secondaries produced with the high intensity beam are detected. An alternative method is to directly reduce the flux by decreasing the beam transmission and hence the number of protons which reach the detector. This could be done by restricting the passage of the beam with small apertured collimators and metal (high Z material) shielding to limit the particle transmission. The different methods were simulated at an arbitrary distance of 30 cm after the nozzle, based on equipment which could be sourced for the experiment given short notice. The lead disc was found to be most effective and the calculated decreases to the beam fluence are listed below in Table 5.5.

Table 5.5: Relative reductions in beam transmission using different filters. The transmission for the no filter case is relative to the fluence directly after the nozzle.

Filter type	**Fluence** [Protons/s/cm^2]	**Transmission** [%]	**Reduction** [%]
None	1.58×10^6	92.98	7.02
Cu foil (0.1 mm thick)	1.26×10^6	80.15	19.85
Steel grid (0.4 mm diameter wires)	1.06×10^6	67.31	32.69
Steel grid (1 mm diameter wires)	9.28×10^5	58.81	41.19
Pb disc (2 mm thick, 250 µm pinhole)	1.57×10^5	9.93	90.07

In addition, multiple solid water absorbers of varying thicknesses were implemented in the simulation to determine the expected proton BP depths necessary to shift the peak relative to the sensor location. This identified the approximate range of PMMA block thicknesses needed to be able to measure along the BP. As the objective was to examine the LET spectra, the LET_d was also scored along the full range as an indication of predicted measurements.

5.5.3 Beam Measurements

The MiniPIX system was placed roughly 16 cm from the patient collimator and firstly aligned perpendicular to the propagation direction of the beam. The first few runs (# 0-2) were performed using a 1 mm diameter nozzle brass collimator and a 2 mm thick sheet of lead with a 200 µm diameter pinhole placed in front of the detector (Appendix B.40). Adjustments were then made with the accelerator to reduce the flux by several orders of magnitude to within the acceptable operational range ($\sim 10^3$-10^4) and to stabilise the beam. Following this, the collimator was retained and the detector was rotated at an angle of 45° to the beam. Data was firstly taken over different acquisition times to select the appropriate settings before the different PMMA blocks were inserted directly upstream of the sensor (Fig. 5.11).

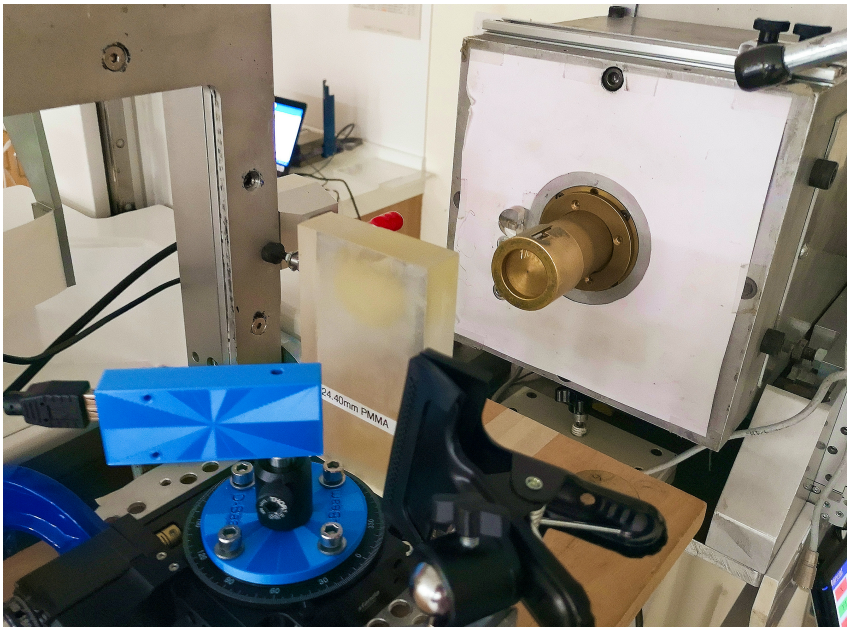

Figure 5.11: The MiniPIX-Timepix system angled at 45° with a 24.4 mm PMMA block to shift the pristine BP onto the sensor.

Having a tilted plane with an incidence angle of >45° has been demonstrated [45] to increase the track acceptance. Therefore, measurements were also performed with the detector angled at 60° in the perpendicular plane. Additional measurements to acquire levels of background radiation were also taken (B1-B4). Statistical data and a description of each run for both angles is provided in Tables 5.6 and 5.7.

Table 5.6: Runs at 45°

Run (#)	**Pb sheet**	**PMMA** (mm)	**Acquisition time** (secs)	**Numbers of clusters**	**Cluster rate** (clusters/s)
0	Yes	0	59.66	2623	550.30
			118.68	4922	252.50
			197.95	4915	656.00
1	Yes	24.40	99.80	79	86.74
2	Yes	20.10	58.44	147	167.40
3	No	24.40	58.44	2609	505.90
			58.44	3445	581.10
4	No	25.48	58.44	2270	460.30
			60.81	1682	433.20
5	No	26.40	58.44	179	203.90
6	No	25.87	58.44	569	288.70
			58.44	569	294.30
7	No	20.10	68.07	7277	909.30
8	No	10.00	131.35	9440	693.90
B1	No		131.25	63	59.26
B2	No		95.26	48	56.60

Table 5.7: Runs at 60°

Run (#)	**PMMA** (mm)	**Acquisition time** (secs)	**Numbers of clusters**	**Cluster rate** (clusters/s)
0	25.48	39.70	86	126.40
		58.44	344	259.20
		90.28	294	201.10
1	24.40	58.44	5325	763.10
2	10.00	58.44	21610	1341.00
B3		43.56	21	55.46
B4		254.58	130	52.24

Measurements were recorded in real time using the Advacam PIXET [222] software. An initial digitisation test showed 0 dead pixels and a recommended bias of 30 V was applied with a frame acquisition time of 10 ms. A visual check is sufficient to ensure that the chosen frame rate is suitable (single tracks appear): if this is too short, the particles are not able to deposit sufficient charge and the detector will register incomplete tracks. The bias threshold is arbitrary as it correlates to some detector specific factor responsible for converting the charge to energy; this is a non-linear relationship and is accounted for in the acquisition software. Data was taken for similar total acquisition times for each run, mainly to acquire adequate statistics. Cluster files reported global frame times every ∼30 ms: this consists of the 10 ms open shutter time with the remaining as dead time for readout (closed shutter), approximating a data capture rate of 33 FPS.

During the 45° runs, online visuals of the hits and cluster statistics indicated the most significant depths. It is difficult to substantiate this from only the cluster statistics (Tables 5.6 and 5.7) as these quantities do not distinguish the different particle types: a larger cluster rate at the fall-off may indicate more secondaries present rather than primary protons. However, there is a clear overall decrease in numbers of clusters with depth and the highest cluster rate is achieved at 24.40 mm which is approximately at the BP. Sudden stringent time limitations meant fewer measurements were possible for the second set of runs and therefore the 60° runs focused on three different depths for comparison. Similar trends in the cluster rates for both angled cases can also be seen. Given these observations, the following was deduced for the different PMMA blocks:

- 10.00 mm: Entrance region
- 20.10 mm: Build-up region
- 24.40 mm: At BP
- 25.48 mm: Just after BP
- 25.87 mm: Beginning of fall-off
- 26.40 mm: Distal fall off

5.5.4 Results

Log files were processed with Advacam proprietary tools to generate different metrics (i.e. energy deposited, track sizes, angle etc.) for the distributions of recorded events

for each run and stored as cluster lists. The program also enabled hits to be visualised as integrated over all frames (Fig. 5.12a) or for a specific frame (Fig. 5.12b). These events are recorded as the charge deposited from individual particles produce hits across multiple pixels and this recruitment of several pixels are termed as '*clusters*'. The software applies pattern recognition and clustering algorithms to resolve pixel clusters based on morphology, spectral and other parameters [220]. Different in-built tools allow further online or offline processing. The numbers and rate of clusters obtained from the post measurement analysis for each run are also presented in Tables 5.6 and 5.7.

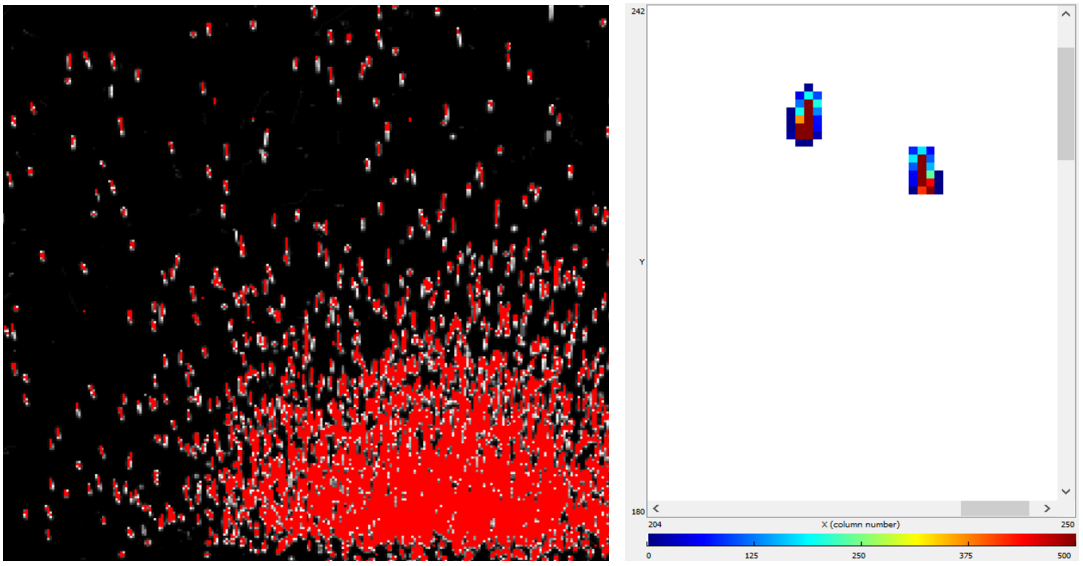

(a) (b)

Figure 5.12: Run 3 repeat, 24.40 mm at 45° a) Track visualisation of all accumulated events. The hits accumulate in the bottom right corner as the sensor was not centred with respect to the beam axis. b) Two clusters in a single frame are displayed showing pixel position and normalised charge.

The detector can image single radiation tracks in high resolution with 100% collection efficiency from the size of the pixel (55 µm) to the sensor thickness (300 µm), given the tilt angle. This position and directional tracking capability combined with the timing and the energy detection for each pixel, enables wide ranging measurements to characterise the beam and radiation field. Given this information, the program can determine particle specific properties including the type, energy loss, LET (0.1 to >100 keV/µm), track mapping and also beam related properties (profile, flux, dose rates etc.). How this is incorporated and analysed by the software is detailed in [45]. For our purposes only the

properties related to the LET spectra were considered: energy loss, elevation angle and 3D path length. Resulting graphs generated by the Pixet proprietary software[‡] show the main cluster properties. The cluster height shows the distribution of the highest energies deposited per pixel, the volume is the deposited energy summed for all pixels in a cluster and the area indicates the number of pixels recruited. For example, plots for both angles at 10.00 mm are shown in Fig. 5.13.

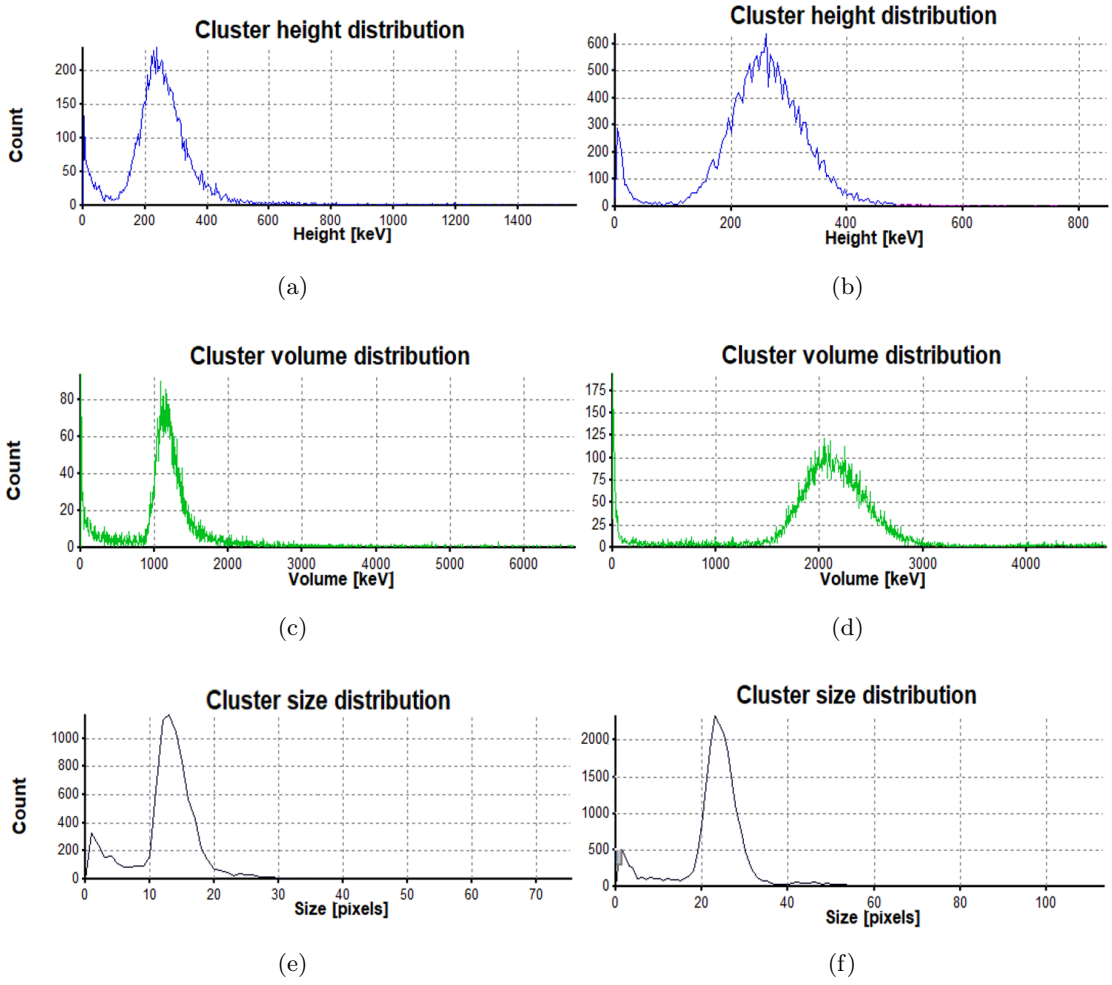

Figure 5.13: Cluster distributions at 10.00 mm for 45° (left) and 60° (right). a, b) Largest deposited energy per pixel. c, d) Energy summed over a cluster. e, f) Cluster area. Note the different axis scales.

Plots for the 24.40 mm case are shown in Fig. 5.14. Similar scaling differences for each cluster property can be seen consistently at both depths and between the different angled cases. In general, a larger sensitive area is exposed as the change by 15° increases the effective depth of the sensor and probability of detecting longer tracks.

[‡]Data and graphs were provided by C Oancea, 2019.

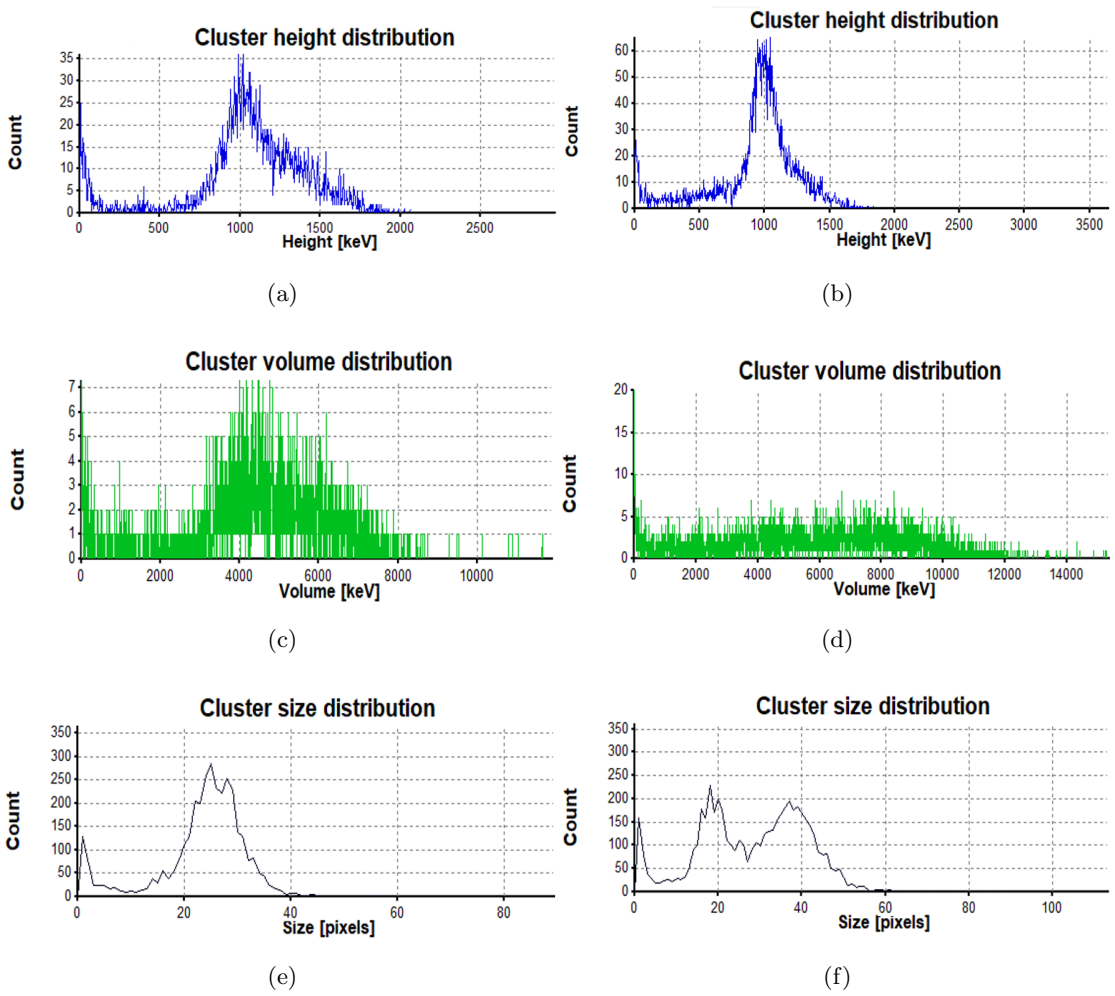

Figure 5.14: Cluster distributions at 24.40 mm for 45° (left) and 60° (right). a, b) Largest deposited energy per pixel. c, d) Energy summed over a cluster. e, f) Cluster area.

Due to the greater statistics of clusters depositing larger amounts of charge, the depth at this position is estimated to correspond to just before the BP. Higher energy levels with a much bigger range of energy per cluster and a multi-peaked distribution of cluster sizes is observed. In particular for the 60° case (Fig. 5.14f), the double peaks at 20 and 40 pixels indicate that the detector has recorded multiple particles resulting in an overlapping of tracks and an artificial increase in the cluster sizes. A peak at the lower end of the spectrum is also evident. This is due to the presence of the aluminium slider which was kept closed as a protective measure initially however remained shut for the remainder of the measurements. Deeper cluster analysis would require technical manipulation of the software and is outside the scope of this thesis. Nonetheless, the LET could be determined using Eq. 5.1 by evaluating the cluster lists and taking the

cluster volume (energy deposition, dE) and cluster size (track length, dl) distributions. As the tracks can be recorded in any orientation, the path length was calculated given the directional angle of the incident track and the measured projected length (Fig. 5.15). The measured energy and calculated LET spectra at each depth for both angles are included in Appendices B.42-B.45 for reference.

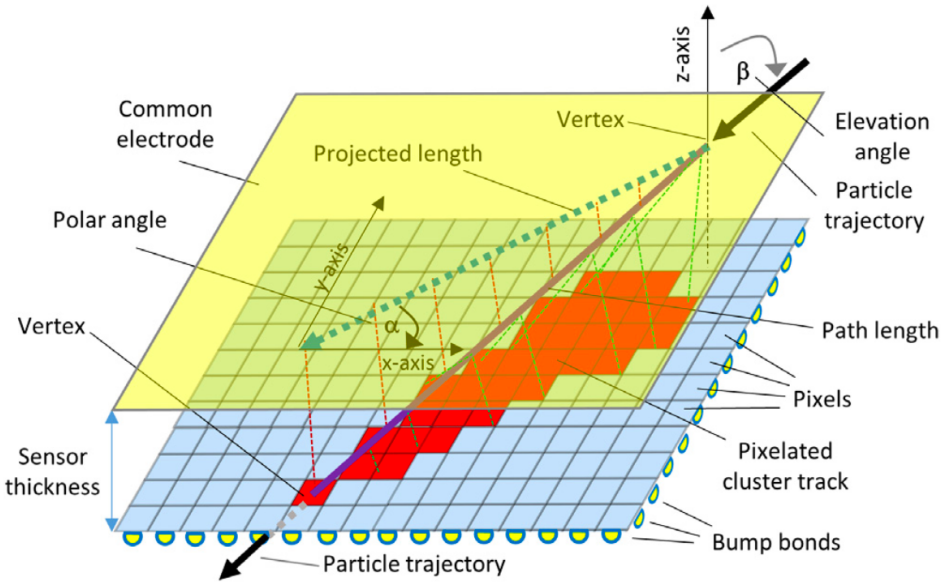

Figure 5.15: Sketch illustrating the particle track parameters and recruitment of pixels. These metrics are used for cluster and morphological identification to resolve different particle properties [220].

Simulation Results

The geometry of the silicon sensor (with aluminium slider) along with the blocks of PMMA were built in the TOPAS model described earlier in the chapter, to simulate the exact experimental conditions for direct comparison with measured results. As only a small number of particles ultimately reach the sensor due to low transmission, a phase space scorer was implemented after the nozzle. This resulted in an output file of ~1 million histories, showing a Gaussian beam with mean energy and spread of 60.04 MeV and 0.48 MeV, respectively. A large number of histories are needed for adequate statistics to replicate the experiment. As the phase space information sufficiently defines each proton, was subsequently used as the particle source to reduce the computational demand. All simulations were performed on a system consisting of 23 CPUs at the University of Oxford. The achieved LET values and related quantities[‡] are presented

[‡]Additional analysis and simulation results were provided by M Brooke.

here however specific details and further application of these for radiobiological modelling can be found in [210]. As only the LET was considered for this work, the empirical LET spectra was resolved from the provided cluster lists and compared directly with simulations.

The ProtonLET scorer was used to obtain the $\mathrm{LET_d}$ in bins of $28 \times 28 \times 784$ (in x, y and z) to represent the silicon sensor. These were chosen as smaller bins demand an increased computational load. As cluster sizes did not exceed ∼40 pixels, these would correspond to an approximate resolution of a single cluster per bin, therefore providing suitable statistics for comparison. For the measured energy spectra, the detected energies required further processing from the cluster volumes. The kinetic energies of each simulated particle were used to interpolate stopping powers and were multiplied by the median measured track lengths to determine the energy deposition within the sensor. The simulated energy spectra are compared with empirical data and this is also included for reference in Appendix B.46.

As the aluminium slider introduced another attenuating layer in addition to the various PMMA blocks used, the water equivalent thickness (WET) was determined as a more precise indicator of the depths. The angular rotation of the detector also resulted in a change to the WET which provided additional depth measurements: all corresponding values are listed in Table 5.8. The cases where particles have undergone almost complete energy loss and are absorbed by the material have a designated WET of ∞.

Table 5.8: Experimental conditions and calculated WET for simulations

Detector angle [°]	**PMMA thickness** [mm]	**Al shielding thickness** [mm]	**WET** [mm]
45	10.00	1.4	14.42
45	20.10	1.4	26.00
45	24.40	1.4	30.87
45	25.48	1.4	31.96
45	25.87	1.4	∞
45	26.40	1.4	∞
60	10.00	2.0	15.64
60	24.40	2.0	32.00
60	25.87	2.0	∞

Therefore, the irradiations covered a wide range of depths to examine the LET_d, particularly around the BP region. As both the simulated and empirical results (Appendices B.44-B.45) demonstrate a spectrum of LET values at each depth, a median or average metric representative of the distribution was determined. The mode, most probable value (MPV), a Landau distribution or other fits were chosen according to which suited the data best in order to obtain a singular LET value. These are discussed in more detail in [210] however the applicable MPVs were provided and are presented below in Fig. 5.16. The simulated dose deposition and the LET_d are also plotted for reference; these were scored in a smaller water phantom of $35 \times 35 \times 35$ mm^3. Only the error bars for the phantom case are included which indicate the variance as reported by TOPAS and the spread of values across the LET spectra are shown in Appendix B.41.

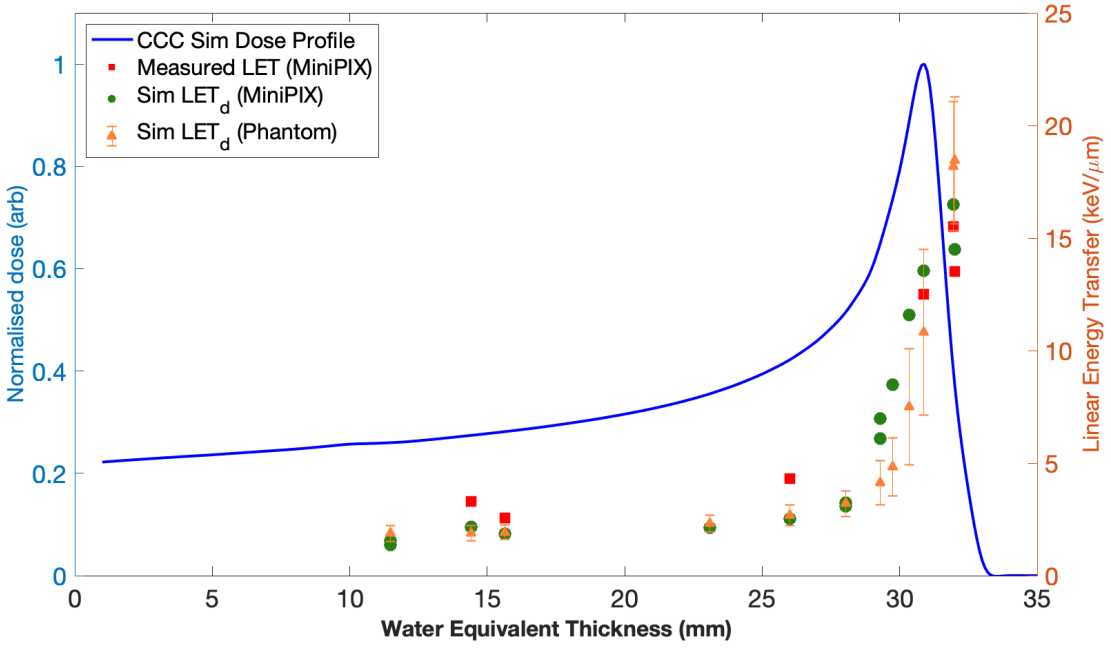

Figure 5.16: Measured and simulated dose averaged LET at the corresponding WET, with the CCC dose profile across a 35 mm depth.

For all cases, the linear energy transfer is maintained below approximately 3 keV/µm before showing a clear upward trend from the BP build-up region to the distal fall-off. This is expected as the increases in the density of ionisation and nuclear interactions cause the protons to slow dramatically; the transfer of energies to secondary particles result in high deposition events in short ranges as demonstrated by the steep rise at the BP. An LET of ∼12 keV/µm is obtained at the BP. This extends past the peak where

the fluence rapidly reduces as protons deposit the majority of their energy downstream, achieving maximum LET values between 13.5-18.2 keV/µm. Larger errors are observed at the fall-off due to statistical fluctuations and the departure of primaries which generate electrons or other secondary particles: these are scattered with a wide range of energies and path lengths. After this point all particles have undergone complete energy loss resulting in no further LET.

The plot shows good agreement for the simulated LET_d cases, particularly at depths before the build-up region. However, as the number of interaction events increase, the LET becomes more difficult to model and the deviation between the data sets is clear. At the BP, the simulated and measured MiniPIX LET values are greater than for the reference phantom, except at 32 mm where they are partly contained within the uncertainty range. The distribution of measurements (Appendices B.42-B.43) are also observed to be skewed to lower energies in comparison to simulations (Appendix B.46), hence corresponding to smaller empirical LET values. However, it is also noted that at this terminal end, the number of simulated particles and recorded MiniPIX events were likely to have been statistically insufficient.

In contrast, in the plateau region before the BP, the empirical data has tended to overestimate the LET. This is largely attributed to the presence of the aluminium slider, complexities with the analysis and retrieving reliable information from the provided cluster files. For example, overlapping events recorded by the detector produced multiple peaks in the cluster distributions for runs with PMMA larger than 24.40 mm. This results in an increase in the range of track lengths and also the variance in the deposited energy per cluster, therefore a greater spread in the energy deposition (Appendix B.46). Further evaluation was necessary to determine the measured energies however an approach to filter the artificial peaks were not pursued. If ideal measurements were attained with the experiment, it is expected that they would agree more closely with the simulated case. It is also thought that the empirical LET values may correspond better if the energy depositions were calculated using the same approach as the simulated LET_d i.e. dose averaged.

Furthermore, the simulated MiniPIX LET is expected to differ from the water phantom LET_d as the experimental setup is inherently different to the reference case. This is due to the presence of the aluminium slider, differences between the physical properties of the absorbing medium and the geometry of the scorers. The bin (voxel) sizes effectively moderate the track lengths and the ProtonLET method averages the energy deposition across this length to overcome this.

In general, the ranging distributions for the different cluster metrics obtained with these measurements were not ideal. It is also unclear if limitations with preparation and beam calibration had a significant effect on device performance: it is expected that the distributions would approach better consistency given increased exposure and counts. The protective aluminium slider also introduced several additional considerations however was implemented in TOPAS to accurately simulate the experimental conditions. The runs at a 60° tilt also provided additional measurement depths and slight differences between the cases occur at the depths corresponding to the BP and fall-off. Nevertheless, the measured LET values are shown to be within expected ranges and correlate well with the simulated data.

5.6 Summary

An improved model of the CCC treatment beamline was redeveloped entirely in TOPAS to provide a more accessible simulation platform for future users of the facility and also to facilitate further applications for radiobiological modelling. The model builds off progress made with GEANT4 described in Chapter 3 and utilises beam information determined by optical modelling in Chapter 4. CAD imports into TOPAS enable highly realistic geometries to be built, representing the actual CCC treatment delivery components. Transverse beam profiles were generated and compared to film measurements, showing an improvement from the previous model. Differences observed are largely due to the beam quality during the film irradiations and potential effects from disparities in modelling components within the dose monitors and dosimetry box. Nevertheless, the dose profile was matched to CCC to simulate the LET_d, providing a parameter for correlation with radiobiological applications.

Experiments were performed with a MiniPIX-Timepix detector to determine the LET at different depths along the BP, using PMMA blocks of various thicknesses. Detector measurements yielded distributions of cluster properties, where the energy spectra and track lengths were evaluated to calculate the LET. The experimental conditions were implemented in the TOPAS model and simulated quantities were compared to detector measurements. General agreement was shown, supporting the validity of the model. These results establish the possibility of utilising the MiniPIX detector and CCC TOPAS model to determine quantities to resolve the linear energy transfer. The outcomes of these studies demonstrate the capabilities of the TOPAS model to accurately simulate the CCC beam.

Chapter 6

VELO Beam Monitor Measurements

The LHCb VELO detector modules were developed into an online beam monitoring system for application in ion beam therapy beamlines. The standalone system was originally adapted for implementation into the CCC facility; beam characterisation and simulation studies were discussed in Chapter 3. In order to investigate the technical capabilities of the detectors and optimise the system for clinical environments, experimental measurements are necessary.

Following recent upgrades to the hardware and software, tests were performed at the University of Birmingham (UoB) which demonstrated for the first time, the functionality of the monitoring system in a medical proton beamline. This chapter overviews the UoB facility, system developments and the experimental campaign. Similar to work in previous chapters, beam measurements were performed and results were compared to EBT3 film and simulation modelling done in GEANT4. The benefits of the VELO system and further opportunities for development are also discussed.

6.1 University of Birmingham Beamline

UoB operates a proton beamline which is mostly used for radioisotope production for medical applications but also supports testing of equipment for various research and commercial purposes. The facility operates a Scanditronix MC40 medical cyclotron, capable of producing a range of particle species at currents from tens of fA to µA at high fluence rates, ideal for testing of electronics and sensors. The facility has been running since 2004; the beam has been characterised and there are several dosimetry and diagnostics systems in place [223]. A switching magnet downstream of the cyclotron allows the beam to be extracted and transported to multiple rooms. For our measurements, the detector system was positioned in the main '*Medical and Nuclear Physics (UOB)*' room adjacent to the cyclotron vault (Fig. 6.1).

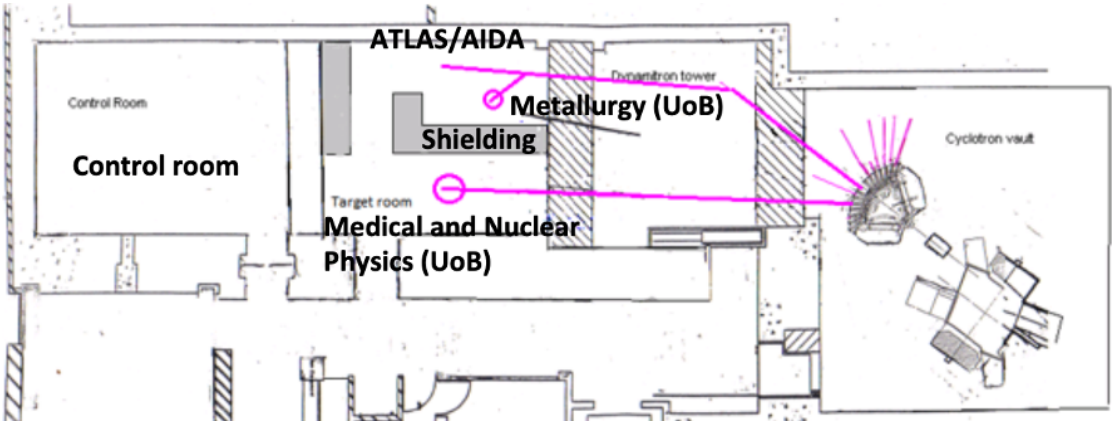

Figure 6.1: Layout of the University of Birmingham facility. Multiple particle species are generated with the MC40 cyclotron and transported across multiple beamlines [223].

6.2 Experimental Method

The entire VELO system was brought to UoB and measurements were performed over the course of 5 days (Fig. 6.2). Set-up and preparations were done in the first two days with running beamtime over the remaining 3 days. Further technical details of the measurements are described in [129] however a summary of the overall experiment is outlined. The objectives of the campaign were primarily: to test the response of the detectors in a proton environment, verify the changes to the synchronised readout scheme and acquire data for different beam currents and sizes.

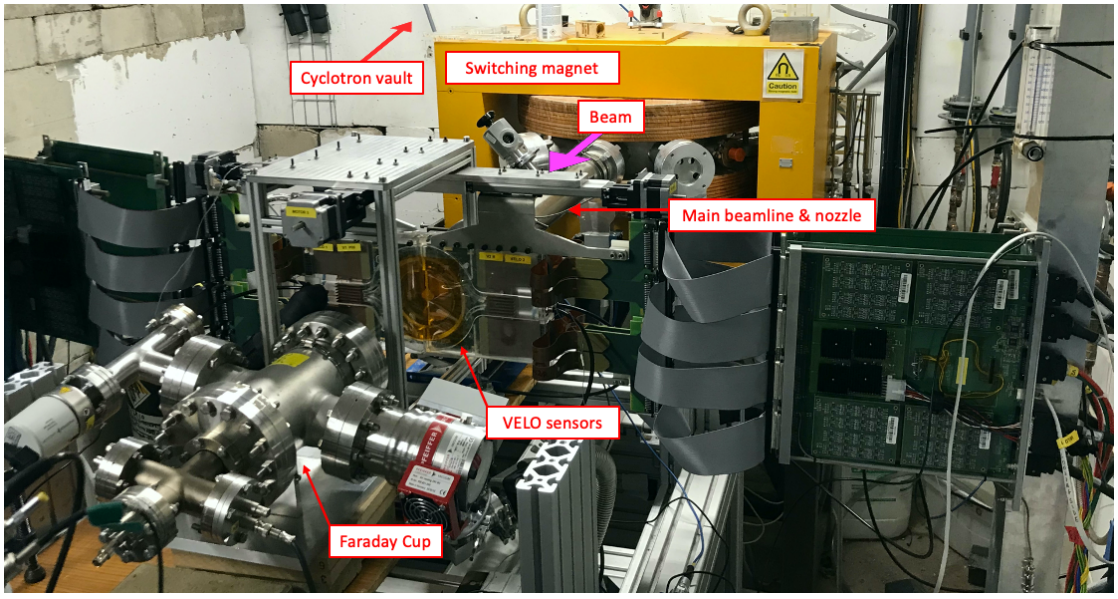

Figure 6.2: Beam monitor positioned after the main beamline nozzle with sensor modules perpendicular to beam propagation direction. The beam originates from the cyclotron vault behind the wall, transported through the switching magnet. Downstream, a faraday cup is aligned to the capture the beam passing between the detector modules.

Details and specifications of the VELO monitor have been previously described in Section 2.3.3 but for relevance to the experiment, key attributes are mentioned. The VELO modules are counting detectors and similar to Medipix3, provide an instantaneous recording of hits by individual particles. An ionisation chamber within the beamline was connected to an electrometer to cross-correlate absolute charge measurements with the monitor. The recent system improvements mainly enable data collection processes to be adjusted for the parameters of different facilities: the Keysight 8110A pulse generator was added as an injected external trigger and the readout software was also updated to enable simultaneous acquisition of data. As the RF frequency of clinical accelerators differ from the LHC bunch crossing frequency, this allows VELO to trigger and collect data in synchronisation with proton bunches at any RF.

To firstly optimise the proton bunches with the data acquisition and readout timing, several 'phase scan' runs were performed at the start of each day. Added delays between 0-40 ns were set with the pulse generator and the total accumulated hits for both modules were recorded. The delay time with the highest number of hits was implemented with the trigger for all the measurements (i.e. 22.5 s and 7.5 s). As encountered at CCC, beam losses due to RF dropouts also occurred and phase scans were repeated to resynchronise

the system. In addition, a phase scan was unable to be performed for the first day as it was discovered that the cyclotron RF frequency (22 MHz) exceeded the upper acceptable limit for the pulse generator. Therefore, the external trigger could not be used to synchronise the data acquisition. As such, the beam energy was decreased from 28 MeV to 18 MeV for the remaining days as the corresponding 18.21 MHz RF frequency is below the 20 MHz scope threshold.

Measurements were taken at varying beam currents, sizes and sensor positions. The VELO modules were translated longitudinally in the z-axis and laterally in the x-axis. The size of the beam was modified by using interchangeable collimators with different diameters, placed on the end of the beam nozzle. The diameters were chosen to restrict the beam distribution such that it would pass straight through the aperture between both sensors without interference. Experimental parameters for days 2 and 3 are listed in Table 6.1; beam currents are later converted to absolute beam intensity measurements. A larger range is listed for day 3 as the holder which physically supported the scattering foil in the beam transport line, melted after the last set of measurements on day 2. This resulted in significant changes to the beam quality as the beam had to be enlarged to practical sizes by the optics. The adjustments to the magnets resulted in a distorted, non-Gaussian beam for day 3. The ion chamber was moved and placed downstream, in front of the modules (Fig. 6.3).

Table 6.1: Measurement conditions with 18 MeV protons.

Parameter	**Day 2**	**Day 3**
Collimator diameter [mm]	7, 10, 15	7, 10, 15
Beam current [nA]	0.5, 1, 2, 3, 4, 5, 6	1.75, 3.5, 7, 10.5, 14, 17.5, 21
Sensor position in x [mm]	0, 4, 8	0, 4, 8
Sensor position in z [cm]	0	6, 12

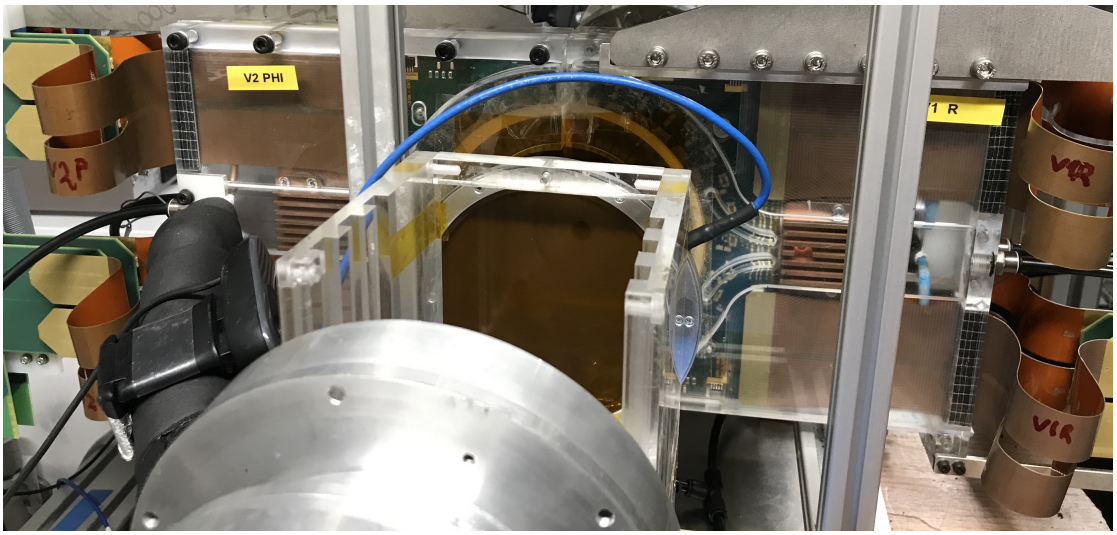

Figure 6.3: Facing outward from the nozzle, the beam passes through an ion chamber before the detector modules.

6.2.1 Film Measurements

In order to correlate the hits recorded by the detector modules, the divergence and distribution of the beam must be well known. This was performed using two comparative methods: film and simulations. 5 pieces of film were placed on the downstream face of the ion chamber (Fig. 6.3) and were simultaneously irradiated to determine the transverse beam profiles (Fig. 6.4).

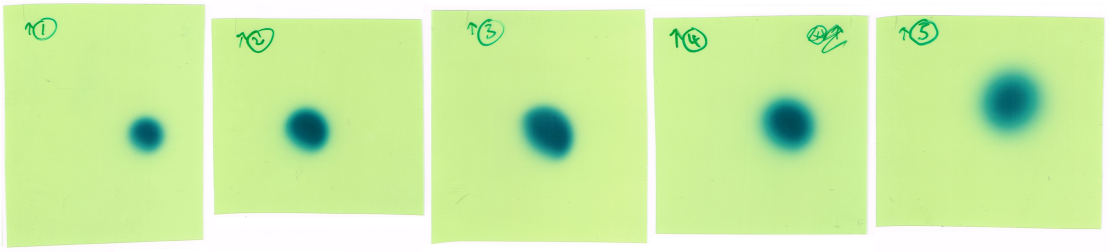

Figure 6.4: Irradiated film from day 3, from left to right: 7 mm, 10 mm, 15 mm and 10 mm at $z = 6$, 12 cm. Beam spots are non-Gaussian due to the removal of the scattering foil.

A calibration set was provided afterwards and a calibration curve was generated (Appendix. B.25). Large error bars are noted due to the large variations in pixel intensities. Slight changes were also applied to accommodate differences with the film and scanner properties in the Matlab script (Appendix C.1). Nevertheless, given the standard analysis procedure described in Section 3.4.2, transverse beam profiles were determined for

each film. The FWHM and area coverage was also determined and these are all included in Appendices B.26-B.30.

The non-uniformity of the beam distributions proved difficult to analyse as taking the ROI across the central third was not equivalent for each beam spot. A smearing effect can be seen (Fig. 6.4) and this reduction in the beam quality appears as a jagged edge on the top of the dose distributions (Appendices B.26-B.30). A Gaussian curve has been fitted to each plot and the area underneath calculated for each half. These also indicate the proportion of the rotation of the beam ellipse in the perpendicular plane and the FWHM provides an indication of the beam width. The beam does diverge, as shown by the differences between the evaluated FWHM and the collimator diameter: it is clear that greater distances along the propagation direction result in a larger beam width. For our applications, the halo is defined as anything peripheral to the distance between the two opposing modules, assigned as 16 mm. The calculated area allows for evaluation of the integral dose, which can be further correlated to density maps of the transverse profile. For now, measurements along the radial axis are only considered and compared later to the R-sensor hits.

Due to the irregularities and non-uniformities, it is difficult to accurately evaluate the beam profiles for this case. Further analysis and better beam modelling would be needed in order to correlate these distributions with measurements. Given this, additional irradiations were performed later on by collaborators once the scattering foil could be used again. Film measurements were repeated to reproduce a standard beam with the same 7, 10 and 15 mm collimator sizes as day 2 (Fig. 6.5).

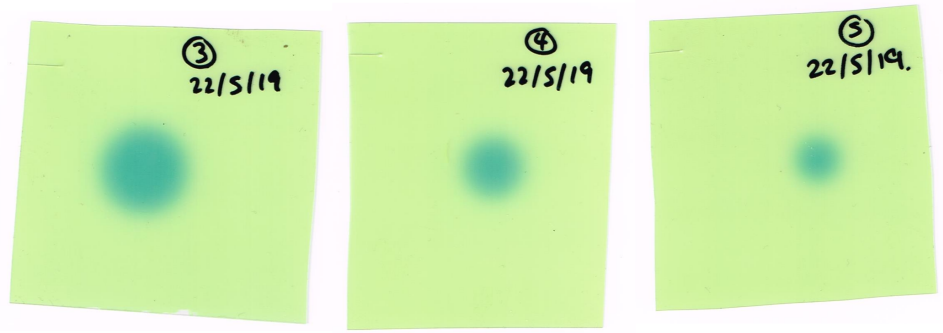

Figure 6.5: Irradiated film for day 2 measurements with varying collimators from left to right: 15 mm, 10 mm and 7 mm.

Additional plots of the profiles, FWHM and dose coverage were determined (Appendices B.31-B.33). These beam profiles are more homogenous. As it is dependent on the beam quality and conditions on the day, there are clear improvements from the previous (day 3) batch of film. Additionally, these have a smaller penumbra on both sides and the low dose tails are not present. Non-uniformities appear again at the peaks, also caused by the uncertainties in the calibration and OD conversion: the lower doses are minimised and the higher doses are augmented by the calibration fit. Nevertheless, the most significant regions are along each side of the beam profiles and comparisons to the hits recorded by the detector are reported later.

6.2.2 GEANT4 Simulation

In order to benchmark both the EBT3 film beam profiles and the hits measured by the detector, the beam was simulated using a validated model of the transport line[‡] with realistic beam parameters in GEANT4 (Fig. 6.6). Parts of the source code were amended and adapted for the requirements of this study and simulations were executed on the same computer (as in Chapter 5).

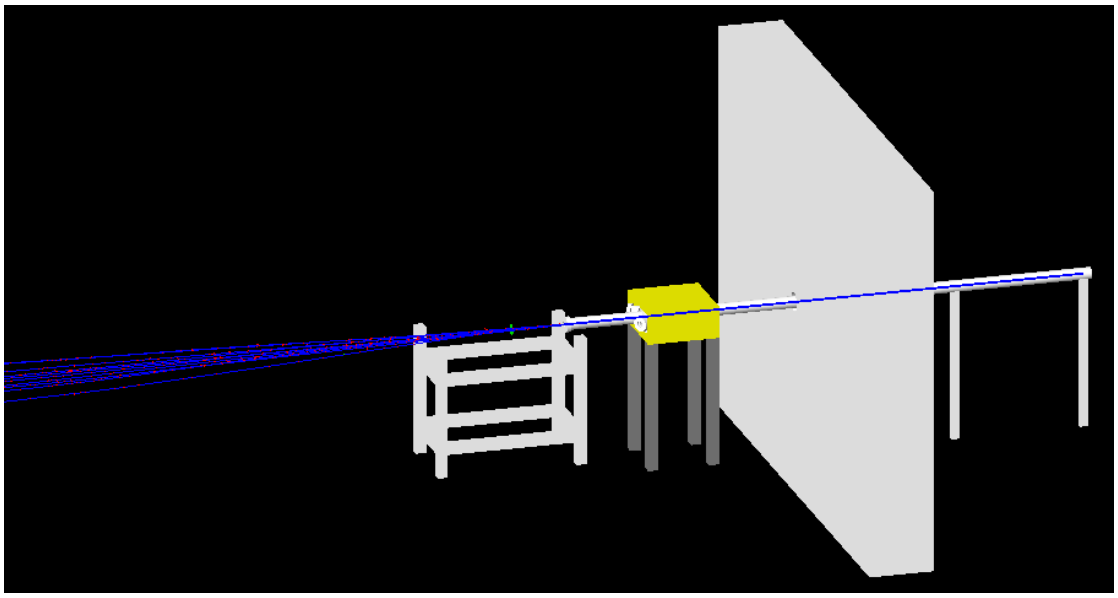

Figure 6.6: UoB beamline simulation model visualised in GEANT4. The input beam is defined upstream of the switching magnet (yellow) showing protons (blue), electrons (red) and film (green square).

[‡]Developed and provided by Tony Price, 2019.

EBT3 film was already defined in the model (27 µm sensitive layer sandwiched between a 130 µm back and front layer) and was positioned at the same experimental z location as the film, 168 mm after the nozzle. Hits were tracked within this sensitive (absorber) layer and phase space information (particle ID, position and momentum in x, y, z, kinetic energy or deposited energy) was recorded as ntuples, filling a '*tree*' written as a root file. This process is handled by the *analysisManager* within the *SteppingAction* and *RunAction* classes. To score in the same way for a plane representing the VELO sensors, the absorber needed to be redefined to fill a tree if the step points of particles were checked as having entered the '*VELO*' (sensitive detector) volume. The VELO geometry was created in the *DetectorConstruction* class as a 20 × 20 cm^2 square of 300 µm thick silicon (Fig. 6.7a). It was placed at the same z position as the monitors in UoB (208 mm after the nozzle) and a switch of the absorber from film to VELO was executed in the run macro file. The collimator (inner) diameter size could also be changed in the macro (Fig. 6.7b).

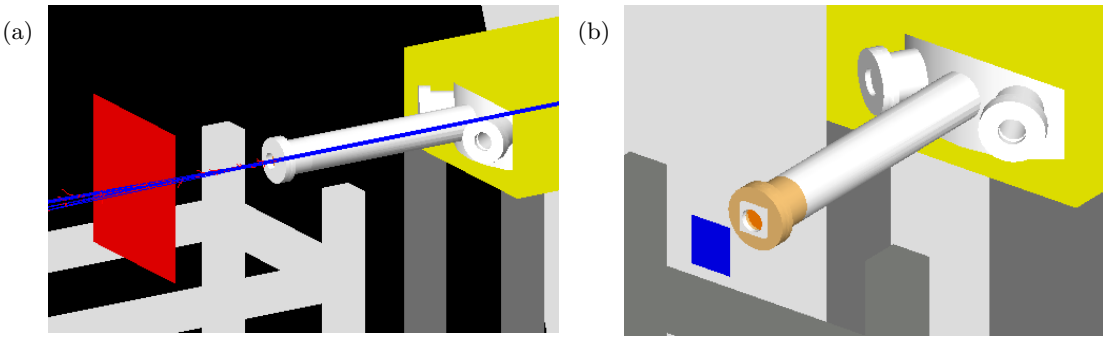

Figure 6.7: a) Redefined absorber volume to score hits in a silicon plane for VELO (red). b) Film absorber placed after the nozzle (orange) which contains the collimator (silver), adjustable for inner diameter.

The root output files contained distributions of hits in the transverse plane and by radial distance. Therefore, beam density maps and radial plots could be obtained for each film for different collimator sizes and positions. Simulations were also run with increasing numbers of initial primary protons, to examine changes in the divergence and numbers of hits for the different beam currents. Strong linearity between the number of input protons and hits indicate that only a linear scaling factor is necessary to account for varying beam intensities. A density map can be obtained and scaled for the applied

beam current, providing relevant quantities for correlation between the halo region and beam core. This halo dose correlation relationship, experimental methods and analysis are further detailed in [129]; the main findings of this experimental campaign are discussed as relevant for this chapter. The viability of this correlation was examined by benchmarking the hits along the radial axis obtained with the R-sensors, against beam distributions achieved by simulations and film. To mitigate the experimental uncertainties, measurements from day 2 with the reproduced film irradiations (Fig. 6.5) are considered and compared with simulated results.

6.3 Results

Experimental data was collected across a range of beam currents to test the response of all four sensors to the 18 MeV proton beam. With the phase scan delays implemented, the electrometer outputs were recorded against total numbers of hits in each sensor. Strong linearity was observed: the total absolute charge increased linearly with the proton beam current for all collimator sizes. Higher uncertainties were seen for the smaller collimators as lesser hits were recorded.

The VELO modules register hits as an Analogue-to-Digital Converter (ADC) signal which correspond to the generation of electron hole pairs in the silicon, depending on the amount of energy deposited. As such, it should be possible to resolve information about each interaction by the resulting ADC count. However, a significant observation was realised from these tests: the majority of hits registered as a maximum ADC value. Any hits above a maximum threshold (127 ADC counts) saturate the modules and it was found that single protons exceeded this limit, even at the most minimal beam settings. Consequently, as the threshold is so low, any hit regardless of energy, particle type or interaction is counted.

Furthermore, as the beam does not diverge much after the nozzle, the beam sizes for the 7, 10 and 15 mm collimators were expected to be smaller than the (16 mm) sensor aperture (Appendices B.31-B.33). Therefore, the beam would completely pass between the two sensors with reasonable clearance. Even so, the detector was observed to be able

to sufficiently detect interactions and counts across the modules. Therefore, indirect measurements without interference to the beam are possible due to the sensitivity of the detector modules; the beam current can be resolved by considering the number of hits as a function of distance along the radial axis. Accordingly, the beam distributions in the transverse plane were obtained with simulations and measurements using the VELO detectors[‡] and EBT3 film. For comparison, each data set was normalised to maximum output values and plotted on the same axes for the three collimator sizes (Fig. 6.8).

(a)

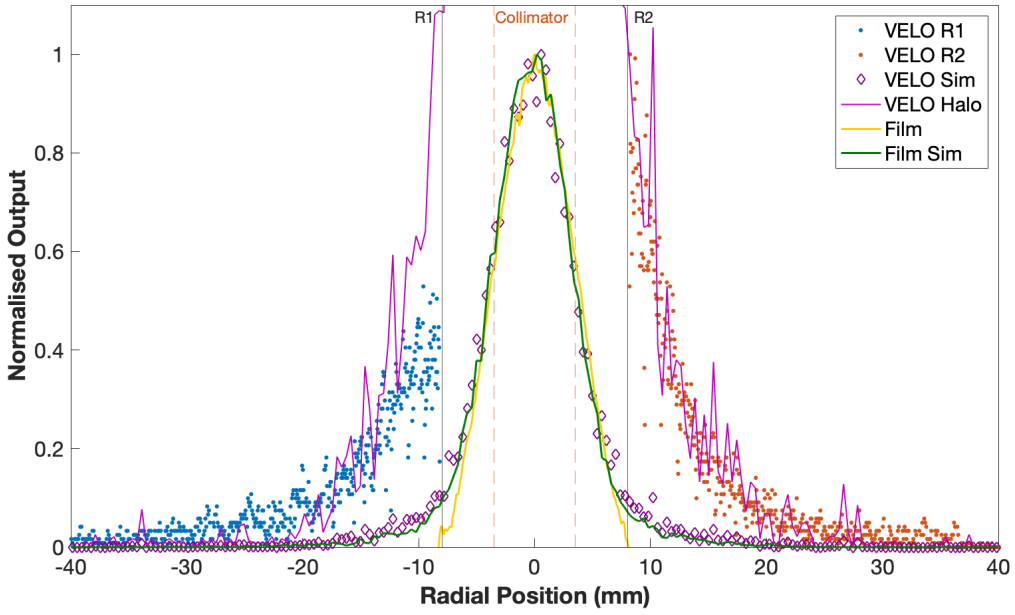

(b)

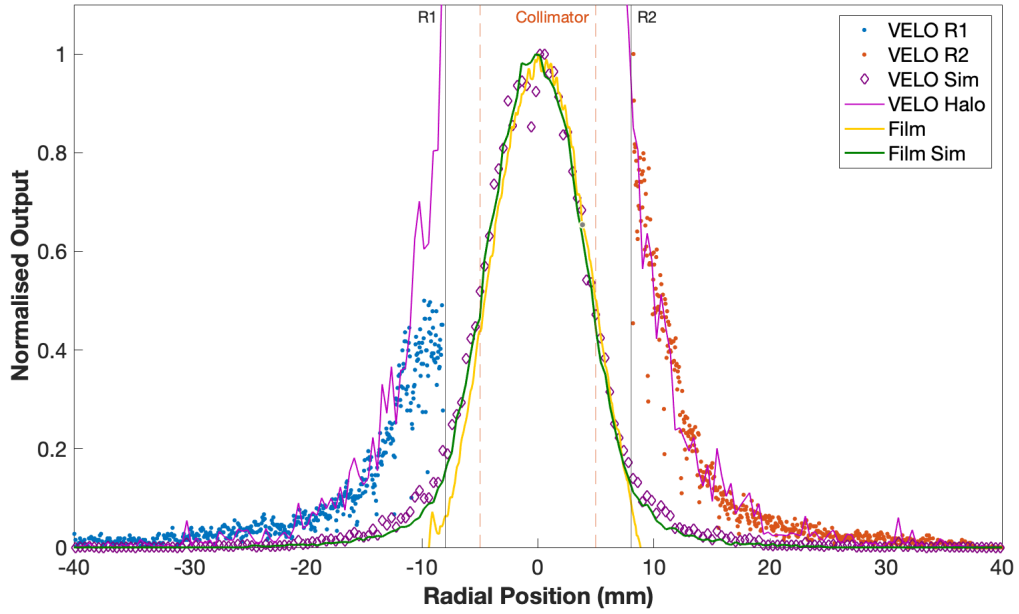

[‡]VELO data was provided by R Schnuerer.

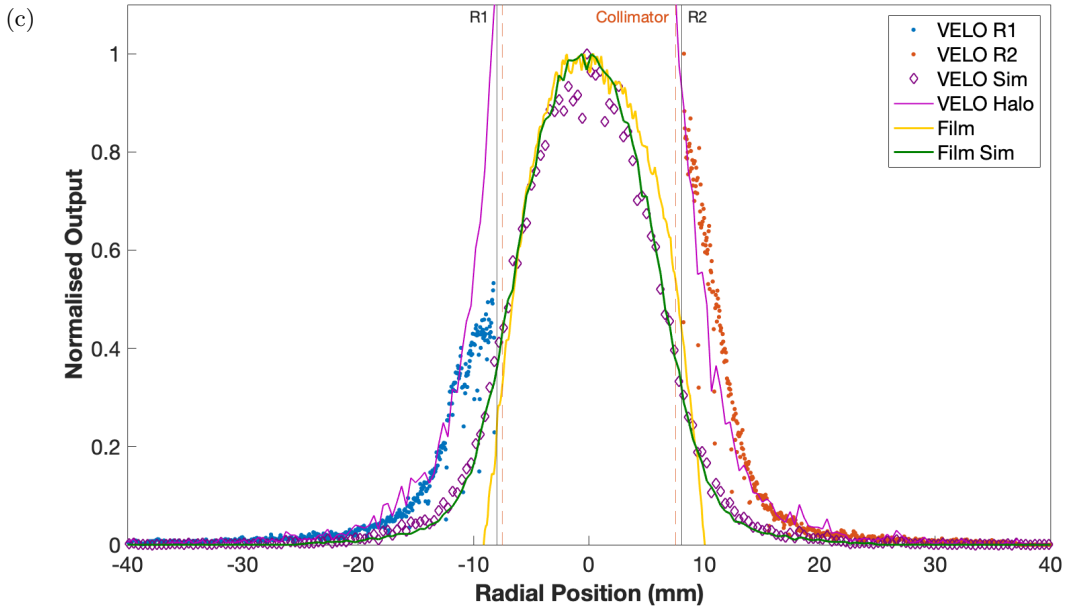

Figure 6.8: Transverse beam distributions measured by the VELO R-sensors, film and simulations for the a) 7 mm b) 10 mm and c) 15 mm cases. The geometrical extent of the >8 mm halo region (vertical black line) and collimator diameter (dashed orange line) is shown.

The film profiles indicate the expected size of the beam and it is clear that only a small proportion of the beam (tails) is detected by the sensors. This is also evident in the more conformal spread of R1 and R2 hits for the 15 mm collimator case due to the larger acquisition of hits and detected signal. The non-uniform hit distribution and higher R2 outputs compared to R1 for all cases also suggest that the modules were misaligned in the perpendicular plane. Nonetheless, the simulated film profile match well with measurements, apart from the low tail regions; these differences are more pronounced with the larger beams. As mentioned, the film has a very sharp distribution with no penumbra, indicating that exposure at low levels has been lost somewhere along the dose conversion process.

The simulated hits from the VELO absorber (VELO Sim) also follow the film profiles closely but there is slight divergence from traversing the 40 mm distance to the sensors which results in some additional scatter at the tails. These are most significant for correlation of the halo region of the beam, with respect to the total dose distribution: the halo is designated as the hits outside the 8 mm R1 and R2 boundaries. Therefore, these simulations give the expected beam profile at the same plane as the VELO sensors

and by taking the halo region, can provide a prediction of the distribution of hits which will be detected. Accordingly, the simulated hits belonging to the halo (VELO Halo) as shown in Fig. 6.8, are normalised to the R1 and R2 boundary output value and similarities between the distributions are observed. Again, the overall agreement is best for the larger 15 mm collimator as more hits are registered.

Although fair initial coherence is seen, it is evident that a better dataset is needed for precise correlation. The misalignment results in the simulated points being skewed slightly (in the positive radial direction) and also extend past the R1 hits. This is effectively an absence of 25% of meaningful halo measurements. Furthermore, the data is noisy and this is due to several mentioned uncertainties. Better results can be obtained with longer acquisition times to record more hits as well as with larger numbers of simulated primaries. As both the film and VELO absorber geometries are very thin, low numbers of particles are tracked even when using an input beam of 100 million protons. Additionally, the small misalignment ($\sim$2 mm) of the modules are shown to result in large differences, around $\sim$50% of the output signal between the R1 and R2 sensors. Positioning errors are amplified as the sensors contain numerous micron sized strips.

6.4 Discussion

These measurements demonstrate for the first time, the proof of concept of the VELO beam monitor in a medical proton beamline, since undergoing several upgrades to adapt the system for application outside of CCC. These studies contribute to ongoing work on the monitoring system; it offers many benefits however further developments are necessary for clinical use.

The system offers a real possibility to enhance the measurements currently offered by commonly used particle therapy beam diagnostics instruments. The novel design of the sensors, among other beneficial properties associated with its initial use in the LHC (i.e. radiation hard, build, data acquisition streams etc.) provides many unique and competitive advantages. The beam can be measured using non-invasive methods with negligible interference and if required, the modules can also be translated laterally. The

sensors themselves are in reality so sensitive such that measurements can still be taken without being in close proximity however there must be a compromise with the detection resolution. This can be compensated to some extent with simulations, although this necessitates that the facility must be well characterised: simulations must be able to reproducibly model the beam across the full range of treatment parameters. As such, a scattered beam is the more ideal candidate and given the present state and capabilities of the system, several limitations are anticipated with scanning systems (i.e. beam movement, varying spot sizes, shapes and intensities etc.).

Furthermore, as the beam monitor directly detects only the halo region which must be correlated, the system may be considered as providing relative measurements: another instrument or method is required to measure the total beam distribution. This was done with film, simulations and a Faraday cup which are common approaches and can be easily performed in a clinical environment. However, a caveat with these are the uncertainties, which scale to large differences at the level of the detectors. Using other methods are advised, such as benchmarking measurements with another profile monitor or also ionisation chambers. As discussed in Section 3.4.4, the Medipix3 detector offers absolute measurements of the beam current and profile and is also suitable for this purpose.

Additionally, since first tests many years ago at the CCC beamline, the system is now able to be implemented in other facilities. The entire system is actually very extensive (numerous components, cabling, equipment and computing power etc.) and requires substantial arrangements for set-up and transport. To exist in the clinical environment and workflow, the system, software and operating processes would need to be streamlined and simplified. An avenue for development in this area would be a framework which connects the functions of the detector and data acquisition with the operation of the accelerator. An added bonus would be incorporating these with simulation or treatment planning software. Related resources for simulations involving pixel detectors (Allpix^2 [224]) exist; expanding from this to integrate with VELO measurements would be a significant development. Even so, just building a graphical user interface to manage detector operations would also be valuable.

With the detector itself, further technical improvements may offer additional features. It was observed that the fine signal thresholding resulted in saturation; adjustments to this could provide more detailed information about each hit, such as the particle type and energy deposition. Additional software upgrades could also synchronise the channels for the different sensor geometries (R and φ) more effectively and utilise the position sensitive capabilities.

6.5 Summary

The LHCb VELO detector modules have been adapted into a standalone beam monitor and first tests were successfully performed at the UoB 35 MeV medical beamline. Measurements of the beam halo were recorded and compared to transverse beam distributions determined with Monte Carlo simulation studies and EBT3 film analysis. Multiple methods were performed to examine the feasibility of the sensors for this application and to benchmark detector hits along the radial axis. The detected signal from the halo can be resolved from simulations for correlation of the halo and scaled for different beam settings.

Several challenges were encountered during the measurement campaign resulting in several uncertainties and relatively noisy data. Despite this, initial coherence between simulated and measured data was achieved. Furthermore, several valuable detector attributes were identified from these tests, indicating the capabilities of the system for clinical applications as well as avenues for further improvements. These measurements demonstrate the possibility of the system as a candidate for online dose monitoring for particle beam therapy.

Chapter 7

Conclusions

7.1 Summary

This thesis described several methods to characterise and model a particle beam for novel beam diagnostics development. Namely, the VELO beam halo monitor was adapted into a standalone system and optimised for implementation into the CCC ocular proton therapy beamline. As the detector provides beam information based on non-destructive measurements of the halo, a comprehensive overview of the cyclotron, beam transport and treatment delivery system at the facility was performed. Clatterbridge is a pioneering PBT centre which supports a wide range of research and offers a unique environment for experimental work. It follows that in order to fully exploit the beamline, the propagation and behaviour of the beam must be well understood. Therefore, simulation studies and experimental measurements were required to precisely model and completely characterise the facility. Several computational tools were developed to accurately reproduce the current state of the facility and physical properties of the beam. This work could also be carried out at similar facilities to study aspects which are necessary for beamline upgrades, optimisation and for the integration of diagnostics.

Firstly, a simulation study was performed using a recent GEANT4 model of the CCC treatment line to investigate the beam propagation and impact of the sensors when positioned in the integration zone. The projected transverse beam profiles were attained, indicating an insignificant effect on the beam performance (0.04 MeV, 0.06% energy loss) thus supporting the feasibility of minimally invasive measurements. Following the

discovery of new facility information and implementation in the model, considerable improvements were made to the code. However, an assessment of the historical input beam parameters revealed a dependency of the results on the defined distribution of the particle source (increases in FWHM up to 2.4 mm and 3.2 mm at the integration zone start and isocentre, respectively). CCC does not maintain any beam diagnostics in the beam transport line and as a result, several approaches were pursued to verify these details: measurements of the transverse beam distribution with film and the Medipix3 silicon detector and also an extensive beam dynamics study.

Irradiations were performed with EBT3 Gafchromic film placed throughout the delivery system and analysed using scripts developed in Matlab to automate the conversion of pixel intensity values to OD and generate plots of the transverse dose distributions. Several uncertainties resulted in quantified differences to simulation results, also influenced by beam quality on the day. As such, additional simultaneous measurements were performed with the Medipix3 detector and these showed good agreement with film, particularly at the lateral edges of the transverse beam profiles. A calibration set performed on the day also had smaller deviation, indicating better beam performance. Moreover, this became the first test using the Medipix3 technology in a clinical proton beam environment. Despite further concerns related to the beam parameters and facility, a linear response and achieved results demonstrated the capability of the detector to provide an absolute representation of the spatial spread of the beam. In addition, several other observations were noted which suggest its possible application in identifying accelerator related issues.

The numerous uncertainties associated with the beam and facility proved challenging. Direct measurements enabled the simulated results to be matched by varying the input source however the beam study established that this would involve testing countless parameters. Therefore, a complete review of the facility was carried out to develop an optical lattice to model and determine the linear beam optics upstream of the treatment room. Based on historically documented information and physical measurements, the quadrupole parameters and beamline was described in models developed in MAD-X and BDSIM. The sensitivity of these parameters and their effects on the resulting beam

sizes were shown, hence an optimised nominal case was determined. This was chosen to constrain the lattice to generate a realistic beam distribution which would be representative of present day conditions. Simulations were compared with film profiles in place of the proposed emittance measurements: similar agreement suggest the applicability of input parameters ($\sigma_{x,y}$ = 6.89, 2.14 mm, $\beta_{x,y}$ = 9.52, 4.59 m and $D_{x,y}$ = 0.01, 0.00 m) determined from the optical study.

Given the breadth of this work and the recognised complexity to fully utilise information across the multiple codes, a completely new CCC simulation model was developed in TOPAS. Although the GEANT4 model itself is a useful tool to study the beamline, the complicated processes, analysis, user interface, as well as discontinuation in user support and development limit its future use. The TOPAS model incorporates everything known about the facility, updated geometry and beam parameters. Results showed an overall improved agreement to the film profiles and the capability to easily score physical quantities such as the LET, enabled correlation for radiobiological applications. Experiments were performed to benchmark the simulation using another silicon detector, the MiniPIX-Timepix. The LET was resolved by evaluating the measured energy depositions and track lengths, showing an expected increasing trend which correlated well with simulations. Empirical LET values of ∼12 keV/µm at the BP and a maximal value of 15.5 keV/µm at the BP fall-off were obtained, falling within expected ranges.

All these tools allow simulations of the CCC beam and the methods presented in this thesis also support the investigation and development of new technologies as diagnostics systems for PBT and potentially, advanced CPT techniques. However, as access to CCC was limited given the extensive setup of the VELO system, experiments were conducted at the UoB proton beamline. These were the first proof of concept measurements with the upgraded system and using the same approaches, were compared with simulations and film. These demonstrated good agreement, particularly for the halo region at higher signal output counts (15 mm collimator case). Several experimental uncertainties and the envisioned clinical capabilities of the monitor were discussed: the positive outcomes indicate the possibilities of the adapted LHCb VELO detectors as a novel beam halo monitoring system for medical proton beamlines.

7.2 Outlook

Beam diagnostics tools are essential components in the PBT workflow which ensure the safe and correct delivery of the beam to provide high quality treatments. The instruments explored in this work show promising capabilities however several areas were identified where further work is necessary to optimise their application in particle therapy. There are also various aspects of development which could improve the computational models presented in this thesis.

The VELO system is highly sensitive and can offer completely non-interceptive relative measurements which could provide the dose online, converted from the signal readout using several benchmarking methods. The potential of the system was demonstrated with the proof of concept measurements achieved at UoB; feasibility in a clinical environment was also previously explored with its integration into the CCC treatment beamline. Recent developments offer additional functionalities such as the external triggering system, enabling synchronisation of the readout and data acquisition with different beam structures: this provides the possibility of adapting the monitor for different facilities. These tests however identified several improvements which could be pursued to enhance the system toward clinical implementation. In general, a reduction of the physical size of the setup, removing the charge threshold and simplifying the processing and operational software would be highly advantageous. Moreover, the VELO detectors have intrinsic capabilities which could also be better utilised, this includes exploiting the combined dual geometry of the modules to access position sensitive information and the sensor hit maps during active operation, rather than only offline during post-processing.

As both CCC and UoB present similar environments (proton beams generated by comparable cyclotrons but at different energies and frequencies), it would also be beneficial to test the system with different accelerator types and delivery methods, to explore the capabilities of the system for wider applications and advanced technologies. In addition to the pulsed structure and intensity variations with a beam produced by a synchrotron, experimental measurements at a facility with active PBS delivery would also offer insight into system performance under different conditions.

Furthermore, due to the non-interceptive nature of the monitors, different approaches are necessary for correlation of the halo to the total beam distribution and then to dose. This requires relevant beam properties to be derived or measured in a way which is accurate, reproducible and which can also be scaled for different beam settings. Typically this involves several instruments including a FC, ion chambers or EBT3 film. However, complimentary devices such as the Medipix3 detector enable direct measurements of the beam and can be easily compared with film however both need to be performed with high precision. Measurements obtained at CCC showed the advanced capabilities of the Medipix3 chip and pixel technology within a PBT environment: the remarkable time resolution alongside overall agreement with the film measurements.

Limitations with the film are due to uncertainties surrounding the analysis and conversion process, as indicated by the error bars in the calibration curves and the irregularity of the attained beam profiles. A way to mitigate this would be to proceed with a more robust process: strictly monitoring the film protocol to maintain uniformity with the film irradiation, development, scanning and analysis; or to attain profiles using well established or commercial methods. For example, using commercial software and hardware to determine the beam profiles from the irradiated film or by direct measurements using commonly used ion chambers for QA or dosimetry. However, it is important to note that with conventional ICs, interception in the beam path reduces the beam quality, has deficiencies with performance and also requires individual and regular calibration and multiple factors to convert the charge generated in gas. A better possibility could be to perform simultaneous measurements with the VELO system and the Medipix3 detector for comparison with simulations. Nonetheless, generating a correlation database of halo measurements from the predicted beam distribution using MC simulations is only applicable if the beam is well characterised.

The computational models of the beam transport and treatment line were optimised and matched as based on available information but would benefit highly from further measurements. The tools used however are highly flexible: the optical lattice and delivery system model can be further adjusted to accommodate findings from future

measurements. For the BTL, carrying out the proposed emittance measurement campaign would be worthwhile in order to determine the emittance, transverse beam sizes and quadrupole parameters. Other approaches to verify the beam profiles at the designated positions between the last quadrupole triplet and the treatment line or arguably, at anywhere along the beamline, contributes additional parameters useful for matching. Alternatively, characterising the quadrupoles by measuring and modelling the fields also provides a more realistic representation of the lattice components. In addition, it is noted that machine learning techniques could be applied to optimise the beam dynamics to determine the optical parameters based on the best achievable quadrupole and dipole field settings. This could similarly be done with a database of beam distributions to parameterise the halo and determine an analytical correlation factor.

For the treatment line, verifying the physical components where there were noticeable deviations between the simulated and film profiles would be valuable to progress the model to approach a more realistic, physical representation of the clinical beam. Additional measurements of the dose deposition (pristine BP and SOBP) and transverse beam profiles with film or other methods, would also assist with model validation. Enhancements can also be made to the TOPAS model source code to improve the computational efficiency and better implement time modulation features to generate a SOBP. As complex geometries can be imported into TOPAS, the VELO detector itself could also be built into the model, offering the ability to score within the actual physical dimensions of the sensor modules and generate hit maps congruent with measured data. For added capabilities, developing radiobiological scorers allows detailed simulations in the cellular and sub-cellular scale, increasing the utility and scope of the model to biological applications. This can all be done in the future as the models are made available for public use.

Finally, developing a system to connect these computational tools with the operation of the beam diagnostics and accelerator control system would be highly useful. The combination of all this work details the basis for a framework to integrate realistic simulation models and advanced beam diagnostics for the enhancement of particle therapy treatments.

Appendices

Appendix A

Original schematics and historical documentation describing the Clatterbridge facility

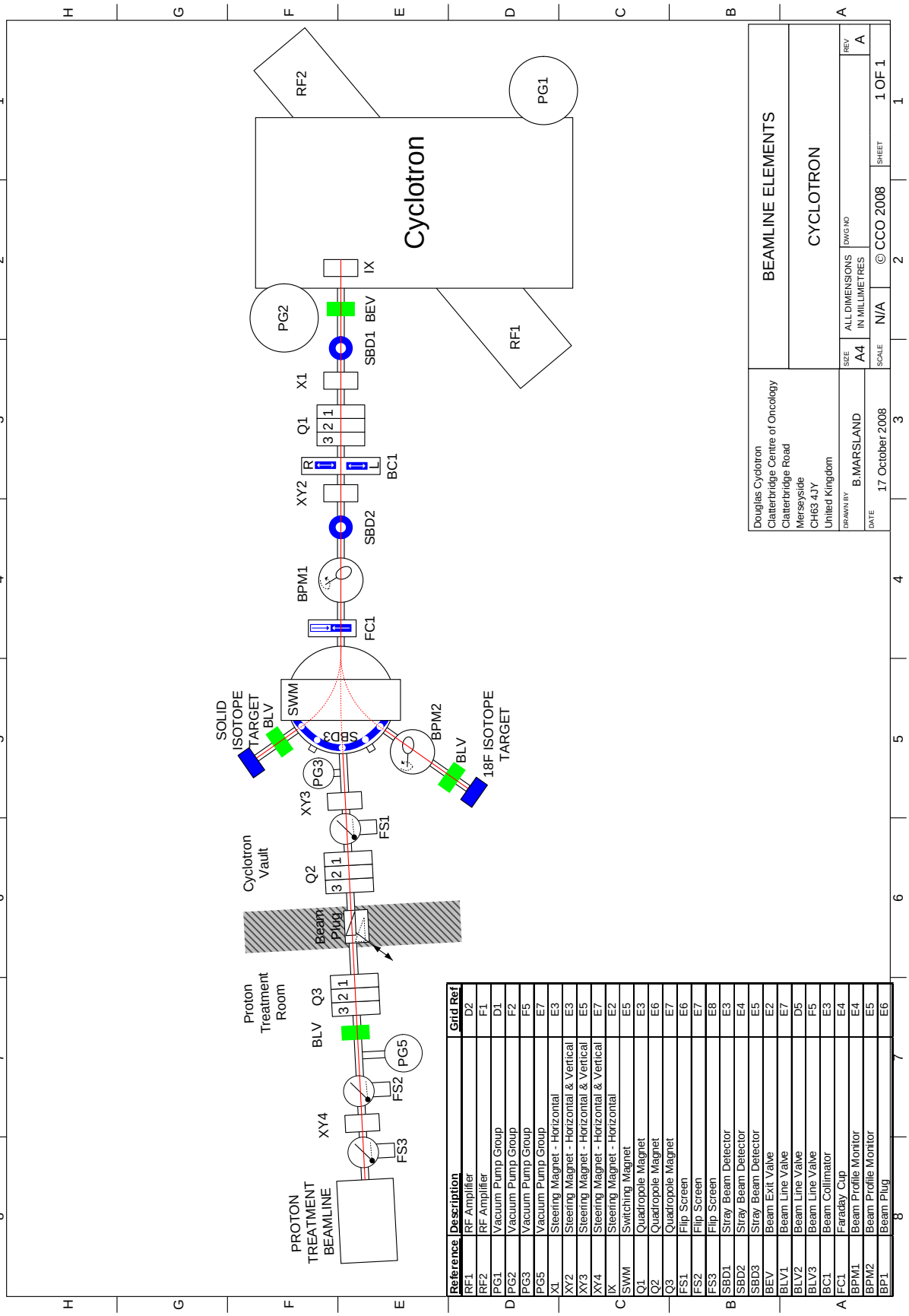

Reference	Description	Grid Ref
RF1	RF Amplifier	D2
RF2	RF Amplifier	F1
PG1	Vacuum Pump Group	D1
PG2	Vacuum Pump Group	F2
PG3	Vacuum Pump Group	F5
PG5	Vacuum Pump Group	E7
X1	Steering Magnet - Horizontal	E3
XY2	Steering Magnet - Horizontal & Vertical	E3
XY3	Steering Magnet - Horizontal & Vertical	E5
XY4	Steering Magnet - Horizontal & Vertical	E7
IX	Steering Magnet - Horizontal	E2
SWM	Switching Magnet	E5
Q1	Quadropole Magnet	E3
Q2	Quadropole Magnet	E6
Q3	Quadropole Magnet	E7
FS1	Flip Screen	E6
FS2	Flip Screen	E7
FS3	Flip Screen	E8
SBD1	Stray Beam Detector	E3
SBD2	Stray Beam Detector	E4
SBD3	Stray Beam Detector	E5
BEV	Beam Exit Valve	E2
BLV1	Beam Line Valve	E7
BLV2	Beam Line Valve	D5
BLV3	Beam Line Valve	F5
BC1	Beam Collimator	E3
FC1	Faraday Cup	E4
BPM1	Beam Profile Monitor	E4
BPM2	Beam Profile Monitor	E5
BP1	Beam Plug	E6

Figure A.1: Full listed schematic of entire CCC beamline.

ENTRY No. 63

NAME OF MACHINE Clatterbridge Cyclotron ..... DATE .....
INSTITUTION ..... Clatterbridge Hospital .....
ADDRESS ..... Clatterbridge Road, Bebington, Wirral, Merseyside L63 4JY. (England) .....
TEL ..... TELEX .....
IN CHARGE ..... REPORTED BY ... T.E. Saxton .....

HISTORY AND STATUS
DESIGN, date ... 1981/82 ... Model tests .....
ENG DESIGN, date ... 1981/82 .....
CONSTRUCTION, date ... 1982 .....
FIRST BEAM, date (or goal) ... 1982/83 .....
MAJOR ALTERATIONS .....
.....
COST, ACCELERATOR .....
COST, FACILITY, total ... Approx. £4.5m .....
FUNDED BY ... Charitable Organizations .....

ACCELERATOR STAFF, OPERATION AND DEVELOPMENT
SCIENTISTS ..... ENGINEERS .....
TECHNICIANS ..... CRAFTS .....
GRAD STUDENTS involved during year .....
OPERATED BY ..... Research staff or ..... Operators
OPERATION ..... hr/wk, On target ..... hr/wk
TIME DISTR. in house ..... %, Outside ..... %
BUDGET, op & dev .....
FUNDED BY ... Medical Research Council .....

RESEARCH STAFF, not included above
USERS, in house ..... outside .....
GRAD STUDENTS involved during year .....
RESEARCH BUDGET, in house .....
FUNDED BY .....

MAGNET
POLE FACE, diameter (compact) 160 cm, R extraction 64 cm
R injection ..... cm
GAP, min 12.3 cm, Field 20.7 kG
max 22.1 cm, Field 13.0 kG } at 280,000
AVERAGE FIELD ~~at R ext~~ 17.7 kG } Ampere turns
B max/ <B> 1.19
NUMBER OF SECTORS { compact 3 / separated ... } Spiral, max 55 deg
SECTOR ANGLE (SSC) ..... deg
TRIMMING COILS ... 4 sets valley coils harmonic
3 sets valley coils gradient
CONDUCTOR, material and type hollow core copper conductor
STORED ENERGY (cryogenic) ..... MJ
POWER : main coils 110 max, kW ; current stability 1×10^{-5}
trimming coils 5 max, kW ; current stability 1×10^{-4}
WEIGHT : Fe 120 tons ; coils 4.4 tons
COOLING system ... Water/Chiller .....
ION ENERGY (bending limit) E/A = 62 q^2/a^2 MeV/amu
(focusing limit) E/A = - q /a MeV/amu

ACCELERATION SYSTEM
DEES, number 2 ; angle 80 deg
BEAM APERTURE 2.5 cm ; DC Bias ..... kV
TUNED by, coarse - fine motor driven capacitor
RF 25.1 to - mHz, stable ± 1×10^{-6}
Orb F 25.1 to - mHz
HARMONICS, RF/Orb F, used 1
DEE - Gnd, max 40 kV, min gap - $\times 10^{-3}$ cm
STABILITY, (pk-pk noise)/(pk RF volt) $< 10^{-5}$
ENERGY GAIN, max 100 kV/turn
RF PHASE, stable to ± 0.5 deg
RF POWER input, max 60 kW
FREQUENCY MODULATION, rate - /s
modulator, type .....
beam pulse, width .....

VACUUM SYSTEM
OPERATING PRESSURE $< 10^{-5}$ Torr or mbar
PUMPS, No, Type, Size .....
2 x 4000 l/sec oil diffusion pump
100 x 20m³/h backing mechanical

ION SOURCES
.....

INJECTION SYSTEM
.....

EXTRACTION SYSTEM
Electrostatic + Electromagnetic + foc channel

FACILITIES FOR RESEARCH
SHIELDED AREA, fixed ..... m² ; movable ..... m²
TARGET STATIONS ..... in ..... rooms
STATIONS served at same time, max .....
MAG SPECTROGRAPH, type .....
COMPUTER model .....
OTHER FACILITIES .....
.....
.....

CHARACTERISTIC BEAMS

PARTICLE	ENERGY (MeV) Goal	Achieved	CURRENT (pμA) Internal	External
p	60		>100	50
SECONDARY			(part/s)	
			50 rad/min at 150cm from	
n			target after filtering	

BEAM PROPERTIES

MEASURED		CONDITIONS
PULSE WIDTH	RF deg	pμ A of .... MeV ... ions
PHASE EXC, max ...	RF deg	pμ A of .... MeV ... ions
EXTRACT eff	%	pμ A of .... MeV ... ions
RESOL ΔE/E	%	pμ A of .... MeV ... ions
EMITTANCE		
(π mm. mrad) { ... axial / .... rad }		..... pμA of ..... MeV ... ions

OPERATING PROGRAMS, time distribution
BASIC NUCLEAR PHYSICS ... SOLID STATES PHYSICS ....
BIOMEDICAL APPLICAT. 100 ISOTOPE PRODUCTIONS ....
.....
.....

REFERENCES/NOTES

Scanditronix Model MC60PF

PLAN VIEW OF FACILITY, NOTEWORTHY FEATURES, COMMENTS

Accelerator Part of Scanditem High Energy Isocentric Neutron Therapy Unit.

Computer controlled.

Figure A.2: Commissioning documentation 63.

ENTRY NO. 68
NAME OF MACHINE ... CLATTERBRIDGE CYCLOTRON
INSTITUTION ... MEDICAL RESEARCH COUNCIL, CYCLOTRON UNIT
ADDRESS ... CLATTERBRIDGE HOSPITAL, BEBINGTON, MERSEYSIDE, L63 4JY
TEL ... 051-334 6366 ... TELEX ... 627035
IN CHARGE ... T.E. SAXTON ... REPORTED BY ... T.E. SAXTON

HISTORY AND STATUS SCANDITRONIX MODEL MC60PF
DESIGN, date ... 1981/82 ... Model tests ...
ENG DESIGN, date ... 1981/82 ...
CONSTRUCTION, date ... 1982/83 ...
FIRST BEAM, date (or goal) ... FACTORY 1983, SITE 1984 ...
MAJOR ALTERATIONS ...
COST, ACCELERATOR ... £1.5M ...
COST, FACILITY, total ... £4.5M ...
FUNDED BY ... U.K. CANCER CHARITIES ...

ACCELERATOR STAFF, OPERATION AND DEVELOPMENT
SCIENTISTS ... 2 ... ENGINEERS ... 3 ...
TECHNICIANS ... 2 ... CRAFTS ... 1 ...
GRAD STUDENTS involved during year ...
OPERATED BY ... Research staff or ... Operators
OPERATION ... hr/wk. On target ... hr./wk
TIME DISTR. in house ... % Outside ... %
BUDGET, op & dev ...
FUNDED BY ... MEDICAL RESEARCH COUNCIL ...

RESEARCH STAFF, not included above
USERS, in house ... outside ...
GRAD STUDENTS involved during year ...
RESEARCH BUDGET, in house ...
FUNDED BY ...

MAGNET
POLE FACE, diameter (compact) ... 160 ... cm, R extraction ... 64 ... cm
R injection ... cm
GAP, min ... 12.3 cm, Field ... 20.7 ... kG
max ... 22.1 cm, Field ... 13.0 ... kG } at ... 280,000 ... Ampere turns
AVERAGE FIELD at R ext ... 17.7 ... kG
B max/ < B > ... 1.19 ...
NUMBER OF SECTORS { compact ... 3 ... separated ... } Spiral, max 55 deg
SECTOR ANGLE (SSC) ... deg
TRIMMING COILS ... 4 SETS HARMONIC COILS ...
... 6 SETS CIRCULAR GRADIENT COILS ...
CONDUCTOR, material and type ... HOLLOW COPPER ...
STORED ENERGY (cryogenic) ... MJ
POWER: main coils ... 110 ... max, kW; current stability ... $1x10^{-5}$
trimming coils ... 5 ... max, kW; current stability ... $1x10^{-4}$
WEIGHT: Fe ... 120 ... tons; coils ... 4.4 ... tons
COOLING system DEMINERALISED WATER ...
ION ENERGY (bending limit) E/A = ... 62 ... q^2/a^2 MEV/amu
(focusing limit) E/A = ... q/a MeV/amu

ACCELERATION SYSTEM
DEES, number ... 2 ... 80 ... deg
BEAM APERTURE ... 2.5 ... cm; DC Bias ... kV
TUNED by, coarse ... fine ...
RF ... 25 ... to ... mHz, stable ± ... $1x10^{-6}$
Orb F ... 25 ... to ... mHz
HARMONICS, RF/Orb F, used ... 1 ...
DEE—Gnd, max ... 40 ... kV, min gap ... cm
STABILITY, (pk-pk noise)/(pk RF volt) ... $<10^{-3}$ ...
ENERGY GAIN, max ... 100 ... kV/turn
RF PHASE, stable to ± ... 0.5 ... deg
RF POWEP input, max ... 60 ... kW
FREQUENCY MODULATION, rate ... /s
modulator, type ...
beam pulse, width ...

VACUUM SYSTEM
OPERATING PRESSURE ... $\leq 10^{-5}$ ... Torr or mbar
PUMPS, No, Type, Size ...
2 x 4000 L/SEC OIL DIFFUSION PUMP ...
100 m^3/HR+BOOSTER, 20 m^3/HR MECHANICAL BACKING ...

ION SOURCES
INTERNAL, COLD CATHODE ...

INJECTION SYSTEM
ELECTROSTATIC+ELECTROMAGNETIC+FOCUSSING CHANNEL ...

EXTRACTION SYSTEM
...

FACILITIES FOR RESEARCH
SHIELDED AREA, fixed ... m^2; movable ... m^2
TARGET STATIONS ... in ...
STATIONS served at same time, max ...
MAG SPECTROGRAPH, type ...
COMPUTER model ...
OTHER FACILITIES ...
...
...

CHARACTERISTIC BEAMS

PARTICLE	ENERGY (MeV) Goal	Achieved	CURRENT (μA) Internal	External
P	60	62.5	>100	50
SECONDARY (part/s)				
n	50 RAD/MIN @ 50CM FROM TARGET AFTER FILTERING			

BEAM PROPERTIES

MEASURED		CONDITIONS
PULSE WIDTH	RF deg	pμ A of ... MeV ... ions
PHASE EXC. max	RF deg	pμ A of ... MeV ... ions
EXTRACT eff	%	pμ A of ... MeV ... ions
RESOL ΔE/E	%	pμ A of ... MeV ... ions
EMITTANCE (π mm. mrad)	axial / rad	pμ A of ... MeV

OPERATING PROGRAMS, time distribution
BASIC NUCLEAR PHYSICS ... SOLID STATES PHYSICS ...
BIOMEDICAL APPLICAT..100%... ISOTOPE PRODUCTIONS ...
...
...

REFERENCES/NOTES
1) SCANDITRONIX MC60PF
2)

PLAN VIEW OF FACILITY, COMMENTS, ETC.
ACCELERATOR USED WITH SCANDITEM HIGH ENERGY ISOCENTRIC NEUTRON THERAPY UNIT. CONTROLLED BY PDP11-23.

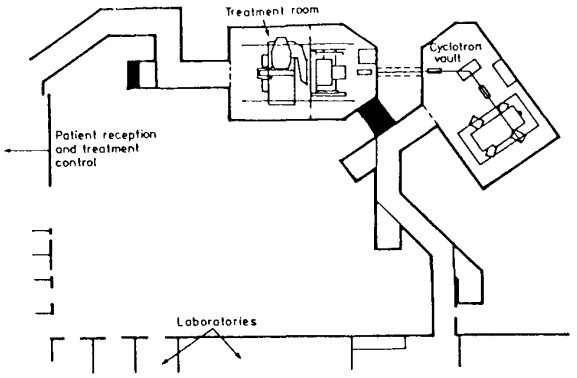

Plan view of Clatterbridge high energy neutron therapy facility.

Figure A.3: Commissioning documentation 68.

ENTRY NO: CU-22
Machine Name: Scanditronix MC-60 PF
Date: 6/6/01 8:55:36 AM
Institution: Douglas Cyclotron Unit, Clatterbridge Centre for Oncology
Address Bebington, Wirral UK
In Charge of Cyclotron: A Kacperek
Telephone: ++44 (0)151 334 6366
Fax: ++44 (0)151 334 2845
Person Reporting: A Kacperek
Web:
E-mail: andrzejk@ccotrust.co.uk

HISTORY
Designed By: Scandidtronix SA
Construction Dates: 1983-84
First Beam Date: 1985
CHARACTERISTIC BEAMS

ions	/ **energy**(MeV/N)/**curre**nt(pps)/**powe**r(w)
p	62 50 uamps

transmision efficiency(source to extract beam)
typical: 70% - **best:** 85%
tranverse emmitance
emmitance definition: not known
vertical: <15π mm mrad
horizontal: <15π mm mrad
longitudinal: < 0.1 % energy(Δ) E/E)%xdeg RF

USES
basic research: % **therapy:** 80%
development: 5% **isotope production:** 10%
other: 5% **maintenance:** %
beam tuning: % **Total Time:** 700h/year

TECHNICAL DATA
a)magnet: **type:** simple yoke
Kb: MeV/A **Kf:** MeV/A
average field (min/max): 1.77 ave. T
number of magnet sectors: 3
hill angular width: hill angular width
spiral (max): deg
pole parameters
diameter: 1.6 m
injection radius: 0 m
extraction radius: m
hill gap: m **valley gap:** m
trim coils
-number: 6x2
-current(max): 260 amp total A-turns
harmonic coils
-number: 4 sets x 3xNsectorsx2
-current(max): A-turns
main coils
number: 1x2
total ampere-turns: A-turns
current: 900 A
stored energy: MJ
weight - iron: 120t coils: t
power
main coils (total): 110 kW
trim coils (total max): 5 kW
refrigerator (cryogenic): 565 kW
b)RF
acceleration
frequency range: 25.7MHz
harmonic modes: 2
number of dees: 2
number of cavities: 2
dee angular width: 80degrees
voltage
at injection: nakV(peak to ground, max)
at extraction: nakV(peak to ground, max)
peak: 40kV(peak to ground, max)
line power(max): 120kW
stability
phase: deg
voltage: <0.1%
injection
c)ion source: PIG 300 mA
external injection:
components:
source bias voltage: 2kV
injection energy: MeV/N
buncher:
injection efficiency: %
d)injector: NA
e)extraction
electromagnetic (EMC) electrostatic deflector (55 Kv)
efficiency
typical: %
best: %
f)vacuum
pumps: 2 x 4000 l/sec oil diff pumps with baffles
achieved vacuum: < 10-5Pa
REFERENCES
BONNETT DE, KACPEREK A, SHEEN MA, GOODALL R and SAXTON TE 1993 The 62 MeV proton beam for the treatment of ocular melanoma at Clatterbridge. British Journal of Radiology 66, 907-914.
EXPERIMENTAL FACILITIES
I treatment room; 4 available beam lines for irradiation;
COMMENTS

Figure A.4: Cyclotron documentation.

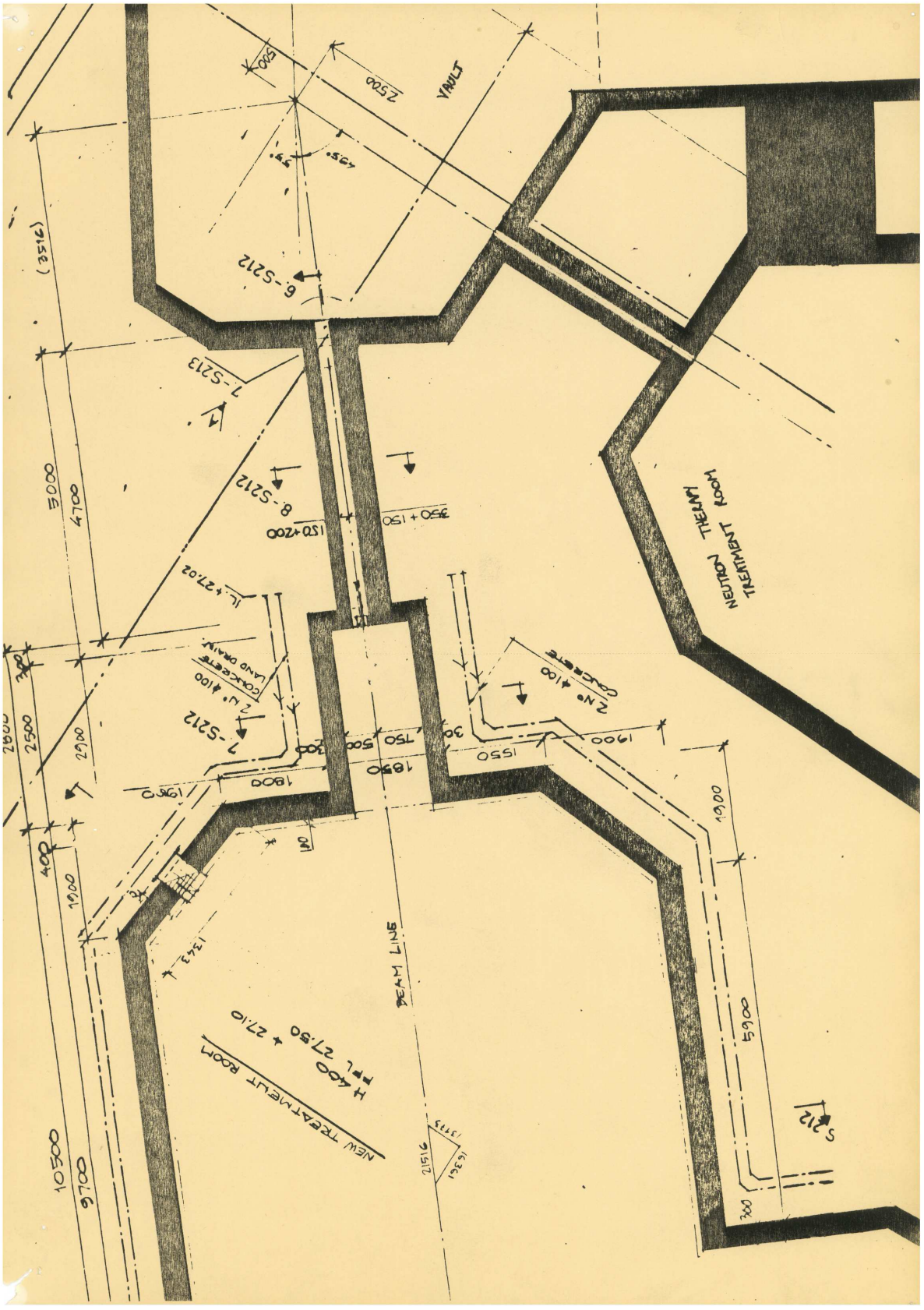

Figure A.5: Bunker schematic.

Appendix B

Additional results and simulation source code.

B.1 CCC GEANT4 Simulation Results

(a)

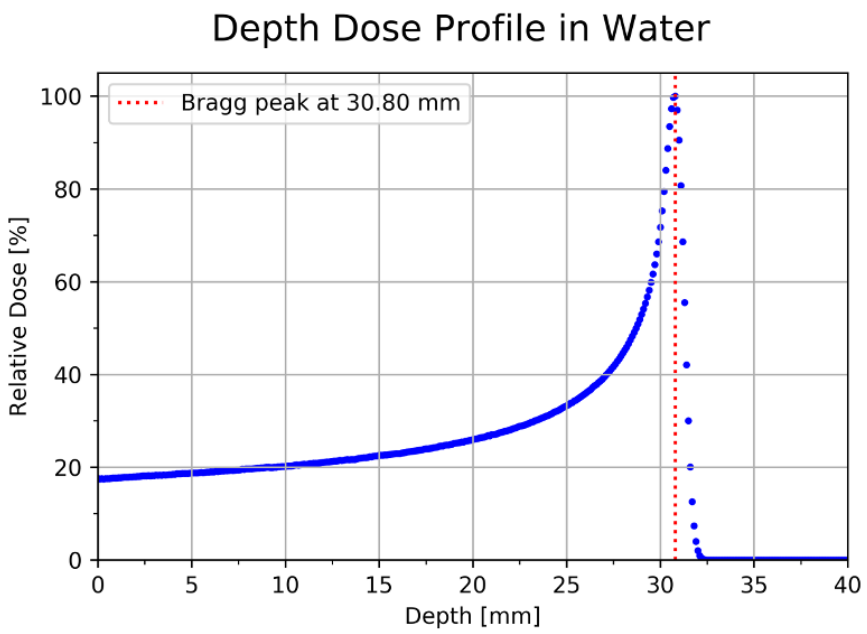

(b)

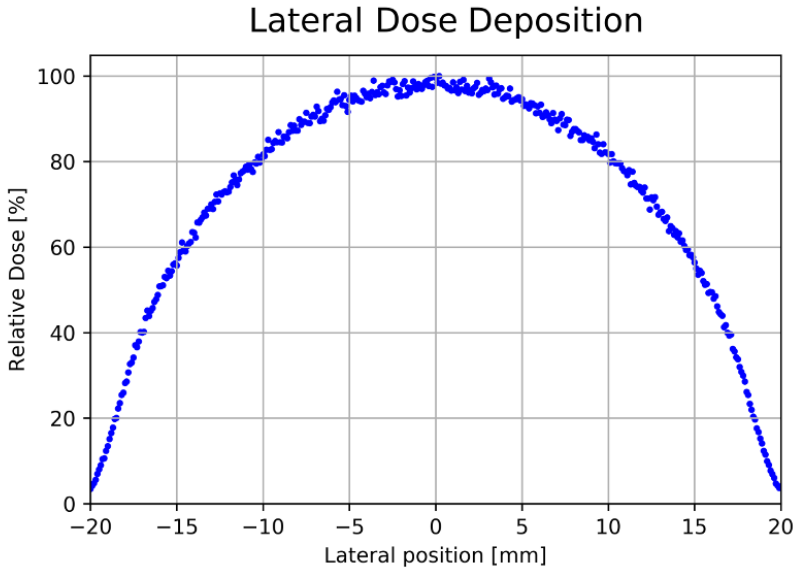

Figure B.1: a) CCC dose and b) lateral beam profile at isocentre ($z = 1829$) as simulated in GEANT4 with 10M primaries scored within 400 bins of a $40 \times 40 \times 40$ mm^3 cube of water.

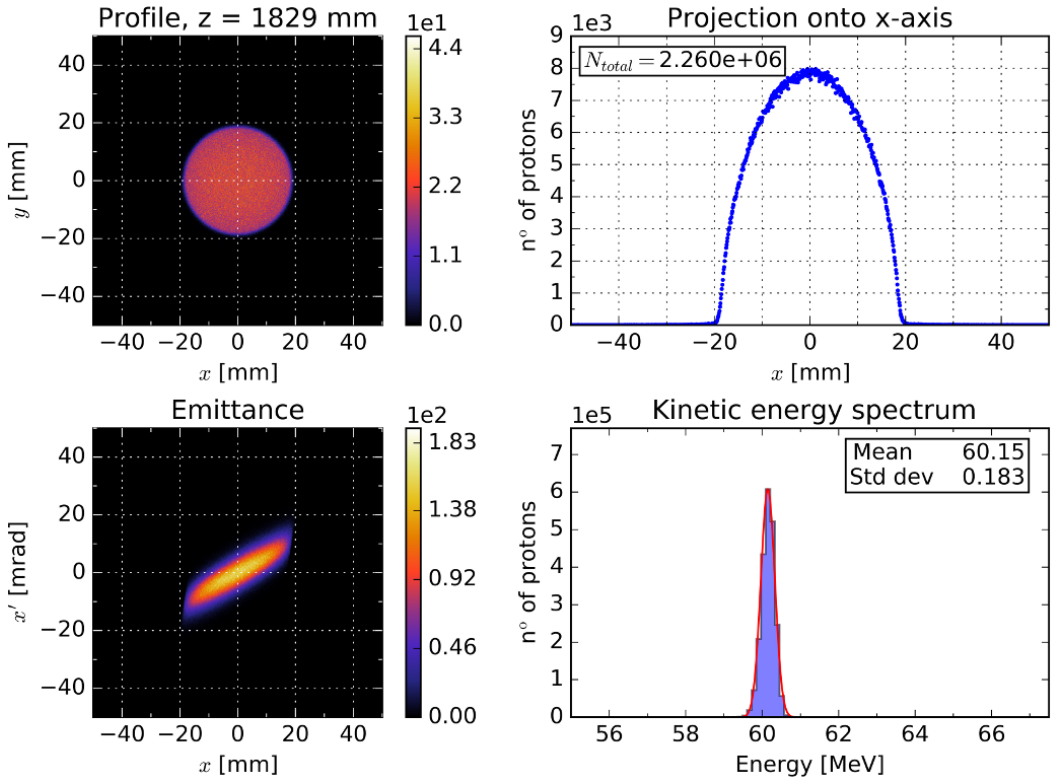

Figure B.2: Characterisation plots at isocentre using default beam parameters.

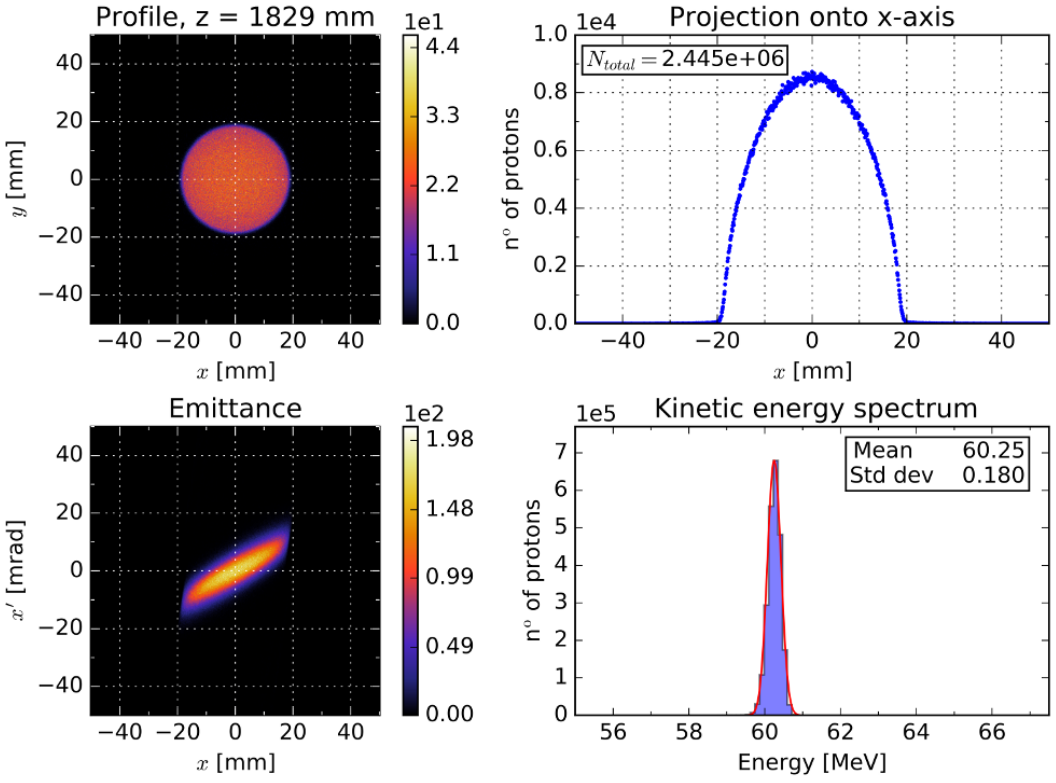

Figure B.3: Characterisation plots at isocentre using default beam parameters with implemented updates to the scattering foil and dose monitor geometries.

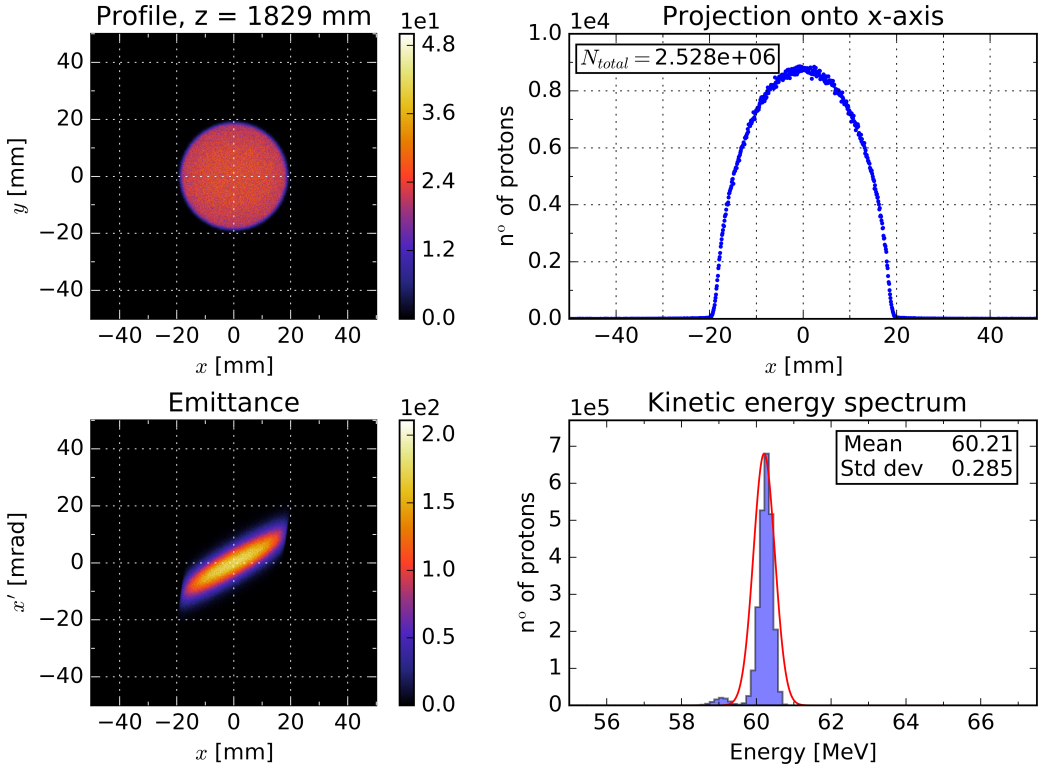

Figure B.4: Characterisation plots at isocentre with a silicon disc at z = 736 mm.

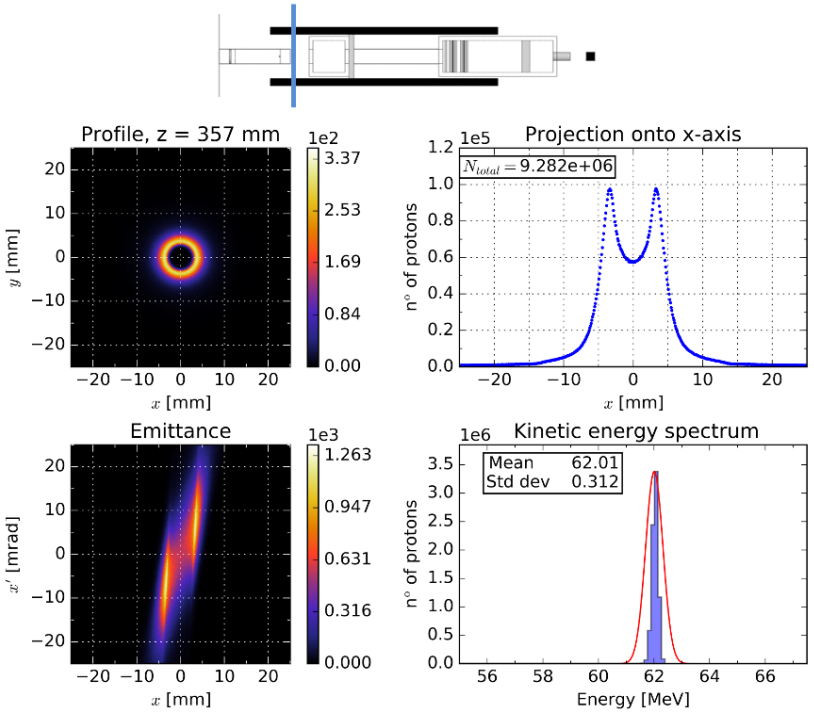

Figure B.5: Characterisation plots, the beam has just exited the kapton window into air.

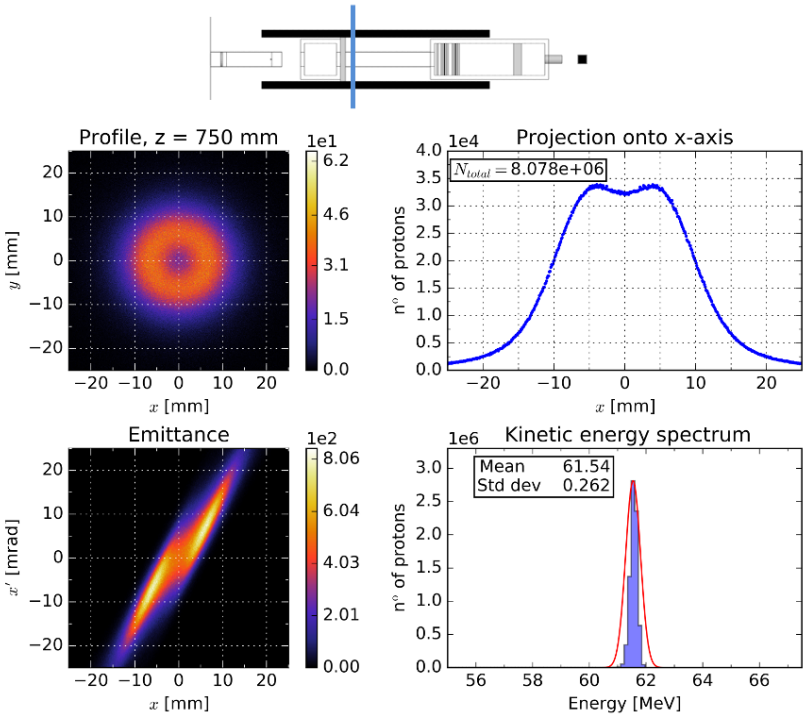

Figure B.6: Characterisation plots, the beam is near the start of the integration zone in the removable aluminium pipe.

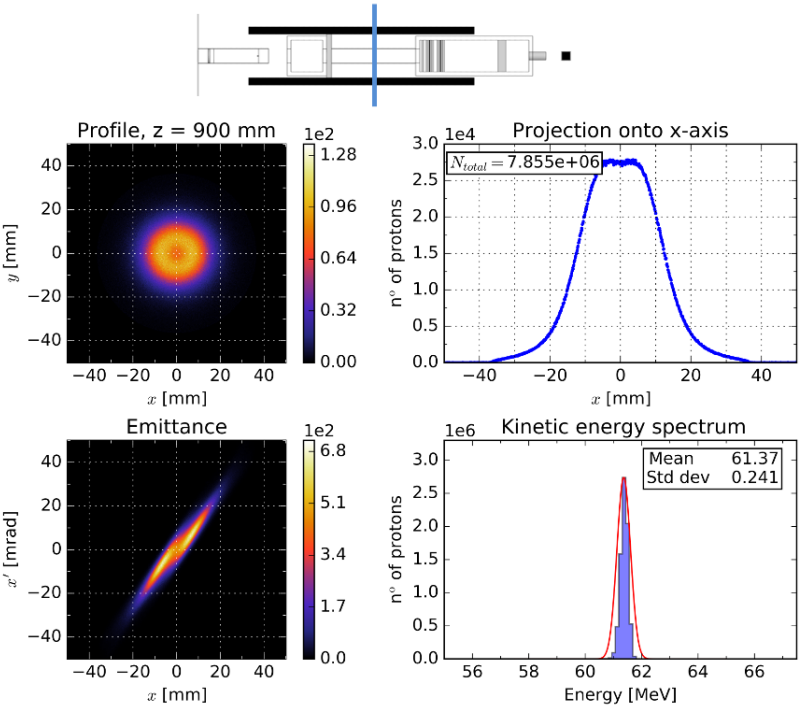

Figure B.7: Characterisation plots, the beam is in the middle of the integration zone.

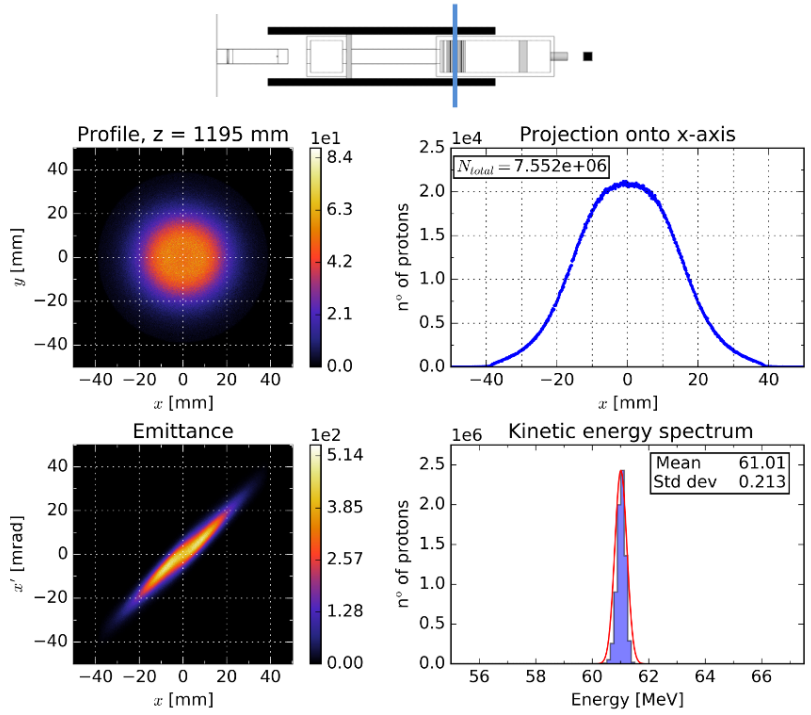

Figure B.8: Characterisation plots, the beam is in the air gap between the dose monitors having just traversed the first ion chamber.

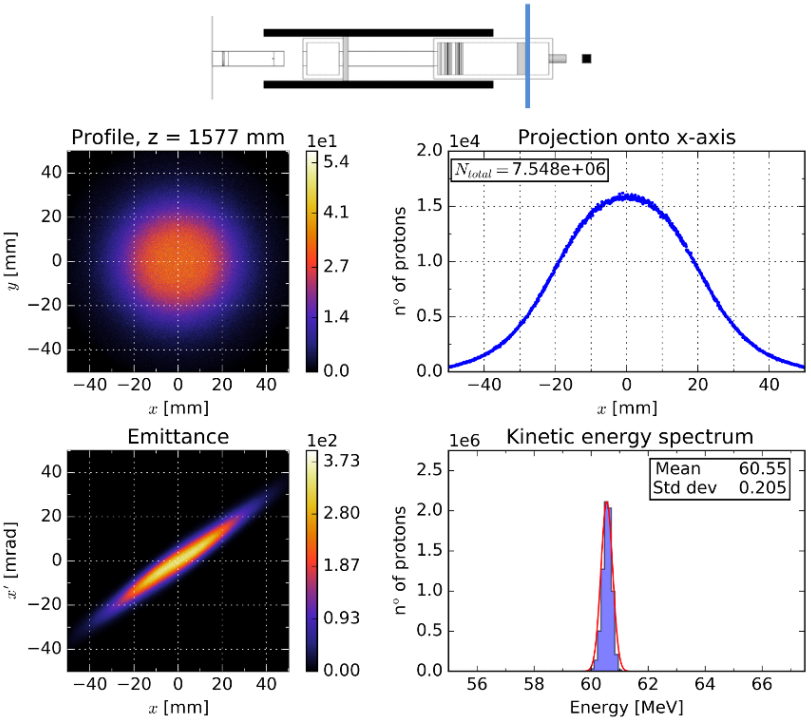

Figure B.9: Characterisation plots, the beam has just passed the cross-wires.

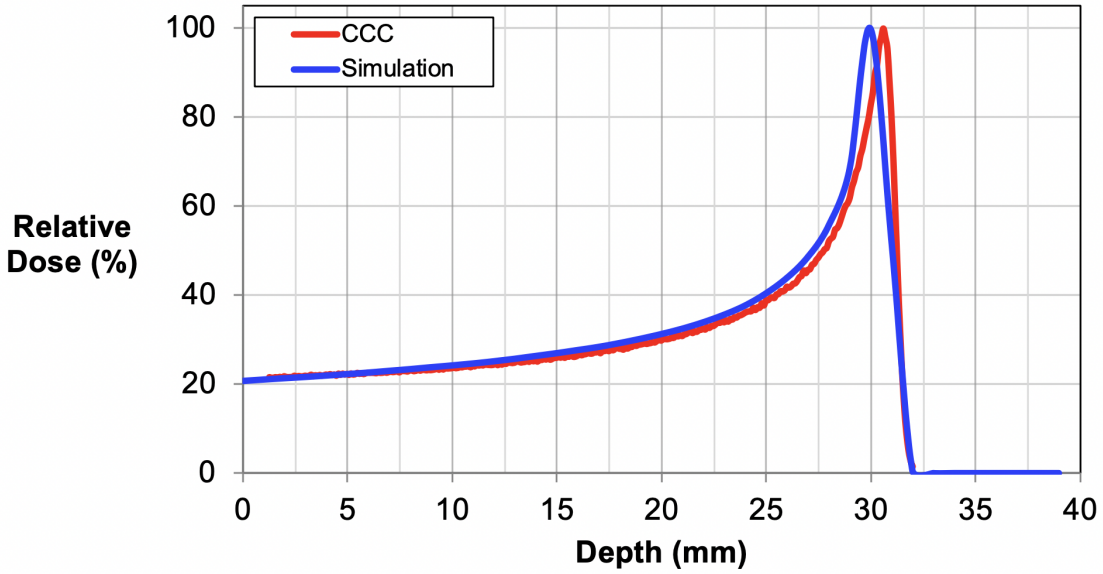

Figure B.10: CCC dose profiles simulated (red) at 30.50 mm and measured (blue) at 30.80 mm.

Table B.1: Proton ranges (in water) calculated from stopping powers on [225].

Energy [MeV]	**Range** [mm]
59.48	30.80
60.00	30.93
62.00	32.81
62.50	33.29

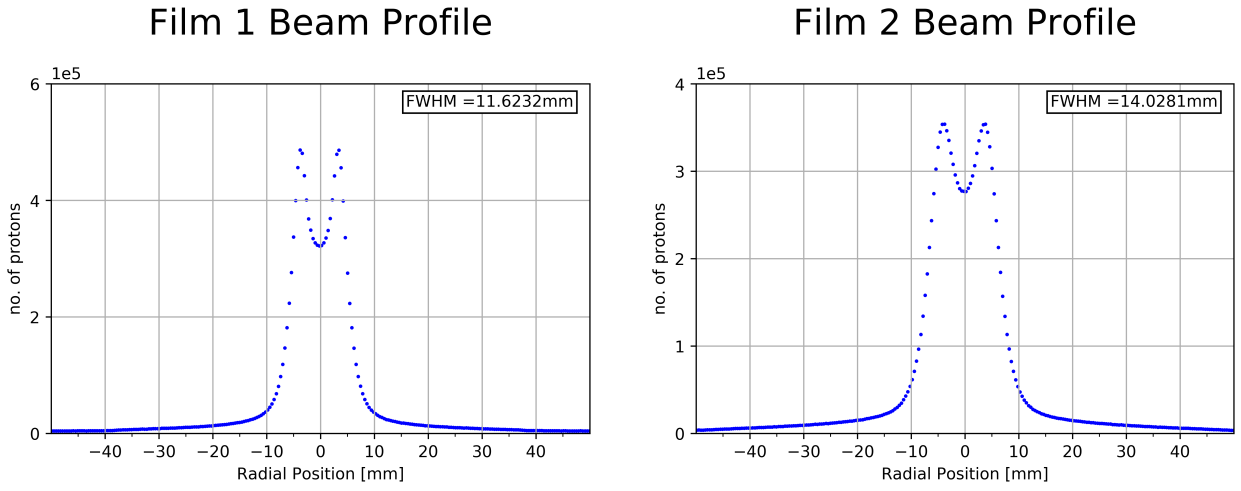

(a) (b)

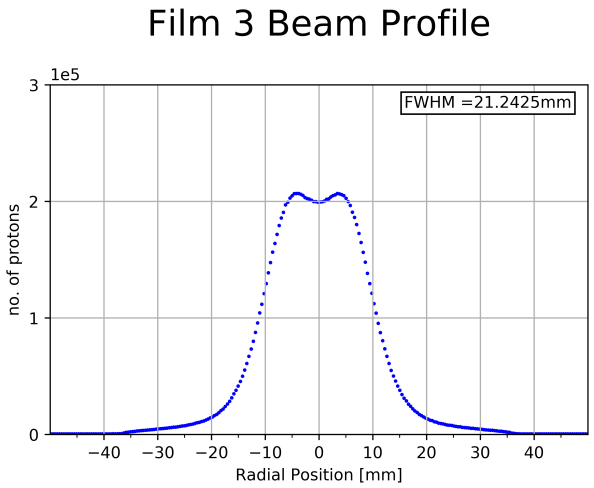

(c)

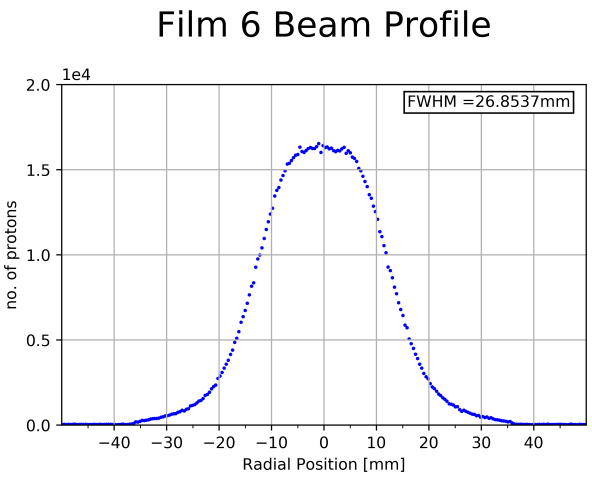

(d)

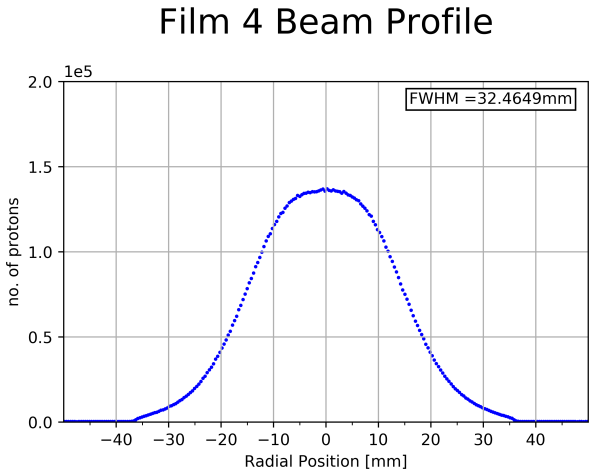

(e)

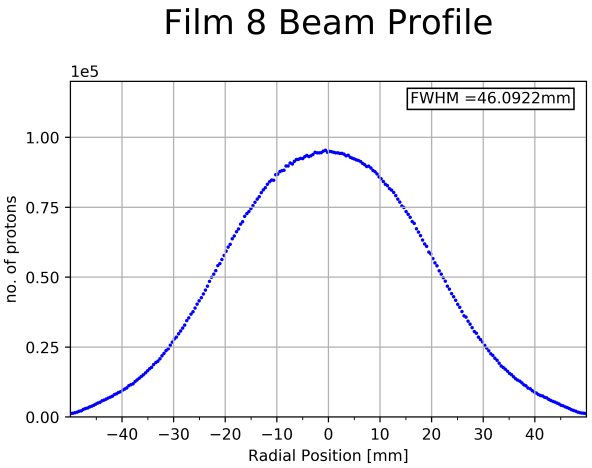

(f)

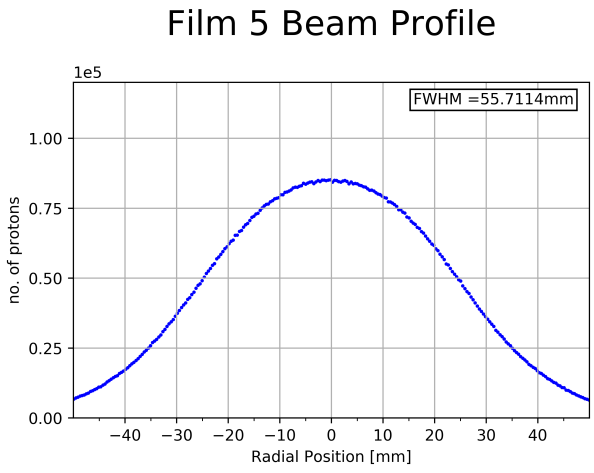

(g)

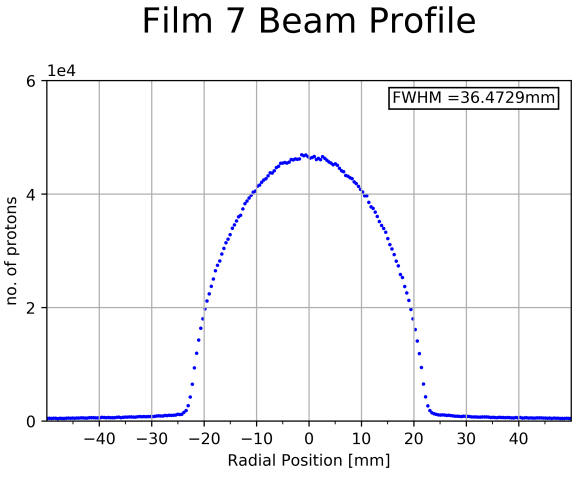

(h)

Figure B.11: Simulated beam profiles in x, at each corresponding film in order of position along beamline: 1, 2, 3, 6, 4, 8, 5 and 7.

B.2 GEANT4 Code

```
// M Hentz, 2016
// Edited J Yap, 2018

#ifndef SteppingAction_h
#define SteppingAction_h 1

#include "G4UserSteppingAction.hh"
#include "G4VProcess.hh"

class DetectorConstruction;
class RunAction;
class SteppingActionMessenger;

class SteppingAction : public G4UserSteppingAction
{
public:
SteppingAction(DetectorConstruction*, RunAction*);
virtual ~SteppingAction();

virtual void UserSteppingAction(const G4Step*);

inline void InitialiseFiles();

// used to set tracking options in macro file
void SetTracking(G4String trackingString)
{
// track at all positions defined in trackingPosFiller below
if (trackingString == "All")
{
isTracked = true;
trackSingle = false;

// For default "All"
//std::vector<int> trackingPosFiller(38);
std::vector<int> trackingPosFiller(9);
//trackingPosFiller = { 0, 45, 79, 81, 100, 150, 200, 250, 299, 300, 307,
350, 400, 449, 471, 629, 676, 700, 750, 800, 850, 900, 950, 1000, 1050,
1099, 1121, 1129, 1141, 1149, 1265, 1535, 1577, 1671, 1759, 1800,
1839, 1881 };

//for beamsize
trackingPosFiller = { 0, 357, 471, 676, 756, 1099, 1265, 1759, 1829 };

//for absorber
//trackingPosFiller = { 0, 1759, 1815, 1827, 1829, 1839, 1850 };
//trackingPosFiller = { 0, 1759, 1800, 1827, 1829, 1839 };

//for no dose monitors
//trackingPosFiller = {0, 1000, 1141, 1265, 1829, 1839};

//for general data set of 15
//trackingPosFiller = { 0, 81, 307, 357, 471, 676, 750, 1099, 1195, 1265,
1577, 1759, 1829, 1871, 1875 };
```

```
54
55 //for integ zone of 16
56 //trackingPosFiller = { 676, 706, 736, 766, 796, 826, 856, 886, 916, 946,
57 976, 1006, 1036, 1066, 1096, 1829};
58
59 //for si disc
60 //trackingPosFiller = { 676, 706, 736, 766, 796, 826, 856, 886, 916, 946,
61 976, 1006, 1036, 1066, 1096, 1829};
62
63 trackingPosVec = trackingPosFiller;
64 }
65 // no tracking
66 else if (trackingString == "None")
67 { isTracked = false; }
68 // track at single position given in the macro
69 else
70 {
71 isTracked = true;
72 trackSingle = true;
73
74 trackerPos = std::stoi(trackingString);
75
76 std::vector<int> trackingPosFiller(1);
77 trackingPosFiller = { trackerPos };
78
79 trackingPosVec = trackingPosFiller;
80 }
81
82 InitialiseFiles();
83 }
84
```

Figure B.12: SteppingAction.hh with z positions defined for beam characterisation and VELO studies.

```
1 ...
2 }
3 //---------------------------------------------------------------------------
4 // Sensitive detector over parameterised volumes
5 // - Same as /all command except over the distances specified below
6 // 40x40x40mm cube after isocentre = 1829. Centred at 1849
7 //   J Yap 23/8/18
8 //---------------------------------------------------------------------------
9
10 if( fDetChoice == "detectorvolume" ){
11
12 // Container - L1
13 // fdetectorvolPosition wtr room ie centred at fdetectorvolPosition=1860
14
15 G4double containerPositionZnew  = -fRoomSizeZ/2 + fdetectorvolPosition;
16 //G4double containerLengthNew = 2100*CLHEP::mm - containerPositionZnew;
17 //take width as fcontainerlength is from proton.mac
18 G4double containerLengthNew  = fRoomSizeZ/4;
```

```
19 G4Box* sParallelContainer = new G4Box( "parallel_container", width/2, width/2,
20 containerLengthNew/2 );
21 G4LogicalVolume* lParallelContainer = new G4LogicalVolume( sParallelContainer,
22 0, "parallel_container" );
23
24 // New position of parallel container - L2
25 new G4PVPlacement( 0, G4ThreeVector(0., 0., containerPositionZnew),
26 lParallelContainer, "parallel_container", lGhostWorld, false, 0 );
27
28 //-------------------------------------------------------------------------
29 // Detector for parametrised volumes - L3
30 // Position relative to room: z = -4200 + fdetectorvolPosition/2
31 //-------------------------------------------------------------------------
32
33 // Container solid and logical volume to be replicated
34 G4VSolid* sParallelDet = new G4Box( "parallel_detector", fContainerLength/2,
35 fContainerLength/2, thickness/2 );
36 G4LogicalVolume* lParallelDet = new G4LogicalVolume( sParallelDet, 0,
37  "parallel_detector" );
38
39 // Construct fNoOfCopies parametrised volumes along the z axis
40 ParallelWorldParam* parametrisation2 = new ParallelWorldParam( fContainerLength,
41 fDetSpacing );
42 new G4PVParameterised( "parallel_detector", lParallelDet, lParallelContainer,
43 kZAxis, fNoOfCopies, parametrisation2 );
44
45 // Define sensitive detector on parametrised volumes
46 PhaseSpaceSD* sd = new PhaseSpaceSD( "/sd/phaseSpace" );
47 SDman->AddNewDetector( sd );
48 lParallelDet->SetSensitiveDetector( sd );
49
50 G4cout << "Value of detector" << fDetChoice << "pos" << fdetectorvolPosition
51 << G4endl;
52
53 ///
54
55 /*// starting position of first parameterised slice
56 G4double detectorvolPositionFirstPos = -950.*CLHEP::mm + (fdetectorvolPosition -
57  fContainerLength/2 + fDetSpacing/2);
58
59 // Define solid and logical volume to be replicated dimensions/2
60 G4VSolid* sParallelDetVol = new G4Box( "parallel_detectorvol", fContainerLength/2,
61 fContainerLength/2, thickness/2 );
62 G4LogicalVolume* lParallelDetVol = new G4LogicalVolume( sParallelDetVol, 0,
63 "parallel_detectorvol" );
64
65 // Construct fNoOfCopies parametrised volumes along the z axis
66 ParallelWorldParam* parametrisation2 = new ParallelWorldParam( fNoOfCopies,
67 detectorvolPositionFirstPos, fContainerLength, fDetSpacing );
68 new G4PVParameterised("parallel_detectorvol", lParallelDetVol, lParallelContainer,
69 kZAxis, fNoOfCopies, parametrisation2);
70
71 // Define sensitive detector on parametrised volumes
72 PhaseSpaceSD* sd = new PhaseSpaceSD( "/sd/phaseSpace" );
73 SDman->AddNewDetector( sd );
74 lParallelDetVol->SetSensitiveDetector( sd );*/
75 }
```

```
76
77  //-------------------------------------------------------------------------------
78  // Sensitive detector on single volume
79  // - Defines sensitive detector on a volume chosen in the macro using the
80  //   /parallel/detector command.
81  // JY 30/01/19
82  // MH defined containervol as 1900mm for this option, for the others JY defined it
83  // as 2400mm (fRoomSizeZ/4) such that it is consistent with the treatment beamline z
84  //-------------------------------------------------------------------------------
85
86  if( fDetChoice != "all" && fDetChoice != "detectorvolume" ){
87  G4String sdVolName = "sd_" + fDetChoice;
88
89  G4Box* sParallelContainer = new G4Box( "parallel_container", width/2, width/2,
90  fContainerLength/2 );
91  G4LogicalVolume* lParallelContainer = new G4LogicalVolume( sParallelContainer, 0,
92  "parallel_container" );
93
94  new G4PVPlacement( 0, G4ThreeVector(0., 0., containerPositionZ), lParallelContainer,
95  "parallel_container", lGhostWorld, false, 0 );
96
97  // Define map of component positions of face closest to the source, ie the face
98  // hit first by the proton beam. This allows retrieving the position by the
99  component's name.
100 // JY - Component position = -1900/2 + (position in z)
101 std::map< G4String, G4ThreeVector > componentPosition;
102 componentPosition["scatterfoil1"] = G4ThreeVector(0., 0., -869.*CLHEP::mm); //81
103 componentPosition["tube1"]        = G4ThreeVector(0., 0., -593.*CLHEP::mm);
104 componentPosition["nozzle"]       = G4ThreeVector(0., 0.,  750.*CLHEP::mm);
105 componentPosition["outside"]      = G4ThreeVector(0., 0.,  818.*CLHEP::mm);
106 // 1768 mm ie 1cm after nozzle
107 // JY - Add sensitive detector to water phantom at BP position
108 componentPosition["phantom"]      = G4ThreeVector(0., 0.,  910.*CLHEP::mm);
109 //1860 mm
110 //add variable component dependent on location z, change z coord here before running
111 componentPosition["film1"]      = G4ThreeVector(0., 0., -593.*CLHEP::mm);
112 componentPosition["film1new"]      = G4ThreeVector(0., 0., -570.*CLHEP::mm);
113 componentPosition["film2"]      = G4ThreeVector(0., 0., -501.*CLHEP::mm);
114 componentPosition["film_integzone"]      = G4ThreeVector(0., 0., -274.*CLHEP::mm);
115 componentPosition["film6"]      = G4ThreeVector(0., 0., -104.*CLHEP::mm);
116 componentPosition["film4"]      = G4ThreeVector(0., 0., 59.*CLHEP::mm);
117 componentPosition["film8"]      = G4ThreeVector(0., 0., 496.*CLHEP::mm);
118 componentPosition["film5"]      = G4ThreeVector(0., 0., 721.*CLHEP::mm);
119 componentPosition["film7"]      = G4ThreeVector(0., 0., 921.*CLHEP::mm);
120
121 // Define volume for sensitive detector
122 G4VSolid* sDetector = new G4Box( sdVolName, width/2, width/2, thickness/2 );
123 //14.*CLHEP::um);//JY//;
124 G4LogicalVolume* lDetector = new G4LogicalVolume( sDetector, 0, sdVolName );
125
126 // Shift position of detector so faces of detector and component volume coincide
127 G4ThreeVector detPosition = componentPosition.at(fDetChoice) + G4ThreeVector(0.,
128 0., 0.5*CLHEP::nm);
129 new G4PVPlacement(0, detPosition, lDetector, sdVolName, lParallelContainer,
130 0, 0, 0);
131
132 // Define sensitive detector on volume
```

```
133 PhaseSpaceSD* sd = new PhaseSpaceSD( "/sd/phaseSpace/" + fDetChoice );
134 SDman->AddNewDetector( sd );
135 lDetector->SetSensitiveDetector( sd );
136
137 ...}
```

Figure B.13: ParallelWorldConstruction.cc adapted from M Hentz, 2018.

```
1  // M Hentz, 2016
2  // J Yap, 2018 edited to get eDep in layers
3
4  #include <iostream>
5
6  #include "RunAction.hh"
7  #include "RunActionMessenger.hh"
8  #include "DetectorConstruction.hh"
9  #include "EventAction.hh"
10 #include "PhysicsList.hh"
11 #include "PrimaryGeneratorAction.hh"
12 #include "RunAccumulator.hh"
13
14 #include "G4Run.hh"
15 #include "G4UnitsTable.hh"
16 #include "G4SystemOfUnits.hh"
17 #include "G4ios.hh"
18 #include "G4Event.hh"
19 #include "Randomize.hh"
20
21 //#include "ParallelWorldConstruction.hh"
22 using namespace std;
23
24 RunAction::RunAction( DetectorConstruction* det, PhysicsList* phys,
25 PrimaryGeneratorAction* kin )
26 :G4UserRunAction(),
27 fAnalysisManager(0),
28 fDetector(det),
29 fPhysics(phys),
30 fKinematic(kin),
31 fLayerEdep(new G4double[MaxLayer]),
32 fEdepTot(0.),
33 fNbPrimarySteps(0),
34 fBufferSize(1000),
35 fDumpSingle(0)
36 {
37 fRunActionMessenger = new RunActionMessenger( this );
38 }
39
40 RunAction::~RunAction()
41 {
42 delete fRunActionMessenger;
43 delete [] fLayerEdep;
44 }
45
```

```
46 void RunAction::BeginOfRunAction( const G4Run* aRun )
47 {
48 G4cout << "### Run " << aRun->GetRunID() << " start." << G4endl;
49
50 // JYAP updated 2018
51 //create messenger link
52 MaxLayer = fDetector ->GetLayerNumber();
53 //MaxLayer = fContainerLength ->GetContainerLength();
54 //MaxLayer = fDetDistance ->GetDetDistance();
55
56 //create edep file
57 // Dump
58 psfile.open( "data/edep.txt",  ofstream::app );
59
60 // Set precision of variables to be dumped
61 psfile
62 <<  setiosflags( ios::fixed)
63 <<  setprecision(8);
64
65 G4String header = "eDep [MeV]";
66 psfile << header << G4endl;
67 psfile.close();
68
```

Figure B.14: RunAction.cc

```
1  ###############################################################################
2  ## This macro file is used to run Geant4 simulations in batch mode.           ##
3  ##                                                                            ##
4  ## - Several settings are preset.                                             ##
5  ## - Comment/uncomment add/remove lines as required.                          ##
6  ## - Parallel simulations can be run, where "parallel" is taken to mean       ##
7  ##   several simulations running concurrently. If doing so, the "parallel"    ##
8  ##   version of the command to execute the gps.mac macro, /control/execute,   ##
9  ##   the command to set the seeds, /random/setSeeds, and the command to run   ##
10 ##   the simulation, /run/beamOn, should be uncommented.                      ##
11 ##   (Don't forget to comment the normal commands.)                           ##
12 ##                                                                            ##
13 ##    Author: 07/03/2018, M. Hentz                                            ##
14 ##                Edited, J. Yap 2019
15 ##                                                                           ##
16 ###############################################################################
17
18 #------------------------------------------------------------------------------
19 # Set verbosity
20 #------------------------------------------------------------------------------
21 /control/verbose 0
22 #/run/verbose 2
23 /run/verbose 0
24 /run/particle/verbose 0
25 #/run/particle/dumpList
26 /tracking/verbose 0
27
```

```
28 #------------------------------------------------------------------------------
29 # Primary generator settings
30 #------------------------------------------------------------------------------
31 # Choose how to generate primary particles and set required settings.
32 #
33 #   1) The macro gps.mac uses /gps/ commands to set desired energy
34 #      distribution, mean energy, std dev, gun position, beam width,
35 #      angular distribution.
36 #
37 #   2) Particles can be generated from a phase space file. The input
38 #      should contain the following values separated by commas:
39 #
40 #        parentID, particleName, x, y, z, mom_x, mom_y, mom_z, ke
41 #
42 #      The positions (x, y, z) should be given in mm and the kinetic
43 #      energy (ke) should be given in MeV. The format of the input
44 #      file can be modified in FileReader.cc.
45 #
46 #      Note: parentID is redundant and is in fact ignored but it is
47 #            simplest to include it anyway as this allows an output
48 #            file from one simulation to be used as the input of
49 #            another.
50 #
51 #      The path to the file used as an input is set with:
52 #           - /primarygenerator/input path/to/file
53 #
54 #------------------------------------------------------------------------------
55
56 ## Use macro to set properties of primaries
57 #/control/execute gps.mac
58
59 # Parallel version
60 /control/execute ../../gps.mac
61
62 ## Reading from phase space file
63 #/primarygenerator/input data/psf_z0_gen.txt
64 #/primarygenerator/input path/input/psf_z81.txt
65
66 # Set position in z particles are generated at
67 /primarygenerator/generateAt 0
68 #/primarygenerator/generateAt 81
69 #/primarygenerator/generateAt 357
70 #/primarygenerator/generateAt 1700
71
72 #------------------------------------------------------------------------------
73 # Detector settings
74 #------------------------------------------------------------------------------
75 # Choose where to record particles and set required settings.
76 #
77 #  1) 'all': record along the beamline at every position at intervals
78 #            and overall distance specified below.
79 #
80 #     Set detector spacing and distance recorded below using:
81 #         - /parallel/detector/spacing
82 #         - /parallel/detector/distance
83 #
84 #     Also pass the parameters to the run action so output files
```

```
#     are written correctly:
#         - /user/run/detector/spacing
#         - /user/run/detector/distance
#
#     Set the size of the vector of hits saved in the run action with:
#         - /user/run/buffer
#
#     Once the vector reaches this size, hits are dumped to output.
#     The ideal value for this will depend on the application. Making
#     it too small results in large overhead from opening and closing
#     files too often. Making it too large leads to too much memory
#     being used. Both cases slow down the simulation considerably,
#     so play around before submitting large runs and choose wisely!
#
#  1.a) 'detectorvolume': record all but in detectorvolume
#                         - Useful for BP simulations
#                   Select detectorvolume to record particles
#                         - /parallel/detector detectorvolume
#                 Uncomment and specify options for:
#                         - /parallel/detector/position
#                         - /parallel/detector/spacing
#                         - /parallel/detector/distance
#                         - /user/run/detector/spacing
#                         - /user/run/detector/distance
#             Set the size of the vector of hits saved in the run action with:
#           - /user/run/buffer
#                 Set detector geometry and options under:
#                         - /cb_sim/det/
#
#  2) <component>: record at the specified components.
#
#     Currently available keywords: - scatterfoil1 (at 81 mm)
#                                   - tube1        (at 357 mm)
#                                   - nozzle       (at 1700 mm)
#                                   - outside      (at 1768 mm)
#
#     Component-position pairs can be added to the component map
#     in ParallelWorldConstruction. The dump function in the run
#     action needs to know if only one position is being recorded
#     so switch on "single" mode and tell it where particles are
#     recorded using:
#         - /user/run/dump/single true
#         - /user/run/detector/position
#
#------------------------------------------------------------------------------

## Choose where particles are recorded
#/parallel/detector all
/parallel/detector detectorvolume      #JY#
#/parallel/detector scatterfoil1
#/parallel/detector tube1
#/parallel/detector nozzle
#/parallel/detector outside
#/parallel/detector phantom
#/parallel/detector film1
#JY#/parallel/detector film1new
#/parallel/detector film2
```

```
#/parallel/detector film_integzone
#/parallel/detector film6
#/parallel/detector film4
#/parallel/detector film8
#/parallel/detector film5
#/parallel/detector film7

## If using 'all'
#/parallel/detector/spacing 25 mm
#/parallel/detector/distance 1900 mm

## If using 'detectorvolume' uncomment all here
/parallel/detector/position 379 mm
/parallel/detector/spacing 27 um #JY#0.1 mm     # slice size, default is 25 mm
/parallel/detector/distance 27 um #JY#40 mm  # length of detector, for BP 40 mm
/user/run/detector/spacing 27 #JY#0.1
/user/run/detector/distance 27 #JY#40       # same as detector distance

# Pass spacing and distance to run action
#/user/run/detector/spacing 25
#/user/run/detector/distance 1900

# Set buffer size
/user/run/buffer 5000 #JY#

## If using a component, set dump mode and detector position
#JY#/user/run/dump/single true
#/user/run/detector/position 81
#/user/run/detector/position 357
#JY#/user/run/detector/position 380
#/user/run/detector/position 449
#/user/run/detector/position 676
#/user/run/detector/position 846
#/user/run/detector/position 1009
#/user/run/detector/position 1557
#/user/run/detector/position 1671
#/user/run/detector/position 1871

#------------------------------------------------------------------------------
# Stepping action settings
#------------------------------------------------------------------------------
# Choose where to kill particles if required. This can be useful if
# only a given section of the beamline needs to be simulated.
#
# To be safe and not accidentally interfere with the ongoing
# simulation, this should ideally be done after the particles have
# been recorded.
#
# Here, particles are killed 1 mm after being recorded.
#
#------------------------------------------------------------------------------

## Kill particles 1 mm after being recorded
#/steppingAction/kill 82
#/steppingAction/kill 358
#/steppingAction/kill 1701
#/steppingAction/kill 1769
```

```
199 #/steppingAction/kill 500
200
201 #------------------------------------------------------------------------------
202 # Set physics process
203 #------------------------------------------------------------------------------
204 # Choose physics list and set range cuts.
205 #
206 # Cuts should be set such that they are no bigger than 10% of slice thickness.
207 #------------------------------------------------------------------------------
208
209 ## Choose physics list
210 /cb_sim/phys/addPhysics QGSP_BIC_HP
211 #/cb_sim/phys/addPhysics QGSP_BIC_EMY
212 #/cb_sim/phys/addPhysics emlivermore
213 #/cb_sim/phys/addPhysics empenelope
214
215 ## Production thresholds
216 /cb_sim/phys/setCuts 0.1 mm
217 #/cb_sim/phys/setGCut 1 um
218 #/cb_sim/phys/setECut 1 um
219 #/cb_sim/phys/setPCut 1 um
220
221 #------------------------------------------------------------------------------
222 # Set detector geometry
223 #------------------------------------------------------------------------------
224 /cb_sim/det/setMaterial PMMA #JY#Water
225 /cb_sim/det/setPosition 0 0 -3820 mm #JY# wrt room ie -4200-(detectorvolume position)
226 /cb_sim/det/setSizeXY 40 mm
227 /cb_sim/det/setSizeZ  27 um #JY#40 mm
228 /cb_sim/det/setSliceSizeXY 40 mm
229 /cb_sim/det/sliceNumber 1 #JY#400
230 #number of layers for edep calc needs to be less than det distance
231
232 #------------------------------------------------------------------------------
233 # Initialize kernel
234 #------------------------------------------------------------------------------
235 /run/initialize
236
237 #------------------------------------------------------------------------------
238 # Activate sensitive detector
239 #------------------------------------------------------------------------------
240 /hits/activate /sd/phaseSpace
241
242 #------------------------------------------------------------------------------
243 # Set seeds for randon number generators
244 #------------------------------------------------------------------------------
245 # If running simulations "in parallel", the variables seed1 and seed2 are set by
246 # the submission script cb_parallel.sh.
247 # Make sure to uncomment the corresponding line.
248 #------------------------------------------------------------------------------
249 #/random/setSeeds 1 100
250
251 # Parallel version
252 /random/setSeeds ${seed1} ${seed2}
253
254 #------------------------------------------------------------------------------
255 # Step limit
```

```
256 #------------------------------------------------------------------------------
257 # Step limit shouls be set such that it is no bigger than 5% of slice thickness
258 #------------------------------------------------------------------------------
259 /cb_sim/stepMax 0.1 mm #JY#
260
261 #------------------------------------------------------------------------------
262 # Print to console
263 #------------------------------------------------------------------------------
264 # Choose how often to print event number to console.
265 #------------------------------------------------------------------------------
266 /cb_sim/event/printModulo 1000
267
268 #------------------------------------------------------------------------------
269 # Run simulation
270 #------------------------------------------------------------------------------
271 # Choose how many primaries should be simulated.
272 #
273 # If running simulations "in parallel", the variable nevents is set by
274 # cb_parallel.sh. Make sure to uncomment the corresponding line. Check the
275 # number of events matches the number of lines in the input file. If that is
276 # not the case, you may get a segmentation fault.
277 #------------------------------------------------------------------------------
278 /run/beamOn 5000
279
280 # Parallel version with split input file
281 #/run/beamOn ${nevents}
```

Figure B.15: proton.mac

B.3 Beam Dynamics Study

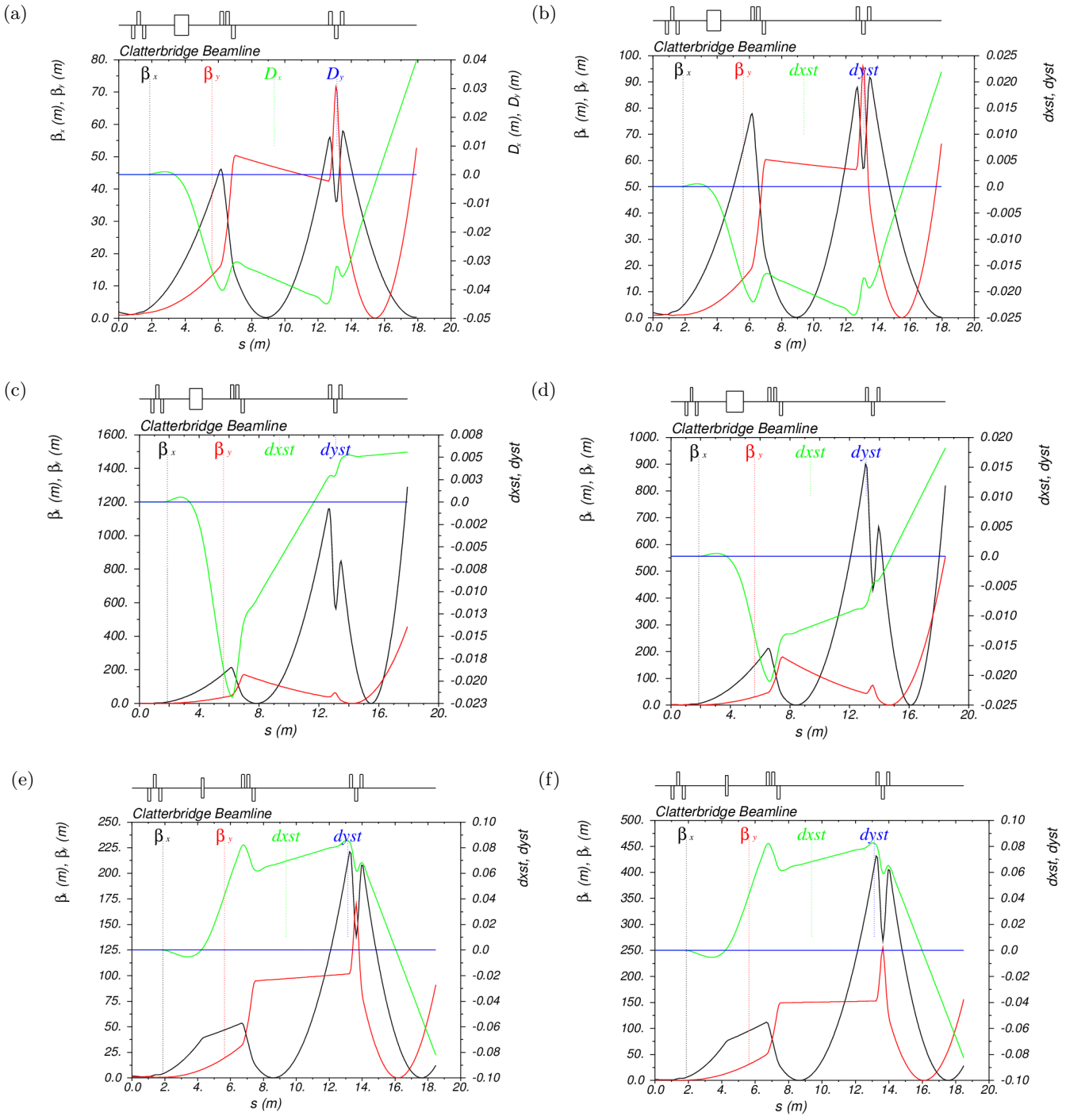

Figure B.16: Iterations of the CCC beamline lattice in MAD-X showing progressive changes to the Twiss functions following the discovery of facility information: emittance values, quadrupole parameters and other measurements.

```
1  ////////////////////////////////////////////////////////////////////
2  //                                                                //
3  // Clatterbridge Cancer Centre 62 MeV eye proton therapy beamline //
4  //                                                                //
5  // J Yap, July 2019                                               //
6  ////////////////////////////////////////////////////////////////////
7
8  // V2 developed using lattice info from OK
9  // V3 improved upon by verifying all lattice information
10 //uncertainty approx +/-10cm (differences between physical & schematics)
11 //experimental measurements providing twiss parameters to follow
12 // V4 replaced all lengths of quads with approximated effective lengths
13 // V6 scaled gradient coefficients
14 // V7 updated measurements
15 // V8 optimised quads, final measurements
16
17 // Limited access.. can't check: Polarities
18 // Physically double checked: Quad currents & Distances to diagnostics positions
19 // Things to consider: Fringe fields
20
21 Title, "Clatterbridge Beamline";
22 Beam, particle=proton,
23 energy:=1.00027, !all in GeV
24
25 //HO emittance 1998
26 !EX=2E-6/pi, EY=1.5E-6/pi, SIGE=    0.0001;
27 //TC emmitance 2012
28 EX=5E-6/pi, EY=1E-6/pi, SIGE=    0.0001;
29 //Documentation emittance - upper end HO paper
30 !EX=15E-6, EY=15E-6, SIGE=    0.0001; unrealistically large
31 !EX=3E-6, EY=3E-6, SIGE=    0.0001;
32
33 e0:=1.00027;
34 pc0:=0.062;
35 m0:=0.93827;
36 gamma:=e0/m0; !for momentum spread correction
37 bc0:=pc0/(m0*gamma); !relativistic beta
38
39 ASSIGN, ECHO="line.echo";
40
41 MAT1:=0.3;//3;
42 MAT2:=0.8;//8;
43 MAT3:=0.8;//8;
44
45 o: DRIFT, L=       0.77 ;
46 Q11: QUADRUPOLE,  L=      0.2,  K1=-11.93294936*MAT1;
47 o11: DRIFT, L=      0.13 ;
48 Q12: QUADRUPOLE,  L=      0.2,  K1=7.348256623*MAT1;
49 o12: DRIFT, L=      0.13 ;
50 Q13: QUADRUPOLE,  L=      0.2,  K1=-6.397589241*MAT1;
51
52 o2: DRIFT, L=      1.73 ;
53 D: RBEND,  L=      0.85,  ANGLE=-0.095993109;
54 o20: DRIFT, L=     1.88;
55
56 Q21: QUADRUPOLE,  L=      0.22,  K1=4.137794811*MAT2;
57 o21: DRIFT, L=      0.13;
```

```
58 Q22: QUADRUPOLE,  L=      0.22,  K1=1.207583305*MAT2;
59 o22: DRIFT, L=      0.13;
60 Q23: QUADRUPOLE,  L=      0.22,  K1=-4.13779481*MAT2;
61
62 o3: DRIFT, L=       5.63/10;
63 Q31: QUADRUPOLE,  L=      0.22,  K1=5.894578456*MAT3;
64 o31: DRIFT, L=      0.13;
65 Q32: QUADRUPOLE,  L=      0.22,  K1=-10.92415638*MAT3;
66 o32: DRIFT, L=      0.13;
67 Q33: QUADRUPOLE,  L=      0.22,  K1=5.894578456*MAT3;
68
69 // total distance to source plane 2.59m //
70 //pipe is 109cm from end of Q3 ie relevant beam sizes for diagnostics
71 o4: DRIFT, L=1.085; //distance from Q3 to beginning of pipe
72 //beginning of pipe / instrumentation location
73 oDiag: DRIFT, L=0.6/11; //first 60cm of pipe (probeam is 54cm)
74 o5: DRIFT, L=0.6/10; //end of pipe
75 o6: DRIFT, L=0.308/5; //bellow and cross to source plane, 30.8cm
76 mS: MARKER; //at source plane, ~2.5mm before Sf1
77
78 //first collimator 6mm diameter before scattering foil
79 oSf1: DRIFT, L= 0.05;
80 mSf1: MARKER; //at collimator
81 oend: DRIFT, L= 1.72; //to end of nozzle
82
83 MACHINE: LINE=(o,Q11, o11, Q12, o12, Q13, o2, D, o20, Q21, o21, Q22,
84 o22, Q23, o3,o3,o3,o3,o3,o3,o3,o3,o3,o3,
85 Q31, o31, Q32, o32, Q33, o4,
86 oDiag,oDiag,oDiag,oDiag,oDiag,oDiag,oDiag,oDiag,oDiag,oDiag,
87 o5,o5,o5,o5,o5,o5,o5,o5,o5,o5,
88 o6,o6,o6,o6,o6,
89 mS, oSf1, msf1, oend);
90
91 setplot, xsize=30, ysize=18;
92 setplot, lwidth=6, !line thickness
93 lscale=1.8, !axis graduation font size
94 ascale=1.5, !function label size
95 rscale=2, !axis title size
96 font=5;
97 option, echo;
98
99 use,period=machine;
100
101 //twiss tables for relativistic values
102 dxst:=table(twiss,dx)*bc0; !dispersion
103 dyst:=table(twiss,dy)*bc0;
104
105 //Plots//
106 !setplot, post=2;
107 select, flag=twiss, clear;
108 //for normal twiss table uncomment the following,
109 //keep commented out for bdsimoptics
110 select,flag=twiss,column=name,keyword,s,
111 betx,bety,dxst,dyst; //,mux,muy,alfx,alfy;
112
113 //twiss, file="twiss.tfs";
114
```

```
115 //OK inputs at entrance of Q1 = initial
116 TWISS,betx=     1.9897, alfx=      0.86,
117 bety=     1.0629, alfy=         0.2685,
118 dx=0, dpx=0, dy=0, dpy=0, file=twiss.tfs;
119
120 plot, haxis=s, vaxis1=betx,bety, vaxis2=dxst,dyst,
121 noversion=true,colour=100,interpolate=true;
122
123 survey,file=survey.cas;
124
125 stop;
```

Figure B.17: Optical lattice defined in MAD-X. Quadrupole parameters have been scaled and optimised.

```
1  ! Wed, 22 May 2019 09:55:20 +0000
2  ! pybdsim.Builder Lattice
3  ! COMPONENT DEFINITION
4
5  O: drift, l=0.77;
6  Q11: quadrupole, k1=-3.579884808, l=0.2;
7  O11: drift, l=0.13;
8  Q12: quadrupole, k1=2.204476987, l=0.2;
9  O12: drift, l=0.13;
10 Q13: quadrupole, k1=-1.9192767725, l=0.2;
11 O2: drift, l=1.73;
12 D: rbend, angle=-0.095993109, l=0.850000000031;
13 O20: drift, l=1.88;
14 Q21: quadrupole, k1=3.31023584864, l=0.22;
15 O21: drift, l=0.13;
16 Q22: quadrupole, k1=0.966066644091, l=0.22;
17 O22: drift, l=0.13;
18 Q23: quadrupole, k1=-3.31023584818, l=0.22;
19 O3: drift, l=0.563;
20 Q31: quadrupole, k1=4.71566276364, l=0.22;
21 O31: drift, l=0.13;
22 Q32: quadrupole, k1=-8.73932510455, l=0.22;
23 O32: drift, l=0.13;
24 Q33: quadrupole, k1=4.71566276364, l=0.22;
25 O4: drift, l=1.085;
26 ODIAG: drift, l=0.05454545455;
27 O5: drift, l=0.06;
28 O6: drift, l=0.0616;
29 OSF1: drift, l=0.05;
30 OEND: drift, l=1.72;
31 theendoftheline: marker;
```

Figure B.18: Optical components equivalent to the optimised MAD-X lattice, defined in BDSIM.

```
! Wed, 22 May 2019 09:55:20 +0000
! pybdsim.Builder
! BEAM DEFINITION

beam,        X0=0.0*m,
Xp0=0.0,
Y0=0.0*m,
Yp0=0.0,
alfx=0.86,
alfy=0.2685,
betx=1.9897*m,
bety=1.0629*m,
dispx=0.0*m,
dispxp=0.0,
dispy=0.0*m,
dispyp=0.0,
distrType="gausstwiss",
emitx=5e-06*m,
emity=1e-06*m,
energy=1.00027*GeV,
particle="proton",
sigmaE=0.0001;
```

Figure B.19: BDSIM beam definition file.

```
###################################
##  Run file                     ##
##  Written by J Yap 2019        ##
###################################

#-- Turn off quickly --#
i:So/BeamSource/NumberOfHistoriesInRun   = 100000
b:Gr/MyViewer/Active = "False"
i:Ts/TrackingVerbosity = 0
i:Ts/EventVerbosity = 0
i:Ts/MaxInterruptedHistories = 1000

#=====================================================================#
#  Parameter file chain
#=====================================================================#
includeFile = Materials.txt

# Run > Materials > BeamSource > Geometry > Visualiser > Scoring
> ParallelScoring >/> FilmScoring
```

Figure B.20: Run.txt parameter file.

```
1  ###################################
2  ##  Input beam                   ##
3  ##  Written by J Yap 2019        ##
4  ###################################
5
6  includeFile = Geometry/Geometry.txt
7
8  #b:Sc/Beam/Active                          = "False"
9  b:Sc/BeamSourceTwiss/Active                = "False"
10
11 s:So/BeamSource/Type                       = "Beam"
12 s:So/BeamSource/Component                  = "BeamPosition"
13 s:So/BeamSource/BeamParticle               = "proton"
14 d:So/BeamSource/BeamEnergy                 = 62.2 MeV
15 u:So/BeamSource/BeamEnergySpread           = 0.53
16 s:So/BeamSource/BeamPositionDistribution = "Gaussian"
17 s:So/BeamSource/BeamPositionCutoffShape  = "Ellipse"
18 d:So/BeamSource/BeamPositionCutoffX       = 6.89 mm #4.0 mm
19 d:So/BeamSource/BeamPositionCutoffY       = 2.14 mm #4.5 mm
20 d:So/BeamSource/BeamPositionSpreadX       = 0.6 mm
21 d:So/BeamSource/BeamPositionSpreadY       = 0.2 mm
22 s:So/BeamSource/BeamAngularDistribution  = "Gaussian"
23 d:So/BeamSource/BeamAngularCutoffX        = 2.3 mrad
24 d:So/BeamSource/BeamAngularCutoffY        = 1.2 mrad
25 d:So/BeamSource/BeamAngularSpreadX        = 0.002 mrad #2.3 mrad
26 d:So/BeamSource/BeamAngularSpreadY        = 0.001 mrad #1.2 mrad
27
28 ## TWISS ##
29 s:So/BeamSourceTwiss/Distribution = "twiss_gaussian"
30 u:So/BeamSourceTwiss/AlphaX = 5.29402
31 d:So/BeamSourceTwiss/BetaX  = 48.73517 m
32 d:So/BeamSourceTwiss/EmittanceX = 0.00005 mm # we don't multiply pi intrinsically.
33 u:So/BeamSourceTwiss/AlphaY = -6.14021
34 d:So/BeamSourceTwiss/BetaY = 13.48019 m
35 d:So/BeamSourceTwiss/EmittanceY = 0.00001 mm
36 u:So/BeamSourceTwiss/ParticleFractionX = 0.683 ## 1 sigma RMS
37 u:So/BeamSourceTwiss/ParticleFractionY = 0.683
38
39 sv:Ph/Default/Modules = 1 "g4em-standard_opt0"
40 #sv:Ph/Default/Modules = 2 "g4em-standard_opt3"
41 "g4h-phy_QGSP_BIC_HP" #"g4em-standard_opt0"
42 ##s:Ph/Default/Type = "QGSP_BIC_HP" #"QGSP_BERT_HP" #"QGSP_BIC_EMY"
43 #d:Ph/Default/CutForAllParticles = 0.05 mm
44 d:Ph/Default/CutForElectron = 0.01 mm
45 d:Ph/Default/CutForProton = 0.01 mm
46 d:Ph/Default/CutForGamma = 0.1 mm
47 d:Ph/Default/CutForPositron = 0.1 mm
48 #b:Ph/ListProcesses = "True"
```

Figure B.21: BeamSource.txt.

B.4 Film and Image Analysis

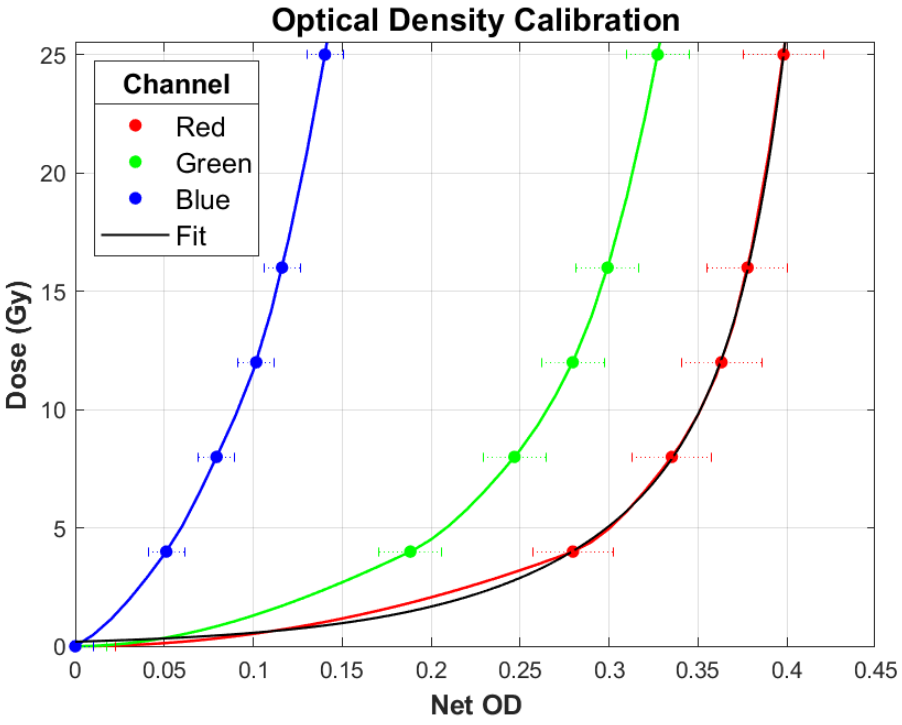

Figure B.22: Calibration curve obtained for Medipix3 measurements.

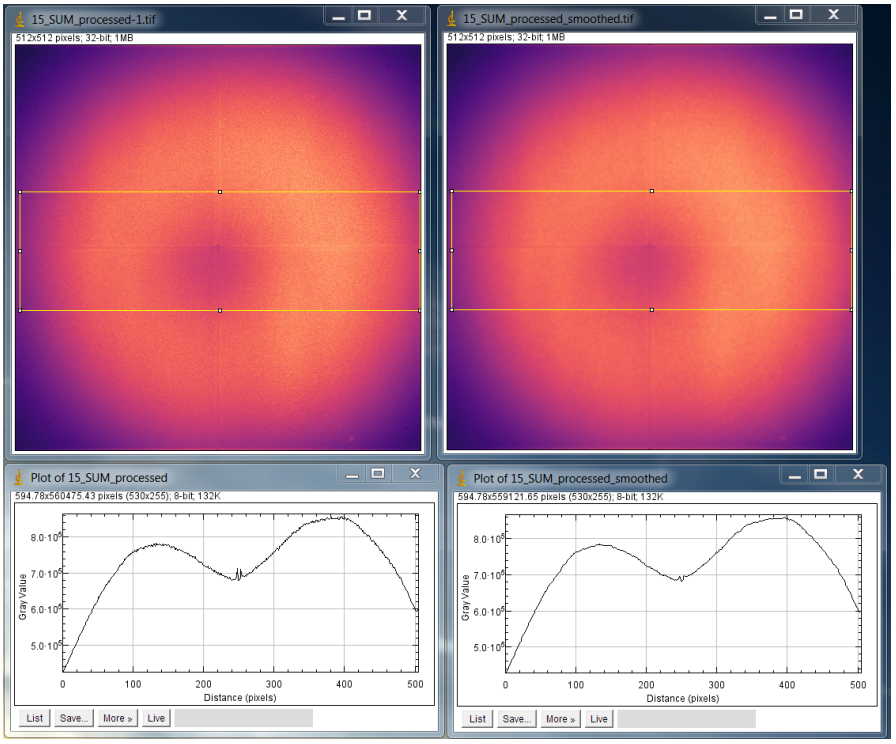

Figure B.23: Images generated from a run with Medipix3 in the integration zone. Intensity values per pixel position are graphed with ImageJ. Original image (left) and after post-processing (right).

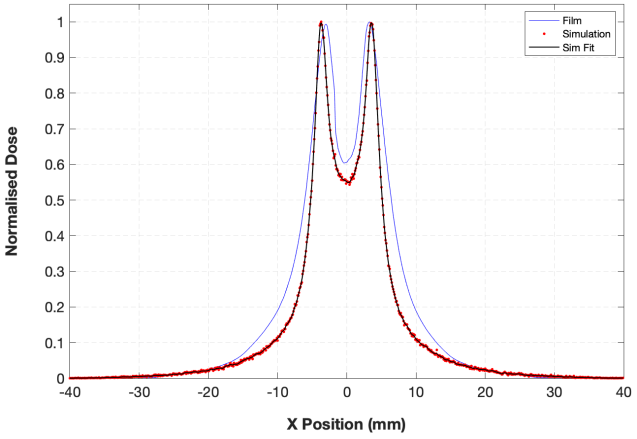
Film
Simulation
Sim Fit
Normalised Dose
X Position (mm)

(a)

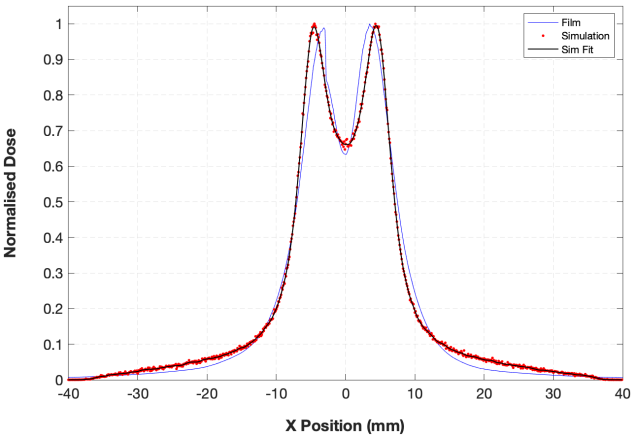
Film
Simulation
Sim Fit
Normalised Dose
X Position (mm)

(b)

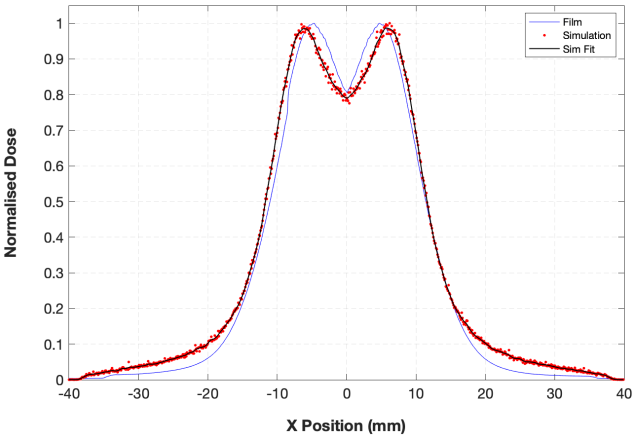
Film
Simulation
Sim Fit
Normalised Dose
X Position (mm)

(c)

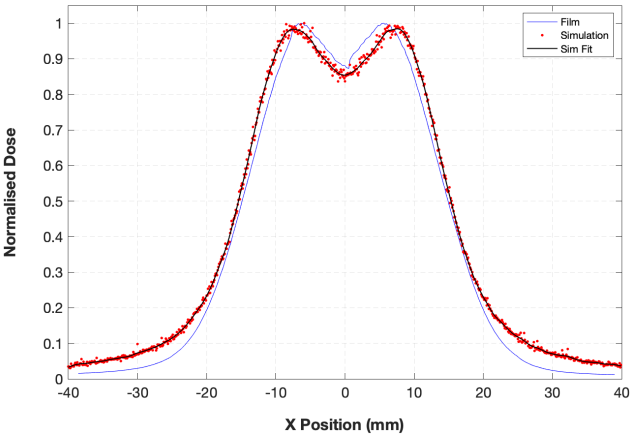
Film
Simulation
Sim Fit
Normalised Dose
X Position (mm)

(d)

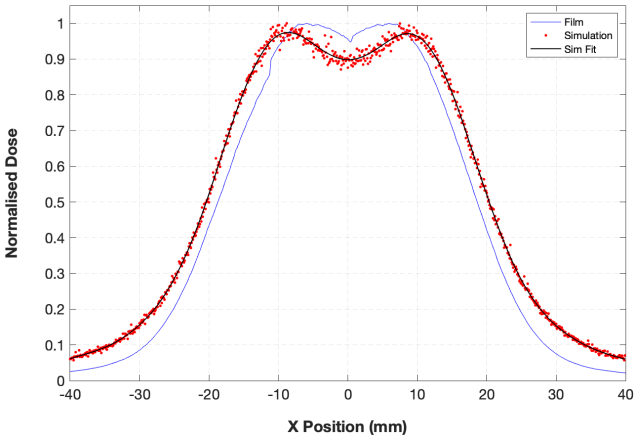
Film
Simulation
Sim Fit
Normalised Dose
X Position (mm)

(e)

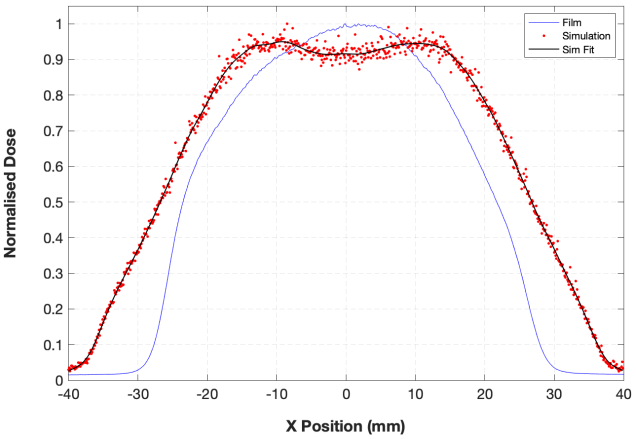
Film
Simulation
Sim Fit
Normalised Dose
X Position (mm)

(f)

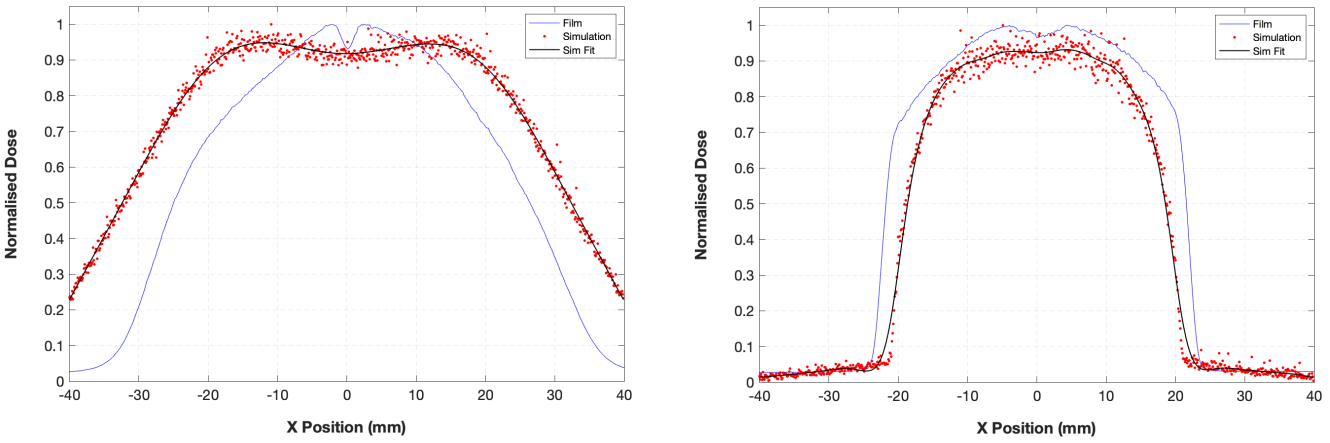

(g) (h)

Figure B.24: TOPAS simulated beam profiles in the x plane, at each corresponding film in order of position along beamline a) 1. b) 2. c) 3. d) 6. e) 4. f) 8. g) 5. h) 7.

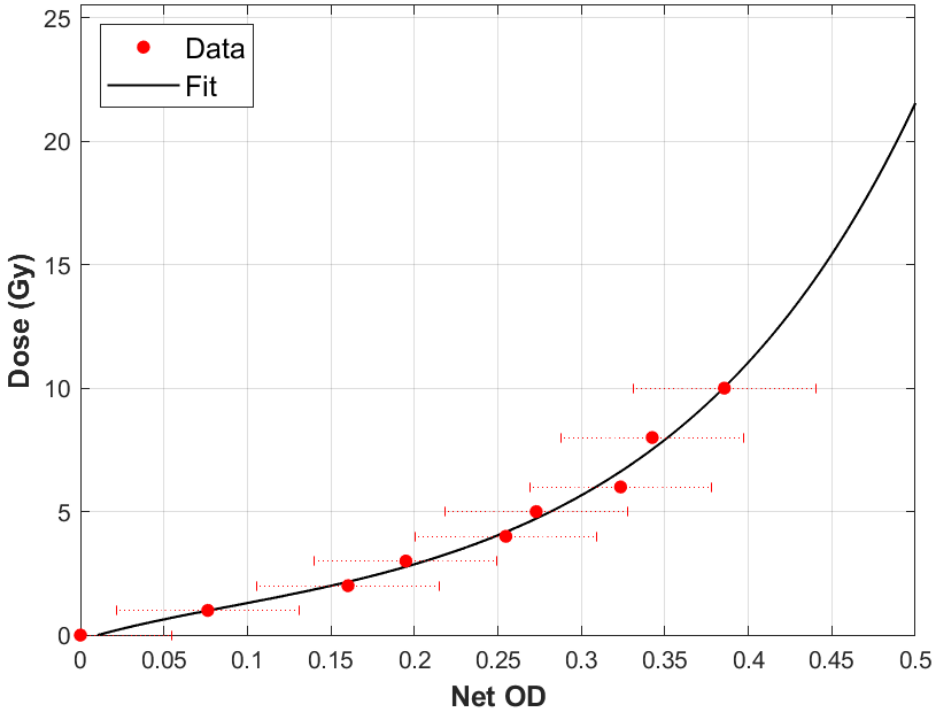

Figure B.25: Calibration curve for red channel obtained for UoB film measurements.

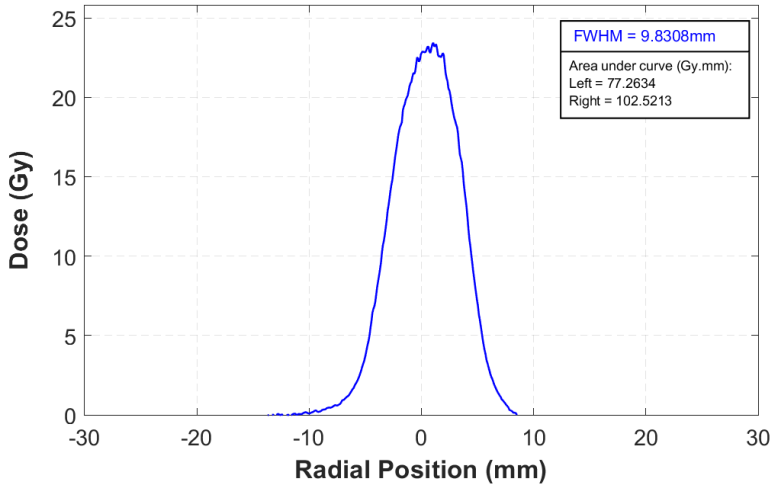

Figure B.26: Film profile with 7 mm collimator.

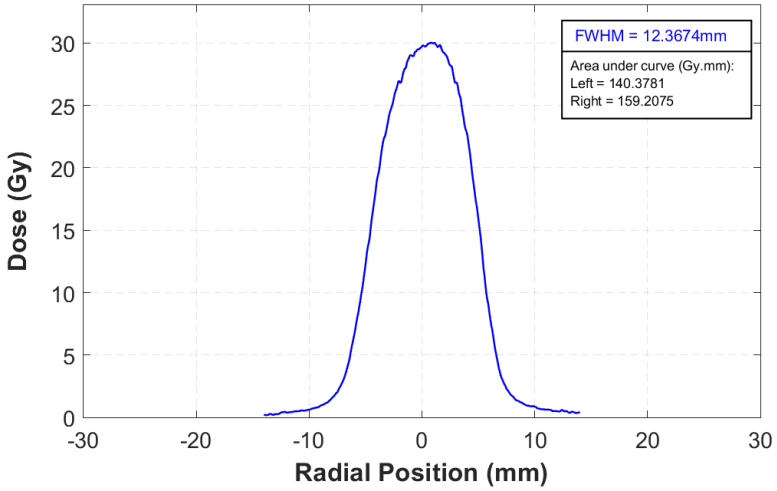

Figure B.27: Film profile with 10 mm collimator.

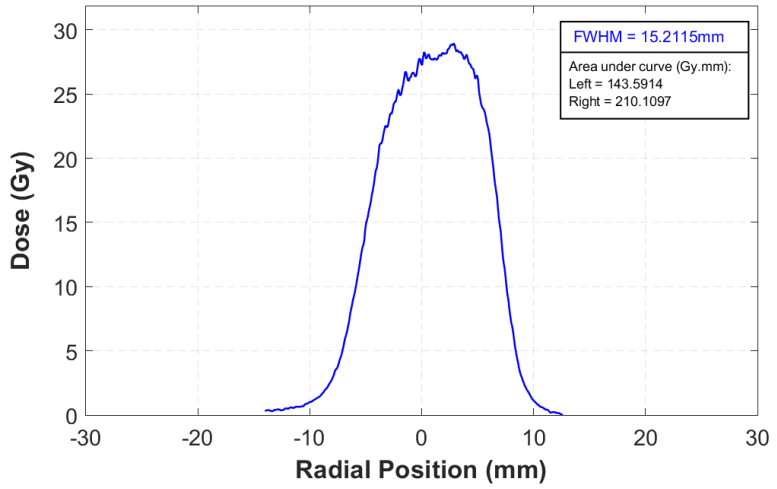

Figure B.28: Film profile with 15 mm collimator.

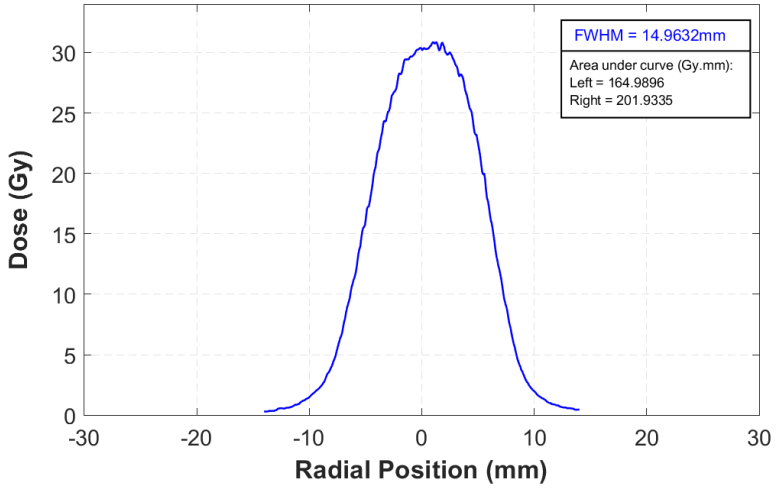

Figure B.29: Film profile with 10 mm collimator at 6 cm distance in z.

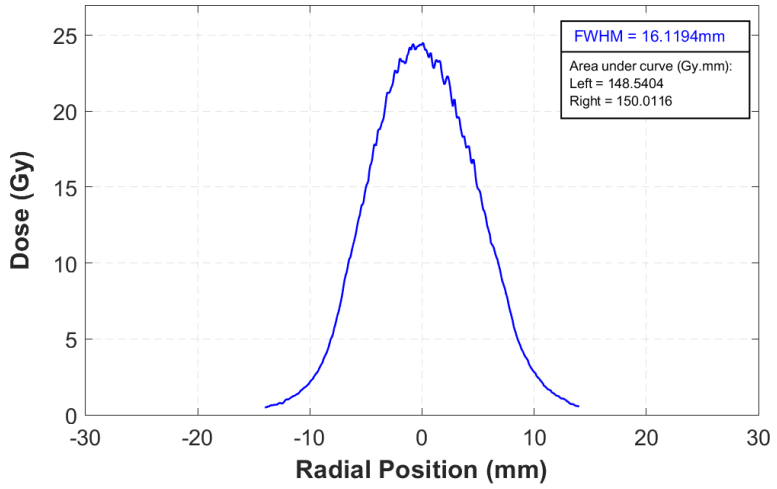

Figure B.30: Film profile with 10 mm collimator at 12 cm distance in z.

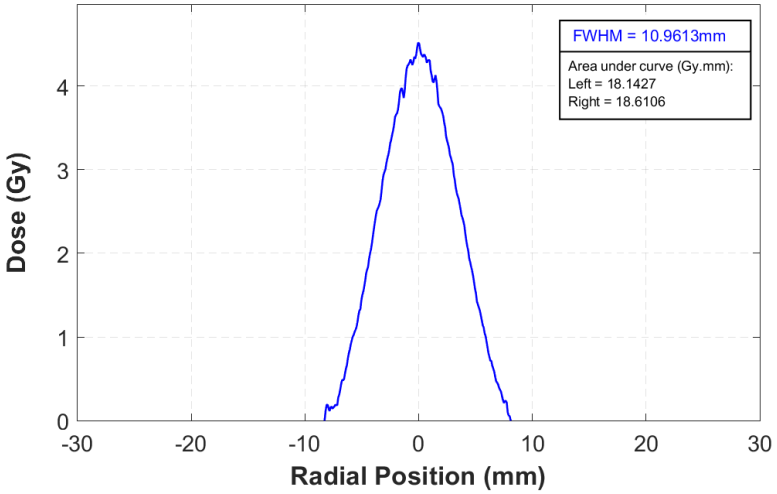

Figure B.31: Film profile with 7 mm collimator.

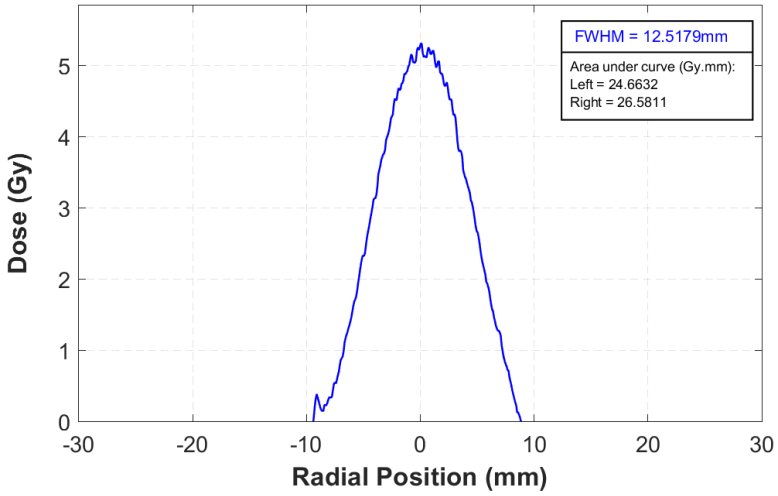

Figure B.32: Film profile with 10 mm collimator.

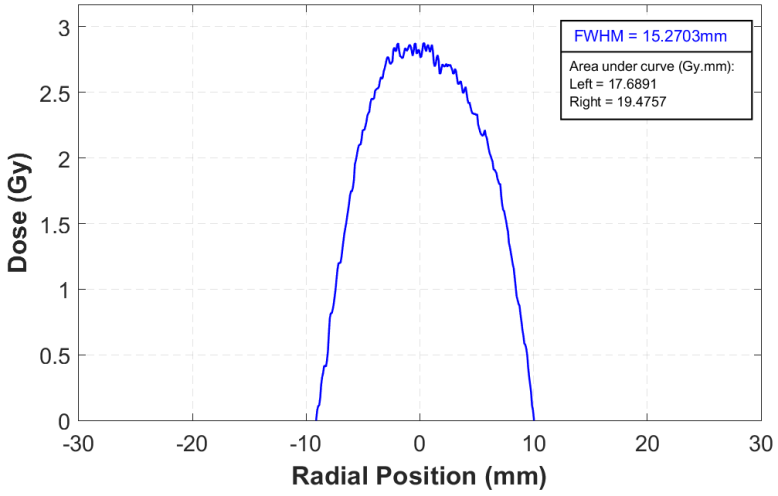

Figure B.33: Film profile with 15 mm collimator.

B.5 TOPAS and MiniPIX Study

Scattering Tube

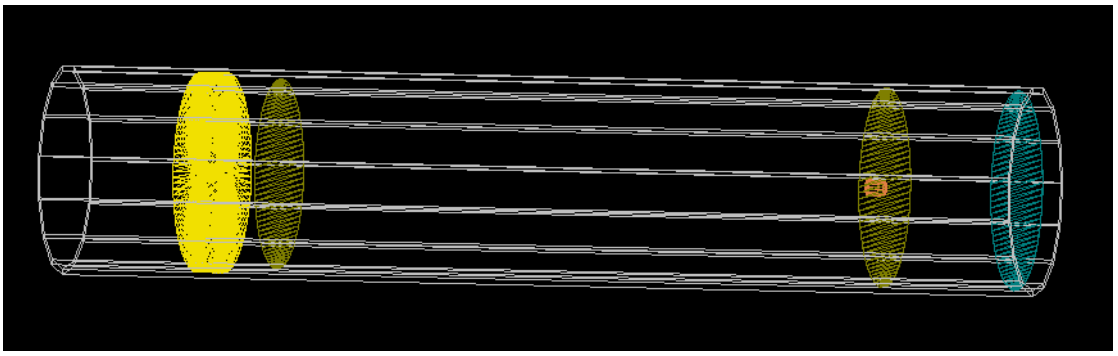

Figure B.34: Beam passes from left to right into this vacuum filled aluminium tube housing the double scattering system: first collimator (yellow), tungsten scattering foils (gold), brass stopper (orange) and kapton window (cyan).

Modulation Box

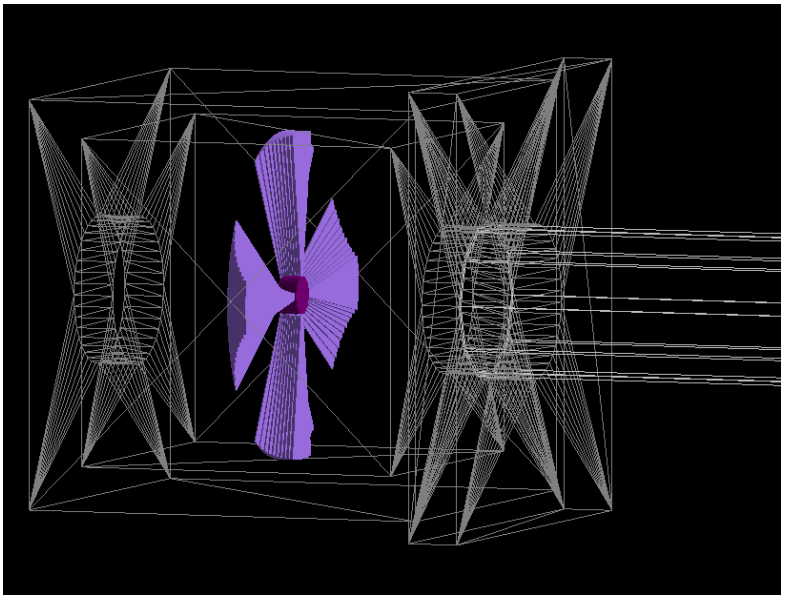

Figure B.35: A rotating modulation wheel to produces a SOBP. This is positioned at the centre of an an aluminium box leading to the designated integration zone (removable second aluminium tube).

Dosimetry Box

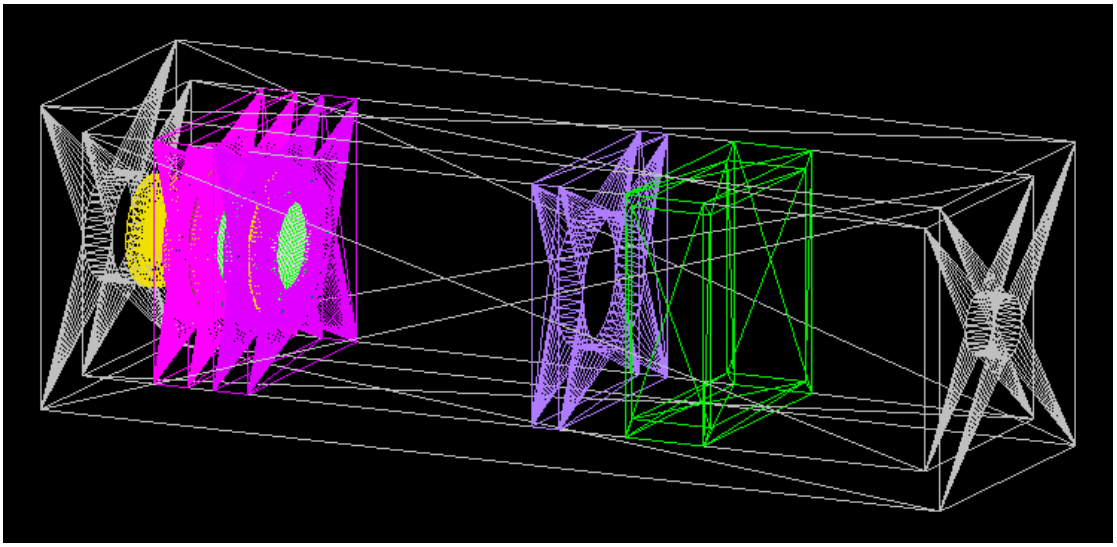

Figure B.36: Second aluminium box containing the diagnostics devices: 2 dose monitors (pink) and wire profile monitor where horizontal and vertical tungsten wires are held to the edges of a (green) box. First brass collimator (yellow) and second aluminium collimator (purple).

Dose Monitors

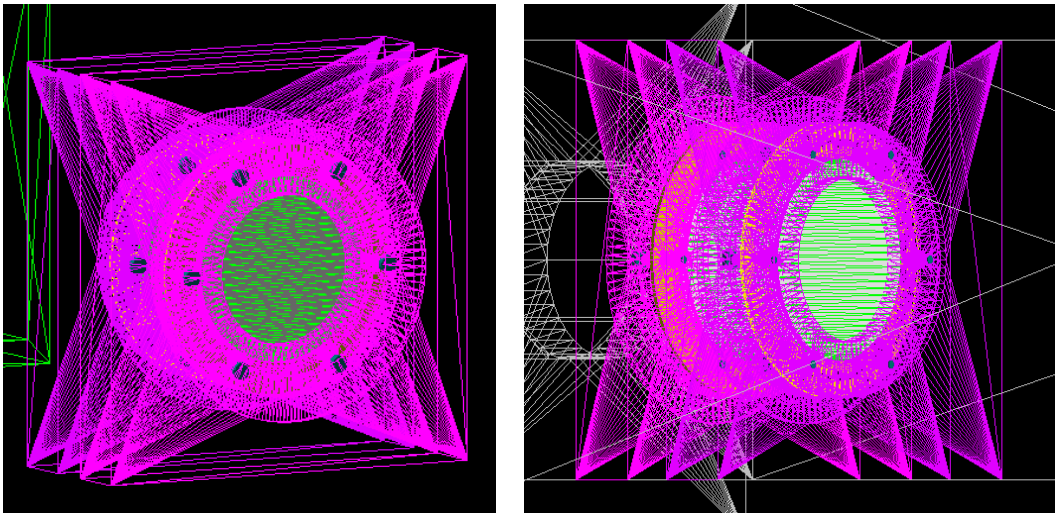

(a) (b)

Figure B.37: Dose monitors: PMMA outer layers (magenta), mylar foils (green), aluminium foils (white), guard rings (orange) and steel bolts (blue). b) Opposing view.

Treatment Nozzle

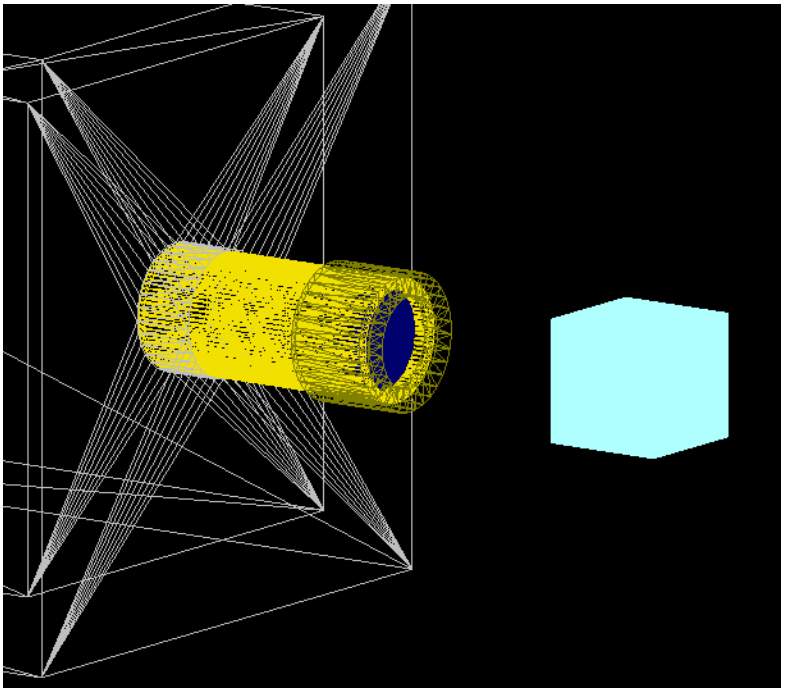

Figure B.38: Treatment nozzle with brass cap, patient collimator (dark blue) and arbitrary phantom for scoring (light blue).

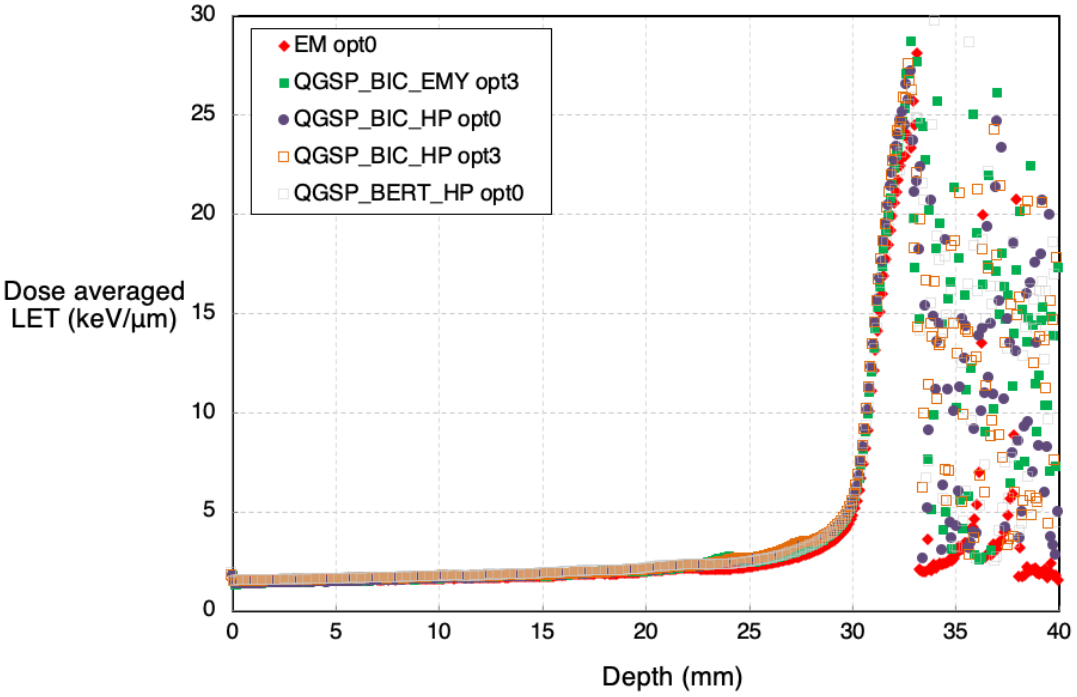

Figure B.39: LET_d scored across a pristine BP using different physics lists.

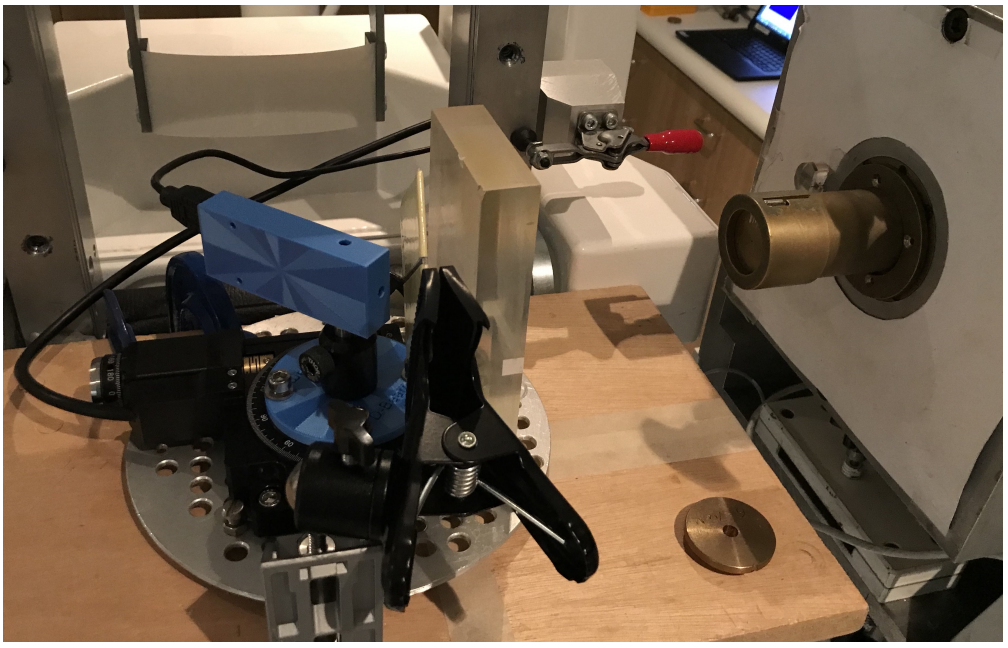

Figure B.40: MiniPIX detector setup with lead sheet for beam calibration.

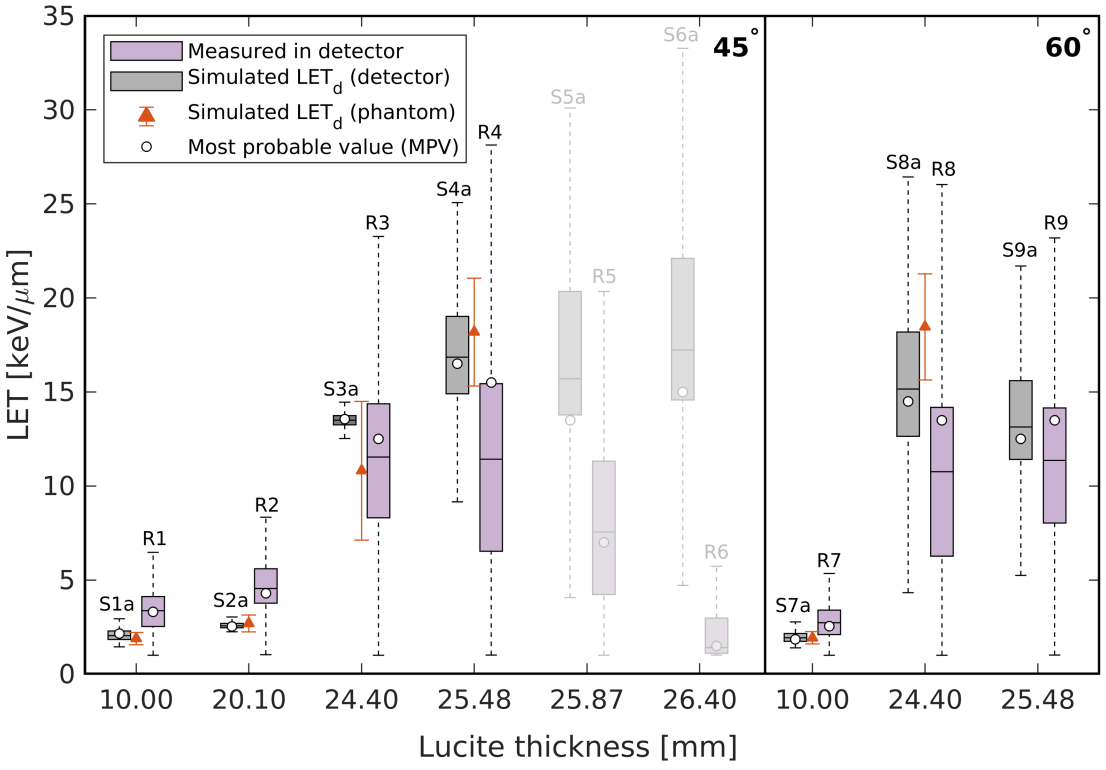

Figure B.41: Boxplots of simulated and measured LET at all depths for 45° and 60°. At greater depths the plots are shaded, corresponding to runs with a designated ∞ WET. Reproduced with permission from [210].

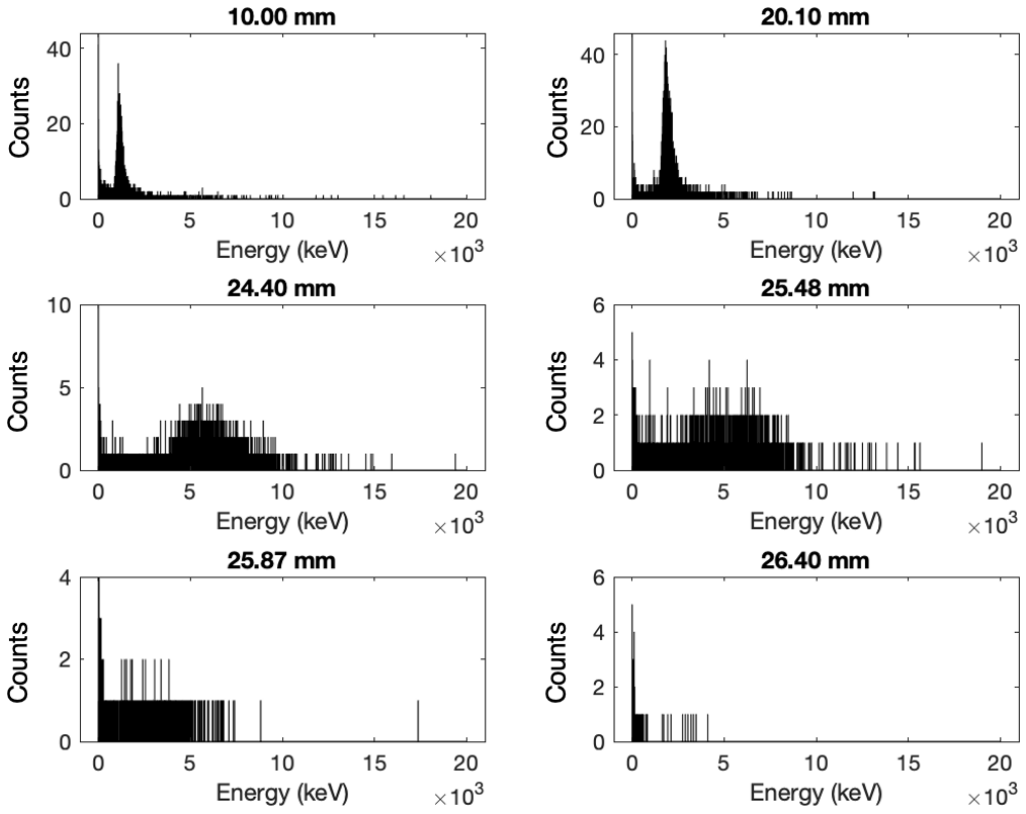

Figure B.42: Measured energy spectra at all depths for 45°.

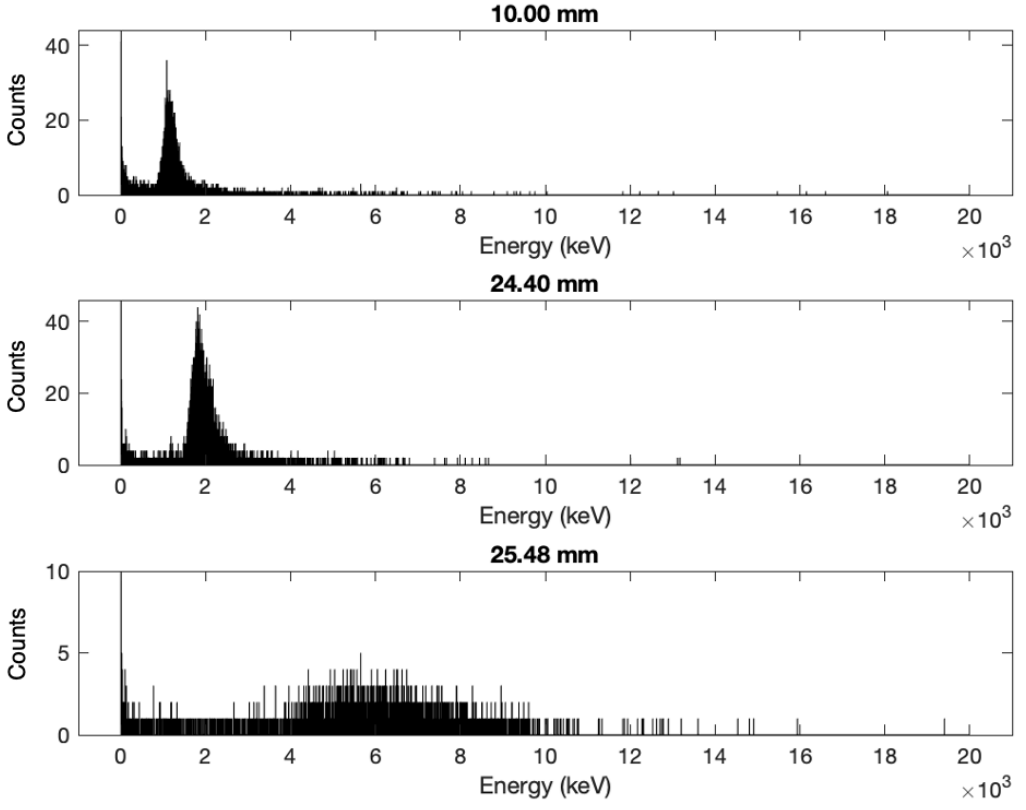

Figure B.43: Measured energy spectra for 60°.

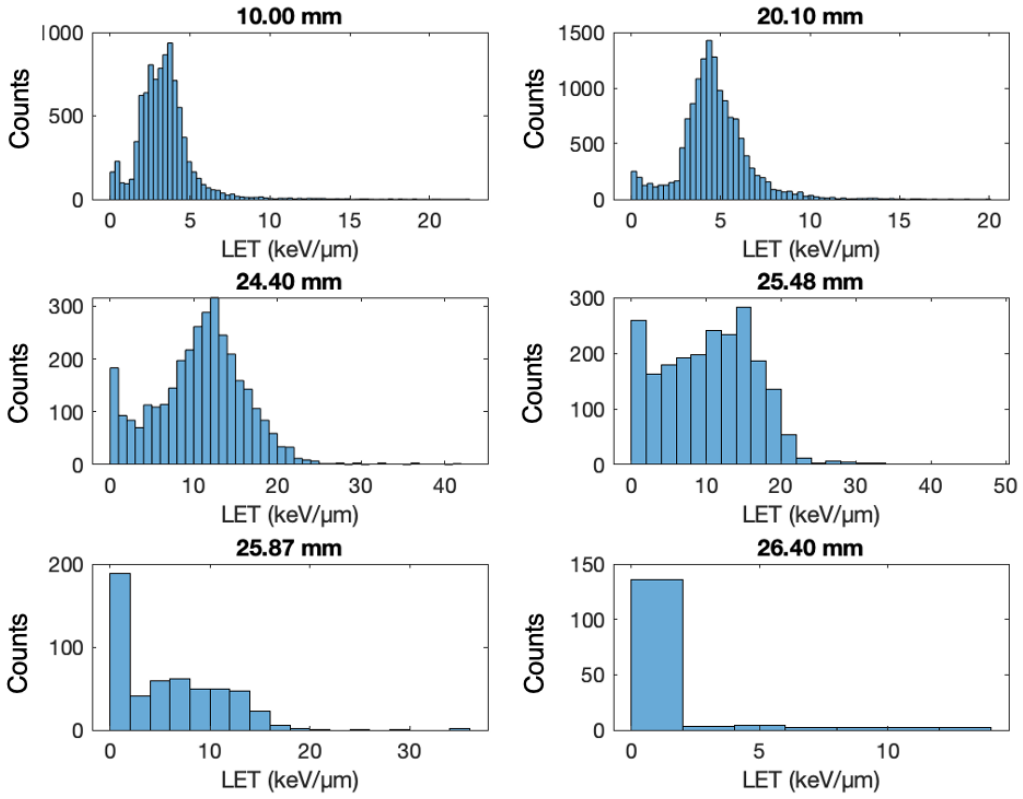

Figure B.44: Empirical LET spectra at all depths for 45°.

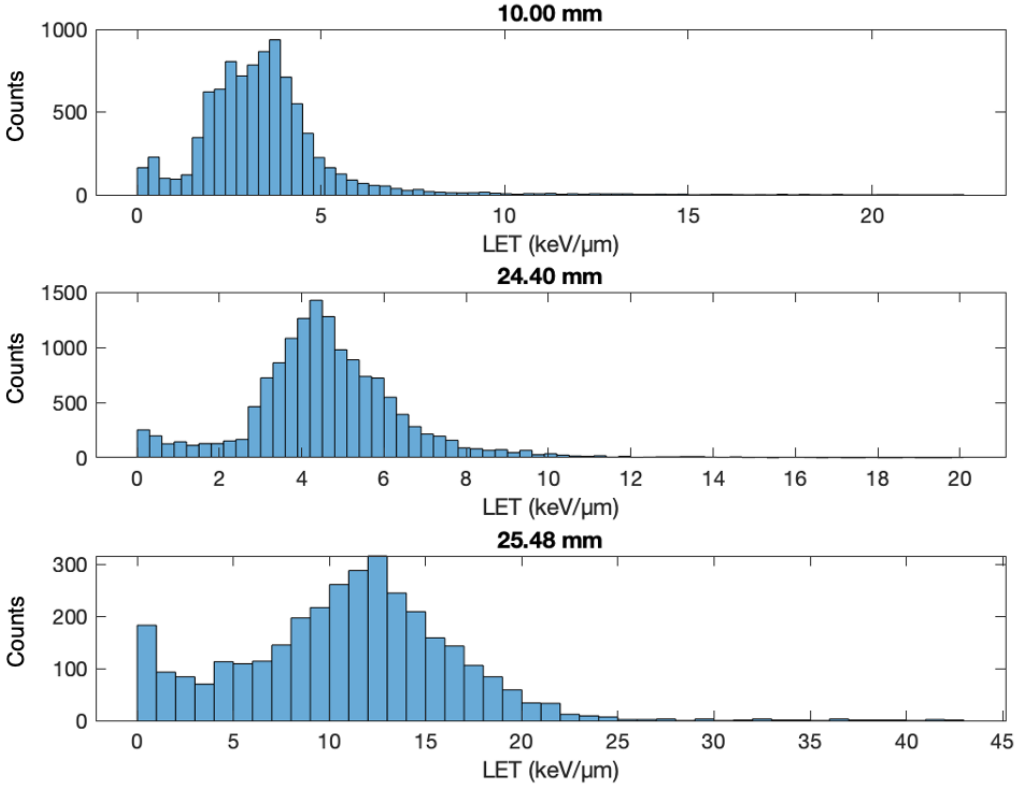

Figure B.45: Empirical LET spectra for 60°.

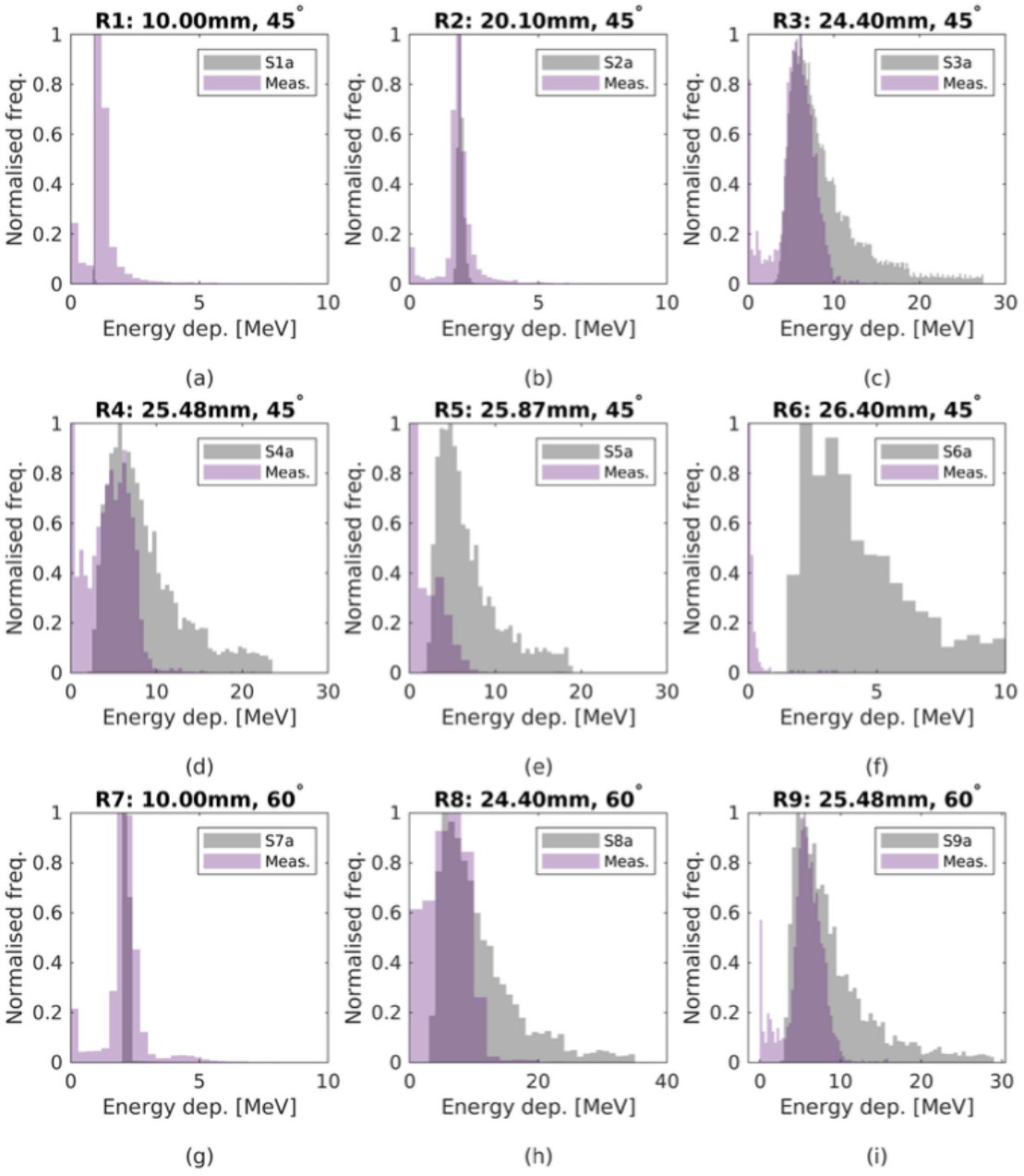

Figure B.46: Comparisons of simulated and measured energies at all depths for 45° and 60°, reproduced with permission from [210].

Appendix C

Supplementary material developed for simulations and experimental analysis.

Protocol for plotting calibration curves and beam profiles from film with MATLAB & ImageJ

Written by Jacinta Yap (April, 2019), revised June 2019. jacinta.yap@liverpool.ac.uk

Preliminary checks

- Make sure all 4 .m files are in the working directory
  - CalibrationODtoDose_CCC.m
  - CalibrationGreen_CCC.m,
  - CalibrationBlue_CCC.m,
  - PlotProfileofScannedFilmWithOD_CCC.m
- Make sure all .txt files are in this same directory
  - red.txt
  - green.txt
  - blue.txt

Calibration Curves

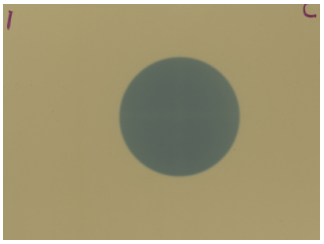

1. Scan film with the following:
   - .tif format
   - 16 bits per pixel
   - 150 pixels per inch

2. Rename all .tif files to their respective irradiated doses (ie 4Gy -> 4.tif)

Creating ROIs for each film spot

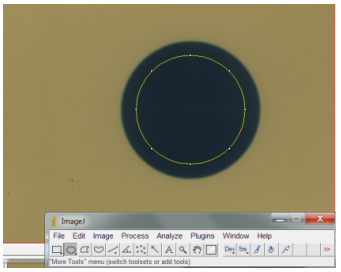

3. Open **ImageJ**, drag and drop all .tif files onto toolbar
   a) Select region of interest (click on the oval tool and draw a circle – hold shift while dragging to maintain/scale diameter for an even circle)
   b) Choose appropriate ROI size for beam spot coverage, this selects area of interest for the Red channel (scroll bar is at left third)
      i.e. Click Edit-> Selection-> Specify, Width = 250, Height = 250, tick for Oval
   c) Press 'ctrl' + 'm' or Analyze -> Measure
      Creates a table of results (Label, Area, Mean, Min, Max)

Save pixel data in each ROI for each film

   d) Click on next .tif image and press 'ctrl' + 'shift' + 'E' to paste ROI
      It should be the same circle, same dimensions and position
      If needed, drag ROI to necessary position

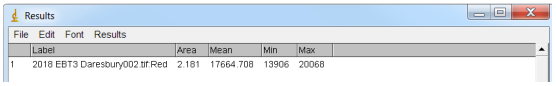

   e) Again, press 'ctrl' + 'm' or Analyze -> Measure
      Generates a table of results for each film
   f) Move ROI onto film background to get a control measurement (0 Gy)
   g) Save file as red.txt
      Move scroll bar on image to middle (green channel) and repeat d) & e), save as green.txt
      Do the same for the blue channel (scroll bar to right) and save as blue.txt

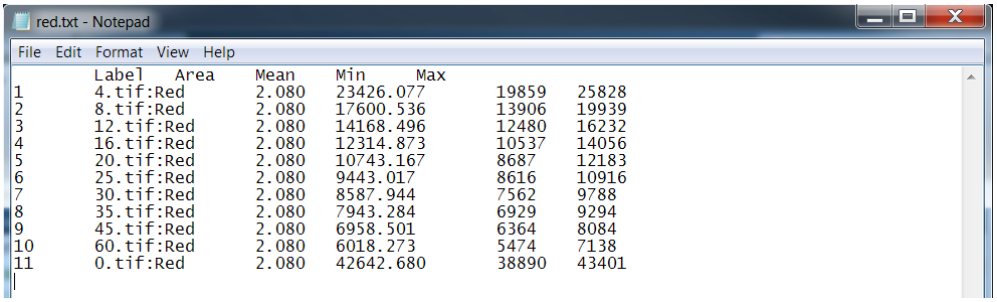

	Label	Area	Mean	Min	Max
1	4.tif:Red	2.080	23426.077	19859	25828
2	8.tif:Red	2.080	17600.536	13906	19939
3	12.tif:Red	2.080	14168.496	12480	16232
4	16.tif:Red	2.080	12314.873	10537	14056
5	20.tif:Red	2.080	10743.167	8687	12183
6	25.tif:Red	2.080	9443.017	8616	10916
7	30.tif:Red	2.080	8587.944	7562	9788
8	35.tif:Red	2.080	7943.284	6929	9294
9	45.tif:Red	2.080	6958.501	6364	8084
10	60.tif:Red	2.080	6018.273	5474	7138
11	0.tif:Red	2.080	42642.680	38890	43401

Analysis

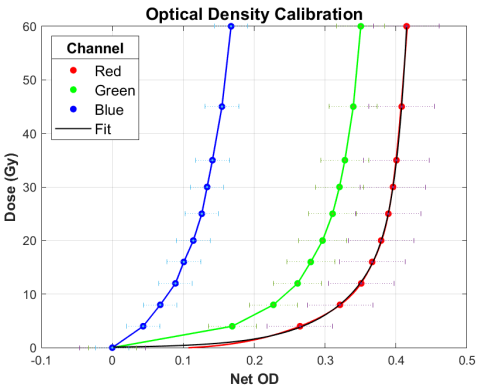

4. Open MATLAB and open all .m files in editor
   a) To generate a plot of the calibration curve, run **CalibrationODtoDose_CCC.m**
      This script reads data from all colour.txt files and generates a plot with:
         NetOD against Dose calibration curves for each channel with error bars
         '**Fit'** line fitted to the red channel

- To see the fit equation, enter 'f' into command window
- The type of fit can be changed in line 57
- To hide the fit, comment out lines 133-135
- To hide from legend table, 156 and uncomment line 157
- For high resolution image uncomment line 164
- To change the plot title, edit line 145
- To view individual channel curves, uncomment lines 70-71 in CalibrationBlue/Green_CCC.m
- The plot is saved automatically in the directory as **date_CalibrationCurve.png**
- Calculation of OD, conversion to dose and errors are calculated using procedures found in literature [1–3]

Beam profile plots

Creating ROIs for relevant film spot

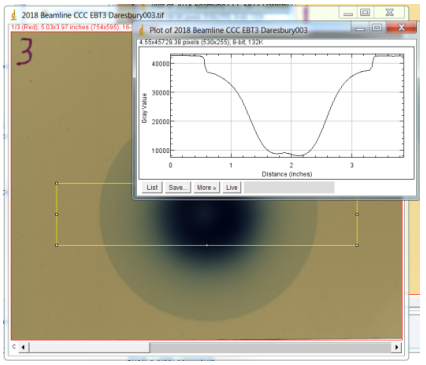

5. Open **ImageJ**, drag and drop the .tif file onto toolbar
   a) Select region of interest (click on the rectangle tool and draw a rectangle on the image
   b) Choose appropriate ROI size for beam spot coverage,
      i.e. Click Edit-> Selection-> Specify, Width = 580, Height = 120

- Ideally the ROI should be larger (better statistics) but also be able to maintain consistency when analysing different beam spot shapes
- Only needs to be done for the Red channel

   c) Press 'ctrl' + 'k' or Analyze -> Plot Profile
      Creates a plot of the grey values by position
   d) Press 'Save...' and rename file, saving data as a .txt file

- You can use 'ctrl' + 'shift' + 'E' to paste ROI from before

Generating the profile plot

- If you have not run the calibration script this session, uncomment line 12
- After running it once, you can comment the line again to speed up the analysis
- This takes the fitted equation from the calibration fits and uses the fit to calculate the doses by pixel

6. Make sure line 7 corresponds to the relevant .txt file
   a) Run **PlotProfileofScannedFilmWithOD_CCC.m**
      Generates a plot with:
         Pixel position in mm
         Dose at each position
         FWHM of the plotted profile

- The FWHM is calculated by 2 methods:
   1. Finds x position of the maximum point and doubles it (default option, works better for symmetrical plots)

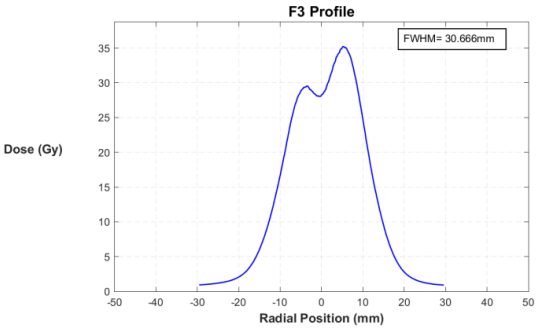

2. Fits a Gaussian to the plot (works better for double peaks)
- To use option **2**, you need to uncomment line 57
- You can preview how the Gaussian fit compares to the plot by displaying it by uncommenting line 86

- To change the graph title, edit line 69
- For high resolution image uncomment line 98
- Automatically saves the graph as **filename_date.png**

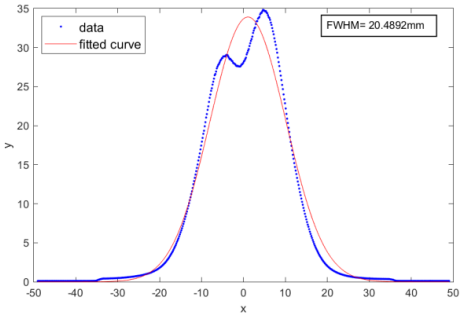

References

1. Vadrucci, M.; Esposito, G.; Ronsivalle, C.; Cherubini, R.; Marracino, F.; Montereali, R. M.; Picardi, L.; Piccinini, M.; Pimpinella, M.; Vincenti, M. A.; De Angelis, C. Calibration of GafChromic EBT3 for absorbed dose measurements in 5 MeV proton beam and 60Co γ-rays. *Med. Phys.* **2015**, *42*, 4678–4684, doi:10.1118/1.4926558.
2. Sorriaux, J.; Kacperek, A.; Rossomme, S.; Lee, J. A.; Bertrand, D.; Vynckier, S.; Sterpin, E. Evaluation of Gafchromic EBT3 films characteristics in therapy photon, electron and proton beams. *Phys. Medica* **2013**, *29*, 599–606, doi:10.1016/j.ejmp.2012.10.001.
3. Battaglia, M. C. Dosimetry studies for radiation therapy with photons and radiobiology using low-energy protons, University of Seville, 2017.

Disclaimer:

This protocol and all scripts were written by Jacinta Yap to demonstrate methods used for analysis of film irradiations performed at the Clattterbridge Cancer Centre, UK. Any work carried out was for the purposes of my PhD thesis. Please email me if you have any questions.

Figure C.1: Protocol documentation for dose conversion specifically for film measurements and analysis done at Clatterbridge. Script uses Matlab and ImageJ to generate calibration curves for each RGB channel, converting grey pixel values to OD to dose and the pixel size and (scanner) dots per inch to lengths in mm. Automates plotting of beam profiles for dose (Gy) against position (mm).

```
%% MATLAB script to plot optical density calibration curved from scanned film %%
% This is for Red channel, will also automatically call the scripts for the
blue & green

% Written by J Yap, Apr 2019 (yapjacinta@gmail.com)

%% Load file - red channel
filename = 'red';
fileID = string(filename)+'.txt';

file = fopen(fileID,'rt');
data = textscan(file,'%d %s %f %10f %f %f','HeaderLines',1); %skip header line
fclose(file);

%% Definitions %%
format long g
A = data{3};
Area = A(1);
ZeroVal = 65535; % grey value from scanner (white pixel)

DoseCol = data{2};
d = split(DoseCol,'.');
DoseVals = d(:,1);

MeanVals = data{4};
MinVals = data{5};
MaxVals = data{6};

%% Control

d1=double(string(DoseVals)); % convert to numbers
DoseData = [d1, MeanVals];
index = find(DoseData==0);
Rcontrol = DoseData(index,2);

%% Optical density %%

OD = -log10((Rcontrol-ZeroVal)./(MeanVals-ZeroVal));
doseRed = sort(d1);
Red = sort(OD);
calibData = [doseRed,Red];

%% Run blue & green scripts %%

CalibrationBlue_CCC;
CalibrationGreen_CCC;

%% Interpolate between points for smooth curves %%

f1 = fit(Red,doseRed,'smoothingspline');
f2 = fit(Green,doseGreen,'linear');
f3 = fit(Blue,doseBlue,'linear');

%% Fit to red channel curve %%

x1=Red(2:end);
y1=doseRed(2:end);
```

```
58 f=fit(x1,y1,'exp2'); %type of fit 'exp1'
59
60 coeff = coeffvalues(f);
61
62 fita = coeff(1);
63 fitb = coeff(2);
64 fitc = coeff(3); %comment out for exp1
65 fitd = coeff(4); %comment out for exp1
66
67 %% Error bars
68
69 Diffred = [d1,MeanVals,MinVals,MaxVals];
70 Diffred = sortrows(Diffred,1);
71 controlred = Diffred(1,:);
72
73 %term1, note variance bckg=0
74 meanUnexpR=controlred(2);
75 minUnexpR=controlred(3);
76 maxUnexpR=controlred(4);
77 uncertaintyUnexposedMinr=(meanUnexpR-minUnexpR)^2;
78 uncertaintyUnexposedMaxr=(meanUnexpR-maxUnexpR)^2;
79 rterm1=(uncertaintyUnexposedMinr+uncertaintyUnexposedMaxr)/2;
80
81 %term2
82 meanExpR=Diffred(:,2);
83 minExpR=Diffred(:,3);
84 maxExpR=Diffred(:,4);
85 varExposedMinr=(meanExpR-minExpR).^2./length(meanExpR);
86 varExposedMaxr=(meanExpR-maxExpR).^2./length(meanExpR);
87 rterm2=(varExposedMinr+varExposedMaxr)./2;
88
89 %term3
90 rterm3=(controlred(2)-ZeroVal)^2;
91
92 %term4
93 rterm4=(Diffred(:,2)-ZeroVal).^2;
94
95 rerrors=(1/log(10))*sqrt(rterm1/rterm3+rterm2./rterm4);
96
97 %% Plotting
98
99 figure
100 set(gcf, 'Units', 'Normalized', 'OuterPosition', [0.2, 0.2, 0.4, 0.6]);
101 arrangement = [0.27 0.12 0.7 0.8]; % [left bottom width height]
102
103 pr=plot(Red,doseRed,'o');
104 pr.DisplayName='Red';
105 pr.Color='red';
106 pr.MarkerSize=5;
107 pr.MarkerFaceColor='red';
108 %interpolated curve
109 hold on
110 f1r=plot(f1);
111 f1r.Color='red';
112 f1r.LineWidth=1.2;
113
114 pg=plot(Green,doseGreen,'o');
```

```
pg.DisplayName='Green';
pg.Color='green';
pg.MarkerSize=5;
pg.MarkerFaceColor='green';
%interpolated curve
f2r=plot(f2);
f2r.Color='green';
f2r.LineWidth=1.2;

pb=plot(Blue,doseBlue,'o');
pb.DisplayName='Blue';
pb.Color='blue';
pb.MarkerSize=5;
pb.MarkerFaceColor='blue';
%interpolated curve
f3r=plot(f3);
f3r.Color='blue';
f3r.LineWidth=1.2;

%plot fitted curve (comment out to hide in plot)
pf=plot(f,'black');
pf.LineWidth=1;
pf.DisplayName='Fit';

rer=errorbar(Red,doseRed,rerrors,'.','horizontal','CapSize',4);
rer.Bar.LineStyle='dotted';
reg=errorbar(Green,doseGreen,gerrors,'.','horizontal','CapSize',4);
reg.Bar.LineStyle='dotted';
reb=errorbar(Blue,doseBlue,berrors,'.','horizontal','CapSize',4);
reb.Bar.LineStyle='dotted';
hold off

title('Optical Density Calibration', 'FontSize',14); % graph title,
change here if needed
grid on
ylabel('Dose (Gy)','fontweight','bold','FontSize',12);
ylim([0,60]);
xlabel('Net OD','fontweight','bold','FontSize',12);
xlim([0,inf]);

% legend
lgd=legend;
lgd.FontSize=12;
lgd.Title.String = 'Channel';
lgd.Location='northwest';
legend([pr pg pb pf]);
%legend([pr pg pb]);

%% Save as picture

savefilename = string(date)+'_CalibrationCurve.png';
saveas(gcf,savefilename);
print(gcf,savefilename,'-dpng','-r600') %high resolution
```

Figure C.2: CalibrationODtoDose_CCC.m

```
%% MATLAB script to plot optical density calibration curved from scanned film %%

% Generates data for the blue channel
% Note: You don't need to open or run this script, it is called from the
Calibration.m script
% Checks: Make sure it is in the same directory as Calibration.m
% Written by J Yap, Apr 2019 (yapjacinta@gmail.com)

%% Load file - blue channel
file = fopen('blue.txt','rt');
datab = textscan(file,'%d %s %f %10f %f %f','HeaderLines',1); %skip header line
fclose(file);

%% Definitions %%
format long g
B = datab{3};
ZeroVal = 65535; % grey value from scanner (white pixel)

DoseColb = datab{2};
db = split(DoseColb,'.');
DoseValsb = db(:,1);

MeanValsb = datab{4};
MinValsb = datab{5};
MaxValsb = datab{6};

%% Control

d1b=double(string(DoseValsb)); % convert to numbers
DoseDatab = [d1b, MeanValsb];
indexb = find(DoseDatab==0);
Bcontrol = DoseDatab(indexb,2);

%% Error bars

Diffblue = [d1b,MeanValsb,MinValsb,MaxValsb];
Diffblue = sortrows(Diffblue,1);
controlblue = Diffblue(1,:);

%term1
meanUnexpB=controlblue(2);
minUnexpB=controlblue(3);
maxUnexpB=controlblue(4);
uncertaintyUnexposedMinb=(meanUnexpB-minUnexpB)^2;
uncertaintyUnexposedMaxb=(meanUnexpB-maxUnexpB)^2;
bterm1=(uncertaintyUnexposedMinb+uncertaintyUnexposedMaxb)/2;

%term2
meanExpB=Diffblue(:,2);
minExpB=Diffblue(:,3);
maxExpB=Diffblue(:,4);
varExposedMinb=(meanExpB-minExpB).^2./length(meanExpB);
varExposedMaxb=(meanExpB-maxExpB).^2./length(meanExpB);
bterm2=(varExposedMinb+varExposedMaxb)./2;

%term3
bterm3=(controlblue(2)-ZeroVal)^2;
```

```
58
59 %term4, matrix
60 bterm4=(Diffblue(:,2)-ZeroVal).^2;
61
62 berrors=(1/log(10))*sqrt(bterm1/bterm3+bterm2./bterm4);
63
64 %% Optical density %%
65
66 ODblue = -log10((Bcontrol-ZeroVal)./(MeanValsb-ZeroVal));
67 doseBlue = sort(d1b);
68 Blue = sort(ODblue);
69 calibDataBlue = [doseBlue,Blue];
70
71 %% Plotting
72
73 %plot(Blue,doseBlue);
74 %errorbar(Blue,doseBlue,berrors,'horizontal');
```

Figure C.3: CalibrationBlue_CCC.m

```
1  %% MATLAB script to plot optical density calibration curved from scanned film %%
2
3  % Generates data for the green channel
4  % Note: You don't need to open or run this script, it is called from the
5  Calibration.m script
6  % Checks: Make sure it is in the same directory as Calibration.m
7  % Written by J Yap, Apr 2019 (yapjacinta@gmail.com)
8
9  %% Load file - green channel
10 file = fopen('green.txt','rt');
11 datag = textscan(file,'%d %s %f %10f %f %f','HeaderLines',1); %skip header line
12 fclose(file);
13
14 alsg = dg(:,1);
15
16 MeanValsg = datag{4};
17 MinValsg = datag{5};
18 MaxValsg = datag{6};
19
20 %% Control
21
22 d1g=double(string(DoseValsg)); % convert to numbers
23 DoseDatag = [d1g, MeanValsg];
24 indexg = find(DoseDatag==0);
25 Gcontrol = DoseDatag(indexg,2);
26
27 %% Error bars
28
29 Diffgreen = [d1g,MeanValsg,MinValsg,MaxValsg];
30 Diffgreen = sortrows(Diffgreen,1);
31 controlgreen = Diffgreen(1,:);
32
33 %term1
```

```
meanUnexpG=controlgreen(2);
minUnexpG=controlgreen(3);
maxUnexpG=controlgreen(4);
uncertaintyUnexposedMing=(meanUnexpG-minUnexpG)^2;
uncertaintyUnexposedMaxg=(meanUnexpG-maxUnexpG)^2;
gterm1=(uncertaintyUnexposedMing+uncertaintyUnexposedMaxg)/2;

%term2
meanExpG=Diffgreen(:,2);
minExpG=Diffgreen(:,3);
maxExpG=Diffgreen(:,4);
varExposedMing=(meanExpG-minExpG).^2./length(meanExpG);
varExposedMaxg=(meanExpG-maxExpG).^2./length(meanExpG);
gterm2=(varExposedMing+varExposedMaxg)./2;

%term3
gterm3=(controlgreen(2)-ZeroVal)^2;

%term4, matrix
gterm4=(Diffgreen(:,2)-ZeroVal).^2;

gerrors=(1/log(10))*sqrt(gterm1/gterm3+gterm2./gterm4);

%% Optical density %%

ODgreen = -log10((Gcontrol-ZeroVal)./(MeanValsg-ZeroVal));
doseGreen = sort(d1g);
Green = sort(ODgreen);
calibDataGreen = [doseGreen,Green];

%% Plotting

%plot(Green,doseGreen);
%errorbar(Green,doseGreen,gerrors,'horizontal');
```

Figure C.4: CalibrationGreen_CCC.m

```
%% MATLAB script to convert scanned film to profile plots %%
% Please see accompanying PDF for protocol to run these scripts

% Written by J Yap, Apr 2019 (yapjacinta@gmail.com)

%% Load file - Enter name of file here without .txt
filenamecal = 'F3';

% Just need to run this calibration script once for the first film, comment it out
% for subsequent analysis (speeds up this script)

CalibrationODtoDose_CCC;

% Only change any of the following if there is a double peak & you need to
% fit a gaussian for the FWHM calculation

```

```
%% Read file %%
file = string(filenamecal)+'.txt';
disptext = ['You are plotting ' char(file)];
disp(disptext)
filmdata = dlmread(file, '', 1,0); %skip header line

%% Definitions

%columns
posXinch = filmdata(:,1);
posXcm = posXinch*25.4; %convert pixel position to cm

%convert pixel values to dose
pixelVals = filmdata(:,2);
converttoOD = -log10((Rcontrol-ZeroVal)./(pixelVals-ZeroVal));
ODtoDose = (fita*exp(fitb.*converttoOD))+(fitc*exp(fitd.*converttoOD));

%symmetrical plotting
centre = max(posXcm)/2;
%invert plot
%minPixelval = min(converttoOD);
%position (x column for plotting)
position = posXcm - centre;
%converted dose (y column)
pixel = ODtoDose;

%% Calculate FWHM

maxy=max(pixel);
halfy=maxy/2;
halfy=str2num(sprintf('%2.f',halfy));
array=[position pixel];
[m,closesty]=min(abs((pixel-halfy)));
index=array(closesty);
fwhms=abs(index)*2;

% Calc FWHM by fitting a gaussian, if using this method uncomment the 4th line
f = fit(position,pixel,'gauss1');
coeff = coeffvalues(f);
fwhm1=2*sqrt(2*log(2))*(coeff(3));
%fwhms=fwhm1;

%% Graph positioning
figure
hold on
set(gcf, 'Units', 'Normalized', 'OuterPosition', [0.2, 0.2, 0.5, 0.6]);
arrangement = [0.27 0.12 0.7 0.8]; % [left bottom width height]
subplot('Position',arrangement);

%% Plot graph
a=plot(position,pixel,'LineWidth',1.2, 'Color',[0,0,1]);
name = [filenamecal ' Profile'];
title(name, 'FontSize',14); % graph title, change here if needed
grid on

set(gca, 'GridLineStyle','--', 'GridColor','[0.3 0.3 0.3]')

```

```
74  xlabel('Radial Position (mm)','fontweight','bold','FontSize',12);
75  xlim([-50,50]);
76
77  yl=ylabel('Dose (Gy)','fontweight','bold','FontSize',12);
78  set(get(gca,'ylabel'),'rotation',0); %rotate y title horizontally
79  set(yl,'Units','normalized');
80  shift=0.15; %shift ylabel left
81  set(yl,'Position',get(yl,'position')-[shift 0 0]) %position ylabel
82  buffery=1.1*(max(pixel)); %increase y graph
83  ylim([0,buffery]);
84
85  %Uncomment to see fitted double gaussian
86  %plot(f,position,pixel); legend('FontSize',12,'Location','northwest');
87
88  %% FWHM box
89  annotate= ['FWHM= ' char(string(fwhms)) 'mm'];
90  annotation('textbox',[0.75 0.75 0.2 0.15],'String',{annotate},'FitBoxToText',
91  'on', 'FontSize',10, 'LineWidth',1, 'BackgroundColor',[1 1 1]);
92  disp(annotate)
93
94  %% Save as picture
95  saveasname_dated=filenamecal+"_"+string(date);
96  saveasname= saveasname_dated+'.png';
97  saveas(gcf,saveasname);
98  %print(gcf,'saveasnameHR.png','-dpng','-r600') %high resolution
```

Figure C.5: PlotProfileofScannedFilmWithOD_CCC.m

Emittance Measurement Scheme

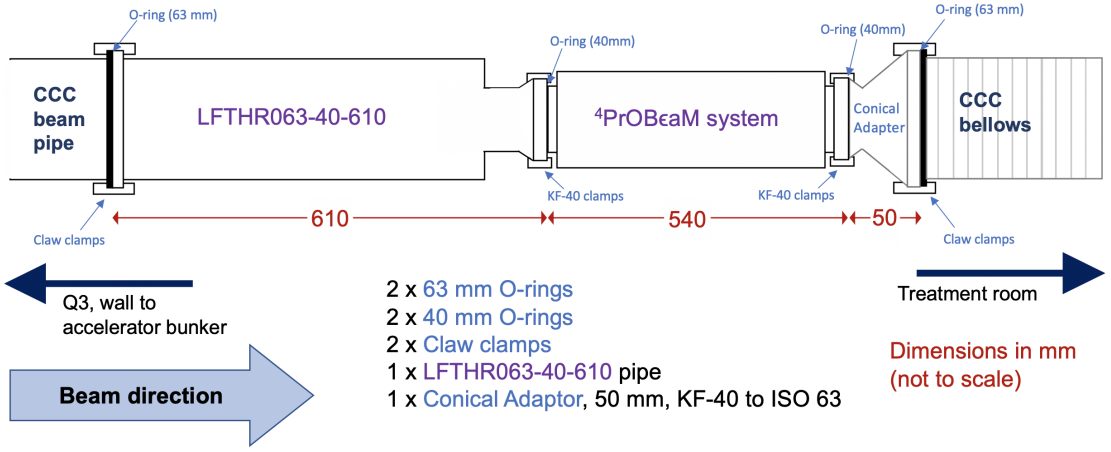

Figure C.6: Sketch of relevant components and dimensions for integration of the ^{4}PrOBϵaM system into the beamline (between Q3 and treatment room) for emittance measurements.

C.1 CCC Component Specifications

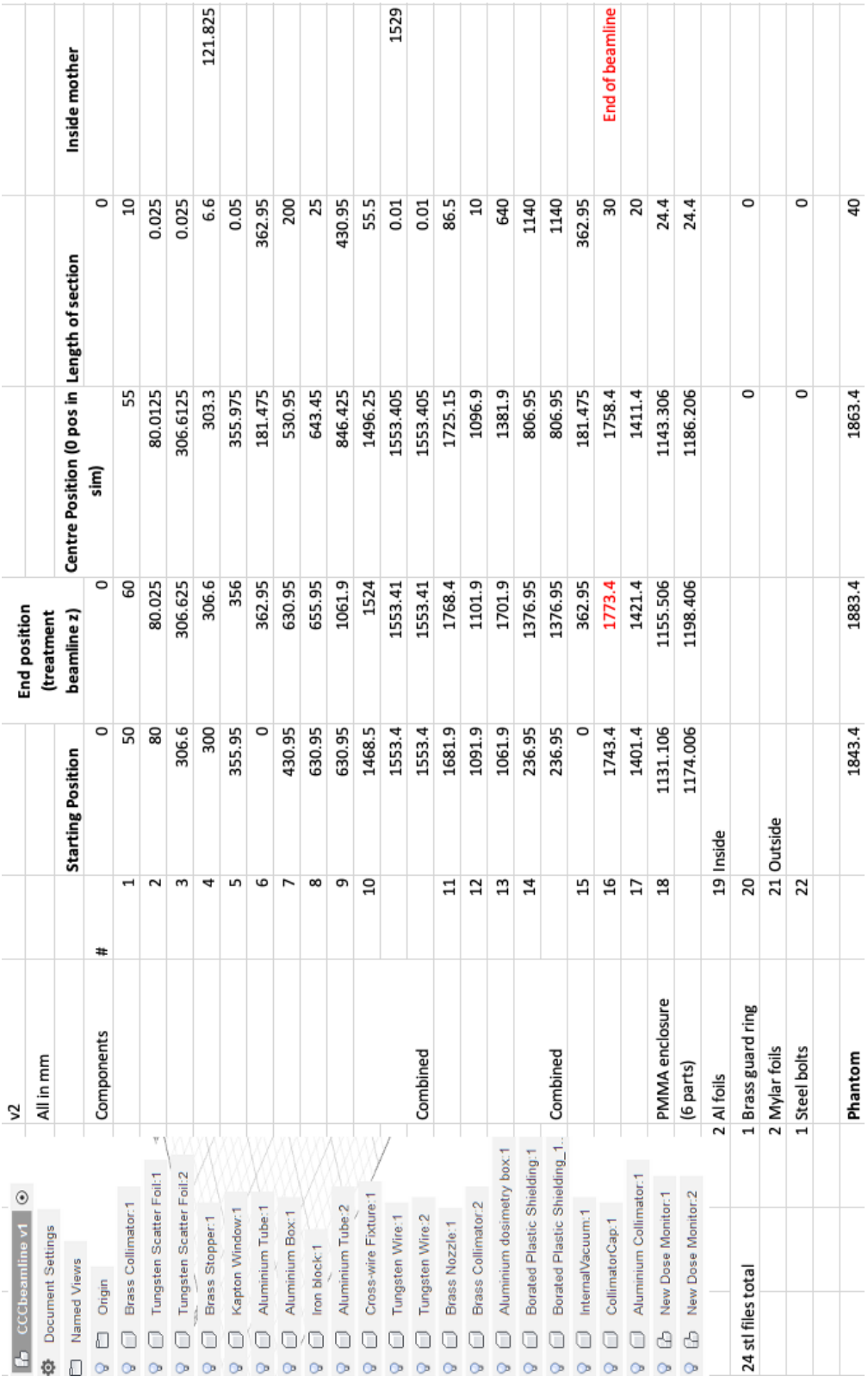

v2									
All in mm									
			Starting Position		End position (treatment beamline z)		Centre Position (0 pos in sim)	Length of section	Inside mother
	Components	#		0		0		0	
CCCbeamline v1									
Document Settings									
Named Views									
Origin									
Brass Collimator:1		1		50		60	55	10	
Tungsten Scatter Foil:1		2		80		80.025	80.0125	0.025	
Tungsten Scatter Foil:2		3		306.6		306.625	306.6125	0.025	
Brass Stopper:1		4		300		306.6	303.3	6.6	121.825
Kapton Window:1		5		355.95		356	355.975	0.05	
Aluminium Tube:1		6		0		362.95	181.475	362.95	
Aluminium Box:1		7		430.95		630.95	530.95	200	
Iron block:1		8		630.95		655.95	643.45	25	
Aluminium Tube:2		9		630.95		1061.9	846.425	430.95	
Cross-wire Fixture:1		10		1468.5		1524	1496.25	55.5	
Tungsten Wire:1				1553.4		1553.41	1553.405	0.01	1529
Tungsten Wire:2	Combined			1553.4		1553.41	1553.405	0.01	
Brass Nozzle:1		11		1681.9		1768.4	1725.15	86.5	
Brass Collimator:2		12		1091.9		1101.9	1096.9	10	
Aluminium dosimetry box:1		13		1061.9		1701.9	1381.9	640	
Borated Plastic Shielding:1		14		236.95		1376.95	806.95	1140	
Borated Plastic Shielding_1..	Combined			236.95		1376.95	806.95	1140	
InternalVacuum:1		15		0		362.95	181.475	362.95	
CollimatorCap:1		16		1743.4		1773.4	1758.4	30	End of beamline
Aluminium Collimator:1		17		1401.4		1421.4	1411.4	20	
New Dose Monitor:1	PMMA enclosure	18		1131.106		1155.506	1143.306	24.4	
New Dose Monitor:2	(6 parts)			1174.006		1198.406	1186.206	24.4	
	2 Al foils	19	Inside						
24 stl files total	1 Brass guard ring	20					0	0	
	2 Mylar foils	21	Outside						
	1 Steel bolts	22					0	0	
	Phantom			1843.4		1883.4	1863.4	40	

Figure C.7: List of each treatment line component and corresponding positions in z (mm) as implemented in TOPAS.

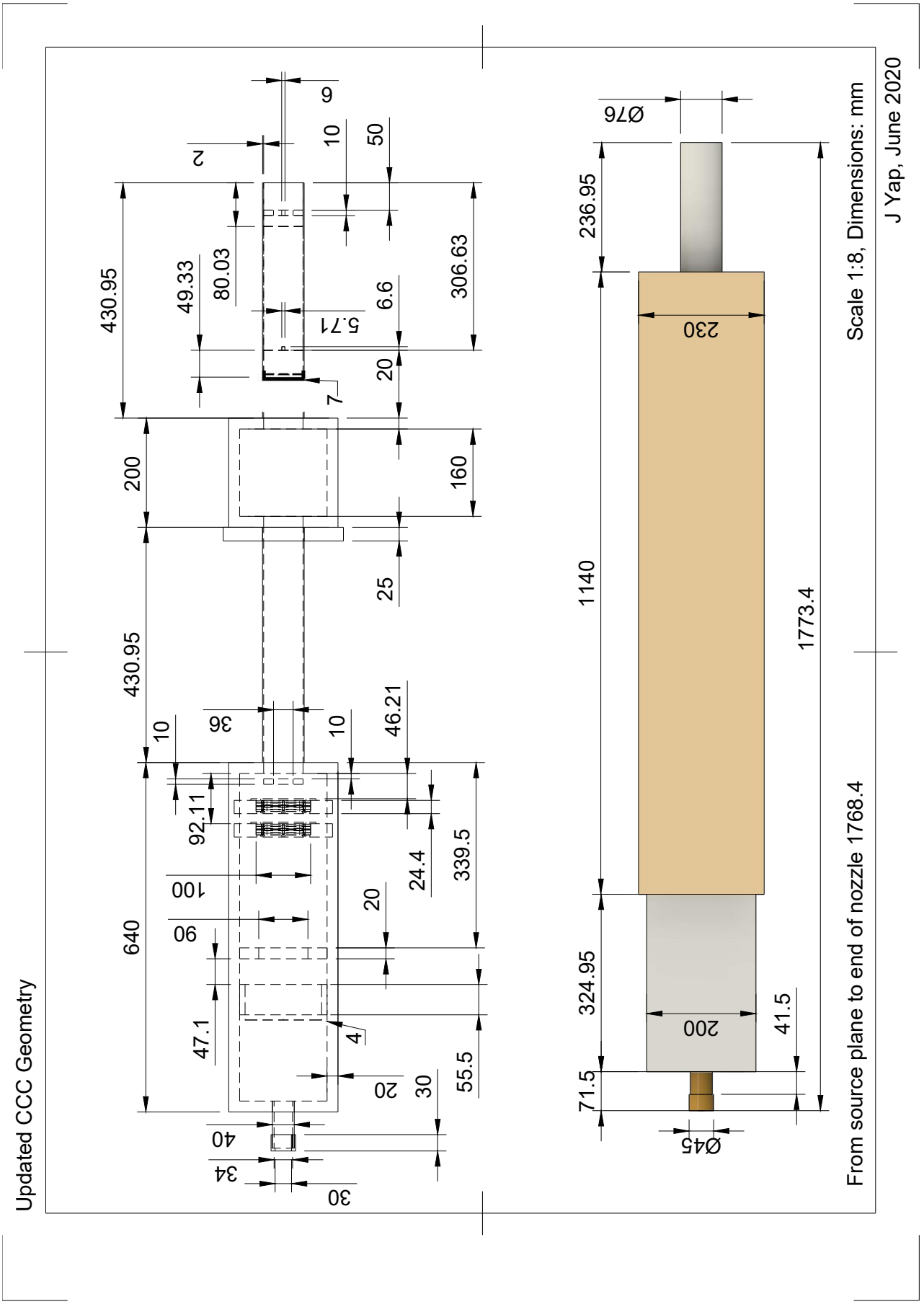

Figure C.8: Drawing of the CCC treatment line with all dimensions listed.

List of Figures

List of Tables

List of Abbreviations

ADC	Analogue-to-Digital Converter
BDSIM	Beam Delivery Simulation
BP	Bragg Peak
BPM	Beam Profile Monitor
BTL	Beam Transfer Line
BTS	Beam Transfer System
CAD	Computer Aided Design
CCC	Clatterbridge Cancer Centre
CERN	Conseil Européen pour la Recherche Nucléaire (European Organization for Nuclear Research)
CPT	Charged Particle Therapy
CT	Computed Tomography
DAQ	Data Acquisition
DNA	Deoxyribonucleic Acid
DSB	Double Strand Break
EBRT	External Beam Radiation Therapy
EM	Electromagnetic
ESS	Energy Selection System
FC	Faraday Cup
FPS	Frames Per Second
FS	Flip Screen
FWHM	Full Width Half Maximum
GDML	Geometry Description Markup Language
GEANT4	Geometry And Tracking
GPS	General Particle Source

HCL Harvard University Cyclotron Laboratory

HEP High Energy Physics

IC Ionisation Chambers

IMPT Intensity Modulated Proton Therapy

IMRT Intensity Modulated Radiation Therapy

LBNL Lawrence Berkeley National Laboratory

LET Linear Energy Transfer

LINAC Linear Accelerator

MAD-X Methodical Accelerator Design

MC Monte Carlo

MCS Multiple Coulomb Scattering

MGH Massachusetts General Hospital

MPV Most Probable Value

MR Magnetic Resonance

MU Monitor Unit

NWCR North West Cancer Research

OD Optical Density

PBS Pencil Beam Scanning

PBT Proton Beam Therapy

PET Positron Emission Tomography

PLY Polygon File Format

PMMA Poly(methyl methacrylate)

PSI Paul Scherrer Institute

QA Quality Assurance

QVS Quadrupole Variation Scan

RBE Relative Biological Effectiveness

RF Radio Frequency

RMS Root Mean Square

ROI Region of Interest

RT Radiation Therapy

SBD Stray Beam Detector

SOBP Spread Out Bragg Peak

SSB Single Strand Break

STL Stereolithography

SWM Switching Magnet

TOPAS Tool for Particle Simulation

TOT Time-Over-Threshold

TPS Treatment Planning Systems

UCL University College London

UOB University of Birmingham

VELO Vertex Locator

WET Water Equivalent Thickness

Bibliography

[1] J. Ferlay, M. Ervik, F. Lam, M. Colombet, L. Mery, M. Piñeros, A. Znaor, I. Soerjomataram, et al., "Global Cancer Observatory: Cancer Today,". URL: `https://gco.iarc.fr/today`.

[2] World Health Organisation, "Cancer,". URL: `https://www.who.int/news-room/fact-sheets/detail/cancer`.

[3] Cancer Research UK, "Cancer Statistics for the UK,". URL: `https://www.cancerresearchuk.org/health-professional/cancer-statistics-for-the-uk`.

[4] D. A. Jaffray and M. K. Gospodarowicz, "Radiation Therapy for Cancer," in *Cancer: Disease Control Priorities*, ch. 14, pp. 1–16, 3 ed., 2015.

[5] Public Health England, "Radiotherapy activity across England," tech. rep., 2017.

[6] R. Atun, D. A. Jaffray, M. B. Barton, F. Bray, M. Baumann, B. Vikram, T. P. Hanna, F. M. Knaul, et al., "Expanding global access to radiotherapy," *The Lancet Oncology*, vol. 16, no. 10, pp. 1153–1186, 2015.

[7] W. Röntgen, "On a new kind of rays," *Science*, vol. 53, no. 1369, pp. 274–276, 1896.

[8] M. Dosanjh, J. Bernier, E. A. Blakely, B. Jones, D. R. Grosshans, R. Mohan, M. Schippers, G. Landry, et al., *Advances in Particle Therapy: A Multidisciplinary Approach*. Series in Medical Physics and Biomedical Engineering, CRC Press, 2018.

[9] M. Mohiuddin, M. Fujita, W. F. Regine, A. S. Megooni, G. S. Ibbott, and M. M. Ahmed, "High-dose spatially-fractionated radiation (GRID): A new paradigm in the management of advanced cancers," *International Journal of Radiation Oncology Biology Physics*, vol. 45, no. 3, pp. 721–727, 1999.

[10] C. Billena and A. J. Khan, "A Current Review of Spatial Fractionation: Back to the Future?," *International Journal of Radiation Oncology Biology Physics*, vol. 104, no. 1, pp. 177–187, 2019.

[11] S. Bartzsch, S. Corde, J. C. Crosbie, L. Day, M. Donzelli, M. Krisch, M. Lerch, P. Pellicioli, et al., "Technical advances in x-ray microbeam radiation therapy," *Physics in Medicine and Biology*, vol. 65, no. 2, 2020.

[12] R. R. Wilson, "Radiological Use of Fast Protons," *Radiology*, vol. 47, pp. 487–491, nov 1946.

[13] A. Brown and H. Suit, "The centenary of the discovery of the Bragg peak," *Radiotherapy and Oncology*, vol. 73, no. 3, pp. 265–268, 2004.

[14] H. Paganetti, "Proton Therapy: History and Rationale," in *Proton Therapy Physics*, pp. 1–18, Boca Raton, Florida, USA: CRC Press, 2012.

[15] A. Kacperek, "Protontherapy of eye tumours in the UK: A review of treatment at Clatterbridge," *Applied Radiation and Isotopes*, vol. 67, no. 3, pp. 378–386, 2009.

[16] Particle Therapy Co-Operative Group (PTCOG), "Statistics of patients treated in particle therapy facilities worldwide,". URL: `https://www.ptcog.ch/index.php/patient-statistics`.

[17] Particle Therapy Co-Operative Group (PTCOG), "Particle therapy facilities,". URL: `https://www.ptcog.ch/index.php/facilities-in-operation`.

[18] B. Gottschalk, "Physics of Proton Interactions in Matter," in *Proton Therapy Physics*, p. 42, Boca Raton, Florida, USA: Taylor & Francis, 2012.

[19] R. Mohan and D. Grosshans, "Proton therapy – Present and future," *Advanced Drug Delivery Reviews*, vol. 109, pp. 26–44, 2017.

[20] H. Paganetti and P. Van Luijk, "Biological Considerations When Comparing Proton Therapy With Photon Therapy," *Seminars in Radiation Oncology*, vol. 23, pp. 77–87, apr 2013.

[21] H. Paganetti, "Relative biological effectiveness (RBE) values for proton beam therapy. Variations as a function of biological endpoint, dose, and linear energy transfer.," *Physics in Medicine and Biology*, vol. 59, no. 22, pp. R419–R472, 2014.

[22] R. Miralbell, A. Lomax, L. Cella, and U. Schneider, "Potential reduction of the incidence of radiation-induced second cancers by using proton beams in the treatment of pediatric tumors.," *International journal of radiation oncology, biology, physics*, vol. 54, no. 3, pp. 824–829, 2002.

[23] K. K. Mishra and I. K. Daftari, "Proton therapy for the management of uveal melanoma and other ocular tumors," *Chinese Clinical Oncology*, vol. 5, no. 4, pp. 1–7, 2016.

[24] H. Paganetti, "Proton relative biological effectiveness-uncertainties and opportunities," *International Journal of Particle Therapy*, vol. 5, no. 1, pp. 2–14, 2019.

[25] M. Dosanjh, B. Jones, J. Pawelke, M. Pruschy, and B. S. Sørensen, "Overview of research and therapy facilities for radiobiological experimental work in particle therapy. Report from the European Particle Therapy Network radiobiology group," *Radiotherapy and Oncology*, vol. 128, no. 1, pp. 14–18, 2018.

[26] J. M. Schippers, A. Lomax, A. Garonna, and K. Parodi, "Can Technological Improvements Reduce the Cost of Proton Radiation Therapy?," *Seminars in Radiation Oncology*, vol. 28, no. 2, pp. 150–159, 2018.

[27] A. Lühr, C. von Neubeck, J. Pawelke, A. Seidlitz, C. Peitzsch, S. M. Bentzen, T. Bortfeld, J. Debus, et al., ""Radiobiology of Proton Therapy": Results of an international expert workshop," *Radiotherapy and Oncology*, vol. 128, no. 1, pp. 56–67, 2018.

[28] B. Jones, "Towards achieving the full clinical potential of proton therapy by inclusion of LET and RBE models," *Cancers*, vol. 7, pp. 460–480, mar 2015.

[29] E. A. Blakely and M. Dosanjh, "Radiobiology and Hadron Therapy," in *Advances in Particle Therapy: A Multidisciplinary Approach*, p. 17, 2018.

[30] G. Landry, G. Dedes, M. Pinto, and K. Parodi, "Imaging and Particle Therapy," in *Advances in Particle Therapy: A Multidisciplinary Approach*, p. 28, 2018.

[31] A. Lomax, "What will the medical physics of proton therapy look like 10 yr from now? A personal view," *Medical Physics*, vol. 45, no. 11, pp. e984–e993, 2018.

[32] J. B. Farr, J. B. Flanz, A. Gerbershagen, and M. F. Moyers, "New horizons in particle therapy systems," *Medical Physics*, vol. 45, no. 11, pp. e953–e983, 2018.

[33] C. Bolan, "The promise of proton therapy," *Applied Radiation Oncology*, 2013.

[34] U. Linz and J. Alonso, "Laser-driven ion accelerators for tumor therapy revisited," *Physical Review Accelerators and Beams*, vol. 19, no. 12, pp. 1–8, 2016.

[35] U. Amaldi, S. Braccini, and P. Puggioni, "High Frequency Linacs for Hadrontherapy," *Reviews of Accelerator Science and Technology*, vol. 02, no. 01, pp. 111–131, 2009.

[36] K. J. Peach, M. Aslaninejad, R. J. Barlow, C. D. Beard, N. Bliss, J. H. Cobb, M. J. Easton, T. R. Edgecock, et al., "Conceptual design of a nonscaling fixed field alternating gradient accelerator for protons and carbon ions for charged particle therapy," *Physical Review Special Topics - Accelerators and Beams*, vol. 16, no. 3, pp. 1–34, 2013.

[37] H. Owen, A. Lomax, and S. Jolly, "Current and future accelerator technologies for charged particle therapy," *Nuclear Instruments and Methods in Physics Research, Section A: Accelerators, Spectrometers, Detectors and Associated Equipment*, vol. 809, pp. 96–104, 2016.

[38] M. Durante and H. Paganetti, "Nuclear physics in particle therapy: A review," *Reports on Progress in Physics*, vol. 79, sep 2016.

[39] R. Schnuerer, J. Yap, H. Zhang, T. Cybulski, T. Smith, G. Haefeli, O. Girard, T. Szumlak, et al., "Development of the LHCb VELO Detector Modules into a Standalone, Non-Invasive Online Beam Monitor for Medical Accelerators," *Instruments*, vol. 3, no. 1, p. 12, 2018.

[40] S. Agostinelli, J. Allison, K. Amako, J. Apostolakis, H. Araujo, P. Arce, M. Asai, D. Axen, et al., "GEANT4 - A simulation toolkit," *Nuclear Instruments and Methods in Physics Research, Section A: Accelerators, Spectrometers, Detectors and Associated Equipment*, vol. 506, no. 3, pp. 250–303, 2003.

[41] Ashland gafchromic™ radiology, "EBT3 film,". URL: `http://www.gafchromic.com/gafchromic-film/radiotherapy-films/EBT/index.asp`.

[42] R. Ballabriga, M. Campbell, E. Heijne, X. Llopart, L. Tlustos, and W. Wong, "Medipix3: A 64 k pixel detector readout chip working in single photon counting mode with improved spectrometric performance," *Nuclear Instruments and Methods in Physics Research, Section A: Accelerators, Spectrometers, Detectors and Associated Equipment*, vol. 633, no. SUPPL. 1, pp. S15–S18, 2011.

[43] CERN, "MAD - Methodical Accelerator Design,". URL: `http://madx.web.cern.ch/madx/`.

[44] L. Nevay, J. Snuverink, A. Abramov, L. Deacon, H. Garcia-Morales, S. Gibson, R. Kwee-Hinzmann, H. Pikhartova, et al., "BDSIM: An Accelerator Tracking Code with Particle-Matter Interactions," *Computer Physics Communications*, p. 107200, 2020.

[45] C. Granja, K. Kudela, J. Jakubek, P. Krist, D. Chvatil, J. Stursa, and S. Polansky, "Directional detection of charged particles and cosmic rays with the miniaturized radiation camera MiniPIX Timepix," *Nuclear Instruments and Methods in Physics Research, Section A: Accelerators, Spectrometers, Detectors and Associated Equipment*, vol. 911, no. September, pp. 142–152, 2018.

[46] U. Linz, *Ion Beam Therapy: Fundamentals, Technology, Clinical Applications*. Springer, 2012.

[47] H. Paganetti, "Proton Therapy," in *Proton Therapy Physics*, Series in Medical Physics and Biomedical Engineering, pp. 1–18, CRC Press, dec 2011.

[48] O. Mohamad, B. J. Sishc, J. Saha, A. Pompos, A. Rahimi, M. D. Story, A. J. Davis, and D. W. Kim, "Carbon ion radiotherapy: A review of clinical experiences and preclinical research, with an emphasis on DNA damage/repair," *Cancers*, vol. 9, no. 6, pp. 1–30, 2017.

[49] S. M. Seltzer, D. T. Bartlett, D. T. Burns, G. Dietze, H. G. Menzel, H. G. Paretzke, and A. Wambersie, "Fundamental quantities and units for ionizing radiation," Tech. Rep. 1, 2011.

[50] W. D. Newhauser and R. Zhang, "The physics of proton therapy," *Physics in Medicine & Biology*, vol. 60, no. 8, 2015.

[51] A. C. Kraan, "Range Verification Methods in Particle Therapy: Underlying Physics and Monte Carlo Modeling," *Frontiers in Oncology*, vol. 5, no. July, p. 150, 2015.

[52] B. Gottschalk, "Physics of Proton Interactions in Matter," in *Proton Therapy Physics*, Series in Medical Physics and Biomedical Engineering, pp. 19–60, CRC Press, dec 2011.

[53] T. Bortfeld, "An analytical approximation of the Bragg curve for therapeutic proton beams.," *Medical Physics*, vol. 24, no. 12, p. 2024, 1997.

[54] E. Pedroni, S. Scheib, T. Böhringer, A. Coray, M. Grossmann, S. Lin, and A. Lomax, "Experimental characterization and physical modelling of the dose distribution of scanned proton pencil beams.," *Physics in Medicine and Biology*, vol. 50, pp. 541–561, 2005.

[55] T. Cybulski, C. P. Welsch, C. Devlin, K. Hennessy, A. Kacperek, B. Marsland, I. Taylor, A. Wray, et al., "DESIGN AND FIRST OPERATION OF A SILICON-BASED NON – INVASIVE BEAM MONITOR," in *Proceedings of IPAC2014*, (Dresden), pp. 3712–3715, 2014.

[56] B. Gottschalk, E. W. Cascio, J. Daartz, and M. S. Wagner, "On the nuclear halo of a proton pencil beam stopping in water," *Physics in Medicine and Biology*, vol. 60, no. 14, pp. 5627–5654, 2015.

[57] A. Ariga, T. Ariga, S. Braccini, A. Ereditato, F. Giacoppo, K. Nesteruk, C. Pistillo, and P. Scampoli, "Characterization of the dose distribution in the halo region of a clinical proton pencil beam using emulsion film detectors," *Journal of Instrumentation*, vol. 10, no. 01, 2015.

[58] V. E. Bellinzona, M. Ciocca, a. Embriaco, a. Fontana, a. Mairani, M. Mori, and K. Parodi, "On the parametrization of lateral dose profiles in proton radiation therapy," *Physica Medica*, vol. 31, no. 5, pp. 1–9, 2015.

[59] J. Schwaab, S. Brons, J. Fieres, and K. Parodi, "Experimental characterization of lateral profiles of scanned proton and carbon ion pencil beams for improved beam models in ion therapy treatment planning.," *Physics in Medicine and Biology*, vol. 56, no. 24, pp. 7813–27, 2011.

[60] B. Gottschalk, E. W. Cascio, J. Daartz, and M. S. Wagner, "Nuclear halo of a 177 MeV proton beam in water: theory, measurement and parameterization," p. 55, 2014.

[61] J. da Silva, R. Ansorge, and R. Jena, "Fast Pencil Beam Dose Calculation for Proton Therapy Using a Double-Gaussian Beam Model.," *Frontiers in Oncology*, vol. 5, no. December, p. 281, 2015.

[62] B. Clasie, N. Depauw, M. Fransen, C. Gomà, H. R. Panahandeh, J. Seco, J. B. Flanz, and H. M. Kooy, "Golden beam data for proton pencil-beam scanning.," *Physics in medicine and biology*, vol. 57, no. 5, pp. 1147–58, 2012.

[63] A. V. Fedotov, "Mechanisms of halo formation," *AIP Conference Proceedings*, vol. 3, pp. 3–8, 2003.

[64] A. Aleksandrov, "Beam halo characterization and mitgation," *Proceedings of IPAC2016*, pp. 2–6, 2016.

[65] M. Valette, M. Valette, P. A. P. Nghiem, N. Pichoff, and C. E. A. D. R. F. Irfu, "CORE-HALO LIMITS AND BEAM HALO FORMATION DYNAMICS CORE-HALO LIMITS AND BEAM HALO FORMATION DYNAMICS," in *Proceedings of IPAC2016*, 2016.

[66] K. Wittenburg, "BEAM DIAGNOSTICS FOR THE DETECTION AND UNDERSTANDING OF BEAM HALO," in *Instrumentations and Beam Material Interactions*, (East-Lansing, MI, USA), pp. 183–186, 2014.

[67] N. Pichoff, P.-Y. Beauvais, and G. Haouat, "Halo From Coulomb Scattering of Beam Particles on Residual Gas," *Particle Accelerator Conference*, vol. 63, pp. 211–233, 2000.

[68] C. K. Allen and T. P. Wangler, "Beam halo definitions based upon moments of the particle distribution," *Physical Review Special Topics - Accelerators and Beams*, vol. 5, no. 12, pp. 48–54, 2002.

[69] K. T. McDonald and D. P. Russell, "Methods of emittance measurement," in *3rd Joint US-CERN School on Particle Accelerators: Frontiers of Particle Beams, Observation, Diagnosis and Correction*, (Capri), 2005.

[70] M. Silari, "Applications of particle accelerators in medicine," *Radiation Protection Dosimetry*, vol. 146, pp. 440–450, jul 2011.

[71] K. Peach, P. Wilson, and B. Jones, "Accelerator science in medical physics," *British Journal of Radiology*, vol. 84, no. Special Issue 2011, pp. 4–10, 2011.

[72] M. Schippers, "Proton Accelerators," in *Proton Therapy Physics*, Series in Medical Physics and Biomedical Engineering, pp. 61–102, CRC Press, dec 2011.

[73] S. Zaremba and W. Kleeven, "Cyclotrons: Magnetic Design and Beam Dynamics," no. 2, pp. 1–63, 2018.

[74] H. Paganetti and T. Bortfeld, "Proton beam radiotherapy - The State of the Art," *New Technologies in Radiation Oncology (Medical Radiology Series)*, 2005.

[75] C. Bert, S. O. Grözinger, and E. Rietzel, "Quantification of interplay effects of scanned particle beams and moving targets," *Physics in Medicine and Biology*, vol. 53, no. 9, pp. 2253–2265, 2008.

[76] U. Amaldi, R. Bonomi, S. Braccini, M. Crescenti, A. Degiovanni, M. Garlasch, A. Garonna, G. Magrin, et al., "Accelerators for hadrontherapy: From Lawrence cyclotrons to linacs," *Nuclear Instruments and Methods in Physics Research, Section A: Accelerators, Spectrometers, Detectors and Associated Equipment*, vol. 620, no. 2-3, pp. 563–577, 2010.

[77] D. Ungaro, A. Degiovanni, and P. Stabile, "LIGHT: A Linear Accelerator for Proton Therapy," *North American Particle Accelerator Conf.(NAPAC'16), Chicago, IL, USA, October 9-14, 2016*, pp. 1282–1286, 2017.

[78] S. Benedetti, A. Grudiev, and A. Latina, "High gradient linac for proton therapy," *Physical Review Accelerators and Beams*, vol. 20, no. 4, pp. 1–19, 2017.

[79] U. Amaldi and A. Degiovanni, "Proton and Carbon Linacs for Hadron Therapy," *Linac2014*, pp. 1207–1212, 2014.

[80] M. C. Vozenin, J. H. Hendry, and C. L. Limoli, "Biological Benefits of Ultra-high Dose Rate FLASH Radiotherapy: Sleeping Beauty Awoken," *Clinical Oncology*, vol. 31, no. 7, pp. 407–415, 2019.

[81] V. Favaudon, L. Caplier, V. Monceau, F. Pouzoulet, M. Sayarath, C. Fouillade, M. F. Poupon, I. Brito, et al., "Ultrahigh dose-rate FLASH irradiation increases the differential response between normal and tumor tissue in mice," *Science Translational Medicine*, vol. 6, no. 245, pp. 1–10, 2014.

[82] M. Durante, E. BräUer-Krisch, and M. Hill, "Faster and safer? FLASH ultra-high dose rate in radiotherapy," *British Journal of Radiology*, vol. 91, no. 1082, pp. 6–9, 2018.

[83] M. Lempart, B. Blad, G. Adrian, S. Bäck, T. Knöös, C. Ceberg, and K. Petersson, "Modifying a clinical linear accelerator for delivery of ultra-high dose rate irradiation," *Radiotherapy and Oncology*, no. 139, pp. 40–45, 2019.

[84] E. Schüler, S. Trovati, G. King, F. Lartey, M. Rafat, M. Villegas, A. J. Praxel, B. W. Loo, et al., "Experimental Platform for Ultra-high Dose Rate FLASH Irradiation of Small Animals Using a Clinical Linear Accelerator," *International Journal of Radiation Oncology Biology Physics*, vol. 97, no. 1, pp. 195–203, 2017.

[85] S. Jolly, H. Owen, M. Schippers, and C. Welsch, "Technical challenges for FLASH proton therapy," *Physica Medica*, vol. 78, no. August, pp. 71–82, 2020.

[86] J. Bourhis, P. Montay-Gruel, P. Gonçalves Jorge, C. Bailat, B. Petit, J. Ollivier, W. Jeanneret-Sozzi, M. Ozsahin, et al., "Clinical translation of FLASH radiotherapy: Why and how?," *Radiotherapy and Oncology*, vol. 139, pp. 11–17, 2019.

[87] K. Petersson, M. Jaccard, J. F. Germond, T. Buchillier, F. Bochud, J. Bourhis, M. C. Vozeninz, and C. Bailat, "High dose-per-pulse electron beam dosimetry - A saturation model for the Advanced Markus ionization chamber," *Strahlentherapie Und Onkologie*, vol. 192, no. 11, pp. 848–849, 2016.

[88] S. van de Water, S. Safai, J. M. Schippers, D. C. Weber, and A. J. Lomax, "Towards FLASH proton therapy: the impact of treatment planning and machine characteristics on achievable dose rates," *Acta Oncologica*, vol. 58, no. 10, pp. 1463–1469, 2019.

[89] E. S. Diffenderfer, I. I. Verginadis, M. M. Kim, K. Shoniyozov, A. Velalopoulou, D. Goia, M. Putt, S. Hagan, et al., "Design, Implementation, and in Vivo Validation of a Novel Proton FLASH Radiation Therapy System," *International Journal of Radiation Oncology Biology Physics*, vol. 106, no. 2, pp. 440–448, 2020.

[90] P. Montay-Gruel, K. Petersson, M. Jaccard, G. Boivin, J. F. Germond, B. Petit, R. Doenlen, V. Favaudon, et al., "Irradiation in a flash: Unique sparing of memory in mice after whole brain irradiation with dose rates above 100 Gy/s," *Radiotherapy and Oncology*, vol. 124, no. 3, pp. 365–369, 2017.

[91] J. R. Hughes and J. L. Parsons, "Flash radiotherapy: Current knowledge and future insights using proton-beam therapy," *International Journal of Molecular Sciences*, vol. 21, no. 18, pp. 1–14, 2020.

[92] R. J. Griffin, M. M. Ahmed, B. Amendola, O. Belyakov, S. M. Bentzen, K. T. Butterworth, S. Chang, C. N. Coleman, et al., "Understanding High-Dose, Ultra-High Dose Rate, and Spatially Fractionated Radiation Therapy," *International Journal of Radiation Oncology Biology Physics*, vol. 107, no. 4, pp. 766–778, 2020.

[93] N. W. Colangelo and E. I. Azzam, "The Importance and Clinical Implications of FLASH Ultra-High Dose-Rate Studies for Proton and Heavy Ion Radiotherapy," *Radiation Research*, vol. 193, no. 1, pp. 1–4, 2019.

[94] R. M. de Kruijff, "FLASH radiotherapy: ultra-high dose rates to spare healthy tissue," *International Journal of Radiation Biology*, vol. 96, no. 4, pp. 419–423, 2020.

[95] J. M. Schippers, "Beam-Transport Systems for Particle Therapy," in *Proceedings of the CAS-CERN Accelerator School: Accelerators for Medical Applications*, vol. 1, pp. 241–252, 2017.

[96] W. P. Jones and G. P. Berg, "Design of a beam transport system for a proton radiation therapy facility," in *Proceedings of the IEEE Particle Accelerator Conference*, vol. 4, pp. 2519–2521, 1999.

[97] M. M. Kats, "Gantry free transport line for a proton/ion therapy," *25th Russian Particle Accelerator Conference, RuPAC 2016*, pp. 120–122, 2016.

[98] S. Yan, H. M. Lu, J. Flanz, J. Adams, A. Trofimov, and T. Bortfeld, "Reassessment of the Necessity of the Proton Gantry: Analysis of Beam Orientations from 4332

Treatments at the Massachusetts General Hospital Proton Center over the Past 10 Years," *International Journal of Radiation Oncology Biology Physics*, vol. 95, no. 1, pp. 224–233, 2016.

[99] W. Wieszczycka and W. H. Scharf, *PROTONTHERAPY ACCELERATORS*. 2001.

[100] J. Flanz, "(The) future (of) synchrotrons for particle therapy,", Lecture notes.

[101] S. Giordanengo, M. Garella, F. Marchetto, F. Bourhaleb, M. Ciocca, A. Mirandola, V. Monaco, M. Hosseini, et al., "The CNAO dose delivery system for modulated scanning ion beam radiotherapy," *Medical Physics*, vol. 42, no. 1, pp. 263–276, 2015.

[102] W. Kleeven, "IBA Proton Therapy Systems - Accelerators, beamlines and gantry technology,".

[103] J. Flanz, "Particle Beam Scanning," in *Proton Therapy Physics*, Series in Medical Physics and Biomedical Engineering, pp. 157–190, CRC Press, dec 2011.

[104] M. Ciocca, G. Magro, E. Mastella, A. Mairani, A. Mirandola, S. Molinelli, S. Russo, A. Vai, et al., "Design and commissioning of the non-dedicated scanning proton beamline for ocular treatment at the synchrotron-based CNAO facility," *Medical Physics*, vol. 46, no. 4, pp. 1852–1862, 2019.

[105] W. F. Hartsell, R. Kapur, S. O. Hartsell, P. Sweeney, C. Lopes, A. Duggal, J. Cohen, J. Chang, et al., "Feasibility of Proton Beam Therapy for Ocular Melanoma Using a Novel 3D Treatment Planning Technique," *International Journal of Radiation Oncology Biology Physics*, vol. 95, no. 1, pp. 353–359, 2016.

[106] IOP, "Particle Physics - it matters," *2009*.

[107] J. Hrbacek, K. K. Mishra, A. Kacperek, R. Dendale, C. Nauraye, M. Auger, J. Herault, I. K. Daftari, et al., "Practice Patterns Analysis of Ocular Proton Therapy Centers: The International OPTIC Survey," *International Journal of Radiation Oncology Biology Physics*, vol. 95, no. 1, pp. 336–343, 2016.

[108] R. Slopsema, "Beam Delivery Using Passive Scattering," in *Proton Therapy Physics*, Series in Medical Physics and Biomedical Engineering, pp. 125–156, CRC Press, dec 2011.

[109] V. Cosgrove, A. Aro, S. Green, M. Scott, G. Taylor, D. Bonnett, and A. Kacperek, "Studies Relating to 62 MeV Proton Cancer Therapy of the Eye," *Radiation Protection Dosimetry*, vol. 44, no. 1/4, pp. 405–409, 1992.

[110] D. E. Bonnett, A. Kacperek, and M. A. Sheen, "Characteristics of a 62 MeV proton therapy beam," in *Proc. EPAC1990*, p. 1787, 1990.

[111] D. E. Bonnett, A. Kacperek, M. A. Sheen, R. Goodall, and T. E. Saxton, "The 62 MeV proton beam for the treatment of ocular melanoma at Clatterbridge," *The British Journal of Radiology*, vol. 66, pp. 907–914, oct 1993.

[112] D. E. Bonnett, "Current developments in proton therapy: a review," *Physics in Medicine & Biology*, no. 38, pp. 1371–1392, 1993.

[113] B. Arjomandy, P. Taylor, C. Ainsley, S. Safai, N. Sahoo, M. Pankuch, J. B. Farr, S. Yong Park, et al., "AAPM task group 224: Comprehensive proton therapy machine quality assurance," *Medical Physics*, vol. 46, no. 8, pp. e678–e705, 2019.

[114] P. Andreo, D. Burns, K. Hohlfeld, M. Huq, T. Kanai, F. Laitano, V. Smyth, and S. Vynckier, "Absorbed Dose Determination in External Beam Radiotheraphy: An International Code of Practice for Dosimetry based on Standards of Absorbed Dose to Water.," Tech. Rep. June, 2006.

[115] S. Giordanengo and H. Palmans, "Dose detectors, sensors, and their applications," *Medical Physics*, vol. 45, no. 11, pp. e1051–e1072, 2018.

[116] S. Giordanengo, L. Manganaro, and A. Vignati, "Review of technologies and procedures of clinical dosimetry for scanned ion beam radiotherapy," *Physica Medica*, vol. 43, no. March, pp. 79–99, 2017.

[117] C. P. Karger, O. Jäkel, H. Palmans, and T. Kanai, "Dosimetry for ion beam radiotherapy," *Physics in Medicine and Biology*, vol. 55, pp. 193–234, 2010.

[118] J. Seco, B. Clasie, and M. Partridge, "Review on the characteristics of radiation detectors for dosimetry and imaging.," *Physics in Medicine & Biology*, vol. 59, no. 20, pp. R303–47, 2014.

[119] O. Jäkel, G. H. Hartmann, C. P. Karger, P. Heeg, and S. Vatnitsky, "A calibration procedure for beam monitors in a scanned beam of heavy charged particles," *Medical Physics*, vol. 31, no. 5, pp. 1009–1013, 2004.

[120] PTC Europe, "Dosimetry and Position Sensing Ionization Chamber for Ion Beam Tracking,". URL: `http://www.ptceurope.com/PTC_Products.html`.

[121] R. Hollebeek, M. Newcomer, G. Mayers, B. Delgado, G. Shukla, R. Maughan, and D. Dolney, "A new technology for fast two-dimensional detection of proton therapy beams," *Physics Research International*, vol. 2012, no. i, 2012.

[122] J. T. Taylor, C. Waltham, T. Price, N. M. Allinson, P. P. Allport, G. L. Casse, A. Kacperek, S. Manger, et al., "A new silicon tracker for proton imaging and dosimetry," *Nuclear Instruments and Methods in Physics Research, Section A: Accelerators, Spectrometers, Detectors and Associated Equipment*, vol. 831, pp. 362–366, sep 2016.

[123] M. Bruzzi, "Novel silicon devices for radiation therapy monitoring," *Nuclear Instruments and Methods in Physics Research, Section A: Accelerators, Spectrometers, Detectors and Associated Equipment*, vol. 809, pp. 105–112, 2016.

[124] A. Vignati, V. Monaco, A. Attili, N. Cartiglia, M. Donetti, M. F. Mazinani, F. Fausti, M. Ferrero, et al., "Innovative thin silicon detectors for monitoring of therapeutic proton beams: Preliminary beam tests," *Journal of Instrumentation*, vol. 12, no. 12, 2017.

[125] A. Rozenfeld, G. Biasi, M. Petasecca, M. Lerch, G. Villani, and V. Feygelman, "Semiconductor dosimetry in modern external-beam radiation therapy," *Physics in Medicine & Biology*, 2020.

[126] CERN, "LHCb Photos,". URL: `http://cds.cern.ch/collection/LHCbPhotos?ln=en`.

[127] Nikhef, "Mechanical Design VErtex LOcator,". URL: `https://www.nikhef.nl/pub/departments/mt/projects/lhcb-vertex/`.

[128] T. Cybulski, *A Non-Invasive Beam Current Monitor for a Medical Accelerator*. PhD thesis, University of Liverpool, 2017.

[129] R. Schnuerer, *Non-invasive, silicon-based beam monitor for medical accelerators*. PhD thesis, University of Liverpool, 2020.

[130] The LHCb Collaboration, "Technical Design Report Reoptimized Detector Design and Performance," Tech. Rep. September, CERN, Geneva, 2003.

[131] The LHCb Collaboration, "The LHCb Detector at the LHC," tech. rep., CERN, 2008.

[132] D. Dossett, "Performance of the LHCb VELO," *Nuclear Instruments and Methods in Physics Research, Section A: Accelerators, Spectrometers, Detectors and Associated Equipment*, vol. 718, pp. 310–311, 2013.

[133] M. Battaglia, D. Schardt, J. Espino, M. Gallardo, M. Cortés-Giraldo, J. Quesada, A. Lallena, H. Miras, et al., "Dosimetric response of radiochromic films to protons of low energies in the Bragg peak region," *Physical Review Accelerators and Beams*, vol. 19, no. 6, p. 064701, 2016.

[134] R. Castriconi, M. Ciocca, A. Mirandola, C. Sini, S. Broggi, M. Schwarz, F. Fracchiolla, M. Martišíková, et al., "Dose–response of EBT3 radiochromic films to proton and carbon ion clinical beams," *Physics in Medicine and Biology*, vol. 62, pp. 377–393, jan 2017.

[135] M. Vadrucci, G. Esposito, C. Ronsivalle, R. Cherubini, F. Marracino, R. M. Montereali, L. Picardi, M. Piccinini, et al., "Calibration of GafChromic EBT3 for absorbed dose measurements in 5 MeV proton beam and 60Co γ-rays," *Medical Physics*, vol. 42, no. 8, pp. 4678–4684, 2015.

[136] S. Devic, J. Seuntjens, G. Hegyi, E. B. Podgorsak, C. G. Soares, A. S. Kirov, I. Ali, J. F. Williamson, et al., "Dosimetric properties of improved GafChromic films for seven different digitizers," *Medical Physics*, vol. 31, no. 9, pp. 2392–2401, 2004.

[137] M. Fuss, E. Sturtewagen, C. De Wagter, and D. Georg, "Dosimetric characterization of GafChromic EBT film and its implication on film dosimetry quality assurance," *Physics in Medicine and Biology*, vol. 52, no. 14, pp. 4211–4225, 2007.

[138] J. Sorriaux, A. Kacperek, S. Rossomme, J. A. Lee, D. Bertrand, S. Vynckier, and E. Sterpin, "Evaluation of Gafchromic EBT3 films characteristics in therapy photon, electron and proton beams," *Physica Medica*, vol. 29, pp. 599–606, nov 2013.

[139] A. Kacperek, "Ocular Proton Therapy Centers," in *Ion Beam Therapy: Fundamentals, Technology, Clinical Applications*, ch. 10, pp. 149–177, 2012.

[140] B. Damato, A. Kacperek, D. Errington, and H. Heimann, "Proton beam radiotherapy of uveal melanoma," *Saudi Journal of Ophthalmology*, vol. 27, pp. 151–157, jul 2013.

[141] C. R. Baker, T. E. Quine, J. N. H. Brunt, and A. Kacperek, "Monte Carlo simulation and polymer gel dosimetry of 60 MeV clinical proton beams for the treatment of ocular tumours," *Applied Radiation and Isotopes*, vol. 67, no. 3, pp. 402–405, 2009.

[142] C. Baker, D. Shipley, H. Palmans, and A. Kacperek, "Monte carlo modelling of a clinical proton beam-line for the treatment of ocular tumours," *Nuclear Instruments and Methods in Physics Research, Section A: Accelerators, Spectrometers, Detectors and Associated Equipment*, vol. 562, no. 2, pp. 1005–1008, 2006.

[143] D. R. Shipley, H. Palmans, C. Baker, and A. Kacperek, "GEANT4 simulation of an ocular proton beam & benchmark against MC codes," in *American Nuclear Society Topical Meeting in Monte Carlo*, pp. 7–8, 2005.

[144] G. A. Cirrone, G. Cuttone, F. Di Rosa, S. L. Nigro, M. G. Pia, L. Raffaele, and G. Russo, "Monte Carlo based implementation of an energy modulation system for proton therapy," *IEEE Nuclear Science Symposium Conference Record*, vol. 4, no. C, pp. 2133–2137, 2004.

[145] G. A. P. Cirrone, G. Cuttone, P. A. Lojacono, S. Lo Nigro, V. Mongelli, I. V. Patti, G. Privitera, L. Raffaele, et al., "A 62-MeV proton beam for the treatment of ocular melanoma at laboratori nazionali del sud-INFN," in *IEEE Transactions on Nuclear Science*, vol. 51, pp. 860–865, 2004.

[146] G. A. P. Cirrone, G. Cuttone, F. Di Rosa, L. Raffaele, G. Russo, and S. Guatelli, "The Geant4 toolkit capability in the hadron-therapy field: simulation of a transport beam line," *9th Topical Seminar on Innovative Particle and Radiation Detectors, Siena, Italy, May 23-26, 2004*, pp. 1–4, 2004.

[147] G. Cirrone, *Medical applications of the GEANT4 toolkit: Monte Carlo simulation of a proton therapy beam line.* PhD thesis, Universita degli Studi Di Catania, 2004.

[148] P. Chaudhary, T. I. Marshall, F. J. Currell, A. Kacperek, G. Schettino, and K. M. Prise, "Variations in the Processing of DNA Double-Strand Breaks Along 60-MeV Therapeutic Proton Beams," *International Journal of Radiation Oncology Biology Physics*, vol. 95, pp. 86–94, may 2016.

[149] G. Cuttone, G. A. Cirrone, G. Di Franco, V. la Monaca, S. Lo Nigro, J. Ott, S. Pittera, G. Privitera, et al., "CATANA protontherapy facility: The state of art of clinical and dosimetric experience," *European Physical Journal Plus*, vol. 126, no. 7, pp. 1–7, 2011.

[150] J. Allison, K. Amako, J. Apostolakis, P. Arce, M. Asai, T. Aso, E. Bagli, A. Bagulya, et al., "Recent developments in GEANT4," *Nuclear Instruments and Methods in Physics Research, Section A: Accelerators, Spectrometers, Detectors and Associated Equipment*, vol. 835, pp. 186–225, 2016.

[151] J. Allison, K. Amako, J. Apostolakis, H. Araujo, P. A. Dubois, M. Asai, G. Barrand, R. Capra, et al., "Geant4 developments and applications," *IEEE Transactions on Nuclear Science*, vol. 53, no. 1, pp. 270–278, 2006.

[152] Geant4 Collaboration, "Geant4 Book For Application Developers,". URL: `http://geant4-userdoc.web.cern.ch/geant4-userdoc/UsersGuides/ForApplicationDeveloper/html/index.html`.

[153] UCL, "Clatterbridge Simulation Model,". URL: `http://www.hep.ucl.ac.uk/pbt/wiki/Clatterbridge`.

[154] S. Guatelli, D. Cutajar, B. Oborn, and A. B. Rosenfeld, "Introduction to the GEANT4 simulation toolkit," *AIP Conference Proceedings*, vol. 1345, pp. 303–322, 2011.

[155] J. Yap, "Clatterbridge Scripts,". URL: `https://github.com/jacyap/Clatterbridge_scripts`.

[156] "ImageJ. Image Processing and Analysis in Java,". URL: `https://imagej.nih.gov/ij/`.

[157] R. Ballabriga, M. Campbell, and X. Llopart, "Asic developments for radiation imaging applications: The medipix and timepix family," *Nuclear Instruments and Methods in Physics Research, Section A: Accelerators, Spectrometers, Detectors and Associated Equipment*, vol. 878, no. June 2017, pp. 10–23, 2018.

[158] J. S. L. Yap, J. Resta-Lopez, R. Schnuerer, C. P. Welsch, N. J. S. Bal, M. Fransen, F. Linde, J. L. Parsons, et al., "BEAM CHARACTERISATION USING MEDIPIX3 AND EBT3 FILM AT THE CLATTERBRIDGE PROTON THERAPY BEAMLINE," in *Proceedings of IPAC2019*, pp. 8–11, 2019.

[159] S. Y. Lee, *Accelerator Physics*. 2011.

[160] H. Wiedemann, *Particle Accelerator Physics*. Springer International Publishing, 4th ed., 2015.

[161] A. Wolski, *Beam Dynamics In High Energy Particle Accelerators*. World Scientific Publishing Company, 2014.

[162] J. R. Rees, "Symplecticity in Beam Dynamics: An Introduction,", SLAC Publication 9939, 2003.

[163] J. Holmes, S. Henderson, and Y. Zhang, "Transverse Beam, Optics Part I,", Lecture Notes.

[164] R. Appleby, "Introduction to Beam Dynamics,", Cockcroft Lectures.

[165] P. Forck, *Lecture notes on beam instrumentation and diagnostics: Joint University Accelerator School*. 2011.

[166] U. Amaldi, P. Berra, K. Crandall, D. Toet, M. Weiss, R. Zennaro, E. Rosso, B. Szeless, et al., "LIBO - A linac-booster for protontherapy: Construction and tests of a prototype," *Nuclear Instruments and Methods in Physics Research, Section A: Accelerators, Spectrometers, Detectors and Associated Equipment*, vol. 521, no. 2-3, pp. 512–529, 2004.

[167] U. Amaldi, "Cancer therapy with particle accelerators," *Nuclear Physics A*, vol. 654, no. 1-2, pp. C375–C399, 1999.

[168] J. A. Clarke, D. M. Dykes, C. W. Horrabin, H. L. Owen, M. W. Poole, S. L. Smith, V. P. Suller, A. Kacperek, et al., "An Updated Assessment of a Medical Cyclotron As an Injector for an Energy Upgrade," in *Proceedings of EPAC1998*, (Stockholm), pp. 630–632, 1998.

[169] T. Cybulski, O. Karamyshev, C. P. Welsch, A. Kacperek, B. Marsland, I. Taylor, A. Wray, and A. Degiovanni, "BEAM EMITTANCE MEASUREMENTS AND BEAM TRANSPORT OPTIMISATION AT THE CLATTERBRIDGE CANCER CENTRE," in *Proceedings of IPAC2013*, (Shanghai, China), pp. 810–812, 2013.

[170] R. Dölling, S. Lin, P.-A. Duperrex, G. Gamma, and B. Keil, "BEAM DIAGNOSTICS FOR THE PROTON THERAPY FACILITY PROSCAN," in *Proceedings of Accelerator Applications 2007*, pp. 152–159, 2007.

[171] J. Yap, J. Resta-López, A. Kacperek, R. Schnuerer, S. Jolly, S. Boogert, and C. Welsch, "Beam characterisation studies of the 62 MeV proton therapy beamline at the Clatterbridge Cancer Centre," *Physica Medica*, vol. 77, no. January, pp. 108–120, 2020.

[172] T. E. Saxton, "Clatterbridge Cyclotron," tech. rep., 1981.

[173] UCL, "Clatterbrige Proton Treatment Centre Image Maps,". URL: `http://www.hep.ucl.ac.uk/pbt/wikiData/clatterbridge/ImageMaps/index.html`.

[174] C. Spencer, "INTRODUCTION to the DESIGN and FABRICATION of IRON-DOMINATED ACCELERATOR MAGNETS,", Lecture Notes.

[175] K. Wittenburg, "Halo and Bunch Purity Monitoring," *CERN Accelerator School, Report No. CERN-2009-005*, p. 557, 2009.

[176] R. Dölling, "Profile, Current, and Halo Monitors of the PROSCAN Beam Lines," in *Beam Instrumentation Workshop*, vol. 732, (Knoxville), pp. 244–252, AIP Conference Proceedings, 2004.

[177] M. Schwickert and A. Peters, "Diagnostic instrumentation for medical accelerator facilities," *8th European Workshop on Beam Diagnostics and Instrumentation for Particle Accelerators, DIPAC 2007*, pp. 381–385, 2007.

[178] J. M. Schippers, J. Duppich, G. Goitein, M. Jermann, A. Lomax, E. Pedroni, H. Reist, B. Timmermann, et al., "The use of protons in cancer therapy at PSI and related instrumentation," *Journal of Physics: Conference Series*, vol. 41, no. 1, pp. 61–71, 2006.

[179] S. H. Park, S. H. Lee, and Y. S. Kim, "Emittance Measurement for Beamline Extension at the PET Cyclotron," *Science and Technology of Nuclear Installations*, vol. 2016, pp. 1–4, mar 2016.

[180] K. Nesteruk, M. Auger, S. Braccini, T. Carzaniga, A. Ereditato, and P. Scampoli, "A system for online beam emittance measurements and proton beam characterization," *Journal of Instrumentation*, vol. 13, jan 2018.

[181] K. Nesteruk, *A New System for Online Measurement of the Beam Emittance of Particle Accelerators for Research and medical Applications.* PhD thesis, University of Bern, 2017.

[182] M. Auger, S. Braccini, T. S. Carzaniga, A. Ereditato, K. P. Nesteruk, and P. Scampoli, "A detector based on silica fibers for ion beam monitoring in a wide current range," *Journal of Instrumentation*, vol. 11, no. 03, p. P03027, 2016.

[183] L. Nevay, S. Boogert, A. Abramov, J. Albrecht, S. Alden, H. G. Morales, S. Gibson, H. Pikhartova, et al., "BDSIM documentation,". URL: `http://www.pp.rhul.ac.uk/bdsim/manual/introduction.html`.

[184] J. Perl, J. Shin, J. Schümann, B. Faddegon, and H. Paganetti, "TOPAS: An innovative proton Monte Carlo platform for research and clinical applications," *Medical Physics*, vol. 39, no. 11, pp. 6818–6837, 2012.

[185] J. Schuemann, A. L. McNamara, J. Ramos-Méndez, J. Perl, K. D. Held, H. Paganetti, S. Incerti, and B. Faddegon, "TOPAS-nBio: An Extension to the TOPAS Simulation Toolkit for Cellular and Sub-cellular Radiobiology," *Radiation Research*, vol. 191, no. 2, p. 125, 2019.

[186] J. Perl, J. Shin, J. Schuemann, J. R. Mendez, D. Hall, A. Biegun, and F. Guan, "TOPAS documentation,". URL: `https://topas.readthedocs.io/en/latest/index.html`.

[187] J. Yap, "TOPAS model of the 60 MeV Ocular Proton Therapy Beamline at the Clatterbridge Cancer Centre (CCC), Wirral, United Kingdom,". URL: `https://github.com/jacyap/ClatterbridgeTreatmentLine`.

[188] Autodesk, "Fusion 360,".

[189] D. A. Granville and G. O. Sawakuchi, "Comparison of linear energy transfer scoring techniques in Monte Carlo simulations of proton beams," *Physics in Medicine and Biology*, vol. 60, no. 14, pp. N283–N291, 2015.

[190] D. T. Goodhead, "Energy deposition stochastics and track structure: What about the target?," *Radiation Protection Dosimetry*, vol. 122, no. 1-4, pp. 3–15, 2006.

[191] H. Nikjoo, S. Uehara, and D. Emfietzoglou, *Interaction of Radiation with Matter*. Boca Raton, Florida, USA: CRC Press, 2012.

[192] M. C. Frese, J. J. Wilkens, P. E. Huber, A. D. Jensen, U. Oelfke, and Z. Taheri-Kadkhoda, "Application of constant vs. variable relative biological effectiveness in treatment planning of intensity-modulated proton therapy," *International Journal of Radiation Oncology Biology Physics*, vol. 79, no. 1, pp. 80–88, 2011.

[193] R. A. Britten, V. Nazaryan, L. K. Davis, S. B. Klein, D. Nichiporov, M. S. Mendonca, M. Wolanski, X. Nie, et al., "Variations in the RBE for cell killing along the depth-dose profile of a modulated proton therapy beam.," *Radiation Research*, vol. 179, no. 1, pp. 21–8, 2013.

[194] M. Fager, I. Toma-Dasu, M. Kirk, D. Dolney, E. S. Diffenderfer, N. Vapiwala, and A. Carabe, "Linear energy transfer painting with proton therapy: A means of reducing radiation doses with equivalent clinical effectiveness," *International Journal of Radiation Oncology Biology Physics*, vol. 91, no. 5, pp. 1057–1064, 2015.

[195] J. J. Wilkens and U. Oelfke, "Optimization of radiobiological effects in intensity modulated proton therapy.," *Medical physics*, vol. 32, no. 2, pp. 455–465, 2005.

[196] H. Paganetti, E. Blakely, A. Carabe-Fernandez, D. J. Carlson, I. J. Das, L. Dong, D. Grosshans, K. D. Held, et al., "Report of the AAPM TG-256 on the relative biological effectiveness of proton beams in radiation therapy," *Medical Physics*, vol. 46, no. 3, pp. e53–e78, 2019.

[197] J. J. Wilkens and U. Oelfke, "A phenomenological model for the relative biological effectiveness in therapeutic proton beams.," *Physics in medicine and biology*, vol. 49, no. 13, pp. 2811–2825, 2004.

[198] J. J. Wilkens and U. Oelfke, "Analytical linear energy transfer calculations for proton therapy.," *Medical physics*, vol. 30, no. 5, pp. 806–815, 2003.

[199] F. Romano, G. a. P. Cirrone, G. Cuttone, F. D. Rosa, S. E. Mazzaglia, I. Petrovic, a. R. Fira, and A. Varisano, "A Monte Carlo study for the calculation of the average linear energy transfer (LET) distributions for a clinical proton beam line and a radiobiological carbon ion beam line," *Physics in Medicine and Biology*, vol. 59, no. 12, pp. 2863–2882, 2014.

[200] M. A. Cortés-Giraldo and A. Carabe, "A critical study of different Monte Carlo scoring methods of dose average linear-energy-transfer maps calculated in voxelized geometries irradiated with clinical proton beams.," *Physics in medicine and biology*, vol. 60, no. 7, pp. 2645–69, 2015.

[201] C. Grassberger and H. Paganetti, "Elevated LET components in clinical proton beams," *Physics in Medicine and Biology*, vol. 56, pp. 6677–6691, 2011.

[202] F. Guan, C. Peeler, L. Bronk, C. Geng, R. Taleei, S. Randeniya, S. Ge, D. Mirkovic, et al., "Analysis of the track-and dose-averaged LET and LET spectra in proton therapy using the geant4 Monte Carlo code," vol. 42, no. November, pp. 1–34, 2015.

[203] A. C.-F. A. Bertolet, M. Cortés-Giraldo, "On the concepts of dose-mean lineal energy, unrestricted and restricted dose-averaged LET in proton therapy," *Physics in Medicine & Biology*, pp. 1–46, 2020.

[204] P. Chaudhary, T. I. Marshall, F. M. Perozziello, L. Manti, F. J. Currell, F. Hanton, S. J. McMahon, J. N. Kavanagh, et al., "Relative biological effectiveness variation along monoenergetic and modulated Bragg peaks of a 62-MeV therapeutic proton beam: A preclinical assessment," *International Journal of Radiation Oncology Biology Physics*, vol. 90, no. 1, pp. 27–35, 2014.

[205] C. M. Nickson, P. Moori, R. J. Carter, C. P. Rubbi, and J. L. Parsons, "Misregulation of DNA damage repair pathways in HPV-positive head and neck squamous cell carcinoma contributes to cellular radiosensitivity," *Oncotarget*, vol. 8, no. 18, pp. 29963–29975, 2017.

[206] R. J. Carter, C. M. Nickson, J. M. Thompson, A. Kacperek, M. A. Hill, and J. L. Parsons, "Characterisation of Deubiquitylating Enzymes in the Cellular Response to High-LET Ionizing Radiation and Complex DNA Damage," *International Journal of Radiation Oncology Biology Physics*, vol. 104, no. 3, pp. 656–665, 2019.

[207] R. J. Carter, C. M. Nickson, J. M. Thompson, A. Kacperek, M. A. Hill, and J. L. Parsons, "Complex DNA damage induced by high-LET α-particles and protons triggers a specific cellular DNA damage response," *International Journal of Radiation Oncology*Biology*Physics*, vol. 100, no. 3, pp. 776–784, 2017.

[208] E. T. Vitti and J. L. Parsons, "The radiobiological effects of proton beam therapy: Impact on DNA damage and repair," *Cancers*, vol. 11, no. 7, pp. 1–15, 2019.

[209] G. A. P. Cirrone, G. Cuttone, F. Di Rosa, S. E. Mazzaglia, F. Romano, A. Attili, F. Bourhaleb, G. Russo, et al., "Hadrontherapy: An open source, Geant4-based application for proton-ion therapy studies," *IEEE Nuclear Science Symposium Conference Record*, no. I, pp. 4186–4189, 2009.

[210] M. Brooke, *Incorporating biological factors in radiation therapy treatment planning.* PhD thesis, University of Oxford, 2020.

[211] X. Llopart, R. Ballabriga, M. Campbell, L. Tlustos, and W. Wong, "Timepix, a 65k programmable pixel readout chip for arrival time, energy and/or photon counting measurements," *Nuclear Instruments and Methods in Physics Research, Section A: Accelerators, Spectrometers, Detectors and Associated Equipment*, vol. 581, no. 1-2 SPEC. ISS., pp. 485–494, 2007.

[212] S. Hoang, L. Pinsky, R. Vilalta, and J. Jakubek, "LET estimation of heavy ion particles based on a timepix-based Si detector," *Journal of Physics: Conference Series*, vol. 396, 2012.

[213] L. Opalka, C. Granja, B. Hartmann, J. Jakubek, O. Jaekel, M. Martisikova, S. Pospisil, and J. Solc, "3D measurement of the radiation distribution in a water phantom in a hadron therapy beam," *Journal of Instrumentation*, vol. 7, no. 1, 2012.

[214] L. Opalka, C. Granja, B. Hartmann, J. Jakubek, O. Jaekel, M. Martisikova, S. Pospisil, and J. Solc, "Linear energy transfer and track pattern recognition of secondary radiation generated in hadron therapy beam in a PMMA target," *Journal of Instrumentation*, vol. 8, no. 2, 2013.

[215] J. Jakubek, C. Granja, B. Hartmann, O. Jaekel, M. Martisikova, L. Opalka, and S. Pospisil, "Selective detection of secondary particles and neutrons produced in ion beam therapy with 3D sensitive voxel detector," *Journal of Instrumentation*, vol. 6, no. 12, 2011.

[216] M. Jakubek, J. Jakubek, J. Zemlicka, M. Platkevic, V. Havranek, and V. Semian, "3D imaging of radiation damage in silicon sensor and spatial mapping of charge collection efficiency," *Journal of Instrumentation*, vol. 8, no. 3, 2013.

[217] N. Stoffle and L. Pinsky, "Identification of stopping ions in a silicon Timepix detector," *Nuclear Instruments and Methods in Physics Research, Section A: Accelerators, Spectrometers, Detectors and Associated Equipment*, vol. 880, no. October 2017, pp. 35–39, 2018.

[218] M. Martišíková, B. M. Hesse, O. Nairz, and O. Jäkel, "Test of an amorphous silicon detector in medical proton beams," in *Nuclear Instruments and Methods in Physics Research, Section A: Accelerators, Spectrometers, Detectors and Associated Equipment*, vol. 633, 2011.

[219] C. Granja, M. Martisikova, J. Jakubek, L. Opalka, and K. Gwosch, "Imaging and characterization of primary and secondary radiation in ion beam therapy," *AIP Conference Proceedings*, vol. 1753, 2016.

[220] C. Granja, J. Jakubek, S. Polansky, V. Zach, P. Krist, D. Chvatil, J. Stursa, M. Sommer, et al., "Resolving power of pixel detector Timepix for wide-range electron, proton and ion detection," *Nuclear Instruments and Methods in Physics*

Research, Section A: Accelerators, Spectrometers, Detectors and Associated Equipment, vol. 908, pp. 60–71, 2018.

[221] C. Granja, J. Jakubek, M. Martisikova, S. Kodaira, S. Polansky, P. Krist, V. Zach, and T. Matlocha, "Dynamic range and resolving power of the Timepix detector to heavy charged particles," *Journal of Instrumentation*, vol. 13, no. 11, 2018.

[222] D. Turecek and J. Jakubek, "PIXET Software package tool for control, readout and online display of pixel detectors Medipix/Timepix,", Advacam.

[223] P. Allport, M. Baca, D. Briglin, J. Broughton, R. Canavan, A. Chisholm, L. Gonella, P. Knights, et al., "Recent results and experience with the Birmingham MC40 irradiation facility," *Journal of Instrumentation*, vol. 12, no. 3, 2017.

[224] S. Spannagel, K. Wolters, D. Hynds, N. Alipour Tehrani, M. Benoit, D. Dannheim, N. Gauvin, A. Nürnberg, et al., "Allpix2: A modular simulation framework for silicon detectors," *Nuclear Instruments and Methods in Physics Research, Section A: Accelerators, Spectrometers, Detectors and Associated Equipment*, vol. 901, pp. 164–172, 2018.

[225] National Institute of Standards and Technology (NIST), "Stopping-Power & Range Tables for Electrons, Protons, and Helium Ions,". URL: `https://www.nist.gov/pml/stopping-power-range-tables-electrons-protons-and-helium-ions`.